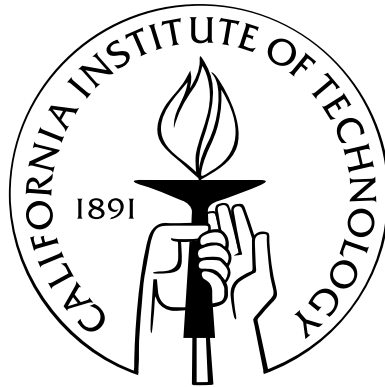


# EXPERIMENTAL AND ANALYTICAL STUDIES OF MERGING PLASMA LOOPS ON THE CALTECH SOLAR LOOP EXPERIMENT

Thesis by  
Rory J. Perkins

In Partial Fulfillment of the Requirements  
for the Degree of  
Doctor of Philosophy



California Institute of Technology  
Pasadena, California

2011  
(Submitted May 9, 2011)



# Acknowledgements

To begin at the beginning, I would like to thank my mother Cathy, who went through many pains to make education a priority for her children, and my father Rich, who taught me many handy skills in the HVAC field that have proved tremendously useful in lab. I would also like to thank my brother Jeff and sister Jenny for putting up with a truant brother and promise to visit home more often.

I am grateful to Professor Paul Bellan for all of his teachings in the classroom, in the laboratory, and in dealing with the culture of the scientific community. Paul is both the smartest and kindest advisor I have worked with, and I can hardly recall a time when Paul would not drop his work to listen to my questions and offer guidance. Not that working for Paul is a walk in the park; the following quote from Rumi captures the essence of writing a paper with Paul:

Although the grapes [graduate students] keep on bleeding blood and saying,  
 "I have had enough of this injustice [revisions] and cruelty [edits],"  
 the Stomper puts cotton in His ears: "I am not pressing out of ignorance.  
 If you wish to deny, you have an excuse, but I am the Master of this work.  
 When you reach perfection through My efforts and treading,  
 then you will thank Me exceedingly."

Perfection is too strong a word, at least according to some reviewers, but I do thank Paul... exceedingly. I also thank Dave Felt for his technical expertise in the realm of electronics and gadgeteering. His craftsmanship shines not only in the equipment he builds but also in the sage design advice he offers to students. I also thank our administrative assistant Connie Rodriguez for always rolling up her sleeves and dealing with the complicated mess of quotes, orders, and reimbursements.

The Japanese word sensei means "one who has walked the path before," and I would like to thank "Sensei" Deepak Kumar for his friendship and assistance both as a graduate student here and also afterwards. Deepak's graduation, though well-deserved, marked perhaps the greatest setback in my own work (in other words, thanks a lot... you jerk). I would also like to acknowledge the current students in the group: Eve Stenson, Auna Moser, Mark Kendall, Bao Ha, Vernon Chaplin, Xiang Zhai, and Zachary Tobin, for many useful discussions. In particular, I thank Vernon for showing me that plasma spectroscopy is not a dry and dreary topic as I once envisioned.

Caltech is wise enough to hire capable staff members to help its graduate students in both

technical and non-technical matters. I thank Joe Haggerty, Ali Kiani, and Brad St. John of the Aeronautic Machine Shop for building many components for our lab. I thank Karen Baumgartner for keeping the number of graduate student deaths to a minimum through her heroic work in the Safety Department. The Caltech yoga instructors Nancy Kyes, Kelley Flynn, and Jose Alavarado, have helped me stave off the back pains that accompany long hours of thesis writing, and I will be hard-pressed to find such a good set of instructors. I would also like to thank Helena Kopecky of the Caltech Counseling Center for all of her guidance and insight.

I have found a number of talented musicians through Caltech. Gerald Miller plays a mean guitar and bass, and I enjoyed many metal concerts with him. I hope that Andy Lamperski keeps Taco Trolley alive in the thumping and drumming of desks and chairs... just not in the room next to me. I hope that our Scottish-dancing singer-drummer James Maiolo has found musical happiness in his new home. To my current band, Jeff Lehew, Morgan Beeby, Mike Szerszunowicz and Arlen Jones, carry on the proud tradition of writing music that is inaccessible to 99% of the public. I am truly indebted to Jeff, through whom my guitar playing has grown tremendously since our first practices in a small Catalina apartment. I expect to see many internet videos of technical guitar covers, sweeps included... make Muhammed and me proud! To Morgan Beeby, self-proclaimed metal-snob and poser... I mean, bassist... thank you for putting up with all the 7/8 time signatures and tapping riffs, and thank you for simultaneously acting as manager and producer. To our singer Arlen, thank you for coming out to Pasadena on short notice; none of us could not have asked for better vocals. And to "Mad Ball" Mike, Lord of Nomenclature, did you ever imagine your name immortalized in scientific writing?

I also need to thank Colby Calvert for introducing me to the fine art of fermentation, Lenny Lucas for nearly killing me with several of his hikes, and Matthew Kelley for getting me out of lab for lunch on many occasions.

Finally, I thank my girlfriend Leslie Wenning for standing by me through this process. Her understanding and emotional support have kept me going through the ups and downs of research, and I wish her the best as she goes through her own process of becoming a doctor... a real one who actually helps people. I would also like to thank Edna Wenning, who made it impossible for me to starve during the writing of this thesis through the tireless cooking of Phillipino food.

Finally, there are several individuals who I would not like to acknowledge. I would not like to acknowledge A. Valadez of Caltech Parking, whose hyper-vigilant watch of the Caltech lots has cost me a pretty penny over the years. I would not like to acknowledge Leslie's cats, Madeleine, Winston, and Zelda, who continuously distracted me during the writing of this thesis. And I certainly do not wish to acknowledge the biologists and chemists who routinely invade the Watson courtyard during lunchtime and take up all the tables. That is all.

# Abstract

Of crucial importance for magnetized plasmas is magnetic helicity, a topological quantity that measures the knottedness or twistedness of the magnetic field. A universal relaxation theory, applicable to astrophysical and laboratory plasmas, dictates the evolution of plasmas towards an equilibrium state based solely on helicity content. The Caltech Solar Loop Experiment creates plasma with injected helicity to study this evolution, which can involve the merging of two plasma loops into a single structure. This thesis studies the merging using two techniques. The first is the construction of an array of vacuum photodiodes to measure extreme ultraviolet radiation from the experiment; the data provides information concerning non-equilibrium radiation losses and magnetic reconnection. The second is a Hamiltonian study of particle orbits to explain how particles can transition from being localized from one plasma loop to being shared among two neighboring loops. This shows how the merging process may initiate and also leads to a general theorem where the action variable serves as a Hamiltonian for the orbit-averaged system.

# Contents

<b>Acknowledgements</b>	<b>iii</b>
<b>Abstract</b>	<b>v</b>
<b>1 Overview and Purpose of the Caltech Experiments</b>	<b>1</b>
1.1 Magnetic Helicity . . . . .	2
1.2 Taylor States and Spheromaks . . . . .	4
1.3 Helicity Injection . . . . .	6
1.4 The Caltech Experiments . . . . .	7
1.4.1 The Caltech Solar Loop Experiment, Bright Spots, and Vacuum Photodiodes	8
1.4.2 Spheromaks, Spider Legs, and Particle Orbits . . . . .	10
<b>2 Nuts and Bolts: Operational Details of the Caltech Solar Experiment</b>	<b>13</b>
2.1 Creating the Plasma . . . . .	13
2.1.1 Vacuum Chamber and Plasma Electrode . . . . .	14
2.1.2 Injecting Neutral Gas . . . . .	15
2.1.3 Bias Magnetic Field . . . . .	17
2.1.4 Main Bank . . . . .	18
2.1.5 General Plasma Behavior . . . . .	19
2.2 Diagnosing the Plasma . . . . .	21
2.2.1 Fast Camera . . . . .	21
2.2.2 Plasma Current and Voltage . . . . .	22
2.2.3 X-Ray Diodes . . . . .	23
2.2.4 Spectrometer . . . . .	24
2.2.5 Data Acquisition . . . . .	25
<b>3 An Array of Vacuum Photodiodes</b>	<b>28</b>
3.1 Setup on the Test Chamber . . . . .	30
3.2 Photoemission and Cathode Design . . . . .	31

3.2.1	Review of the Photoelectric Effect in the UV . . . . .	32
3.2.2	Cathode Material and Surface Conditioning . . . . .	33
3.2.3	Measuring the Photocurrent . . . . .	34
3.2.4	The Need for a Bias Voltage . . . . .	36
3.3	Noise Issues . . . . .	39
3.3.1	Capacitive Coupling and Cathode-Anode Layout . . . . .	40
3.3.2	Inductive Pick-Up and Ground Loops . . . . .	43
3.3.3	Cables And Electrical Feedthroughs . . . . .	44
3.3.4	Blind Channel . . . . .	45
3.3.5	RF Noise and Ground Currents . . . . .	46
3.4	Charged Particle Background and Deflecting Magnets . . . . .	47
3.4.1	Examples of Spurious Signals . . . . .	47
3.4.2	Investigating the Spurious Signals . . . . .	48
3.4.3	Transient Voltages . . . . .	49
3.4.4	Upgrading the Magnets . . . . .	50
3.5	Physical Layout and Geometry . . . . .	51
3.5.1	Array Positioning . . . . .	51
3.5.2	Support System . . . . .	52
3.5.3	Collimation . . . . .	52
3.6	Final Product . . . . .	56
<b>4</b>	<b>Radiation Power and Electrode Detachment</b>	<b>65</b>
4.1	Radiative Losses, Ohmic Heating, and Line Emission . . . . .	65
4.1.1	Vacuum Photodiode Power Flux . . . . .	66
4.1.2	Ohmic Heating and Radiative Losses . . . . .	67
4.1.3	Hydrogen Line Emission . . . . .	71
4.1.4	Other Emission Processes . . . . .	77
4.2	Co- Vs. Counter-Helicity Merging . . . . .	80
4.2.1	Comparing Co- and Counter-Helicity Plasmas . . . . .	80
4.2.2	Magnetic Reconnection, Current Sheets, and Energetic Electrons . . . . .	83
4.3	Counter-Helicity Behavior as a Function of Neutral Gas Levels . . . . .	84
4.4	Bias Field Configuration . . . . .	87
4.5	Conclusions and Directions for Future Work . . . . .	88
<b>5</b>	<b>Hamiltonian Mechanics and Single Particle Motion</b>	<b>103</b>
5.1	A Theorem on the Action Integral of Periodic Motion . . . . .	104
5.1.1	A Clock Analogy . . . . .	104

5.1.2	Net Displacements and Differentiating the Action Variable . . . . .	106
5.1.3	Example: The Trivial Case . . . . .	108
5.1.4	Example: Kepler Motion . . . . .	108
5.1.5	Example: Vector Potentials and Charged Particles . . . . .	110
5.1.6	Example: Relativistic Mechanics and Relativistic $\mathbf{E} \times \mathbf{B}$ Drift . . . . .	110
5.1.7	Drifts and Averaged Coordinates . . . . .	115
5.1.8	Adiabatic Evolution and Reduced Systems . . . . .	116
5.1.9	Example: Particle in a Groove . . . . .	119
5.2	Charged Particle Motion in a Magnetic Field . . . . .	121
5.2.1	The Connection Between $J$ and $\mu$ . . . . .	121
5.2.2	The Grad-B Drift . . . . .	123
5.2.3	Parallel Dynamics: The Magnetic Mirror Force . . . . .	123
5.2.4	$\mathbf{E} \times \mathbf{B}$ Drifts . . . . .	126
5.2.5	Magnetic Flux Enclosed by a Gyro-Orbit . . . . .	130
5.2.6	Drift, Action, and Euler's Formula . . . . .	131
5.3	Conclusions . . . . .	131
<b>6</b>	<b>Plasma Loop Merging and the Two-Wire Problem</b>	<b>137</b>
6.1	Single Wire and $\mathbf{B} \sim \hat{\phi}/r$ Fields . . . . .	138
6.1.1	The Action and Drift Velocity for Planar Orbits . . . . .	139
6.1.2	Non-Planar Orbits . . . . .	142
6.1.3	Time-Varying Currents . . . . .	143
6.2	The Two-Wire Problem . . . . .	148
6.3	Time Dependence and Orbit Transitions . . . . .	151
6.3.1	Axial Electric Fields . . . . .	151
6.3.2	Computing the Field . . . . .	153
6.3.3	Drift Velocity . . . . .	155
6.4	Conclusions and Directions for Future Work . . . . .	155
<b>7</b>	<b>Conclusion</b>	<b>161</b>
<b>A</b>	<b>Improvements to the Plasma Current and Electrode Voltage Diagnostics</b>	<b>164</b>
A.1	Optoelectric Modules . . . . .	164
A.2	The HV Probe Grounding Clip . . . . .	165
A.3	Ground Loops and Isolation Transformers . . . . .	165
A.4	HV Probe Termination, Compensation, and Attenuation . . . . .	168
A.5	Reducing Noise . . . . .	170

<b>B</b>	<b>Magnetic Scattering of Charged Particles</b>	<b>172</b>
B.1	The Stormer Region . . . . .	172
B.2	Estimates of the Dipole Moment . . . . .	175
B.3	Estimates of Stormer Lengths . . . . .	178
B.4	Deflection Near Magnets . . . . .	180
<b>C</b>	<b>Review of Action-Angle Variables</b>	<b>182</b>
C.1	Canonical Transformations . . . . .	182
C.2	Action-Angle Variables . . . . .	184
C.3	Action-Angle Transformations for Multi-Dimensional Systems . . . . .	186
<b>D</b>	<b>Additional Calculations</b>	<b>189</b>
D.1	First-Order Correction and Guiding Center Definitions . . . . .	189
D.2	Cyclotron-Driven Pondermotive-Potential . . . . .	190
D.3	A Lemma on Averaging . . . . .	191
D.4	Flux Enclosed by an Orbit: Lab Frame Calculation . . . . .	192
D.5	Phase Space Contours . . . . .	194
	<b>Bibliography</b>	<b>197</b>

## Chapter 1

# Overview and Purpose of the Caltech Experiments

A plasma is an ionized gas that is thus subject to both fluid-type forces and electromagnetic forces. Of crucial importance for magnetized plasmas is the concept of magnetic helicity, a topological quantity that measures the knottedness or twistedness of the magnetic field. Helicity is approximately conserved throughout plasma evolution and often dissipates more slowly than magnetic energy. A universal relaxation theory, which applies to both astrophysical and laboratory plasmas, dictates that magnetized plasmas will naturally evolve towards an equilibrium state based on the helicity content of the plasma. Both the Caltech Solar Loop Experiment and the Caltech Spheromak Experiment create plasmas with injected helicity so that the evolution towards these relaxed equilibria can be studied. The evolution involves the merging of two or more plasma loops into a single structure, and this thesis studies the merging using two techniques. The first is the design, construction, and utilization of an array of vacuum photodiodes to measure extreme ultraviolet radiation from the Caltech Solar Loop Experiment; the data from the array provides information concerning both radiation losses and magnetic reconnection during the merging. The second is an analytical study of charged particle orbits in magnetic fields aimed at explaining how particle orbits can transition from being localized from one plasma loop to being shared symmetrically among two or more neighboring loops. This study gives insight into how the merging process is initiated.

The remainder of this chapter further develops the motivating ideas behind these studies. The concept of magnetic helicity is explored in more detail along with two additional topics: Woltjer-Taylor states and helicity injection. Woltjer-Taylor states are plasmas with a minimum of magnetic energy given a fixed helicity content, while helicity injection is the process of introducing helicity into a plasma in the first place. The Caltech experiments are grounded in these principles: both utilize novel plasma guns to inject helicity into plasmas and to observe their evolution towards Woltjer-Taylor states. Both projects described in this thesis are motivated by particular observations from these experiments.

Chapter 2 describes the Caltech Solar Loop Experiment and explains how the plasmas are formed and develop helicity. Vacuum photodiodes are then discussed in Chapter 3, which details the construction of the array and noise reduction techniques. Chapter 4 presents the measurements from the array together with other diagnostic data in the study of counter-helicity merging on the Solar Loop Experiment. Strong bursts in extreme ultraviolet radiation are observed; these bursts tend to be localized in space and time and are believed to be related to magnetic reconnection. Chapter 5 presents a new theory of Hamiltonian dynamics that originated from studies of particle trajectories in the Caltech experiments; we find that the action integral for the fastest periodic motion acts as an effective Hamiltonian for the reduced system. This chapter also applies this theorem to charged particle motion in magnetic fields. Chapter 6 presents a model to explain the onset of two plasma loops merging; the model shows how charged particles orbiting two parallel current channels can transition from orbits that remain confined to one current channel to orbits shared symmetrically between both channels. Finally, the appendices contain a description of modifications made to the voltage and current diagnostics for improved measurements, application of Stormer theory to the deflection of charged particles from a diagnostic, a review of action-angle variables and a canonical transformation to the orbit-averaged Hamiltonian system, and additional calculations concerning the application of the new Hamiltonian theory to charged particle motion.

## 1.1 Magnetic Helicity

Magnetic helicity is a measure of how knotted and twisted the magnetic field of the plasma becomes. Just as a head of hair can get tangled and twisted, so too can the magnetic field lines of a plasma knot and link each other. Magnetic helicity, like magnetic energy, is a conserved quantity for an ideal perfectly conducting plasma; for a realistic plasma with non-zero resistivity, magnetic helicity is often more resilient to resistive decay than magnetic energy. These properties have made helicity a key concept in fusion devices such as tokamaks and spheromaks and astrophysical plasmas such as solar coronal loops.

Magnetic helicity can be defined as the volume integral of a rather unusual quantity [1, ch. 3] [2, ch. 11] [3]:

$$K = \int \mathbf{A} \cdot \mathbf{B} \, d^3r, \quad (1.1)$$

where  $\mathbf{A}$  is a vector potential associated with  $\mathbf{B}$ :  $\nabla \times \mathbf{A} = \mathbf{B}$ . The above definition must be supplemented by the condition that the magnetic field cannot penetrate the boundary surface of the volume,  $\mathbf{B} \cdot d\mathbf{S} = 0$ , to ensure  $K$  is unchanged by a gauge transformation. We can prove this by making a gauge transformation  $\mathbf{A} \rightarrow \mathbf{A} + \nabla f$  and evaluating Eq. (1.1):

$$K = \int (\mathbf{A} + \nabla f) \cdot \mathbf{B} \, d^3r = \int \mathbf{A} \cdot \mathbf{B} \, d^3r + \int \nabla \cdot (f\mathbf{B}) \, d^3r \quad (1.2)$$

$$= \int \mathbf{A} \cdot \mathbf{B} \, d^3r + \oint f \mathbf{B} \cdot d\mathbf{S} = \int \mathbf{A} \cdot \mathbf{B} \, d^3r, \quad (1.3)$$

where the surface integral vanishes precisely because of the condition  $\mathbf{B} \cdot d\mathbf{S} = 0$ .  $K$  is thus independent of gauge even though the local helicity “density”  $\mathbf{A} \cdot \mathbf{B}$  is gauge-dependent. This suggests that helicity is not a local quantity but rather a quantity associated with an entire field line.

Eq. (1.1) obscures the physical interpretation of helicity as the knotting and twisting of the magnetic field. To make this connection, consider two closed flux tubes that link each other as shown in Fig. 1.1; one can show that Eq. (1.1) evaluates to

$$K = 2\Phi_1\Phi_2, \quad (1.4)$$

where  $\Phi_1$  and  $\Phi_2$  are the magnetic fluxes of the two flux tubes [2, ch. 11] [4]. If, however, the two flux tubes did not link each other, then the integral of Eq. (1.1) would vanish. This shows the topological nature of helicity. Analogous scenarios exist in fluid mechanics regarding the fluid vorticity [5].

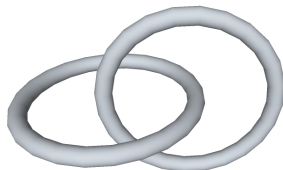


Figure 1.1: Two magnetic flux tubes, or bundles of magnetic field lines, that link each other have non-zero helicity content.

The above example shows that helicity measures the linkage of flux tubes, but helicity is also present when a flux tube is twisted. The flux tube depicted in Fig. 1.2 has a helical magnetic field that can be decomposed into an axial field and an azimuthal field. The azimuthal field clearly wraps around and links the axial field, so the helical magnetic field configuration also has helicity.

Remarkably, magnetic helicity is conserved under ideal magnetohydrodynamic<sup>1</sup> (MHD) conditions. This can be proved by taking a time derivative of Eq. (1.1) [1, sec. 3.7], but an intuitive picture is as follows. In ideal MHD, each magnetic field line retains its identity and cannot break or tear [6]. In this case, the analogy to hair is quite accurate; it is as if the magnetic field lines were actual physical strands that cannot be unlinked without tearing the strands themselves. For instance, under ideal MHD evolution, the two flux tubes in Fig. 1.1 would remain forever linked.

In non-ideal plasmas, electrical resistivity causes diffusion of the magnetic field inside the plasma

---

<sup>1</sup>Magnetohydrodynamics is one of several possible descriptions of plasma; it treats the plasma as a conducting fluid that carries a current [2, sec. 2.6]. Ideal MHD assumes that the plasma has no resistivity.

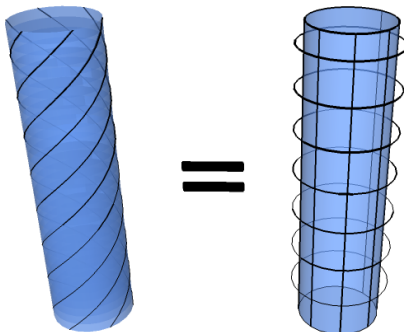


Figure 1.2: A helical flux tube contains helicity and can be thought of as a superposition of an axial field and a toroidal field.

so that field lines do not retain their identity and can meld with each other, but magnetic helicity is remarkably still conserved even under such conditions [1, sec. 3.9 - 3.12]. This process of field lines melding is known as magnetic reconnection [7] and typically involves the annihilation of a component of magnetic field and dissipation of magnetic energy. For instance, the two linked loops can reconnect and form a larger loop as shown in Fig. 1.3. While reconnection typically lowers the magnetic energy of the plasma, the global magnetic helicity is much more nearly conserved. For instance, in Fig. 1.3, helicity has not been destroyed but is rather changed from the linkage of two flux tubes to twist or writhe in the final flux tube. The skeptical reader is referred to Ref. [8], which explains how the above transition of helicity can be seen quite intuitively using simple household items.

## 1.2 Taylor States and Spheromaks

The idea that magnetic helicity is better conserved than magnetic energy was pushed to an extreme by Taylor, who reasoned that a plasma would continue to undergo magnetic reconnection until it reached a state of minimum magnetic energy given the constraint of constant helicity [6]. Such a variational problem had been proposed by Woltjer [9], who concluded that such plasmas must satisfy

$$\nabla \times \mathbf{B} = \lambda \mathbf{B}, \quad (1.5)$$

where  $\lambda$  is a constant. Since  $\nabla \times \mathbf{B} = \mu_0 \mathbf{J}^2$ , this condition states that the current density is everywhere parallel to the magnetic field. Such states are now known as Woltjer-Taylor states and

---

<sup>2</sup>In MHD, the displacement current in Ampere's law is quite small and ignored.



Figure 1.3: With electrical resistivity, magnetic reconnection allows the flux tubes to meld and unlink. However, the helicity lost in the linkage of the flux tubes is now found in the twist of the final flux tube.

are supposed to be equilibrium states as follows. The equation of motion for ideal MHD is

$$\rho \frac{d\mathbf{u}}{dt} = -\nabla P + \mathbf{J} \times \mathbf{B}, \quad (1.6)$$

where  $\rho$  is the mass density,  $\mathbf{u}$  is the velocity, and  $P$  is the pressure. Eq. (1.6) is essentially Newton's second law for a continuous fluid; the lefthand side of Eq. (1.6) is the inertial term, and the righthand side consists of forces acting on the plasma. For many plasmas, the magnitude of the pressure  $P$  is much less than the magnetic energy density  $B^2/2\mu_0$ , and the pressure term in Eq. (1.6) can be ignored. Such plasmas are referred to as low  $\beta$ , where  $\beta = 2\mu_0 P/B^2$ , the ratio of the thermal energy density to the magnetic energy density. For a low  $\beta$  plasma that is also in equilibrium, the lefthand vanishes as well. Eq. (1.6) is then  $0 = \mathbf{J} \times \mathbf{B}$ , which is satisfied when  $\nabla \times \mathbf{B} = \lambda \mathbf{B}$ .

It should be noted that the condition  $\mathbf{J} \times \mathbf{B} = 0$  is satisfied more generally by a field

$$\nabla \times \mathbf{B} = \lambda(\mathbf{r})\mathbf{B}, \quad (1.7)$$

where  $\lambda$  is now not constant but is a function of position. Plasmas that satisfy Eq. (1.7) are known as force-free plasmas. Clearly, all Woltjer-Taylor states are force-free, but the converse is not true. Force-free plasmas may be in equilibrium, but they generally contain more magnetic energy than the Woltjer-Taylor states with the same helicity, since the latter minimize energy by definition. Therefore, while force-free states may be in equilibrium, the equilibrium is unstable as the plasma can further shed magnetic energy via reconnection.

A plasma, in the absence of outside constraints, naturally tends towards a Woltjer-Taylor state

determined solely by the magnetic field boundary conditions and the amount of helicity in the plasma. This is a powerful concept with applications to both laboratory devices and astrophysics. Using this idea, Taylor explains why laboratory devices such as a reverse-field pinch always settle down to the same state despite variations of experimental parameters [6]. Allowing the plasma to reach a Woltjer-Taylor state in a simply connected volume gives the configuration known as a spheromak, a magnetic-confinement concept aimed at achieving nuclear fusion [2, 10]. Astrophysical plasmas, including solar coronal loops, are also frequently assumed to be in Woltjer-Taylor states [11, 12, 13, 14, 15].

### 1.3 Helicity Injection

Magnetic helicity is an important concept but is only well-defined when the magnetic field lines do not penetrate the bounding volume. In situations such as the one depicted in Fig. 1.4, helicity is not well-defined because the volume of interest does not enclose all field lines. However, in such situations, it is possible to define a new but related quantity, called relative helicity, that is gauge-independent [1, sec. 3.5] [3, 16]. Relative helicity is essentially the difference in helicity of the magnetic field from a reference field; it resolves the gauge ambiguity while preserving the essence of helicity.

In such situations, it is possible to *inject* relative helicity into the system by applying a voltage between the points at which the magnetic field enters and leaves the volume [1, sec. 3.7]. The rate for helicity injection is, ignoring dissipation,

$$\frac{dK}{dt} = 2V\Phi, \quad (1.8)$$

where  $V$  is the voltage difference and  $\Phi$  is the magnetic flux penetrating the boundary. Helicity injection can be understood intuitively as follows. Suppose that in Fig. 1.4 the field lines inside the flux tube point axially along the tube with no wrapping or twisting around the tube. A voltage applied between the points where the field lines penetrate the boundary drives currents along these field lines, and these currents generate their own field that wraps around the original field lines according to the righthand rule. The superposition of the original field, which is directed along the flux tube, and the field generated by the currents, which wraps around the flux tube, is a helical field which twists in proportion to the current driven. As twisted field lines contain helicity, we see that the applied voltage is indeed increasing the helicity content of the plasma. Indeed, this is precisely what happens in the Caltech experiments and will be discussed further in Sec. 2.1.3

The concept of helicity injection may seem incompatible with Woltjer-Taylor states because the former implies a time-varying helicity content whereas the latter describes an equilibrium. Nonetheless, it is often assumed in many spheromak experiments that the rate of helicity injection is slow

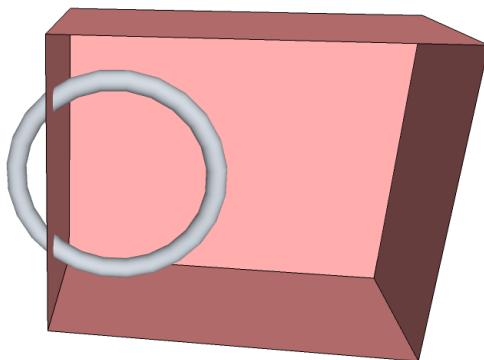


Figure 1.4: If the magnetic field penetrates the boundary, depicted by the red box, then the usual definition of helicity becomes gauge-dependent. In such cases, it is possible to define a relative helicity that is gauge-independent, and it is possible to inject relative helicity into the volume by applying a potential difference between the points where the magnetic field enters and leaves the volume.

enough so that the plasma settles down to the Woltjer-Taylor state determined by the instantaneous value of the plasma gun current. This scenario is called a “driven spheromak” [1, ch. 11].

## 1.4 The Caltech Experiments

Woltjer-Taylor states depend solely on the magnetic boundary conditions and helicity content with no dependence on the plasma density, temperature, or flow. Plasmas starting with varying densities, flows, etc., may, by Taylor’s theory, evolve to the same equilibrium state as determined by the total helicity content. However, it is not clear exactly how the plasma evolves towards this equilibrium: the plasma may evolve through a sequence of Woltjer-Taylor states throughout its entire lifetime as in the driven spheromak picture, or it may be out of a force-free state in its initial stages.

The Caltech experiments allow research into plasma formation and the steps needed to reach a Woltjer-Taylor state. Both Caltech experiments use planar magnetized plasma guns to create plasma and inject helicity into them. These planar guns, in contrast to the typical coaxial design, allow direct observation of the plasma in its infantile stages. Experiments at Caltech have shown that modeling plasma evolution as a sequence of Woltjer-Taylor states is too simplistic and that plasma flows and pressures *are* important [17].

The two topics of this thesis, an array of vacuum photodiodes and a Hamiltonian picture for particle orbits, evolved out of helicity studies done on both the Solar Loop Experiment and the Spheromak Experiment. We describe each in turn.

### 1.4.1 The Caltech Solar Loop Experiment, Bright Spots, and Vacuum Photodiodes

The Caltech Solar Loop Experiment creates plasma arcs resembling solar coronal loops on the sun's surface [18, 19, 20] as shown in Fig. 1.5. While there is an obvious discrepancy in size, temperature, density, and field strength between a laboratory plasma and the solar corona, the underlying physics is the same [21, sec. 1.3.1] [18]. Indeed, the solar corona is often modeled as a force-free or Woltjer-Taylor state [11, 12, 14, 15], so studies of near force-free plasma loops in the laboratory are expected to give insight into solar phenomena, particularly the impulsive eruption of coronal loops [22].

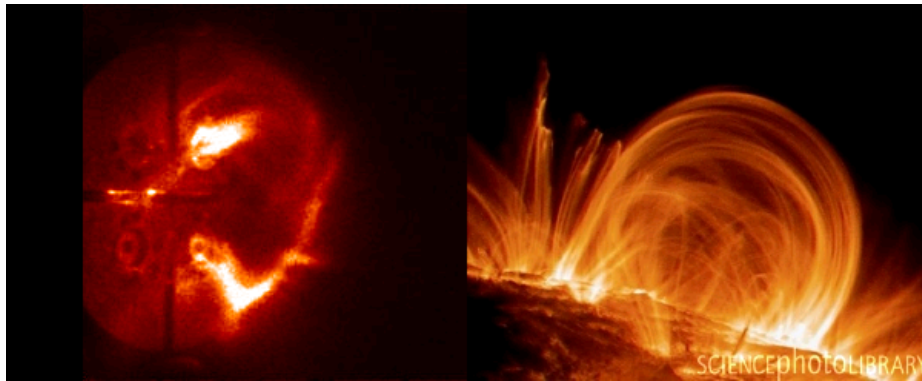


Figure 1.5: The plasma loops created by the Caltech Solar Loop Experiment are designed to resemble plasma structures on the surface of the sun. The image on the right is from the TRACE satellite.

It has been proposed that the sudden eruption of solar prominences might be triggered by the interaction of two magnetic structures [15], and this possibility was explored on the Caltech Solar Loop Experiment by producing two loops side-by-side [20]. The loops carry parallel currents and hence attract each other and merge together. Previous studies of two merging plasmas suggest that the final state after the merging is determined by the initial helicity content in accordance with Taylor's theorem [23, 24, 25, 26]. Similarly, the Caltech Solar Loop Experiment produces two loops with either the same helicity, called co-helicity, or opposite helicities, called counter-helicity, and the difference in helicity content results in different plasma behavior. In co-helicity experiments, one of the two loops tends to expand sooner and faster than the other. In counter-helicity experiments, a bright spot appears at the loop apex, and, around the same time, a burst of soft x-rays registers on a set of x-ray diodes. Fig. 1.6 shows an example of both the bright spot and the x-ray burst, and the possible correlation of these two events forms the original motivation for the array of vacuum photodiodes, as will be discussed.

The reason for both the bright spot and the x-ray bursts is believed to be the extra amount of magnetic reconnection that occurs for counter-helicity merging. Magnetic reconnection is present in both co- and counter-helicity merging because the azimuthal field, the field that is generated

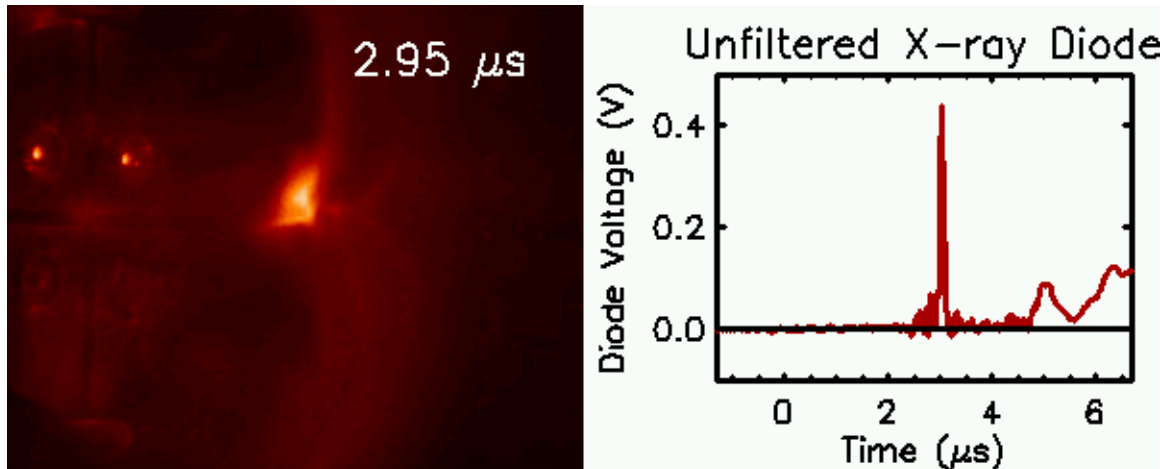


Figure 1.6: In counter-helicity merging, a bright spot forms in the central regions. At the same time, a burst of soft x-rays registers on the x-ray diodes. The array of vacuum photodiodes was constructed to study these phenomena further.

by the plasma current and that wraps around the plasma loop, is the same for both experiments and is annihilated as the loops merge; see Fig. 1.7. There is additional magnetic reconnection in counter-helicity experiments because the axial fields also annihilate, as shown in Fig. 1.7. This additional reconnection is not present in co-helicity experiments because, in that case, the axial fields are parallel, not anti-parallel, and do not annihilate. Magnetic reconnection involves a decrease in magnetic energy that is transferred to the plasma particles [7], and both the bright spot and the x-ray bursts are thought to be energized by the additional amount of reconnection, and hence energy released, in counter-helicity experiments. The bright spot is believed to be caused by the formation of a strong current sheet between the two loops as they merge; the current sheet deposits thermal energy into the plasma by Ohmic dissipation, and this thermal energy is then lost to radiation [27, sec. 1.2]. The enhanced x-ray emission might be due to a population of energetic electrons that are accelerated by the reconnection process [28, 29]; these energetic electrons would emit x-rays through bremsstrahlung. The correlation between x-rays and MHD activity such as sawtooth oscillations has been known for some time [30], but recently these x-rays have been ascribed to electrons directly energized by the magnetic reconnection associated with the MHD activity [31, 32].

This pair of phenomena, bright spots and x-ray bursts, motivate the vacuum photodiode array described in Chapter 3. The bright spot forms consistently from shot to shot, but the x-ray bursts are rather fickle. Indeed the large variations in the x-ray signals are documented by Hansen et. al., who quoted x-ray signals, averaged over a number of shots, of  $176.3 \pm 100.6$  mV [20]. The possible explanation for such large variations are numerous. The x-ray burst might not happen every shot, or perhaps it emits in variable directions. The x-ray diodes have a single line of sight to the plasma, and their alignment is quite sensitive to small changes in its inclination angle, so perhaps the x-ray bursts

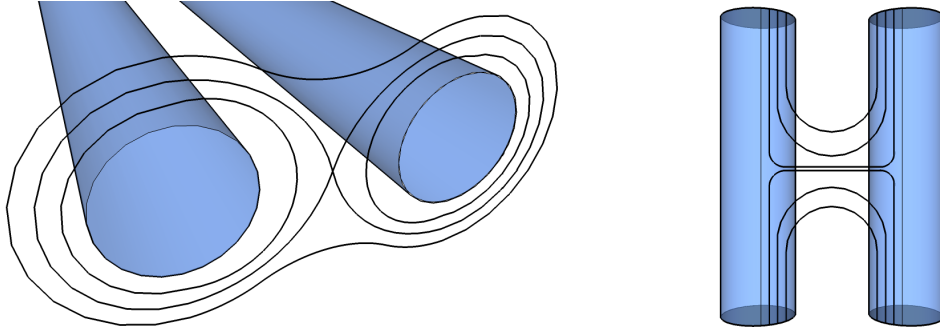


Figure 1.7: Counter-helicity merging involves two types of magnetic reconnection: (a) the azimuthal component, generated by the plasma current, and (b) the axial component, generated by the bias field coils. Co-helicity merging only involves the first type.

occur consistently but are not observed consistently by the diodes. To address these possibilities, an array of radiation detectors was needed to provide spatial as well as temporal resolution, and vacuum photodiodes were selected based on their low material cost and potential to scale into an array. The design of the array is discussed in Chapter 3, while Chapter 4 presents the experimental results.

#### 1.4.2 Spheromaks, Spider Legs, and Particle Orbits

The Spheromak Experiment produces spheromaks using a novel plasma gun in which the electrodes are co-planar and concentric as opposed to being coaxial cylinders. The planar electrodes allow direct observation of the plasma during its initial stages when, as shown in Fig. 1.8, the plasma consists of eight loops, or “spider legs.” This eightfold symmetry occurs because the gas for the plasma is injected through eight pairs of gas inlets; the eightfold symmetry is in contrast to the initial magnetic field, which is generated by a coil of wire behind the electrodes and is entirely axisymmetric. The Woltjer-Taylor state for the magnetic boundary conditions is hence axisymmetric, and, indeed, the spider legs quickly expand and merge to form an axisymmetric plasma, as shown in Fig. 1.8. The exact mechanism of how the plasma transitions from the eightfold symmetry of the initial gas distribution to the axisymmetry of the magnetic field boundary conditions is not clear, and an explanation is sought by studying the motion of single charged particles in magnetic fields that model the Spheromak Experiment.

Single particle motion provides a rather detailed perspective of plasma by following one particle through the electromagnetic field of the plasma. Such an approach is quite different from but complementary to a fluid-like description such as MHD. A robust approximation scheme to the motion of a charged particle through rather arbitrary magnetic fields was developed by Alfvén [33]. In a uniform magnetic field, particle motion in the plane normal to  $\mathbf{B}$  is perfectly circular and is referred to as Larmor motion. Alfvén studied particle motion when the strength and direction of

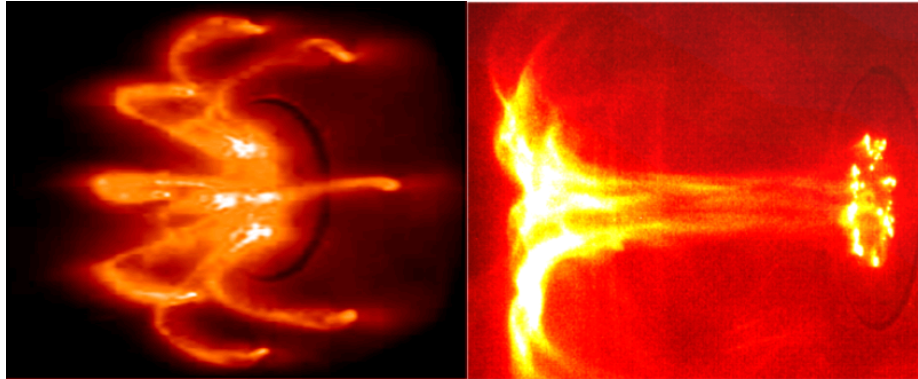


Figure 1.8: The spheromak starts out as eight discrete spider legs but eventually merges into an axisymmetric configuration.

the magnetic field varied and concluded that the particle still executes Larmor-like motion except that the center of the circle slowly drifts over the course of many orbits. A set of equations, known as guiding center theory [2, ch. 3], describes the average position of the particle without providing the details of the Larmor motion. These equations provide a substantial simplification of the exact equations of motion and hold quite generally as long as the magnetic field does not change much over the course of a Larmor orbit. These equations can be derived by averaging Newton's law:

$$m \frac{d\mathbf{v}}{dt} = q\mathbf{E}(\mathbf{r}, t) + q\mathbf{v} \times \mathbf{B}(\mathbf{r}, t). \quad (1.9)$$

To study particle motion in the Spheromak experiment, we employ a Hamiltonian approach. Hamiltonian mechanics is a formulation of mechanics in which a single function, the Hamiltonian, generates all equations of motion. Hamiltonian mechanics is entirely equivalent to using Newton's law but often leads to different insights. In this case, the Hamiltonian approach reveals a surprising connection between the guiding center equations and another aspect of charged particle motion, adiabatic invariants [2, sec. 3.3] [34, sec. 49], which are quantities that are approximately conserved over long periods of time even when other quantities, such as energy, are not. For instance, the first adiabatic invariant  $\mu$  [33, sec. 2.3] is

$$\mu = \frac{(1/2)mv_L^2}{B}, \quad (1.10)$$

where  $v_L$  is the Larmor velocity. Up to three adiabatic invariants can be found for charged particle motion [35]. The Hamiltonian theory presented in this thesis states that the adiabatic invariant associated with the fastest periodic motion acts as an effective Hamiltonian for the reduced or orbit-averaged system. For charged particle motion, this means that  $\mu$  acts as a Hamiltonian for the guiding center motion. The strength of the new Hamiltonian theory presented here, however, is that it applies more generally than charged particle motion, and, in this way, concepts from guiding center theory are generalized to a broader class of systems.

Chapter 5 describes the new Hamiltonian theory in its full generality and also applies it to charged particle motion in electromagnetic fields. Chapter 6 returns to the original problem of explaining the merging of the spider legs. There, a model magnetic field for the experiment is introduced that supports two classes of trajectories, those shared symmetrically between two plasma loops and those confined to a single loop. A mechanism for transitions between the two classes is then proposed. Although the model greatly simplifies the complexity of the actual experiment, it provides a good starting point for future investigation.

## Chapter 2

# Nuts and Bolts: Operational Details of the Caltech Solar Experiment

The Solar Loop Experiment starts with nothing: no gas and no electromagnetic fields. Into this vacuum, the gas and magnetic field are introduced a few milliseconds prior to the experiment. At a precisely timed moment, a large capacitor bank discharges across the electrodes, initiating breakdown of the neutral gas and forming a plasma that lasts less than 10  $\mu\text{s}$ . In this short time window, a set of diagnostics acquire a variety of data such as fast camera images, the plasma current, the electrode voltage, and x-ray emission levels. All of this occurs literally faster than the blink of an eye.

This chapter describes the Caltech Solar Loop Experiment both in setup and in operation. Sec. 2.1 outlines the steps taken to create a plasma, the experimental parameters that can be controlled, and the general plasma behavior. Sec. 2.2 then details the existing diagnostics along with their specifications. These diagnostics include fast cameras, a Rogowski coil, a high-voltage probe, x-ray diodes, and an optical spectrometer.

### 2.1 Creating the Plasma

This section discusses the steps taken to create the plasma: the injection of neutral gas, the creation of a bias magnetic field, the discharge of the main bank, breakdown, and general plasma behavior. Concurrent with this description, we shall see the different experimental parameters that can be controlled to obtain different plasma behavior. These parameters include the gas species, gas line pressure, gas valve supply voltage, bias field configuration and strength, and main discharge voltage. Different permutations of these parameters yield a wide variety of plasmas to study.

### 2.1.1 Vacuum Chamber and Plasma Electrode

The Solar Loop Experiment is contained in a large vacuum vessel so that the plasma does not interact with the vessel walls. The chamber is about 1.58 meters long and 1.4 meters in diameter, while the plasma loop is less than twenty centimeters in diameter. Hence, the plasma only interacts with the metallic wall boundary at the footpoint of the loop. This simulates the boundary conditions of a solar coronal loop on the surface of the sun and is distinguished from many other laboratory plasmas that fill up the volume of the vacuum vessel and interact with the vessel walls over large areas. Indeed, the Caltech chamber is so large that the opposite side houses an entirely different experiment, the Caltech Spheromak Experiment. A schematic of the vacuum chamber and all the diagnostics to be discussed is shown in Fig. 2.1.

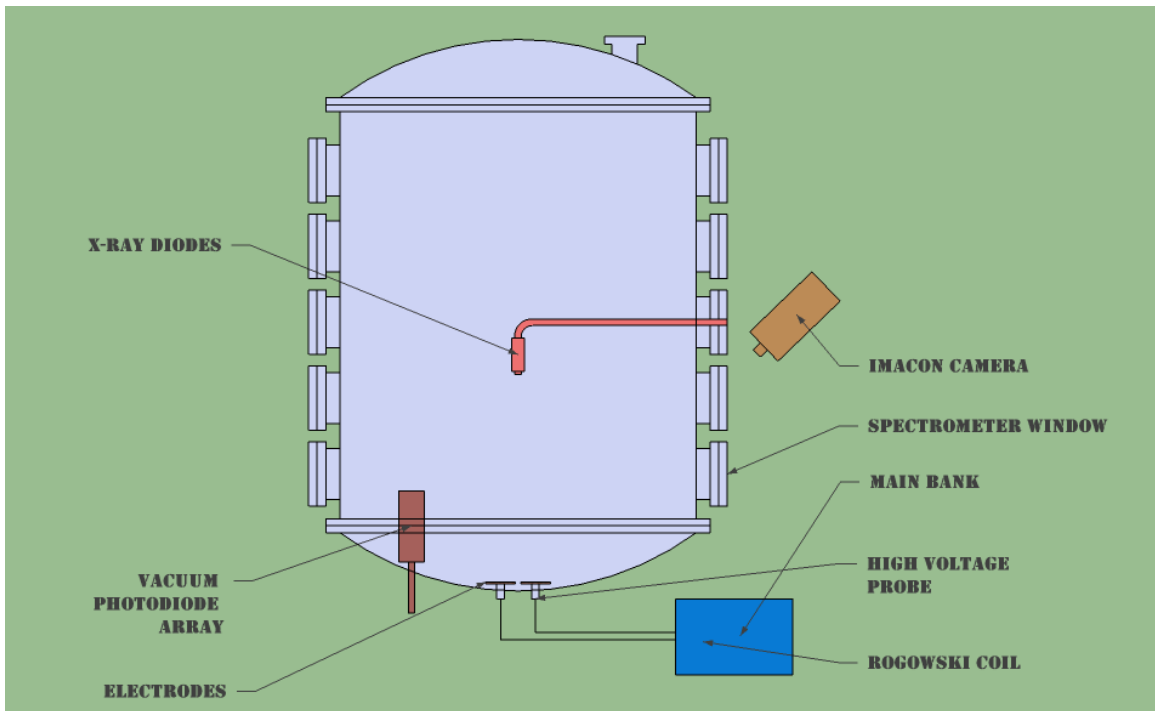


Figure 2.1: A bird's eye view of the vacuum chamber and the positioning of the diagnostics.

The electrodes themselves are copper plates shaped into quarter circles as shown in Fig. 2.2. The top two electrodes are cathodes while the bottom two are anodes. A hole, or gas inlet, in the center of each electrode allows neutral gas to be puffed into the chamber, and coils of wire behind the electrodes generate a magnetic field that links the anode and cathode. The planar nature of the electrodes is based on the Spheromak experiment [18], allowing direct observation of the plasma formation during helicity injection.

### 2.1.2 Injecting Neutral Gas

The species of gas chosen for the plasma affects the plasma properties through the differences in atomic masses, the number of electrons to contribute to the free electron density, and differences in atomic line emission. The Caltech Experiment is designed with a flexible plumbing system [36, pg. 22] to make switching gas species an easy process. The plasmas studied in this thesis are hydrogen unless otherwise noted, but other options include nitrogen, argon, and deuterium.

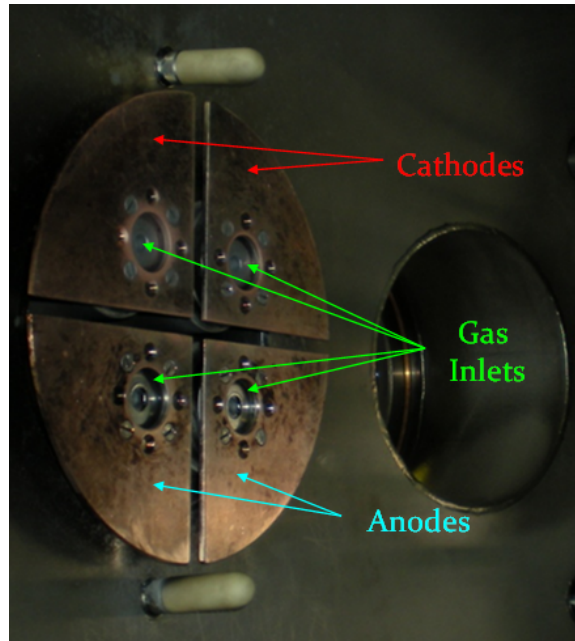


Figure 2.2: The electrodes consist of four planes of copper with gas inlets bored through to allow neutral gas into the chamber.

The vacuum chamber is maintained at a pressure of roughly  $10^{-7}$  torr, and neutral gas is injected into the chamber milliseconds before forming a plasma. This contrasts with many other plasma experiments where the entire chamber is pre-filled at the desired pressure. A fast gas valve separates the vacuum from the reserve of neutral gas, which is typically pressurized from 60 to 100 PSI. The gas valve, designed by Prof. Bellan and shown in Fig. 2.3, consists of a plenum filled with high-pressure gas and a metallic valve held in place by a spring. The spring presses the valve onto an o-ring that maintains vacuum. Milliseconds before the shot, a capacitor bank is discharged into a coil of wire below the valve producing a magnetic field that pushes the valve open against the spring and allows gas to flow for a brief amount of time. The gas in the plenum then travels through a tube at roughly its sound speed to the electrodes. As shown in Fig. 2.2, gas inlets bored through the electrodes allow the gas to expand outward into the vacuum chamber.

The amount of gas admitted by the gas valve can be controlled by adjusting the charging voltage of the gas valve power supply. The amount of gas admitted can be roughly measured by pulsing

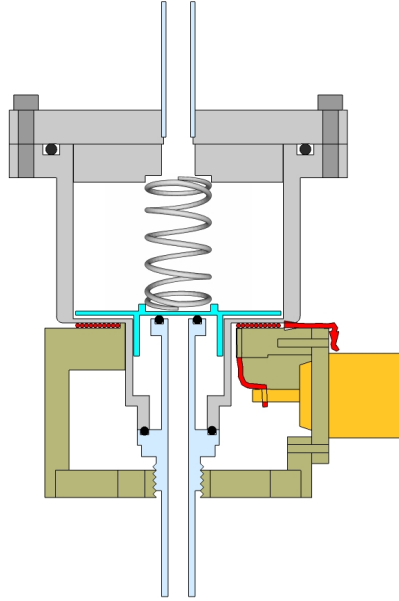


Figure 2.3: A fast gas valve keeps the high pressure gas isolated from the vacuum. When triggered, the valve opens briefly, admitting a small amount of gas.

the gas valve and recording the rise in chamber pressure, which is proportional to the number of particles admitted. The results of this experiment, performed on a smaller test vacuum chamber with valve identical to the ones on the main experiment and using the actual power supply, are shown in Table 2.1 for the three main gas species used. Note that the amount of hydrogen admitted rises rapidly and non-linearly with the charging voltage.

The values reported in Table 2.1 do not necessarily reflect the actual dependence of the plasma density. While increasing the charging voltage of the gas valve power supply lets more gas into the chamber, this higher throughput reflects the total amount of gas that passes the gas inlets integrated over the entire gas puff. What truly matters for the plasma is the instantaneous density of the neutral cloud in front of the electrodes and in the gas inlets at the moment the main bank discharges. The larger values of admitted gas obtained by increasing the charging voltage could be caused by a longer, more sustained gas puff, which would not necessarily provide more gas to the plasma. In order to truly ascertain the instantaneous value of the neutral cloud density, a fast ion gauge should be constructed for the Solar Loop Experiment. We also point out that, on the Solar Experiment, one gas valve feeds *two* gas inlets. The amount of gas admitted and resulting plasma densities will be an important issue in Chapter 4.

Gas Valve Charging Voltage	Hydrogen Pressure	Argon Pressure	Nitrogen Pressure
400 V	21 mtorr	0 mtorr	4 mtorr
450 V	83 mtorr	4 mtorr	11 mtorr
500 V	183 mtorr	10 mtorr	23 mtorr
550 V	436 mtorr	18 mtorr	45 mtorr
600 V	810 mtorr	32 mtorr	74 mtorr
650 V	1314 mtorr	46 mtorr	112 mtorr

Table 2.1: The pressure rise in the small vacuum chamber resulting from a single puff of a fast gas valve as a function of the charging voltage of the gas valve power supply. The hydrogen gas line is pressurized to 100 PSI, while the nitrogen and argon lines are pressurized to 60 PSI; these gas line pressures are used consistently in the experiments presented in this thesis. The amount of hydrogen puffed is a rapidly increasing and decidedly non-linear function of charging voltage. This does not necessarily reflect the density of the neutral cloud at the instant the main bank fires; this must be determined by building a fast ion gauge for the Solar Loop Experiment. On the Solar Loop Experiment a single gas valve feeds two gas inlets.

### 2.1.3 Bias Magnetic Field

The fast gas valve provides the matter that forms the bulk or “body” of the plasma, but another key ingredient is a background or bias magnetic field to serve as an initial “skeleton” over which the plasma forms. The bias field links the anode to the cathode and is responsible not only for the arched nature of the plasma but also for helicity injection once current flows. The bias field is created by discharging capacitor banks into four coils of wire, each located behind one of the electrode quadrants. The coils are energized 1.7 ms before plasma formation to allow the field time to diffuse through the metal chamber and electrodes. It is important to note that, on the microsecond timescale of the plasma, magnetic fields do not have enough time to diffuse through the electrodes. As the bias field evolves on a millisecond timescale and the plasma lasts roughly ten microseconds, the bias field can be considered stationary over the plasma’s lifetime, and the magnetic boundary conditions are essentially “locked in” by the instantaneous value of the bias field when the main bank fires.

The bias field can be modified in two ways. First, the charging voltage of their power banks can be varied continuously, allowing the strength of the magnetic field to be changed. A stronger magnetic field is harder to bend [2, pg. 372], so adjusting the charging voltage allows some degree of control over the rigidity of the plasma. However, the coils are wrapped around iron cores that are saturated by the field. Because of this saturation, the magnetic field is not proportional to the charging voltage but instead varies only weakly with charging voltage in the typical operating regime. Second, one can reverse the polarity of the bias field, which in turn reverses the helicity of the plasma. This can be seen most immediately from Eq. (1.8); reversing the direction of the bias field reverses the sign of the flux  $\Phi$  and hence the sign of  $dK/dt$ . A more intuitive picture will be provided in Sec. 2.1.5. The polarity of the bias field is reversed by switching the hook-ups of the coils to the capacitor banks. Dual-loop experiments may be performed with any combination of field

polarities; in particular, both co- and counter-helicity configurations are accessible.

To describe the bias field configuration, we use the following notation. To determine the handedness of each loop, we use the following convention. Point the thumb of your right hand in the direction of the axial magnetic field. If your fingers curl in the same sense as the azimuthal field, the loop is righthanded, and we denote this helicity by the letter R. If the azimuthal field points in the opposite sense of your fingers, the field is lefthanded, denoted as L. Since the azimuthal field is generated by the axial current, the field is automatically righthanded when the current is parallel to the axial magnetic field and lefthanded when the current is anti-parallel to the axial field. As each loop is either right- or lefthanded, we denote the bias field configuration for dual-loop experiments by concatenating “R” or “L” for each loop, the first letter denoting the left loop and the second letter denoting the right loop. The RL and LR configurations are both counter-helicity, while the RR and LL configurations are both co-helicity. These configurations are depicted in Fig. 2.4

We mention in advance that the plasma behaves asymmetrically between the counter-helicity field configurations RL and LR. The cause for this asymmetry has not yet been identified, but, barring asymmetries in the experimental setup, this asymmetry is quite surprising, as MHD predicts that reversing the magnetic field would simply produce a mirror image of the original plasma. This phenomenon, along with fast camera images, is discussed in Sec. 4.4.

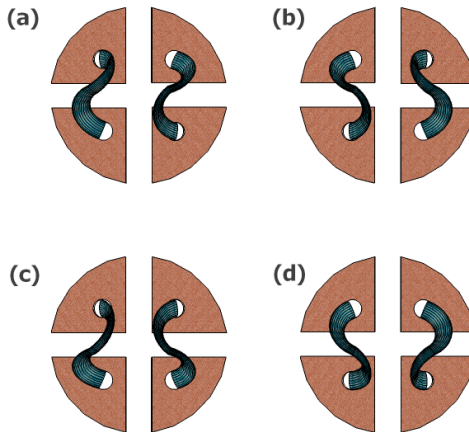


Figure 2.4: Dual-loop experiments can be configured in four different ways: two co-helicity and two counter-helicity. (a) Both loops are right-handed, denoted as RR. (b) Both are left-handed, denoted as LL. (c) The left loop is right-handed, but the right one is left-handed, denoted as RL. (d) The left loop is left-handed, but the right one is right-handed, denoted as LR.

#### 2.1.4 Main Bank

Having admitted gas and established a bias magnetic field, the main capacitor bank then fires, initiating breakdown and bringing the plasma to life. The main bank has a 59  $\mu\text{F}$  capacitor that is switched by an ignitron and is connected to the electrodes by low-inductance cables designed by

Professor Bellan. The bank can be charged up to 6 kV, storing about a kilojoule of electrical energy. When fired, the capacitor first establishes a large potential difference across the electrodes, but current cannot yet flow across the electrodes because the gas has not yet ionized. During this time, free electrons are accelerated by the electric field from cathode to anode along the bias magnetic field lines. These accelerated electrons collide with and ionize neutral gas atoms, creating ions and more electrons. If an electron ionizes several atoms before reaching the anode, we have a multiplication of electrons, also known as an avalanche effect, which leads to full breakdown. At this point, the current begins to flow across the electrodes.

The electrodes have been carefully designed so that breakdown is most favored along the arched path between the gas inlets as opposed to the narrow gap between the electrodes. This is possible due to the Paschen curve, which dictates when breakdown is most likely [1, pg. 227]. The gap between electrodes is so narrow and the gas density there is so low that an electron is unlikely to make any ionizing collisions before reaching the anode. However, later into the shot, arcing is observed between and behind electrodes, presumably because the distribution of gas and plasma has changed.

For the Spheromak Experiment, the main capacitor bank acts as a current source for the plasma after breakdown [37]. This is because the impedance of the ignitron and cables greatly exceeds that of the plasma itself, and we expect similar behavior from the Solar Experiment. However, as will be discussed in Chapter 4, the plasma loops can detach from the electrodes, breaking the conducting path between electrodes. Electrically speaking, the impedance of the plasma load could rapidly change from extremely low to near infinite, and large disruptions are indeed seen in the plasma current. We thus assume that the main bank is a current source with the possible exception of the plasma undergoing a significant change such as detachment.

### 2.1.5 General Plasma Behavior

Plasma created by the Caltech Solar Loop Experiment can have a variety of behaviors based on the setting of the experimental parameters. There are, however, some general features that are common to most or all plasmas formed by the experiment. These features include twisting, kinking, expansion, and collimation.

The electrodes inject helicity into the plasma loops, inducing twisting and kinking. The twisting can be understood as follows. Current flowing axially through the plasma generates its own magnetic field, different from the bias field, that wraps around the loop in a righthand fashion. The total magnetic field is the vector sum of the bias field and the field generated by the plasma current and is thus helical. The stronger the field generated by the plasma current, the lower the pitch of the helices. The plasma current grows over the course of the shot, and the field lines are thus continually twisting. The plasma, which can be considered frozen to the magnetic field lines [2, sec.

2.6.4], also starts to twist. The kinking of the loop is essentially a version of the Kruskal-Shafranov kink instability [38, 39], which the plasma eventually undergoes due to its increasing current and length. Intuitively, the kinking can be understood by trying to twist a rope or string as much as possible; eventually, the rope tries alleviate the twist by kinking. In the Solar Loop Experiment, the kink gives rise to an apparent central dip in the loops, as shown in Fig. 2.5.

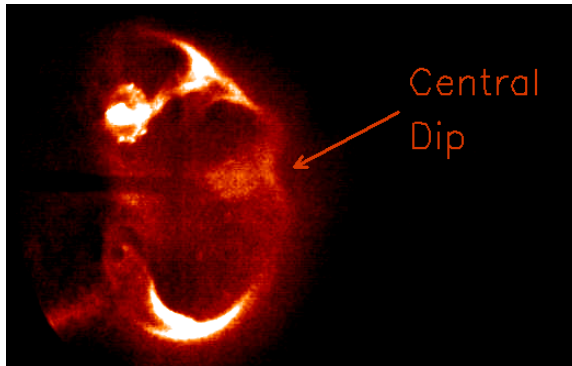


Figure 2.5: A central dip forms in the plasma due to the kinking of the column in response to the increase in magnetic helicity.

The plasma loops expand outward due to the hoop force [2, pg. 311]. The hoop force is a magnetic force that a loop of current exerts on itself; it tends to cause the loop to expand radially. The rate of expansion is influenced both by the plasma current and also by the mass of the plasma as will be shown in Chapter 4. Additionally, it is sometimes observed that the legs of the plasma loop will expand faster than the central region, or that one of the upper or lower legs will expand faster than the other.

The plasmas created are remarkably collimated and remain so throughout the experiment. Similar behavior has been observed in actual solar coronal loops, and an explanation for this universal plasma behavior involves a close look at the MHD forces at work [40], which we outline here. Suppose, for illustrative purposes, that the plasma loops are axisymmetric. Radial equilibrium implies that the radial pressure gradient balances the magnetic pinch force; from Eq. (1.6),

$$\frac{\partial P}{\partial r} = -J_z B_\phi. \quad (2.1)$$

One can integrate and obtain

$$P(r, z) - P(0, z) = - \int_0^r J_z(r', z) B_\phi(r', z) dr'. \quad (2.2)$$

If the plasma loop is bulged and has a radius that varies with axial position, the current density and magnetic field will likewise vary with axial position. The resulting pressure will also depend on  $z$ , which results in an axial pressure gradient that pushes plasma towards the bulged region.

This plasma convects toroidal magnetic field into the bulged region, increasing the pinch force and causing collimation. Since the Caltech plasmas are slightly bulged towards the apex where the bias field is weakest, the MHD forces pump plasma from the gas inlets towards the central region from *both* anode and cathode. Such flows have been observed on both the spheromak experiment [41] as well as the Solar Loop Experiment [42, 43].

## 2.2 Diagnosing the Plasma

A suite of diagnostics are available to study the many aspects of the plasma: fast cameras take pictures of optical emission, the plasma current and voltage are monitored with a Rogowski coil and high-voltage probe, x-ray diodes measure high-energy radiation, and an optical spectrometer provides spectral resolution. The physical layout of all these diagnostics in and around the main chamber is depicted in Fig. 2.1. In this section, we briefly describe each diagnostic as well as the typical uses for their data. The vacuum photodiode array, a new diagnostic, will be described in Chapter 3. Also, modifications made to the current and voltage diagnostics will be discussed in Appendix A.

### 2.2.1 Fast Camera

The Imacon camera (DRS Hadland Imacon 200, 10 bit dynamic range, 1200 x 980 pixels) is a multi-frame, high-speed intensified CCD camera suitable for taking optical images of the plasma. The Imacon consists of eight individual cameras each capable of taking two frames per shot. Unfortunately, one camera is not working, so the images presented here have only fourteen frames. The timings of these frames can be programmed to almost any desired timing sequence. Comparing Imacon images from different shots, the plasma is seen to be highly reproducible. The Imacon is typically located at a side viewport, as indicated in Fig. 2.1, but can be moved to almost any window.

The Imacon images are invaluable for determining the position and overall state of the plasma. Certain quantities such as the expansion speed can be estimated from these images, and major events such as detachment from the electrodes can also be seen and hence timed. Imacon images also reveal inhomogeneity in relative brightness of the plasma and readily identify peculiar optical activity such as the bright spot described in Sec. 1.4.1. However, a significant amount of plasma activity occurs in the ultraviolet or x-ray regime that is missed by the Imacon photos. For instance, at late times the Imacon images show that the plasma has detached and drifted far away from the electrodes, but the current trace shows a large current flowing through the electrodes at this time, and the radiation diagnostics shows significant radiation levels. The Imacon camera provides a great deal of information but does not tell the complete story.

## 2.2.2 Plasma Current and Voltage

The current flowing through the plasma is a fundamental quantity; it determines the toroidal magnetic field, which pinches the plasma radially against the internal pressure, and is a crucial ingredient of the MHD pumping force described in Sec. 2.1.5, which depends the square of the current. A Rogowski coil [2, pg. 245] is used to measure the plasma current. A Rogowski coil is a toroidal solenoid that surrounds a current-carrying wire; the magnetic field from the wire links the turns in the coil and induces a voltage proportional to the time derivative of the current. This signal is passed through an RC integrating circuit, as shown in Fig. 2.6, whose output is then proportional to the original current. The Rogowski coil is placed around one of the capacitor electrodes in the main bank, as indicated in Fig. 2.1. The integrated signal is passed to a optoelectric converter that transmits the signal to the data acquisition device (DAQ). Appendix A contains a discussion of the optoelectric converters and noise issues related to the current measurements.

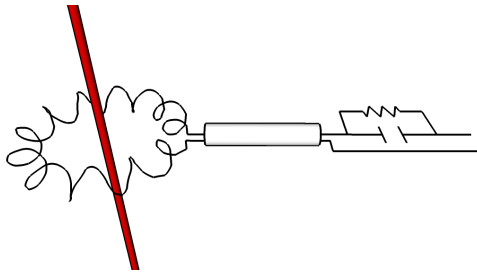


Figure 2.6: A Rogowski coil, shown on the left, encircles a wire, shown in red, and produces an output voltage proportional to the time derivative of the current. The output is fed into a passive RC integrator, shown on the right.

Another important electrical property of the plasma is the voltage across the electrodes. This voltage is a combination of the Ohmic voltage drop and the inductive voltage drop due to the change in the flux linking the plasma:

$$V = IR_p + \frac{d\Phi}{dt} = IR_p + \frac{d(L_p I)}{dt}, \quad (2.3)$$

where  $R_p$  is the plasma resistance and  $L_p$  is the plasma inductance. As the plasma inductance is strongly related to the plasma loop geometry, sudden jumps in the voltage are indicative of sudden changes in the loop geometry and, perhaps, magnetic field topology as well. For instance, if the plasma loop detaches from the electrode, one would expect the voltage to rise sharply in attempt to maintain the current flow and sustain the enclosed flux.

The voltage is measured using a Tektronic P6015 high-voltage probe clipped to the upper right aluminum clamp that connects the capacitor bank cable to the electrode. Like the output of the Rogowski coil, the voltage signal is transmitted to the DAQ by optoelectric conversion. A number of modifications were made to the probe and the accompanying electronics; for instance, the ground

clip of the probe was attached to the lower electrode to improve voltage measurements. These modifications are detailed in Appendix A.

Fig. 2.7 contains a generic example of current and voltage data and provides an overview of the plasma evolution. When the main bank first fires, the voltage increases sharply but current does not yet flow because the plasma is not ionized. The duration of this period depends on several factors such as the amount of gas injected into the chamber and the discharge voltage. At some point, the plasma fully breaks down, resulting in a sharp drop in voltage and the beginning of the current flow. Simultaneously, spurious oscillations associated with the main bank firing and the ignitron switching appear in the current data; these oscillations are discussed in Appendix A. As mentioned above, the change in plasma geometry (in this case, plasma formation) is associated with a sharp change in voltage. The main bank then acts more or less as a current source, and the current trace strongly resembles damped oscillation characteristic of an LCR circuit. The behavior of the voltage trace depends strongly on the plasma itself; in general, though, rapidly expanding plasmas tend to maintain a higher voltage because of the faster rate of change of flux through the plasma loop. The timescale of this plot is selected to show the full discharge; the plasma, however, typically only lasts about  $10 \mu\text{s}$  at most.

### 2.2.3 X-Ray Diodes

A set of four International Radiation Detector Corporation AXUV-HS5 x-ray diodes monitor soft x-ray levels. The diodes are placed inside the vacuum chamber because the soft x-rays will not transmit through the viewports of the chamber [36, pg. 104]. The diodes are thus affixed to the end of a support arm inside the chamber and look head-on at the electrodes, as shown in Fig. 2.1.

The yield of a bare x-ray photodiode is shown in Fig. 2.8 and is about 1 electron per photon at photon energies of 10 eV. The yield increases by about 17% per 1 eV increase in photon energy. In the set of diodes installed on the Caltech chamber, one diode is bare, while the other three have filters in front of them. The filters are a 200 nm thick sheet of aluminum, which transmits 15-62 eV photons, a 50 nm sheet of titanium, which transmits photons of wavelength less than 15 nm (energies greater than 83 eV) photons, and a 500 nm sheet of titanium, which transmits energies greater than 200 eV. The transmission curves for these filters can be calculated at Ref. [44] and are plotted in Fig. 2.9. No signal has been observed through the 500 nm Ti filter, so that the x-rays produced in the Caltech experiment have energies less than 200 eV per photon. Note that hydrogen lines, whose energies are less than 13.6 eV per photon, are not transmitted by any filter. Thus, a signal registered by the filtered x-ray diodes for a hydrogen plasma is caused by something other than line emission.

The x-ray diodes are extremely fast; their time resolution is enhanced by back-biasing the diodes in order to reduce their parasitic capacitance, allowing them to register very fast x-ray bursts. Their

primary limitation is that they have a single line of sight and thus cannot determine from where in the plasma the x-rays originate. Also, due to the construction of the diodes' support arm and their large distance to the electrodes, slight variations in the diodes' inclination angle drastically change the direction of their line of sight. It is perhaps these two issues that introduce large variations in the x-ray diode signals discussed in Sec. 1.4.1. When an x-ray burst is not observed, it is not clear whether the plasma did not emit x-rays or the detectors simply missed the burst. The array of vacuum photodiodes was constructed to address these types of questions.

## 2.2.4 Spectrometer

The spectrometer measures the relative intensities of different wavelengths of light in a small spectral window. The spectrometer consists of a diffraction grating, which disperses light at different angles according to wavelength, and a CCD camera, which registers the incident radiation. The intensity of light upon a particular CCD pixel is indicative of the number of photons at the corresponding wavelength. This intensity is not calibrated absolutely, but the relative intensity within a spectral window is very accurate. A twelve-channel fiber optic bundle carries the plasma light from the chamber to the spectrometer located across the room. The input to the fiber array is placed outside a viewport of the vacuum chamber as indicated in Fig. 2.1, and each channel views a different spatial chord through the plasma. Light from the plasma enters the fiber optic cables and is transmitted to the spectrometer. The CCD camera can measure each channel independently and simultaneously, providing spectroscopic data from twelve different chords through the plasma.

Spectroscopic data have many different uses, but in this thesis they will be used to estimate the electron density by measuring the Stark broadening of the Balmer  $H_\beta$  line. This technique has been previously utilized on the Spheromak Experiment [45, 36]. For light-emitting hydrogen atoms in a plasma, the local electric field created by the surrounding electrons and ions broadens the spectral line according to the formula [36, pg. 75]:

$$w_s = 2.5 \times 10^{-14} \alpha_{1/2} n_e^{2/3}, \quad (2.4)$$

where  $n_e$  is the electron density in  $\text{m}^{-3}$ ,  $w_s$  is the width of the  $H_\beta$  line in nanometers with instrumental and Doppler broadening subtracted out, and  $\alpha$  is the so called half-width [36, pg. 78]. The spectrometer can also detect the presence of impurities in the plasma and determine their ionization state. If multiple lines are present in the same spectral window, the ratio of the lines can give some indication of the electron temperature under the assumption of local thermodynamic equilibrium. Finally, spectral data can also indicate the speed of a plasma via the Doppler shift of the atomic lines, although this technique will not be employed in this thesis.

The spectrometer's CCD camera opens for a single time window during a shot, and the spec-

trometer's output is an integration of data over this time window. The duration of the time window is limited by the requirement of receiving enough light to distinguish the signal from the noise. Measurements of the  $H_\beta$  line typically require a gating period of  $0.5 \mu\text{s}$ . The spectral window observed by the CCD camera is typically 4 - 5 nm wide [36, pg. 40]. Although the spectrometer is sensitive from 200 - 500 nm, the lower wavelength limit is actually set by the transmittance of the port windows on the vacuum chamber. Special windows were custom-made out of borosilicate [36, pg. 104] which will start to attenuate light somewhere between 350 - 400 nm.

### 2.2.5 Data Acquisition

The data acquisition is handled by fast digitizing boards (SiS GmbH SIS3300) mounted on a VME crate. The boards sample data at 100 MHz, giving a 10 ns time resolution. There are twelve boards with eight channels each for a total of 96 synchronized channels. Every channel has a built-in  $50 \Omega$  termination for impedance matching to  $50 \Omega$  cables. The dynamic range is  $\pm 0.5 \text{ V}$ , and data beyond this range will be clipped. The VME crate is electrically connected to the vacuum chamber through the building ground, and this has important implications for diagnostics using the DAQ. As the ground of the VME crate is connected to the chamber and also to the ground of any diagnostic cable plugging into it, any additional contact between the diagnostic ground and the chamber will result in a ground loop, as is discussed in more detail in Sec. 3.3.2. The crate is powered by an isolation transformer so that it does not additionally couple to ground through its power cord.

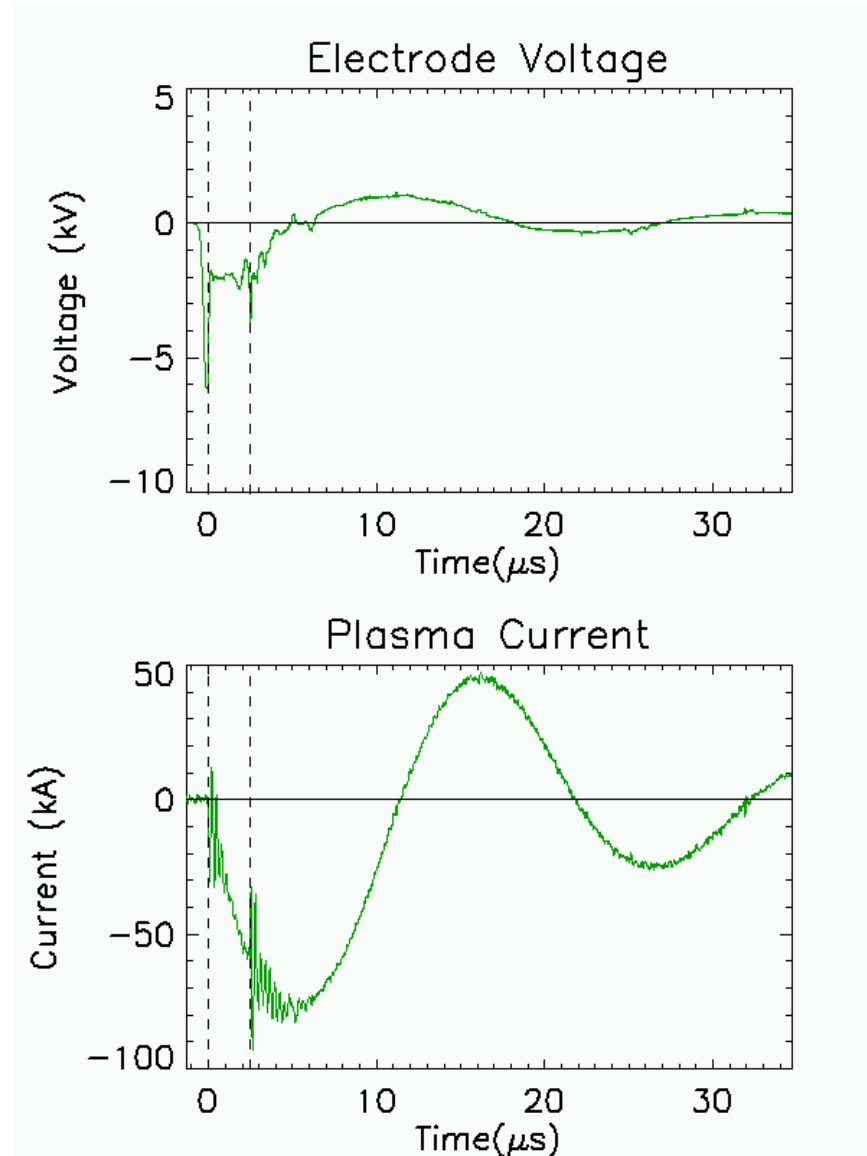


Figure 2.7: The electrode voltage (top) and plasma current (bottom) for a counter-helicity hydrogen plasma (shot 8205). The data are plotted until  $35 \mu\text{s}$  to show the *RLC*-like ringing of the current, but the main plasma activity occurs most before  $\sim 8 \mu\text{s}$ . The leftmost horizontal line is at  $0.0 \mu\text{s}$ , the time at which the plasma breaks down, at which time the voltage plummets while the current starts to flow. The rightmost vertical line is at  $2.5 \mu\text{s}$ . At this time the voltage spikes. At both vertical lines, large oscillations appear on the Rogowski coil. These oscillations are believed to be spurious electrical pick-up; see Appendix A. The voltage spike is, perhaps, indicative of rapid changes in magnetic field topology which result in electrical noise such as the oscillations seen on the current channel.

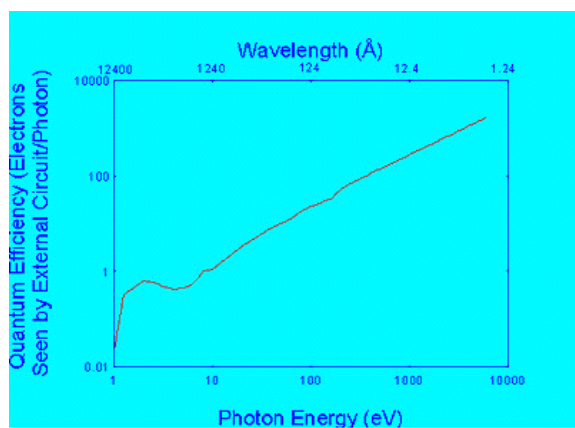


Figure 2.8: The yield, or quantum efficiency, of a bare AXUV-HS5 diode shows that the diodes have a much more favorable response to higher-energy photons.

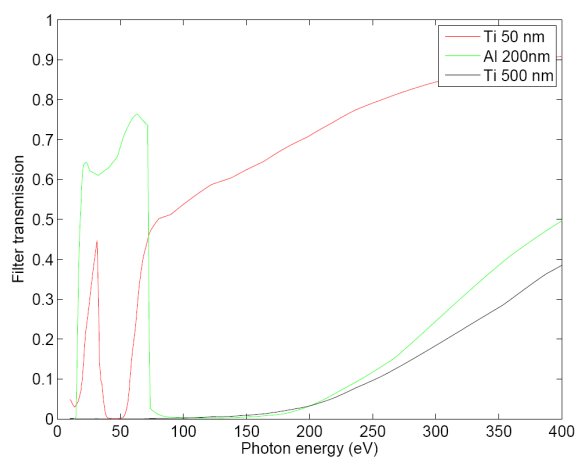


Figure 2.9: The transmission curves for the filters used on the x-ray diodes roughly complement each other in the energy range 10 - 200 eV. The transmission curves are obtained from Ref. [44].

## Chapter 3

# An Array of Vacuum Photodiodes

Plasma radiation contains valuable information concerning internal plasma dynamics. In the Caltech experiments, spectrometer data measures plasma flows [42] and unexpectedly large densities [45, 46]. Soft x-ray and vacuum ultraviolet measurements yield ion and electron temperatures during spheromak merging [47], and, on tokamaks, provide information about confinement, MHD instabilities [30, 48, 49], impurity levels [48, 50], and the presence of energetic electrons [31, 32]. This chapter reports the development of an array of vacuum photodiodes for broadband extreme ultraviolet (EUV) measurements of the Caltech Solar Loop Experiment. The data from the array provides important information regarding radiative losses from the plasma as well as magnetic reconnection during loop merging, as will be discussed in Chapter 4.

The need for an array of vacuum photodiodes originates from limitations encountered with the x-ray photodiodes described in Sec. 2.2.3. The x-ray diodes revealed energetic radiation bursts that occur simultaneously with the formation of a central bright region during counter-helicity merging [20]. However, the x-ray diodes have a single line of sight and cannot determine from where in the plasma the bursts originate. Their signals also have significant shot-to-shot variation even though the experiment is very reproducible. To address these issues, a twelve-channel array of vacuum photodiodes has been built to provide spatially and well as temporally resolved radiation data. The array can detect variations in radiation along the plasma loops as well as variations of emission from the loop apex as the plasma expands outward.

Vacuum photodiodes are simple and cost-effective radiation diagnostics that respond primarily to EUV radiation [48, 50]. The EUV radiation band, defined below, is important for colder plasmas such as those produced by the Caltech Solar Loop Experiment because such plasmas tend to radiate away large quantities of heat via EUV line emission, as will be discussed in Chapter 4. Vacuum photodiodes operate on the photoelectric effect: sufficiently energetic photons strike a metal plate, called the cathode, and eject electrons that are then collected at the anode, as shown in Fig. 3.1. The resulting current is measured and gives an estimate of the incident photon flux. Vacuum photodiodes have an excellent time response due to the near-instantaneous nature of the photoelectric

effect, allowing for sub-nanosecond time resolution [51, 52]. Their simplicity and compact size allow many detectors to be fielded on an experiment. Historically, vacuum photodiodes were extremely important during the 1970's and 1980's when conventional silicon x-ray diodes had a dead layer that prevented them from detecting UV radiation [49]. They were used for temperature studies of fast laser-produced plasmas [53], for impurity measurements on tokamaks that did not emit significantly in the soft x-ray regime [48], and for the study of edge-plasma phenomena such as plasma-wall interactions and H-mode phenomena [49]. In the early 1990's, International Radiation Detectors manufactured silicon photodiodes without a dead layer, and since then silicon diodes have been adopted as the standard for soft x-ray work [54]. However, vacuum photodiodes are still in use and are being considered for fusion-grade tokamaks such as ITER and JET where the radiation levels are too strong for non-metallic components [55, 56].

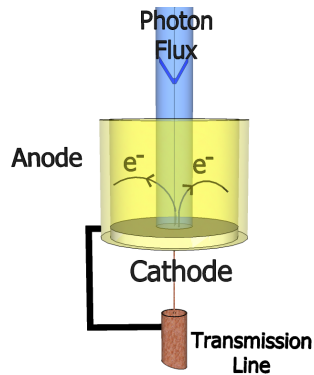


Figure 3.1: A vacuum photodiode consists of a cathode, in this case a metallic disk, that photoemits electrons when irradiated by EUV photons, depicted here by the blue incident column. The emitted electrons are then collected at the anode, a metallic cylinder coaxial with the cathode. The photocurrent from cathode to anode is measured and gives an estimate of the photon flux.

The range of sensitivity of bare (unfiltered) tungsten cathodes is quoted at 20 - 120 nm [48] and 5 - 120 nm [50], and this range is largely independent of the cathode metal, as will be discussed in Sec. 3.2.1. The photoyield for aluminum is shown in Fig. 3.2, and the peak response lies in the EUV wavelength range. For reference, the wavelengths and photon energies for various types of ultraviolet radiation are as follows: the UV range spans 100 - 400 nm (3.1 - 12.4 eV), vacuum ultraviolet (VUV) spans 10 - 200 nm (6.2 - 124 eV), and EUV spans the more restrictive range 10 - 121 nm (10.2 - 124 eV) [57]. Higher energy photons are typically classified as soft x-rays, although the exact distinction between EUV and x-ray seems to be a matter of opinion.

Vacuum photodiodes present an attractive means of studying bright spot formation on the Solar Experiment. Since the material cost of each individual detector is small, a large array can be constructed for a low cost, with the main expenditures coming from auxiliary equipment such as cables and mechanical support. Each detector is sufficiently fast to resolve the radiation bursts, and an array of such detectors will give the desired spatial resolution. This chapter details the design

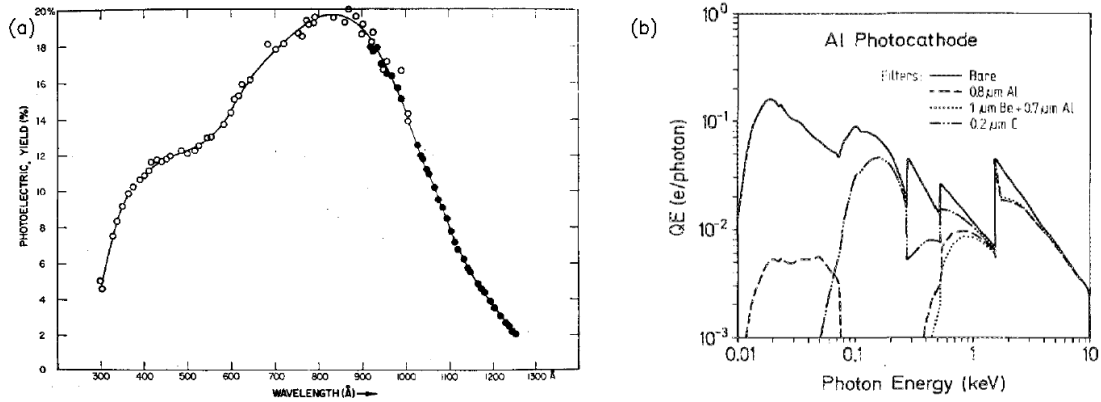


Figure 3.2: (a) The photoelectric yield of an aluminum cathode, plotted as a function of wavelength, reproduced from Ref. [58] (b) The yield of an aluminum cathode, as a function of energy, over a very broad range, reproduced from Ref. [49]. The peak in yield is in the EUV range. These yields will hold for an average aluminum cathode to within  $\pm 30\%$  [59]

and construction of the array. Section 3.1 describes the experimental setup used to test vacuum photodiode prototypes. Section 3.2 discusses the photoelectric effect, cathode design, means for measuring the photocurrent, and the need for a bias voltage. Section 3.3 discusses various types of electrical interference along with measures taken to suppress them in the detector signals. In Sec. 3.4, the problem of the charged particle background is analyzed along with a magnetic shielding scheme. In Sec. 3.5, the physical layout of the array is discussed, and the collimation system used to isolate the field of view of each detector is described in detail.

### 3.1 Setup on the Test Chamber

Preliminary work with the photoelectric effect and vacuum photodiode prototypes was conducted on a small vacuum chamber, called the test chamber, where UV radiation was generated by a PerkinElmer short-arc xenon flashlamp [60] rather than by a plasma experiment. This provided a reproducible and reliable UV source without the electrical noise associated with the main experiment. The flashlamp pulse duration was roughly  $10 \mu\text{s}$ , comparable to the lifetime of the Solar Loop Experiment. Also, the test chamber could be brought up to atmospheric pressure and opened in a matter of an hour, which allowed for more frequent testing and changing of detector design.

Fig. 3.3 shows the setup on the test chamber. Cathodes were mounted in a BNC feedthrough flange opposite to the flashlamp. The flashlamp, however, cannot simply face into the chamber through outside a window port because EUV radiation does not transmit efficiently through quartz windows<sup>1</sup>. To solve this problem, a mount was designed<sup>2</sup> to eliminate the need for a window by

<sup>1</sup>For various window transmission curves, see Ref. [61].

<sup>2</sup>The mount was designed by Shreekrishna Tripathi, whom the author graciously acknowledges for assistance in the early stages of this work.

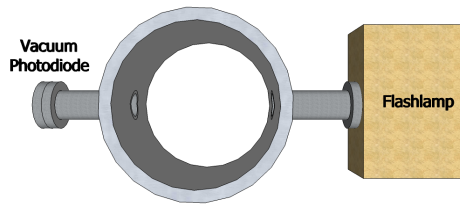


Figure 3.3: For preliminary testing of vacuum photodiodes, a xenon flashlamp was mounted directly on a small vacuum chamber to provide a reproducible source of EUV radiation.

Wavelength (nm)	Fraction of Output Power
100-150	.09
150-200	.10
200-250	.15
250-300	.10
300-400	.10
400-500	.14
500-600	.07
600-700	.05
700-800	.04
800-900	.07
900-1000	.05
1000-1100	.04

Table 3.1: The power distribution of the xenon flashlamp extends into the UV and EUV range. These numbers do not account for the attenuation introduced by the window of the flashlamp.

holding the flashlamp flush against the port on the test chamber. An o-ring between the lamp and port maintains vacuum. This setup guarantees maximal transmission of EUV light.

The flashlamp radiates from 1100 nm down to about 100 nm, so part of its spectrum is detectable by a vacuum photodiode. Table 3.1 shows the flashlamp power distribution as a function of wavelength, but the window of the flashlamp itself attenuates a portion of this radiation. For the window believed to be installed on the flashlamp, attenuation begins at 200 nm, and at wavelengths below 105 nm no radiation is transmitted. The exact transmission curve can be found in the flashlamp manual [60]. In spite of the window attenuation, sufficient EUV radiation was transmitted to produce a readable signal on the vacuum photodiodes.

## 3.2 Photoemission and Cathode Design

The photoelectric effect is usually discussed for photons at or near the work function of the emitting metal. The photoelectric effect induced by EUV photons, whose energies are several times the work function, is quite different and has implications for the design of a vacuum photodiode cathode. In this section, we review the photoelectric effect in the UV range, discuss options for cathode design,

introduce schemes for measuring the photocurrent, and demonstrate the need for a bias voltage.

### 3.2.1 Review of the Photoelectric Effect in the UV

Photoelectric emission by UV photons is different from emission by visible light; the UV yields are 10 to 100 times higher and are more stable with respect to surface conditions. These effects can be explained by invoking a surface and volume effect. The following section reviews the early literature on the subject.

The photoelectric effect has a much greater yield in the UV range than from visible and near-UV photons, as was observed in the first measurements of the photoelectric yield in UV [62] and repeatedly in subsequent work. For Pt and Ta, the yields at wavelengths less than 100 nm are 10 to 100 times higher than for wavelengths 200 - 300 nm [63]. These high yields have important implications in various gas discharges such as glow discharges, sparks, and Geiger counters [64, 63]. For vacuum photodiodes, this increase in yield is a double blessing. First, the increased yield bolsters the signal-to-noise ratio, helping the signal stand out above the inevitable electrical noise. Second, the increase of yield in the UV makes the detector relatively insensitive to visible and near-UV light in comparison with EUV radiation.

UV photoemission is not as sensitive to surface conditions as emission in the visible and near ultraviolet, which is “extremely sensitive to the past history of the surface” and requires “careful outgassing procedures” [65]. The change in UV yield due to surface conditions is at most a factor of 10 instead of 50 to 500 for the visible [64]. No appreciable change in UV photoyield was found after exposure to air for 17 hours following heat treatment [63], and the yield has been repeatable upon multiple exposures to air [65]. Even more convincing, the response of a set of vacuum photodiodes was stable over several months of use in a tokamak [48, 50]. The yield is not completely independent of surface conditions; sand-blasting an aluminum surface drops the yield by a factor of two [58], and all previous workers have at the very least sanded the surface and cleaned it with solvents to remove gross surface contaminants. However, more extreme measures such as heat treatment, frequently used in work with the photoelectric effect induced by visible or near-UV light, are not needed for vacuum photodiodes, and their signals appear to suffer little long-term degradation.

Cairns and Samson measured the yields of relatively untreated metals and concluded that untreated photocathodes can be used with a probable uncertainty of about  $\pm 30\%$  in the range 110 to 40 nm [59]. They focused on the reproducibility of the yield and tested “normally available samples” instead of specially prepared and ultra-pure samples. They stated that “different samples can be expected to have similar yields only if their surfaces are smooth and polished” but “a mirror-like finish, is, however, not essential.” Exposure to He, Ar, and Xe did not alter the yields nor did exposure to air at atmospheric pressure, and the yield of silver at 58.4 nm remained constant over 50 hours at  $10^{-5}$  torr.

The different yields between the UV and visible ranges can be explained by proposing two types of photoelectric emission: a surface effect and volume effect. The surface effect denotes emission from the first several monolayers of the metal and is produced by photons just above the threshold frequency. In contrast, the volume effect is produced by UV photons that penetrate the surface of the metal and eject electrons from the bulk. Hinteregger proposed a theoretical model involving the volume effect to explain the rise in yield in the UV, the lower energy distribution of emitted electrons, the relative insensitivity to air exposure, and why increased temperature causes a decrease in emission [66]. It should be noted, however, that Cairns and Samson attribute the stability of the yield in the UV to the decrease in reflectance as opposed to the onset of a volume effect [59].

In summary, the photoelectric effect is easier to work with in the UV range than in the visible range. The yields are appreciably greater, which helps distinguish the signal from the inevitable electrical noise of plasma experiments. The yields are also not overly sensitive to surface conditions and are stable over long periods of time. These two features make vacuum photodiodes an attractive and low-maintenance diagnostic.

### 3.2.2 Cathode Material and Surface Conditioning

Cathode properties such as area, material, and surface condition all affect the amount of charge emitted during a shot and hence the size of the signal. Due to the large power levels of the Caltech experiment, the vacuum photodiode signals are quite large, so the cathodes do not need to be optimized for maximum signal size. Instead, the cathodes are designed for reproducibility, robustness, and simplicity, in the spirit of Ref. [59]. The cathodes in use on the array are aluminum disks that were lightly sanded, but other options were tested, as is discussed below.

The light sanding of the aluminum cathodes removes gross surface contaminants and improves the signal strength. Further surface conditioning can improve the signal levels even more but is not a robust technique. We have found that rigorously sanding the cathode surface to a shine boosts the signal by a factor of eight immediately afterwards, but this increase in yield gradually fades with time as a new oxide or surface layer slowly forms. Similar observations have been made by other researchers: even a laser-cleaned magnesium surface suffers an emissivity drop after only fifteen minutes *in vacuum* [67]! Thus, extreme surface conditioning may create a photoyield that slowly drifts with time. However, a light sanding improves the overall yield even in the long term and is a good practice provided that the sanded cathode is allowed some time in atmospheric conditions to equilibrate.

The choice of cathode material is not critical, as the yields for various metals are similar in the UV range to within a factor of unity [64, 59]. Our first choice of material was magnesium because of its low work function, but magnesium actually has an abnormally low yield in the UV [62]. Aluminum, on the other hand, has been used in previous photodiodes [49, 53] and is readily available. We

tested the differences between aluminum and magnesium by placing a cathode of each material side-by-side on a conflat flange with two isolated electrical feedthroughs, allowing both cathodes to be tested simultaneously. Both disks were sanded to a shine and were then exposed to identical conditions (i.e., humidity, atmospheric pressure, vacuum). The yields, measured over the course of weeks, showed that aluminum emits more electrons than magnesium when irradiated by the flashlamp. The difference in yield diminished somewhat over time, but after several weeks the ratio of aluminum to magnesium yields settled to a value around three. Thus, aluminum was chosen for the final cathode material.

When used in the actual plasma experiment, the vacuum photodiode signals are quite large and do not require more emissive surfaces. Should there be a need for larger signal amplitudes, perhaps if a filter is being used, simply increasing the cathode area might be sufficient. Another trick would be to tilt the cathode, which can increase the yield due to a decrease in reflections [58].

### 3.2.3 Measuring the Photocurrent

Here, we discuss possible schemes for measuring the photocurrent, namely, with and without amplification. On the actual plasma experiment, the vacuum photodiode signals are large enough to be read directly without amplification, simplifying auxillary electronics and reducing potential sources of noise. However, amplification was needed for work on the test chamber where the signals were generated by the flashlamp. Amplification might also be required if filters are placed on the vacuum photodiodes.

The simplest scheme for measuring the photoelectric signal is to run the photocurrent  $I(t)$  through a resistor  $R$  and to measure the voltage drop  $V(t) = R \cdot I(t)$ . For various reasons,  $R$  should be  $50 \Omega$ ; this choice (i) avoids reflections in the signal line (ii) minimizes RC distortion due to stray capacitance, and (iii) is the built-in termination of the DAQ. These issues are discussed below. This scheme works well for large signals, such as those produced by the main chamber, but proves problematic for smaller signals, such as those produced by the flashlamp. Preliminary calculations for the flashlamp predict a photocurrent per unit cathode area of  $10^{-5} \text{ A cm}^{-2}$ ; across a  $50 \Omega$  resistor, this gives signals in the range of  $5 \cdot 10^{-4} \text{ V}$ , which is at the limit of the DAQ's sensitivity.

Reflections in a cable occur when the termination of the cable differs from its characteristic impedance [68, ch. 2], which is typically  $50 \Omega$ . Reflections become problematic when the pulse duration is short and the cable is long. The cables used for the array are about ten meters long, and the speed of signals in this cable is approximately  $c_c = 2 \cdot 10^8 \text{ m/s}$ , so reflections become an issue when the signal varies on a timescale faster than  $\tau = 2 \cdot l/c_c = 100 \text{ ns}$ . Since the vacuum photodiodes are built to observe fast UV spikes, an impedance mismatch is unacceptable, and a  $50 \Omega$  termination is required.

RC distortion is an unwanted effect where stray capacitance in the cable and detector smears

out the signal. The RC circuit is formed by the cable and vacuum photodiode capacitance together with the termination resistance, as shown in Fig. 3.4. We can work out the distortion by modeling the vacuum photodiode as a current source  $I(t)$  and solving for the voltage across the resistor  $V_R(t)$ , which is the voltage measured by the DAQ. The photocurrent flows both into the resistor and capacitor:  $I = I_R + I_C$ . Since the capacitor charge is  $Q(t) = \int_0^t I_C(t')dt'$  and  $V_R = V_C$ , we have

$$V_R = I_R R = \frac{1}{C} Q = \frac{1}{C} \int_0^t I_C(t') dt' = \frac{1}{C} \int_0^t (I(t') - I_R(t')) dt'. \quad (3.1)$$

Differentiating and rearranging,

$$I(t) = RC \frac{dI_R}{dt} + I_R. \quad (3.2)$$

This differential equation can be integrated after multiplying by the integrating factor  $\exp(t/RC)$ :

$$V_R(t) = RI_R(t) = \frac{1}{C} e^{-t/RC} \int_0^t e^{t'/RC} I(t') dt'. \quad (3.3)$$

This is the exact solution, and is not equal to the desired output  $V_R = RI(t)$ . However, we obtain  $V_R \approx RI(t)$  when the time scale of the pulse is much greater than  $RC$ . One can see this by changing the integration variable of Eq. (3.3) to  $\tau = t - t'$  and then assuming  $I(t - \tau) \approx I(t)$ . In the opposite limit where the pulse is much shorter than  $RC$ , the circuit acts like an integrator,  $V_R(t) \approx \int I(t')/C dt'$ , and washes out the time resolution. Thus, compensating for low signal levels by using a larger termination resistance leads to signal distortion if the RC time approaches the signal duration. The effects of RC distortion can be avoided by keeping the termination resistance small. In fact, with  $R$  equal to the cable's characteristic impedance, there is absolutely no distortion, as the perfectly matched resistive load simply absorbs the signal with no reflection.

This model for RC distortion was verified on the test chamber by changing the length of cable used to carry the signal. The different lengths of cable had different capacitances that, combined with the 1 M $\Omega$  resistance of an oscilloscope, formed RC circuits with varying time constants.  $V(t)$  was measured for each cable and found to be different even though the vacuum photodiode and flashlamp were unaltered. However, using  $V(t)$  for each cable and inverting Eq. (3.3) for  $I(t)$ , the photocurrent trace for each cable was found to be more or less the same. That is, the differences in  $V(t)$  came from cable distortion rather than an actual change in photosignal.

Signal amplification was required for work on the test chamber. One possible amplifier, shown in Fig. 3.5, is a modification of an inverting amplifier for use with a current source such as a vacuum photodiode. The input current flows across the top resistor so that the op-amp output voltage is  $IR$ . A small capacitor added across the resistor reduces ringing, although this slows the time response because it forms an RC circuit. For work on the test chamber, a 5 pF capacitor and a 50 k $\Omega$  potentiometer were selected to work with an AD711 op-amp; this circuit only slightly rounds a

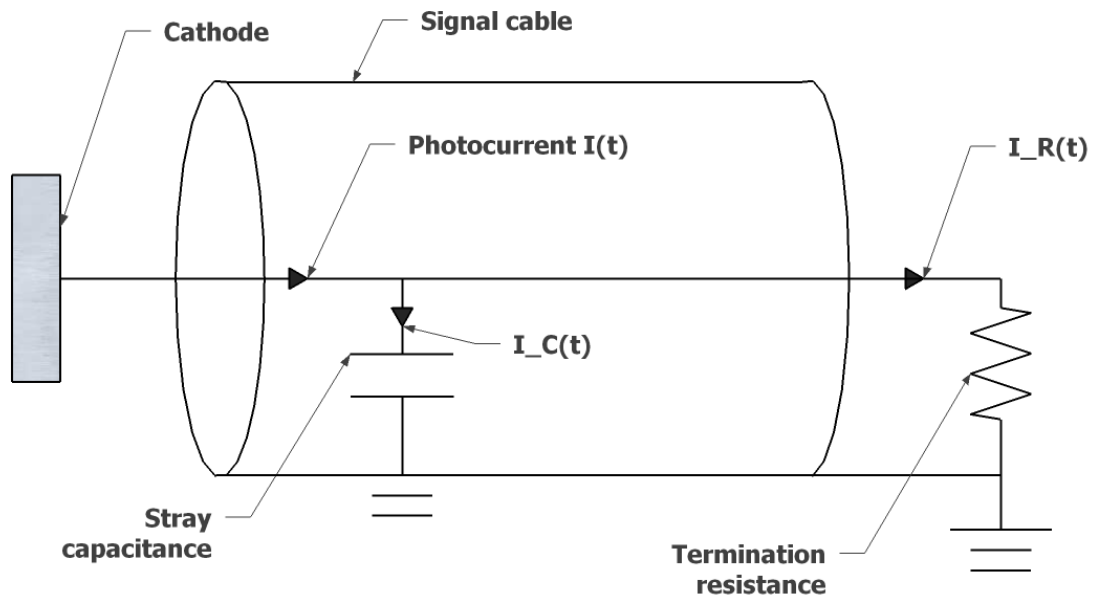


Figure 3.4: A circuit diagram showing the stray capacitance of the vacuum photodiode and cable. The stray capacitance combines with the termination resistance to form an  $RC$  circuit that distorts the photosignal.

$10 \mu\text{s}$  square pulse. The signals on the main chamber are big enough to do away with the amplifier; quite the contrary, they actually require attenuation rather than amplification.

### 3.2.4 The Need for a Bias Voltage

A bias voltage between the cathode and anode is vital both for detector performance and troubleshooting. The bias helps overcome space-charge limitations, which inhibit full collection of the emitted charge. Also, changing the bias strength and polarity tests the vacuum photodiode for proper performance and helps identify the source of spurious signals. For these reasons, a significant amount of effort was invested in establishing a robust system for applying a bias voltage.

Space-charge limitation is an undesirable effect that takes place within a vacuum photodiode and can compromise the detector's accuracy. In a vacuum photodiode, electrons are emitted from the cathode and are collected on the anode, as shown in Fig. 3.1. However, an electron just above the cathode surface feels the negative potential of other recently emitted electrons on their flight to the anode; if this negative potential is sufficiently strong, the newly emitted electron might be reabsorbed by the cathode. This effect is known as space-charge limitation [69] and clearly is a potential source of error, as not every emitted electron is collected. Clearly, the larger the photocurrent, the larger the space-charge. However, the faster the electrons move from cathode to anode, the smaller the space-charge, and this last feature can be exploited to minimize the effects of space-charge.

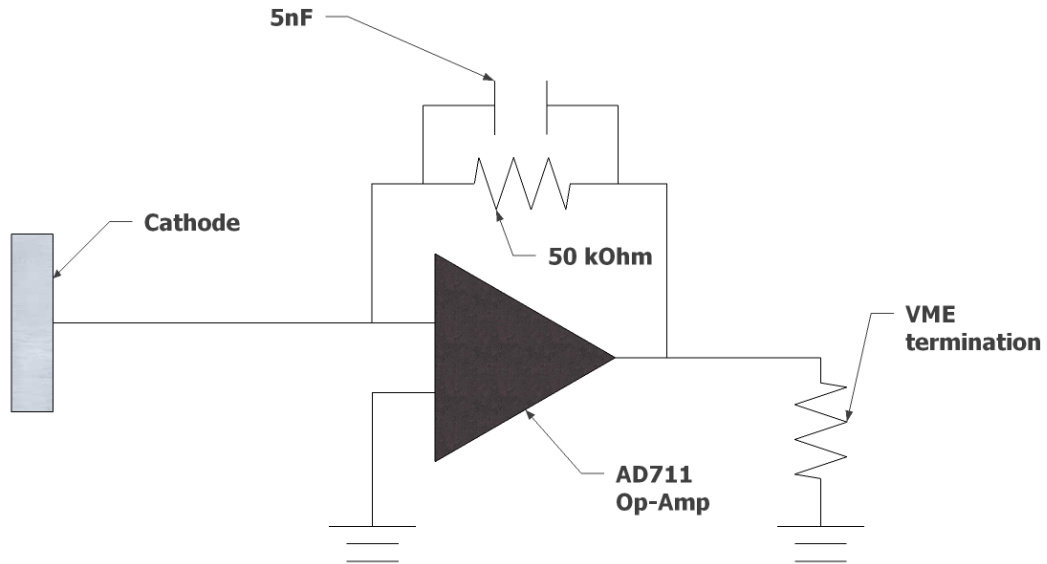


Figure 3.5: An amplifier for use with a vacuum photodiode. The op-amp converts the input current to an output voltage.

A proper bias lowers the cathode voltage relative to the anode so that the electric field rapidly moves emitted electrons from cathode to anode and lowers the negative charge density. With a large enough bias voltage, every electron that is emitted will be collected. In contrast, a reverse bias puts the cathode potential above the anode and inhibits the photocurrent to the point where no emitted electrons reach the anode. A reversed bias prevents accurate measurements but is useful for diagnosing the detector and also for estimating the energy distribution of the emitted electrons.

Space-charge effects are observed experimentally on both the test chamber and in the actual plasma experiment. The results of such an experiment performed on the test chamber are shown in Fig. 3.6. The horizontal axis is the applied bias voltage, which was varied with every shot. The vertical axis is the total *collected* charge, obtained by time-integrating the detector's signal. Three different cathodes are tested; each cathode has a different emissivity either through its total area, material, or surface conditioning, as discussed in Sec. 3.2.2. Thus, even though each cathode is exposed to the same level of radiation from the flashlamp, they emit different amounts of electrons. Fig. 3.6 shows several important features. First, the collected charge increases as the bias is made more negative, indicating that space-charge effects are limiting the collection of charge but can be overcome with a strong bias voltage. Second, as shown by cathode 1, the amount of collected charge plateaus as a function of bias voltage, indicating that every emitted electron can be collected.

However, by comparing cathode 1 to cathodes 2 and 3, the more charge emitted from a cathode, the stronger the bias voltage needed to reach the plateau, an observation consistent with space-charge limitation. On the main chamber, a bias of  $-66$  V is used to guarantee accurate measurements; the difference between a  $-66$  V bias and a typical  $-16$  V bias is shown in Fig. 3.7. Returning to Fig. 3.6, with a reverse (positive) bias, the signal reversed polarity and became independent of the cathode! In this case, all electrons emitted from the cathode were reabsorbed due to the reversed bias voltage. These observed signals come from electrons emitted from the chamber wall and attracted to the cathode; the number of such electrons is obviously independent of the cathode.

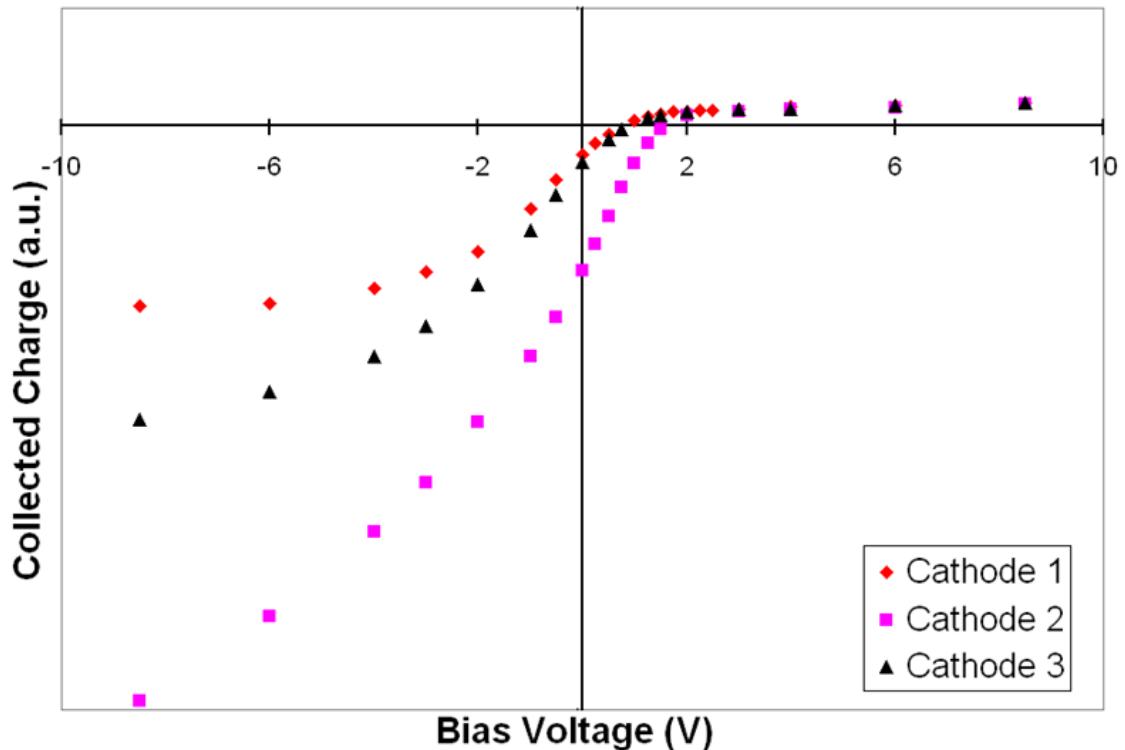


Figure 3.6: A sweep of the bias voltage reveals the effects of space-charge limitation on the amount of charge collected. Here, three different cathodes of varying emissivity were exposed to the flashlamp. Applying a more negative bias resulted in greater charge collection, indicating that the signals are space-charge limited.

A bias voltage is essential but must be carefully implemented. An ordinary voltage or battery placed directly into the signal line may carry unwanted stray capacitance and inductance. A solution proposed by Professor Paul Bellan places a capacitor in series with the detector as shown in Fig. 3.8. The capacitor is charged by a battery through large resistors; the RC time of the charging circuit greatly exceeds the shot length, so the photocurrent flows almost entirely through the capacitor. At the beginning of a shot, the capacitor is fully charged and holds the cathode potential below the anode potential. During the shot, the photocurrent discharges the capacitor, but if C is large enough

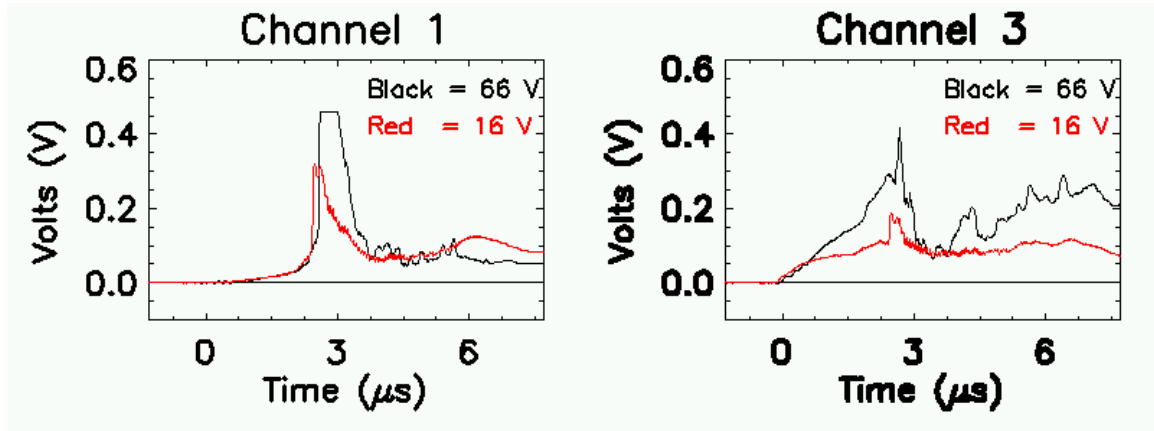


Figure 3.7: Vacuum photodiodes signals can be space-charge limited. Here, data obtained with different bias voltages are compared; vacuum photodiode channels 1 and 3 from the array are chosen as representative plots. The red traces are signals taken with a  $-16$  V bias, and the black traces are taken with a  $-66$  V bias. As shown, the larger bias voltage helps in the collection of photoemitted particles. The clipping seen in channel 1 is due to saturation of the DAQ and can be remedied by using attenuators.

then the bias voltage is more or less constant throughout the shot. In between shots, the battery slowly recharges the capacitor. For the array,  $C = 100$  nF and  $R = 470$  k $\Omega$ , giving  $RC \sim .1$  s, which is much longer than the  $10$   $\mu$ s duration of the plasma. The charge on the battery is  $Q = CV$ , so even a  $-10$  V bias gives  $Q = 10^{-6}$  C. In some of the most intense experiments performed at Caltech<sup>3</sup>, the vacuum photodiode cathodes emit  $Q \leq 1.1 \cdot 10^{-8}$  C; thus, the capacitors are not significantly drained over the course of a shot.

A non-trivial amount of work went into designing a circuit box to hold the bias circuits very close to the DAQ. The current design mounts directly to the boards on the DAQ so that no extra lengths of cable are needed in between the circuit box and the DAQ. This is done because, as discussed in Sec. 3.3.3, the use of braided coaxial cable introduces significant noise into the signal, and semi-rigid cables are rather expensive.

### 3.3 Noise Issues

In the author's opinion, no discussion of plasma diagnostics would be complete without some discussion of electromagnetic noise. As pointed out by Professor Bellan, the  $59$   $\mu$ F capacitor in the main bank stores about one kilojoule of energy when charged up to  $6$  kV; this energy is released in a matter of  $10$   $\mu$ s, giving power levels of  $100$  MW. Meanwhile, a diagnostic such as a vacuum photodiode produces signals on the order of  $1$  V across  $50$   $\Omega$ , which corresponds to  $2$  mW of power. Therefore, if even  $0.00000001\%$  of the power stored in the main bank couples to the vacuum photodiode, the

<sup>3</sup> Counter-helicity merging at a main discharge voltage of  $6$  kV and a gas supply voltage of  $500$  V. See, for instance, shots 7754, 7755, 7758, and 7759.

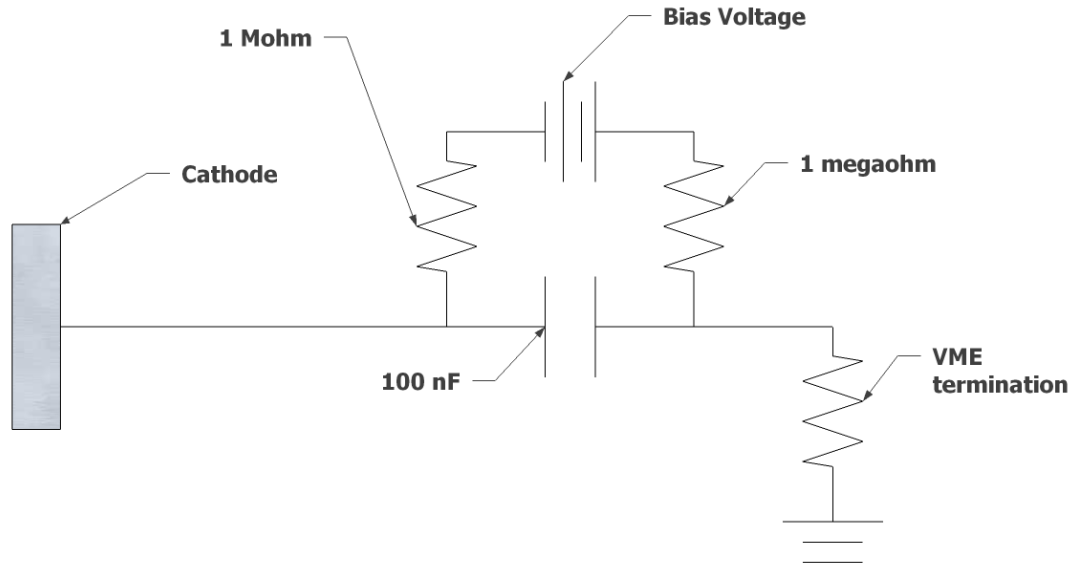


Figure 3.8: The circuit used to establish a bias voltage on the vacuum photodiodes. The signal is AC coupled to the DAQ through a 100 nF capacitor charged through large resistors. The  $RC$  time of the circuit greatly exceeds the shot duration, meaning the charging circuit is effectively isolated over the course of a shot.

desired signal will be overwhelmed.

Here, we discuss measures taken against electromagnetic noise, including the layout of the cathode and anode, use of an enclosure, use of semi-rigid coaxial cables, and dealing with radio-frequency (RF) ground loops. In some cases, several different changes were simultaneously implemented in a detector prototype to aggressively suppress the noise. Unfortunately, these simultaneous changes make it difficult to evaluate how well one particular noise-reduction technique worked independently of the others, and these instances are noted in the text.

### 3.3.1 Capacitive Coupling and Cathode-Anode Layout

Two types of electrical noise, capacitive and inductive pick-up, can plague plasma diagnostics and must be taken into consideration when designing the layout of the vacuum photodiode. Capacitive pick-up can be avoided by enclosing the detectors inside a metallic enclosure, or shield, and also by carefully laying out the anode and cathode. Inductive pick-up will be discussed in Sec. 3.3.2 and 3.3.5.

Capacitive coupling occurs between any two conductors as their relative voltage changes in time. Consider the “capacitor” formed by the detector cathode and one of the plasma electrodes. As shown in Fig. 3.9, if the electrode voltage is  $V(t)$ , then a charge  $Q(t) = CV(t)$  is induced on the

detector cathode, with  $C$  being the capacitance between the two conductors. As  $V(t)$  varies in time, charge flows to and from the cathode and would be read as a photocurrent. Capacitive coupling can be eliminated by placing a third conductor, known as a shield or enclosure, between the first two. An enclosure from CompacRF serves as the shield; it encloses the detectors and intercepts the electric field lines between the detectors and the plasma electrodes. The enclosure makes direct electrical contact with the chamber wall, so enclosing the detectors essentially transfers the capacitive coupling between the plasma electrodes and detectors to coupling between the plasma electrodes and the enclosure. Of course, small holes are drilled through the enclosure to allow the detectors to see out into the plasma; these holes are further collimated as discussed in Sec. 3.5.3.

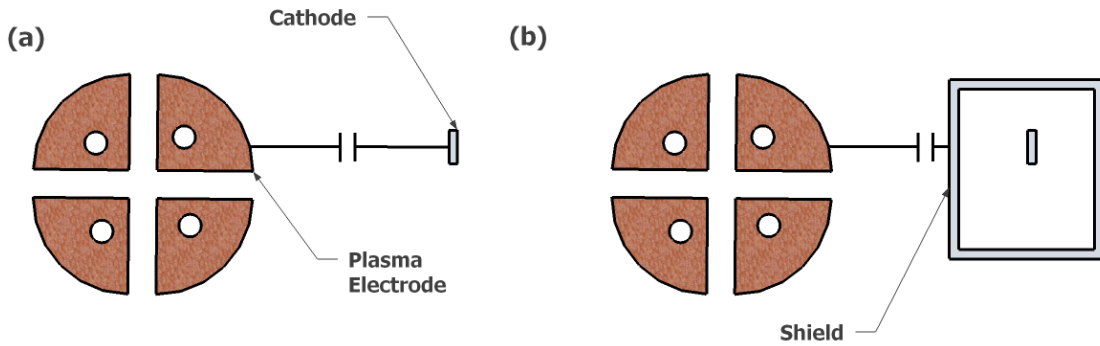


Figure 3.9: (a) Capacitive coupling between the detector cathode and the plasma electrode. (b) A shield placed between the two conductors stops the coupling.

It is suspected that further coupling to the detector cathode can exist even when the detector is housed inside the enclosure. In principle, one expects the enclosure to act as a Faraday shield and neutralize all interior fields. However, as will be discussed in Sec. 3.4.3, large interior electric fields still appear inside the enclosure because the enclosure does not fully enclose the detector; after all, the detector cables have to exit the enclosure through an aperture. Because of these large interior fields, further work must be done to reduce capacitive coupling between the enclosure and the cathode. The main idea is to shield the detector cathode as much as possible with the detector anode. This works because, while coupling to the cathode creates spurious signals, coupling to the anode is not detected because induced charge flows to the anode from ground rather than through the DAQ. The final layout, then, seeks to “enclose” the cathode as much as possible with the anode.

Early anode-cathode designs from detector prototypes provide examples of such coupling and proper shielding. In the first prototype, shown in Fig. 3.10.a, the cathodes were affixed with Torr Seal to the ends of long copper tubes that served as both anodes and collimators. These tubes were themselves glued with Torr Seal into holes drilled through the enclosure and protruded out. It was supposed that plasma hitting the anode/collimator would simply flow to ground without inducing a signal. However, the prototype was tested by firing the spheromak experiment, located

at the opposite end of the vacuum chamber. No signal was initially registered, as expected, but after about  $80 \mu\text{s}$ , as plasma from the spheromak finally reached the collimator/anodes, a signal was induced. This signal is believed to be caused by capacitive coupling between the anode and cathode<sup>4</sup>. Clearly, the anode should remain shielded inside the chassis, and the collimator should instead be an extension of the enclosure.

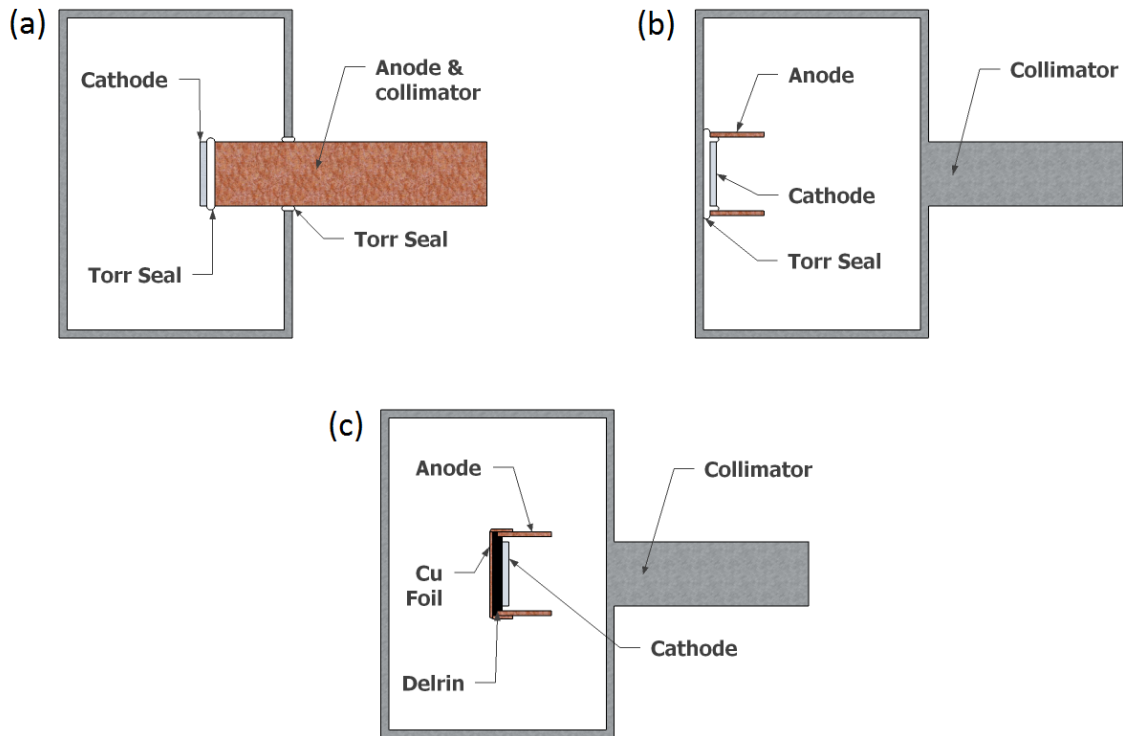


Figure 3.10: (a) The first cathode design used the anode as a collimator. This design does not keep the anode shielded, and it is suspected that anode-cathode coupling induced spurious signals. (b) Both anode and cathode are now shielded inside the detector, but the cathode was so close to the enclosure wall that strong enclosure-cathode coupling was suspected. (c) In the final design, the cathode is located in the middle of the enclosure and is surrounded, as much as possible, by the anode.

In another prototype, both anode and cathode were located inside the enclosure as shown in Fig. 3.10.b. The cathodes were affixed with Torr Seal to the far wall of the enclosure directly across the collimators. This design suffered from enclosure-to-cathode coupling rather than anode-to-cathode coupling, and the noise issues were not resolved in this prototype.

The final design further shielded the cathode from capacitive coupling by moving it away from the enclosure wall and surrounding it with the anode. The cathode was a circular aluminum disk, and the anode was a short length of copper tubing. The cathode was affixed to a delrin disk machined to fit inside the copper tubing, and a screw and nut were used to connect the cathode to the centerline

<sup>4</sup>The coupling could also be magnetic due to the current flowing from the anode to ground. Regardless, the conclusion is the same: the anode should be shielded inside the enclosure.

of the coaxial cable used to transmit the signal. Copper foil was wrapped around the back of the delrin holder and clamped to the cylindrical anode to shield the back of the cathode. The detector was suspended in the middle of the chassis by a planar piece of delrin so that the added spatial separation between the detector and the enclosure further reduced coupling. This layout eliminated much of the noise; however, other design modifications were simultaneously implemented. A high-quality enclosure was purchased from Compac RF to replace the thin aluminum chassis previously used, and electrical feedthroughs were eliminated by using semi-rigid coaxial cable to transmit the signal as discussed in Sec. 3.3.3. It is not certain which design modifications were most responsible for the improved signals.

### 3.3.2 Inductive Pick-Up and Ground Loops

Whereas capacitive pick-up is caused by time-varying electric fields, inductive pick-up results from time-changing magnetic fields. Should the conductors of a detector form a closed loop, then any change in the magnetic flux through that loop induces a voltage somewhere along the loop by Faraday's law. This voltage, or the currents associated with it, can couple to the signal and induce false readings. In particular, a closed loop may inadvertently be formed in the grounding of various instruments; this is called a ground loop and, although subtle, can easily distort the desired signal.

In many diagnostics, a ground loop can form along the outer conductor of the signal cable and the vacuum chamber as follows. The signal cables go to the DAQ where the outer conductor of the cable connects to the DAQ ground. The DAQ itself is grounded by a thick braided cable that connects to pipes in the ceiling, which is electrical ground for the building. The vacuum chamber is likewise electrically connected to building ground and hence to the DAQ ground. Therefore, the ground of a diagnostic is automatically connected to the chamber ground by virtue of being plugged into the DAQ. Now suppose that the diagnostic cable touches the chamber. This second connection forms a large ground loop spanning the laboratory, as shown in Fig. 3.11. Special care must be taken to electrically insulate the diagnostic from the chamber to avoid forming such loops.

Figure 3.11 shows the deleterious effects of a ground loop on a vacuum photodiode prototype. In the top plot, the uninsulated cable carrying the signal inadvertently made contact with a support rod in the ceiling. The resulting ground loop caused strange oscillations in the signal; in particular, the signal became negative, which is a clear indication of a spurious effect, as a vacuum photodiode signal is always positive. By simply moving the cable away from the ceiling rod, the ground loop was undone, and the signal returned to normal, as shown in the bottom plot<sup>5</sup>. As a second example of how ground loops can creep into the system, a small tear developed in the insulating sleeve of the signal line that allows contact between the signal cable and the chamber. The resulting ground loop

<sup>5</sup>Ironically, the ground loop suppresses the high-frequency noise, presumably by shunting some of the high-frequency ground currents. These ground currents will be discussed in Sec. 3.3.5.

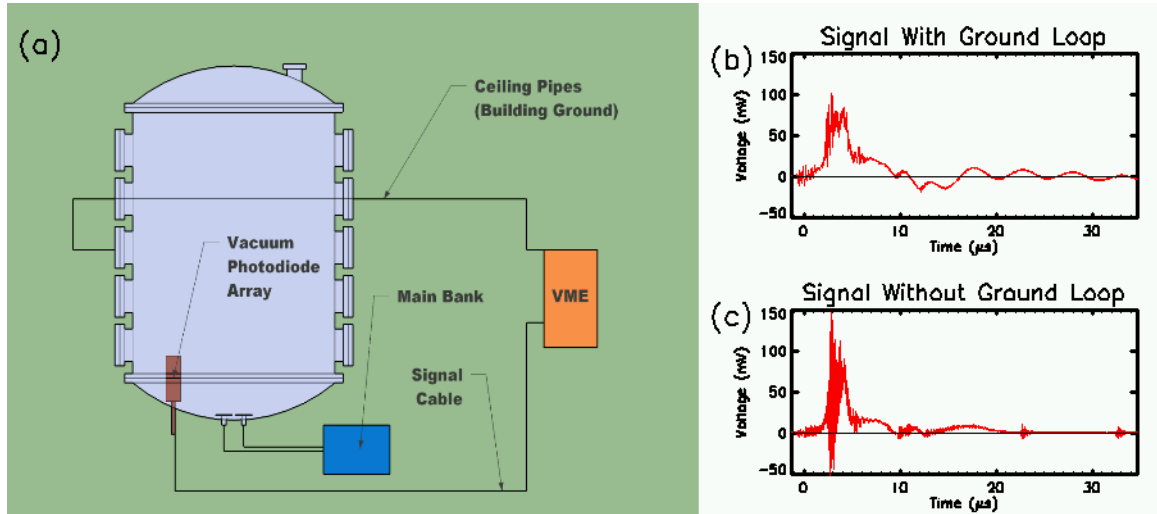


Figure 3.11: (a) Electrical contact between the vacuum photodiode array and the chamber will result in a ground loop extending back to the DAQ. (b) A vacuum photodiode signal taken with a ground loop in the system. Oscillations are observed, and the negative signal must be spurious, as the photosignal is strictly positive. (c) The signal with the ground loop removed.

induced a large spurious signal, but, worst of all, the contact between grounds was only maintained when the vacuum photodiode was rotated to face the plasma. When the detector was rotated away from the plasma, the contact pressure was released and the ground loop disappeared. This gave the ground loop signal the appearance of a plasma effect. When unusual signals such as the one in Fig. 3.11, appear, it is best to check for ground loops immediately.

### 3.3.3 Cables And Electrical Feedthroughs

Tests on a detector prototype showed that using semi-rigid coaxial cable (coax) to transmit the signal significantly reduces the noise levels. Semi-rigid coax has a solid and continuous outer conductor, in contrast with ordinary coax whose outer conductor is a braid of fine wires. Use of braided coax typically results in large noise levels at 1 - 2 MHz; semi-rigid coax not only reduces the noise amplitude but also results in noise of a higher-frequency, typically 3 - 5 MHz. The higher frequency noise is easier to distinguish from the actual photosignal. The solid outer conductor is a more effective shield [70] but is still flexible and easy to work with, although it is also significantly more expensive.

The use of semi-rigid coax presents a solution to a second problem: how to take the signal out of the vacuum chamber. Vacuum flanges with electrical feedthroughs are available, but either (i) force a non-coaxial geometry, making the signal more susceptible to noise, or (ii) only offer a small number of feedthroughs per flange. Non-coaxial feedthroughs are a prime suspect for the large noise seen on prototypes. Instead of using a feedthrough flange, we decided to run semi-rigid coax through

holes drilled in a cylindrical piece of delrin fit inside a length of steel tubing as shown in Fig. 3.12. The tubing exits the chamber through a quick-disconnect flange. The cables hold vacuum within themselves, and Torr Seal was applied to the small space between the cables and the delrin and also between the delrin and the tubing. Within the tubing, a vacuum-compatible insulating jacket is sleeved over the cables to insulate them from the tubing. This scheme allows many cables to exit vacuum through a relatively small space while maintaining vacuum and electrical isolation. With the thirteen-channel array, only a single small leak was found that was quickly fixed with a second application of Torr Seal.

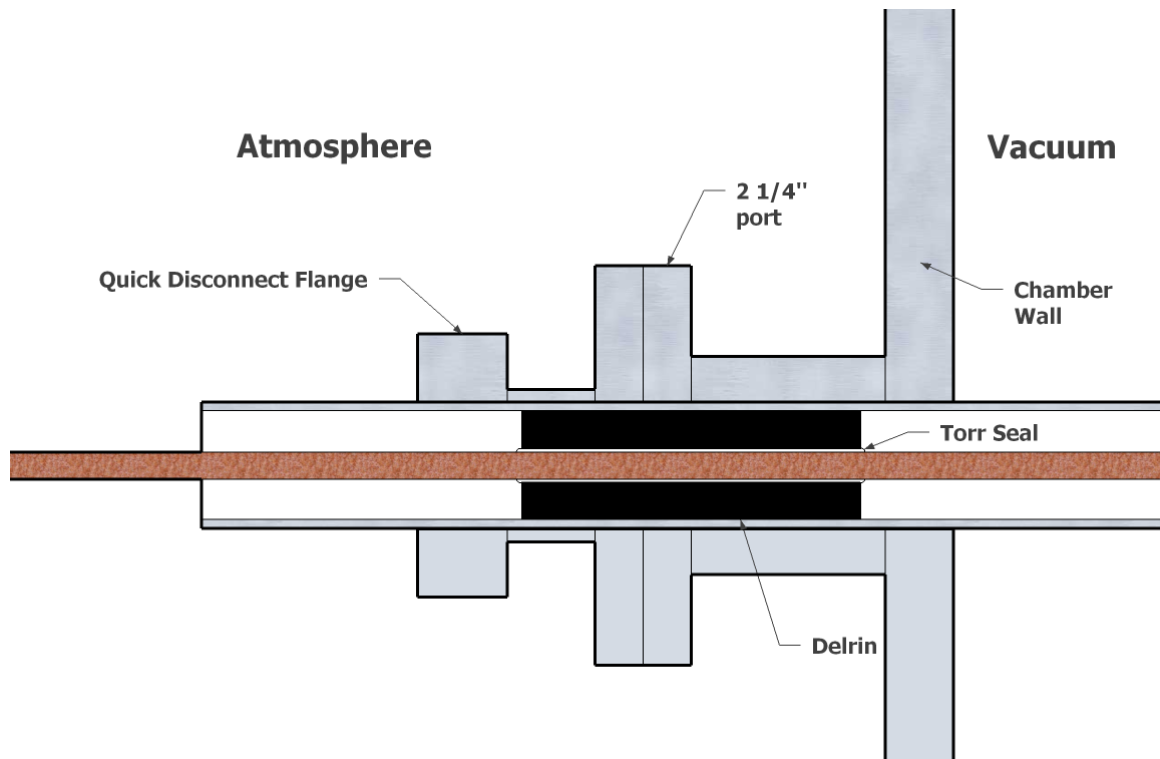


Figure 3.12: The semi-rigid cables exit the chamber through small holes drilled through a delrin piece. Only one cable is depicted in this figure, but this configuration allows the thirteen cables of the array to exit vacuum.

### 3.3.4 Blind Channel

When electrical noise appears on a diagnostic signal, it is difficult to determine whether the noise enters the signal in the detector itself or rather in the cables and electronics used to transmit the signal. A handle on the electrical noise is obtained by adding a blind channel to the array, as suggested by Professor Bellan. This channel is identical in construction to the other detectors, but there is no hole drilled in the enclosure to open the field of view of the blind channel to the plasma. Any signal read by the blind channel must be due to electromagnetic noise. The blind channel

typically shows only high-frequency oscillations with zero mean value. If an unusual signal appears on the other channels but not the blind channel, then the signal must result from the vacuum photodiode being open to the plasma as opposed to noise.

### 3.3.5 RF Noise and Ground Currents

Despite the precautions described in this section, radio-frequency (RF) noise appeared in the vacuum photodiode signals, including the blind channel signal. As can be seen in Fig. 3.13, the noise amplitude was so large that it obscured the desired photosignal. The problem was eventually ascribed to large RF currents flowing on the outer conductors of the signal cables. Ideally, such ground currents should not affect the actual photosignal propagating inside the cable, but small apertures in the bias circuit box allowed the RF ground currents to magnetically (inductively) couple to the photosignal. This coupling between signal and shield current is called surface transfer impedance [70] and can be difficult to identify. For instance, to test whether the bias circuit box was admitting noise, the signal cables were disconnected from it to isolate the noise admitted by the circuit box from noise admitted elsewhere in the circuit. However, no noise was detected because the RF ground currents were also disconnected. This test would have identified electrostatic (capacitive) coupling of noise through the circuit box apertures but failed to detect the *magnetic* coupling.

To eliminate the noise, the RF ground currents are diverted around the circuit boxes as follows. The outer conductor of each cable is shunted to the DAQ ground by attaching a clip between the cable and the DAQ frame. This shunt provides an alternate path for the RF ground current to flow. Ferrite cores placed around the cables downstream of the shunt increase the inductance of the path through the circuit box, and the ground current flows preferentially through the low impedance shunt. This strategy diverts almost all of the current and drastically eliminates the RF noise, as shown in Fig. 3.13.

The RF ground currents most likely result from an RF ground loop. Recall from Sec. 3.3.2 that a ground loop was avoided by insulating the signal cables from the chamber. As discussed in Sec. 3.3.3, this is achieved by sleeving the cables as they run through the support arm into the vacuum chamber. However, the cables are physically very close to the support arm, and there is a fair amount of capacitance between them. This capacitance can close the ground loop for RF currents because the capacitive impedance is very low and is effective a short as such high frequencies. The ground loop only exists for RF signals and hence is called an RF ground loop. The coupling could perhaps be reduced by shortening the length of the support arm or increasing its radius to reduce the capacitive coupling to the cables.

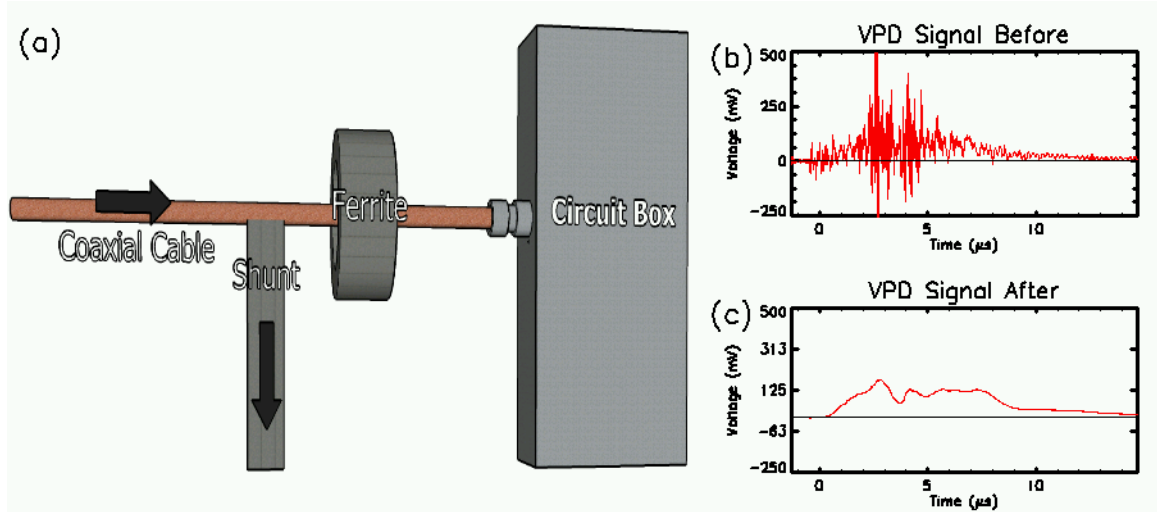


Figure 3.13: Large ground currents couple to the signal at the bias circuit box, introducing massive noise. By providing an alternate path for the current to flow and using ferrite cores to make the path through the circuit box high impedance, the large current are diverted from the circuit box, drastically reducing noise.

### 3.4 Charged Particle Background and Deflecting Magnets

Vacuum photodiodes work by the photoemission and collection of electrons. Unfortunately, plasma particles entering the detector can also be collected, in which case the detector output is no longer an accurate representation of the photon flux. These spurious effects can be avoided by placing a permanent magnet in front of the detector to deflect charged particle while allowing photons to pass. The effectiveness of such magnet in deflecting charged particles is discussed in Appendix B

The array was first built with a single neodymium magnet<sup>6</sup> placed on each collimator. These magnets were believed to be strong enough to deflect all charged particles, but spurious signals appeared on the array. These signals were not electromagnetic interference, because the blind channel did not register them. This section outlines the investigation into these signals, but the issues discussed are not necessarily unique to vacuum photodiodes and could be of use in a variety of instruments. Ultimately, the spurious signals were credited to a collusion of energetic ions passing the magnets and a large and unexpected electric field that appeared inside the array. All shots presented here were made with hydrogen gas in the counter-helicity configuration RL (see Sec. 2.1.3) with the charging voltage of the gas valve power supply voltage set to 500 V (see Sec.2.1.2).

#### 3.4.1 Examples of Spurious Signals

A vacuum photodiode in proper operation should only output positive signals; that is, the only flow of charge should be electrons photoemitted from the cathode and collected at the anode. However,

<sup>6</sup>McMaster-Carr, part number 5902K61

the array occasionally produced negative signals, usually in very brief bursts but sometimes for more extended periods of time. The array also produced exceedingly large positive bumps at late times when no special optical activity was observed; these signals were also believed to be spurious. Specific examples of these two types of spurious signals are shown in Fig. 3.14. Note that the array has twelve channels, but often a single channel is plotted. The single channel shown is not necessarily representative of the entire array, as there is plenty of variation within the different channels in a single shot.

Fig. 3.14.a shows the trace from channel 5 of shot 6952; it has two negative spikes around  $3.7 \mu\text{s}$ . These spikes must be spurious, as the photoelectric effect only produces positive signals. Channel 3 of shot 6953 has a large positive bump that occurs around  $6.7 \mu\text{s}$ , as shown in Fig. 3.14.b. At this time, the Imacon images look dimmer than at earlier times in the shot, so this late peak is suspicious. The clipping seen here is saturation of the DAQ and is resolved by placing attenuators on the signal output. Fig. 3.14.c shows data from channel 4 of shot 6960; it contains a negative spike preceding the large positive peak; this has been observed on other shots as well. Fig. 3.14.d shows another late positive peak, this time from channel 5 of shot 7064, but these data are obtained with no bias voltage applied to the detector. Without the bias voltage, the photosignal is suppressed, leaving the late positive peak in isolation.

### 3.4.2 Investigating the Spurious Signals

Adjustments of the array's bias voltage influenced the amplitude of the negative signals, suggesting that charged particles were responsible. The bias voltage was adjustable within from 0 to -16 V, and shots taken with half strength or no bias voltage produced larger and more frequent negative signals. This not only implied charged particles as the source of the negative signals but also suggested that these charged particles had energies on the order of 16 eV. Increasing the bias voltage to -66 V eliminated almost all negative signals apart from rare and very brief spikes. Secondary electrons are typically defined as electrons with energies less than 50 eV [71], so the fact that a -66 V bias eliminated the negative signals implies secondary electrons. The increased bias did not eliminate the late positive peaks. Also of note, the negative signals were disproportionately worse at discharges of 6 kV and 5 kV than at 4 kV.

The appearance of the negative signals was puzzling. The most likely explanation was that energetic electrons were passing the magnets and striking the cathode. However, Stormer analysis, discussed in Appendix B, suggested that an electron must have very high velocities, over  $10^7$  m/s or 300 eV, to pass the magnets. This scenario was rather unlikely. First, we did not anticipate such energetic electrons and certainly not in such large quantities. Second, altering the bias voltage, which was of the order of 16 V, influences the level of negative signal. 300 eV electrons would not have been affected by such a relatively small bias.

However, Stormer analysis suggested that moderately energetic ions could pass the magnet. Ions striking the cathode would produce a positive signal, explaining the large positive bumps. Ions could induce the negative signals as well through secondary electron emission such as Auger ejection, where an ion absorbs an electron from a nearby metallic surface and simultaneously liberates a second electron [72, 73]. However, there was a problem with this explanation. For ion energies below 1 keV, kinetic ejection of secondary electrons is improbable [73]. The primary means of secondary production is Auger ejection, meaning the secondary electrons must have an energy that is at most equal to the ionization potential of the ion minus two times the work function of the metal. For hydrogen, this maximum energy is 13.6 eV minus twice the work function, which is typically on the order of 3 or 4 eV. Since the bias voltage keeps the cathode at roughly 16 V below the anode, how could such electrons overcome the  $-16$  V bias voltage to reach the cathode?

For completeness of discussion, there are other mechanisms for producing electrons inside the detector. UV radiation might photoemit electrons from the collimator wall, but this effect is expected to be negligible due to the small solid angle of the collimator as seen by the plasma. UV radiation could photoionize neutral gas inside the chassis, but the number of neutrals inside the array should be negligible. Neutral particles might also pass the magnet unaltered and create secondary electrons, although, at particle energies around 10 eV, this is practically ignorable [48].

### 3.4.3 Transient Voltages

The negative signals were finally explained when a potential difference between the vacuum photodiodes and the array enclosure was hypothesized and then measured. The voltage, plotted in Fig. 3.16, could reach over 600 V and reversed polarity around  $5.7 \mu\text{s}$ . The origin of this voltage will be discussed below. When this voltage was positive, it provided a mechanism whereby secondary electrons could become sufficiently energetic to strike the cathode as follows. Energetic ions passed the magnets and entered the array; the transient voltage then repelled the ions away from the detector towards the enclosure wall, as shown by the red line in Fig. 3.15. At the wall, secondary electrons were ejected and then accelerated by the induced voltage towards the detector. Energized to hundreds of electron volts, the electrons were energetic enough to overpower the bias voltage and strike the cathode. However, this is not the complete story since a  $-66$  V bias stopped all electrons from reaching the cathode. Since the anode was closer to the enclosure wall than the cathode, the electric field lines probably ended on the anode. Electrons likely struck the anode and produced more secondaries<sup>7</sup> [74]. These secondaries, if sufficiently energetic, could strike the cathode, as shown by the green lines in Fig. 3.15.

The late times of the positive peaks can likewise be explained due to the reversal of the induced

---

<sup>7</sup>Kinetic ejection of secondary electrons from primary electrons seems much more probable than kinetic ejection from primary ions. This is probably due to the inefficient energy transfer of ion-electron collisions [2, pg. 16].

voltage around  $5.7 \mu\text{s}$ . After this time, ions were attracted towards the detectors. Above, we argued that the electric field lines end on the anode, but the ions must have collided with the cathode to produce a positive signal. Since ions are far more massive than electrons, it is conceivable that ions acquire enough forward momentum to reach the cathode directly, as suggested in Fig. 3.15, even if the field lines mostly end on the anode. Also, if the ions strike the anode, they might bounce and reach the cathode.

The origin of this transient voltage lies in the fact that the array has two “grounds:” the “detector” ground consisting of the anode and outer conductor of the signal cables, and the “chamber” ground consisting of the chamber and enclosure, as discussed in Sec. 3.3.1. Because the two grounds are kept electrically isolated in the vicinity of the chamber and because of the large distance of cable connecting them, a transient potential can develop between them. The potential difference might be due to inductive pick-up; consider the loop that follows the signal cable to the DAQ and then travels back to the chamber along building ground and finally jumps across the gap to join its starting point on the signal cable; see Fig. 3.11. This loop encloses a rather large area that is in the vicinity of the main capacitor bank. By Faraday’s law, if the magnetic flux through the loop changes in time, then the line integral of the electric field must not vanish. However, most of the loop lies along conducting metal, so the electric field must, by and large, lie across the gap between the detector and the enclosure.

Finally, we note that the induced voltage is disproportionately smaller at low discharge voltages (3 and 4 kV) than at 5 kV or 6 kV. Fig 3.16 compares the voltage for 4 kV and 6 kV discharges. At 6 kV, the voltage reaches almost 700 V. At 4 kV, however, the voltage has at peak oscillation only 200 V, and the mean voltage is roughly 30 V. The amplitude of the transient voltage is thus non-linear in the discharge voltage. This explains why 6kV discharge voltage produced disproportionately more negative signals than 4kV. Also, in studying the difference between co- and counter-helicity merging [20], the amount of soft x-rays emitted likewise has a non-linear dependence on the discharge voltage. The two observations are perhaps related.

#### 3.4.4 Upgrading the Magnets

Both types of observed spurious signals, negative dips and late positive peaks, are believed to be caused by ions entering the chassis and causing secondary electron emission. It is a rather bizarre conclusion that *positive* charge entering the array can ultimately lead to a spurious signal due to *negative* charge hitting the cathode. The large potential difference between the detector and the chassis, however, provides a mechanism for this phenomenon.

An obvious solution to these spurious signals, then, is to upgrade the magnets guarding the collimator entrance to deflect ions more effectively. As discussed in Appendix B, the deflecting power of a magnet is determined both by the field strength and also the spatial extent of this field.

To improve deflection, a new set of ultra-strong neodymium magnets was ordered, and the geometry of the magnets was changed. Two magnets are now used on each collimator and are seated in notches cut into the collimator to form a high-field gap region, as shown in Fig 3.17. In the original single magnet setup, the field strength decays rapidly with distance from the magnet, but in the new geometry the field is uniformly large within gap. The magnet upgrade successfully eliminates spurious signals. The field strength around the gap has been measured, so, if spurious signals do arise, the energies of the energetic ions passing the magnet can be estimated; see Appendix B.

## 3.5 Physical Layout and Geometry

This section focuses on the physical layout of the array, including its positioning in the vacuum chamber, its support system, and collimation. The array is situated to look across the electrodes, as shown in Fig. 2.1. In total, the array has thirteen channels, but one of them is the blind channel described in Sec. 3.3.4. The twelve active channels are arranged in a T-shape with seven channels in the vertical direction and six in the horizontal. This allows variations in the emission of the loop apex to be observed as the plasma expands outward and asymmetries between the top and bottom halves to be identified. The number of channels was limited by several factors. The method of taking the signal cables out of the chamber, described in Sec. 3.3.3, cannot support many more than thirteen cables; this limitation is actually set more by the size of the BNC connectors on the cable ends rather than by the radius of the cables themselves. Also, many of the DAQ channels are occupied by other diagnostics, and making more vacuum photodiode channels would require other diagnostics to be disconnected.

### 3.5.1 Array Positioning

Vacuum photodiodes need to be placed *inside* the vacuum chamber, in contrast to optical spectrometers and photodiodes that can leisurely measure plasma radiation through window ports. There are two reasons for this. First, EUV radiation suffers extreme attenuation through the vacuum windows used on the vacuum chambers [36, pg. 104]. Even  $\text{MgF}_2$  windows, which will transmit UV, cut off photons of wavelength less than 150 nm [61]. Second, experiments on the test chamber indicate that vacuum photodiode signals fall off as the vacuum chamber pressure increases, and previous work on photocathodes also showed that pressures less than  $10^{-4}$  torr are required [59]. For these reasons, the detector itself must be located inside the vacuum chamber. This requires that all material used to construct the detector must be vacuum compatible and that the signal cables must be taken out of the chamber, as discussed in Sec. 3.3.3. Moreover, the available ports on the chamber are not always aligned with the preferred line of sight, forcing the experimentalist to design a support system to hold the array in place, as discussed in Sec. 3.5.2.

The array currently looks across the electrodes as shown in Fig. 3.18; this positioning is chosen not only to view a profile of the plasma loops but also to avoid viewing arcing that occurs at the electrodes. Such arcing is suppressed early in the shot because of the design of the plasma electrodes, as discussed in Sec. 2.1.4. However, later in a shot, arcing is observed between and behind the electrodes, and such arcing produces radiation that vacuum photodiodes can detect. Since this radiation is not from the plasma itself, the detectors must be strategically placed to view the plasma but not the electrodes. The need for such strategic placement was made clear by a vacuum photodiode prototype placed on an angle port directly facing the plasma electrodes. The prototype's signal extended well past the lifetime of the plasma and looked like a rectified version of the current trace, as shown in Fig. 3.19; this signal was produced by arcing roughly in proportion to the absolute value of the current. The Imacon images in Fig. 3.19 confirmed that the interelectrode arcing dimmed at precisely the zeros of the current trace. To avoid picking up this signal, the array now looks across the electrodes with its vertical channels located 10.6 cm above the electrodes. Note that the x-ray diode head is pointed directly at the electrodes, so a portion of their signals might be from arcing rather than from the plasma.

### 3.5.2 Support System

The array is rather heavy and needs to be suspended in the chamber to look across the electrodes. The resulting torque on the support arm is significant, and a support system was implemented<sup>8</sup> to provide the mechanical strength needed to hold the array in place. The support arm for the array is 1" diameter stainless steel tubing, which runs through a 1" quick-disconnect flange. To add mechanical support, an aluminum bushing was machined and is held in place by two aluminum brackets, as shown in Fig. 3.20. The bushing keeps the support arm from bending too much under the torque, especially during installation and rotation. Two set screws in the bushing hold the tubing in place when tightened down.

### 3.5.3 Collimation

Each vacuum photodiode in the array should view a different area of the plasma. To prevent the fields of view from overlapping, collimating tubes are placed in front of each detector. The length and diameter of the collimator are chosen to maximize the area viewed while keeping each field of view separate. Here, we calculate the area viewed by each detector as well as an effective area that accounts for the shadow of the collimator; at the electrodes, each detector views an area of 69.3 cm<sup>2</sup> but an effective area of only 2.6 cm<sup>2</sup>.

---

<sup>8</sup>Similar supports have been designed by Carlos Romero and Dave Felt for use with magnetic probe arrays. The author also acknowledges Joe Haggerty, Ali Kiani, and Brad St. John of the GALCIT shop for suggesting design improvements and for machining various components for this system.

Given a collimator of radius  $R$  and length  $L$ , we can calculate the detector's view cone, shown in Fig. 3.21. If we assume that the distance from the middle of the collimator to the plasma is  $D$ , then, at the plasma, the detector's view cone has a radius  $r_0$  given by

$$r_0 = D \frac{2R}{L}. \quad (3.4)$$

The collimators have an inner radius of 0.38 cm and a length of 5.5 cm. The distance from the center of the electrodes to the middle of the array is 42 cm, and the distance from the center of the array to the center of the collimator is 7.8 cm, giving  $D = 34$  cm. We then have  $r_0 = 4.7$  cm. In an array, if the fields of view of each detector are not to overlap, then each detector should be separated a distance  $2r_0$  from its neighbors. The collimator dimensions were chosen so that the twelve active detectors could cover most of the plasma without overlapping. Fig. 3.22 shows a picture of the electrodes along with the central axes of the vacuum photodiodes, showing the vacuum photodiode spacing relative to the electrode size. Also plotted in Fig. 3.22 is the effective viewing area of each vacuum photodiode, which will be computed below.

Although the detector's field of view is calculated as above, not all points within this field of view illuminate the detector equally. Plasma at the edge of the field of view weakly illuminates the detector because the collimator casts a shadow over the detector, as shown in Fig. 3.23. The detector thus responds differently to plasma at the edge of its field of view than to plasma at the center of its field of view. This is important when using the vacuum photodiode signals to estimate the radiation power density of the plasma. Our goal is to compute an effective viewing area that accurately reflects the amount of radiation a collimated detector sees given the shadowing effects of the collimator. This statement will be made precise by first considering the response of a non-collimated detector to a uniformly emitting source.

For a detector without collimation, it is straightforward to estimate how the detector will respond to an emitting source. First, let a point source emitting power  $P$  isotropically be given with a distance  $\rho$  to the detector and with angle  $\alpha$  between the detector's normal vector and the line connecting the detector and point source. If the detector has area  $A_d$  with  $A_d \ll 4\pi\rho^2$ , the power  $P_d$  intercepted by the detector is

$$P_d(\rho, \alpha) = P \frac{A_d \cos \alpha}{4\pi\rho^2}. \quad (3.5)$$

The fraction in Eq. (3.5) is the ratio of the detector area presented to the point source divided by the surface area of a sphere of radius  $\rho$ . For a distributed source, one computes the detector response by integrating Eq. (3.5) over the distribution:

$$P_d = \int d(P_d(\rho, \alpha)) = \int \frac{A_d \cos \alpha}{4\pi\rho^2} dP. \quad (3.6)$$

In practice, the source is usually located far enough away from the detector that the variations in  $\rho$  and  $\alpha$  are small, and both  $\rho$  and  $\alpha$  are held fixed at some representative values. We also assume that the source is essentially planar and radiates homogenously with some power per unit area  $\sigma$ , so  $dP = \sigma dA_e$ , with  $dA_e$  being a differential surface element of emitting plasma. The detector response is then estimated using Eq. (3.5) with Eq. (3.6):

$$P_d = \frac{A_d \cos \alpha}{4\pi\rho^2} \sigma \int dA = \frac{A_d A_e}{4\pi\rho^2} \sigma \cos \alpha, \quad (3.7)$$

where  $A_e$  is the area of emitting plasma. For this discussion, the key quantity is the product  $A_d A_e$ , the detector area times the emitter area, as the detector response is proportional to this value assuming constant  $\sigma$ ,  $\rho$  and  $\alpha$ .

For a collimated detector,  $A_d$ , the area of the detector presented to the emitter, changes at different points in the emitter. Again, Fig. 3.23.a shows that only a fraction of the detector is illuminated by a point source not centered on the collimator axis. Equation 3.7 would then be

$$P_d = \frac{\int A_d(\mathbf{r}) dA_e}{4\pi\rho^2} \sigma \cos \alpha, \quad (3.8)$$

where  $A_d(\mathbf{r})$  represents the detector area presented to a point source located at  $\mathbf{r}$ . Our task is to first compute  $A_d(\mathbf{r})$  as a function of position. Second, we would like to define an effective emitter area  $A_e^*$  such that

$$A_d A_e^* = \int A_d(\mathbf{r}) dA_e. \quad (3.9)$$

$A_e^*$  would be the area of an uncollimated detector that would have the same response to the uniformly emitting source as the collimated detector.  $A_e^*$  will be used to estimate the power radiated per unit area,  $\sigma$ , from the power incident on the detector:

$$\sigma = \frac{4\pi\rho^2 P_d}{A_d A_e^* \cos \alpha}. \quad (3.10)$$

We begin by determining the detector area presented to different points of the emitting plane. We first need to coin names for the different parts of the collimator. The collimator is sketched in Fig. 3.23.b, where we have labeled the top circle and bottom circle. We are interested in the illumination of the cathode, but this is equivalent to the illumination of the bottom circle. We then place our origin at the center of the bottom circle. Let a point source be located at a height  $z$  and at a cylindrical radius  $r$ . Because of cylindrical symmetry, we orient a Cartesian coordinate system such that the point source is located at the coordinates  $(r, 0, z)$ . The boundary of the shadow cast by the collimator is determined by drawing lines from the point source to the various points on the top circle; we then follow each line until it intersects the  $z = 0$  plane. We call this procedure projecting,

and our first step is to work out the equations of projection.

We first project a point  $(a, b, c)$  onto the  $z = 0$  plane. We call the  $x$  and  $y$  coordinates of the projection  $x_p$  and  $y_p$  respectively; these points are drawn in Fig. 3.23.c. The vector joining the point  $(r, 0, z)$  to  $(a, b, c)$  is parallel to the vector joining  $(a, b, c)$  to  $(x_p, y_p, 0)$ . Therefore, these vectors must be proportional to one another with a constant of proportionality  $\lambda$ :

$$(r, 0, z) - (a, b, c) = \lambda [(a, b, c) - (x_p, y_p, 0)] \quad (3.11)$$

Using the  $z$  component of this equation, we get  $z - c = \lambda c$  or  $\lambda = (z - c)/c$ . We can now use  $\lambda$  to solve for  $x_p$  and  $y_p$ . The  $x$  and  $y$  components of Eq. (3.11) are

$$r - a = \lambda(a - x_p) \quad (3.12)$$

$$-b = \lambda(b - y_p) \quad (3.13)$$

Solving for  $x_p$  and  $y_p$  gives

$$x_p = \frac{az}{z - c} - r \frac{c}{z - c} \quad (3.14)$$

$$y_p = \frac{bz}{z - c}. \quad (3.15)$$

Using Eq. (3.14) and (3.15), we can project the entire front circle. We parameterize the front circle by the angle  $\theta$  so that the circle is the collection of points  $(R \cos \theta, R \sin \theta, L)$ . The projection of each point is

$$x_p(\theta) = \frac{z}{z - L} R \cos \theta - r \frac{L}{z - L} \quad (3.16)$$

$$y_p(\theta) = \frac{z}{z - L} R \sin \theta. \quad (3.17)$$

This projection is itself a circle of radius  $Rz/(z - L)$  centered at  $x = rL/(z - L)$ , as shown in Fig. 3.23.d. The illuminated area of the bottom circle, then, is the intersection of the bottom circle with this projected circle. This area, denoted by  $A_d(r, z)$ , is computed numerically once the collimator dimensions  $R$  and  $L$  have been specified.

We can now use  $A_d(r, z)$  in Eq. (3.8). We assume again that the distance  $\rho$  and angle  $\alpha$  can be held fixed. The integral,

$$\int A_d(r, z) dA_e = \int_0^{r_0} A_d(r, z) 2\pi r dr, \quad (3.18)$$

can be computed numerically, from which,

$$A_e^*(z) = \frac{\int_0^{r_0} A_d(r, z) 2\pi r dr}{A_d}. \quad (3.19)$$

Electrode Position	$z$	$A_e^*$
Closer edge of electrode	24 cm	1.1 cm <sup>2</sup>
Closer gas inlet	33 cm	2.0 cm <sup>2</sup>
Middle of electrodes	37 cm	2.6 cm <sup>2</sup>
Further gas inlet	41 cm	3.1 cm <sup>2</sup>
Further electrode edge	49 cm	4.5 cm <sup>2</sup>

Table 3.2: The effective viewing area of a collimated vacuum photodiode computed at various points on the plasma electrodes.

Let us compute the effective area  $A_e^*$  at the midpoint of the electrodes. At the midpoint of the electrodes,  $z = D + L/2$ , and  $A_e^* = 5.0 \text{ cm}^2$ . This area corresponds to a circle of radius  $r^* = \sqrt{A_e^*/\pi} = 1.3 \text{ cm}$ . Note that this effective radius is significantly smaller than  $\rho_0 = 4.7 \text{ cm}$ , the radius of the field of view, but larger than  $R = 0.38 \text{ cm}$ , the radius of the collimator. In fact,  $r^*$  is closer to the geometric mean:  $\sqrt{R\rho_0} = 1.3 \text{ cm}$ .

Because of the gapped magnets in front of the collimator, the above calculation of  $A_e^*$  is too large because the magnets will further shadow the detector. The geometric consideration of incorporating the magnets into the above calculations are considerable. Instead, we note that the magnets occupy about half of the collimator area and estimate  $A_e^*$  to be about half its value computed above:  $A_e^* = 2.57 \text{ cm}^2$ . The effective areas at other distances from the array are shown in Table 3.2.

### 3.6 Final Product

The final version of the array contains twelve fully functional channels arranged in a T-shape to measure both vertical and horizontal variations. In summary,

- Aluminum disks with a light sanding serve as photoemitting cathodes, providing large signals that do not require amplification.
- A bias voltage is needed to overcome space-charge limitations.
- The detector must be carefully shielded both by using an enclosure and by careful layout of the anode and cathode to protect against capacitive coupling.
- Ground loops are prevented by not electrically connecting detector ground to the chamber ground. However, RF ground loops are still present, and these ground currents have been diverted from the cables by the combined use of ferrites and shunts.
- The use of semi-rigid coaxial cables reduces noise and provides a means of taking the detector signals out of the vacuum chamber.
- Magnets placed on the collimators deflect incoming charged particles. If energetic ions manage to pass the magnet, they can induce both positive and negative spurious signals, in part due

to a transient voltage that appears inside the enclosure during a shot.

- Each detector is collimated so that it views an individual area of the plasma. The effective area seen by the detector is less than its full field of view but larger than the collimator cross-sectional area and is estimated at  $2.6 \text{ cm}^2$ .

Thus, the difficulties encountered in implementing vacuum photodiodes on the Caltech Solar Loop Experiment have been resolved, and it would be straightforward to build and install more of these detectors on either the Solar Loop or Spheromak Experiments. The true utility of this diagnostic, however, is the subject of the next chapter.

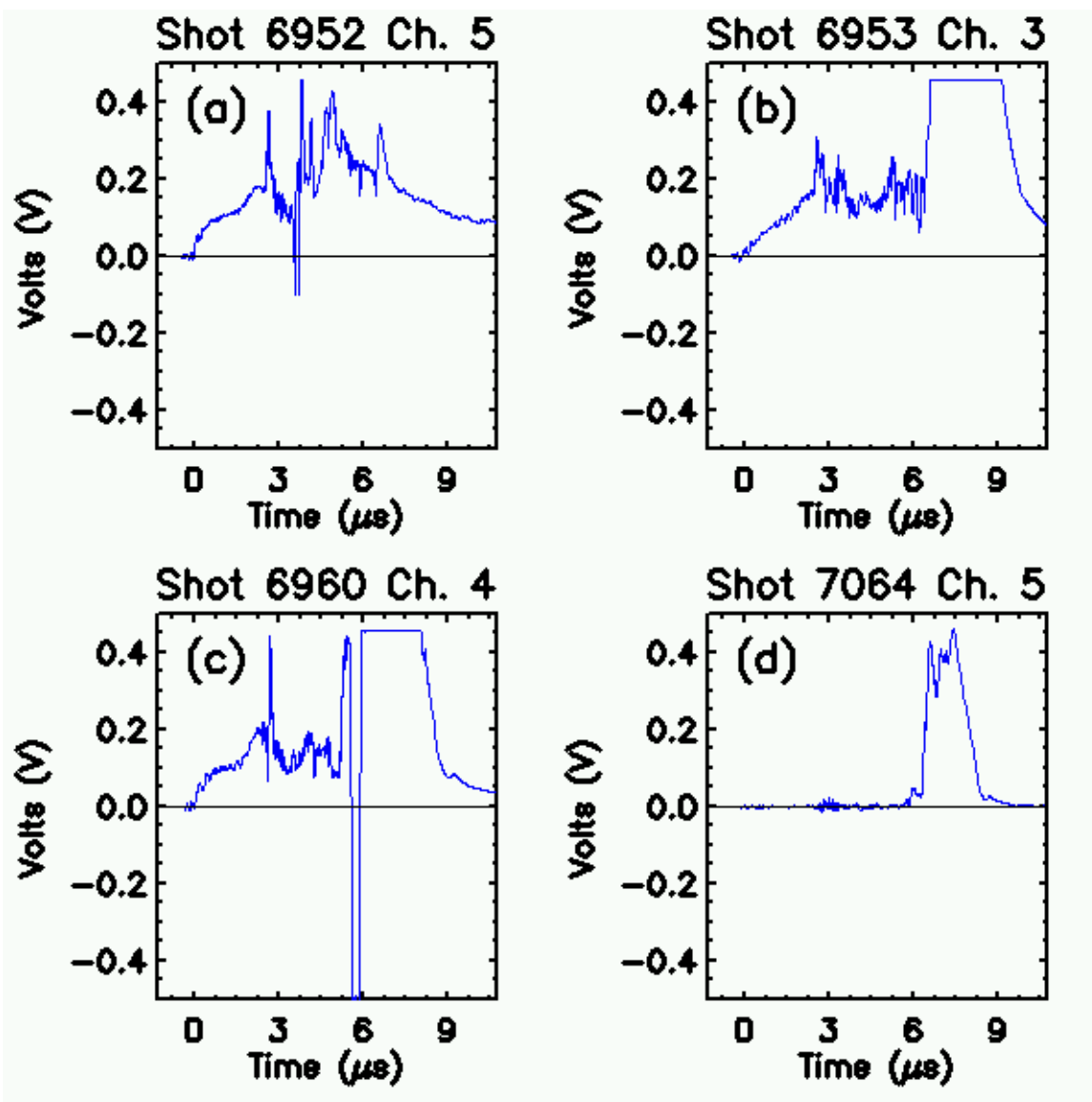


Figure 3.14: A collection of vacuum photodiode data with spurious signals due to charged particles: (a) a shot with negative spikes (b) a shot with a large positive signal late into the plasma lifetime (c) a shot with a negative dip preceding a positive peak (d) a shot with a late positive peak obtained with no bias voltage.

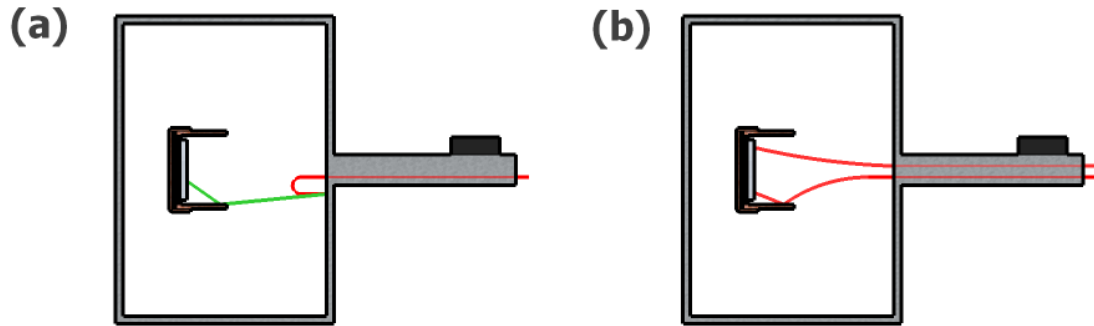


Figure 3.15: The transient voltage between the vacuum photodiode and the enclosure is responsible for positive and negative spurious signals. In this figure, energetic ions that pass the magnet are shown in red, whereas secondary electrons are shown in green. (a) When the transient voltage is positive, secondary electrons produced by the incoming ions are accelerated towards the anode, where they generate more secondaries that strike the cathode. This produces the negative spurious signals. (b) When the transient voltage is negative, the ions themselves are attracted to the detector and induce the late positive spurious signals. They might strike the cathode directly or bounce off the anode first.

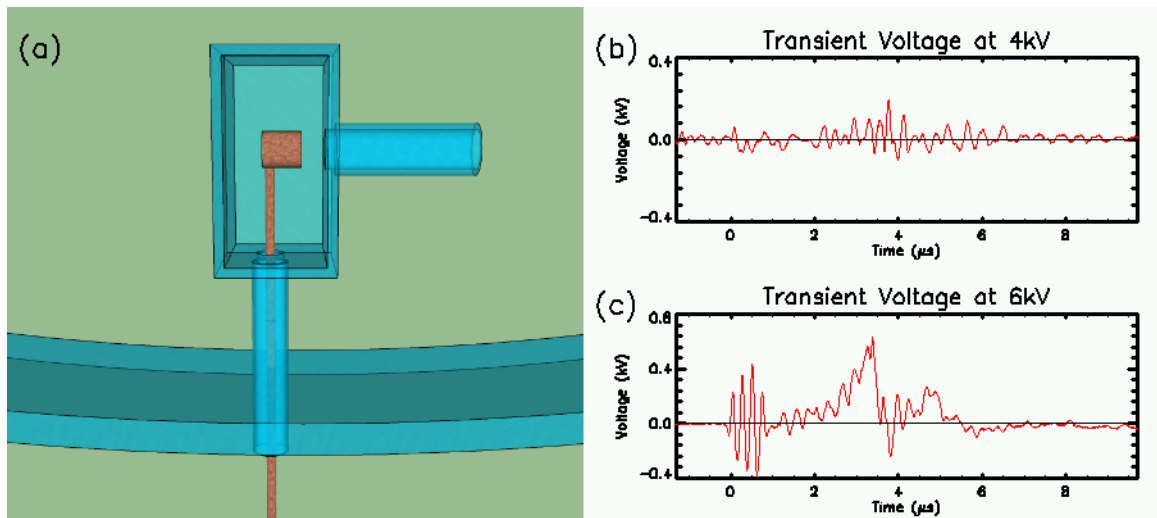


Figure 3.16: (a) There are two “grounds” on the detector: the detector ground shown in red, and the chamber ground shown in blue. The two grounds are ultimately connected through a long path, but the distance is large enough that the two grounds can be at different potentials. (b) The voltage between these two “grounds,” as measured with a high-voltage probe, for a 4 kV counter-helicity discharge (c) The same measurement for a 6 kV discharge.

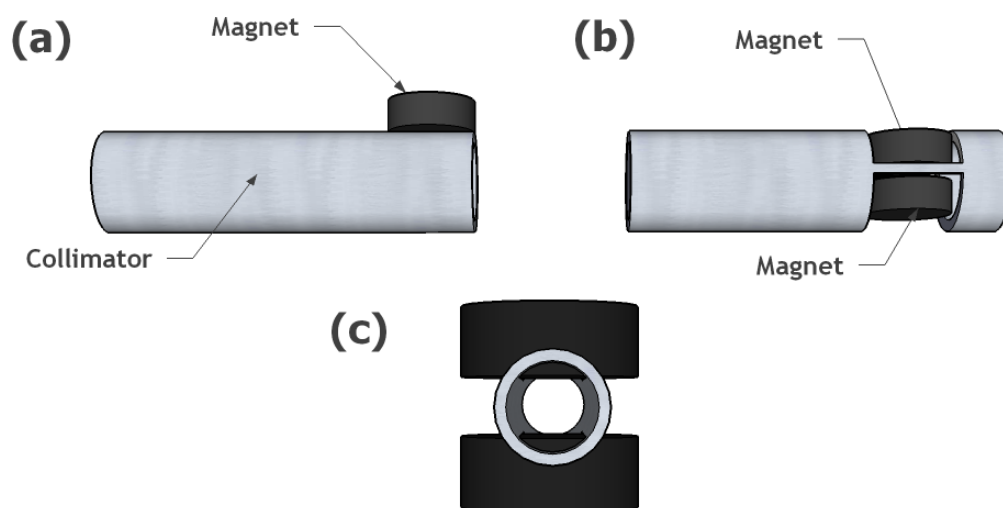


Figure 3.17: (a) The original collimator had a single magnet. (b) The upgraded collimator uses two magnets placed in notches. (c) The gap region has a uniformly high field strength.

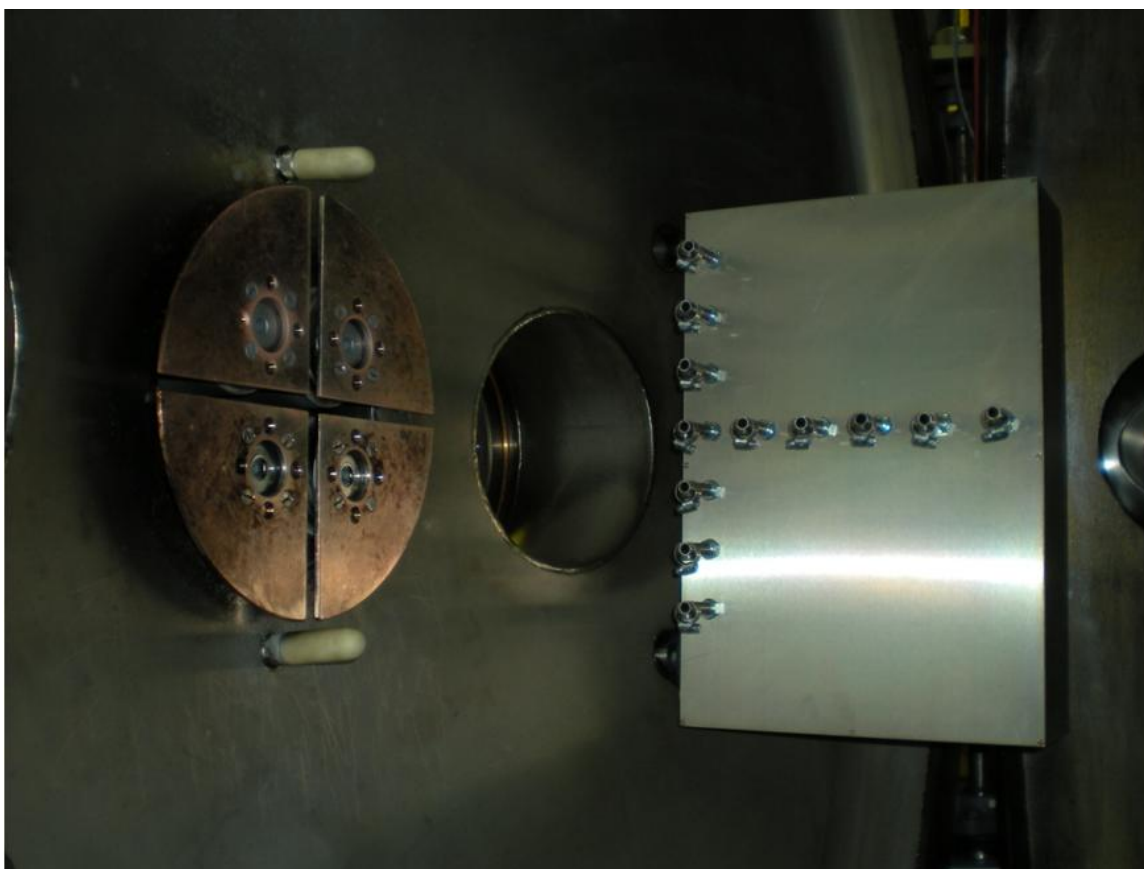


Figure 3.18: The array consists of twelve active channels, seven vertical and six horizontal, and looks across the electrodes.

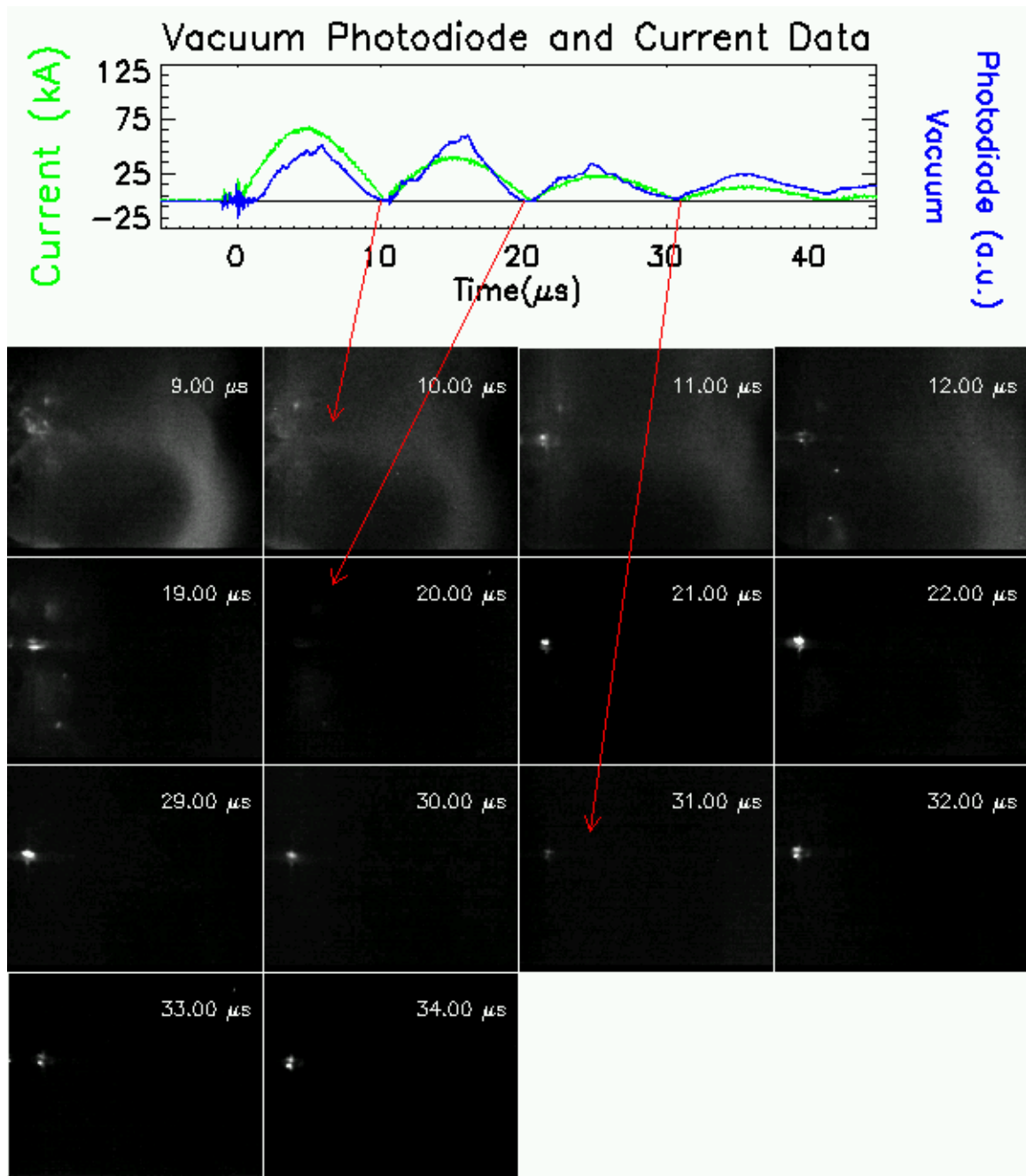


Figure 3.19: Vacuum photodiodes can detect radiation emitted by electrode arcing, which obscures the desired photosignal from the plasma. The vacuum photodiode data, plotted in blue, is overlaid with the absolute value of the current trace, plotted in green. The vacuum photodiode signal looks like a rectified version of the current trace, and the minima of the photodiode signal coincide with the zeros of the current. This plot extends to  $45 \mu\text{s}$ , while the plasma only lasts until  $\sim 12 \mu\text{s}$ . Thus, the data after  $\sim 12 \mu\text{s}$  is not from the plasma itself. In the Imacon image, the frames have been timed to take pictures very late into the shot in order to observe what is happening at the electrodes after the plasma. Localized arcing is observed between the electrodes. The arcing abates at the minima of the vacuum photodiode signal, implying that the late signal is due to the arcing.

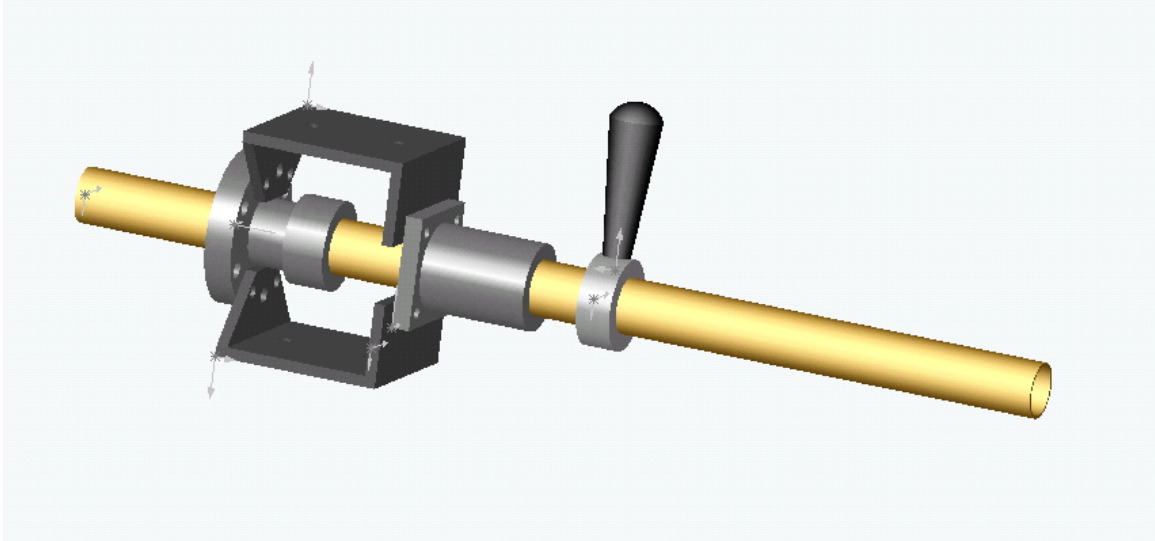


Figure 3.20: A support system is needed to handle the torque of the array. The long tube is the 1" stainless steel support arm of the array. Starting from the left of the figure, the first component is a quick-disconnect flange that mates with a 2 1/4" port on the chamber. After that are two aluminum brackets followed by an aluminum linear bearing. The linear bearing prevents bending of the support arm against the torque of the array. The aluminum brackets hold the bearing in place. Finally, a collar and fluted handle provide a grip for rotating the array.

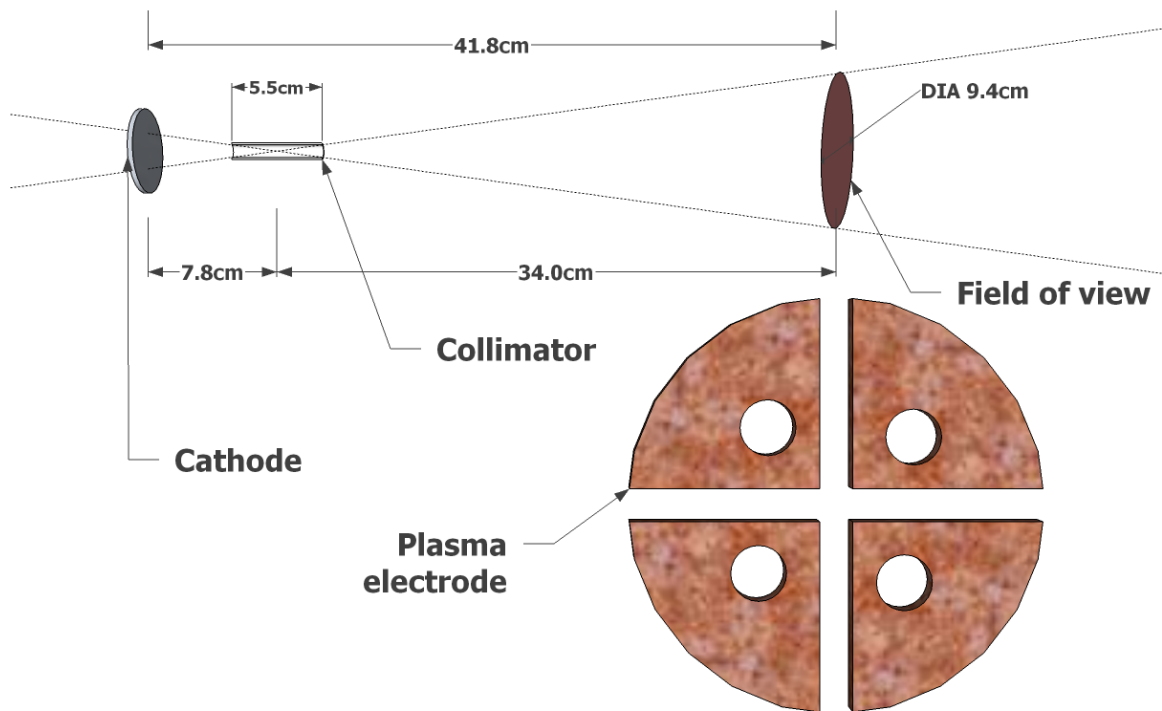


Figure 3.21: Given the collimator dimensions, the detector's view cone, depicted by the dashed lines, can be determined. At the center of the electrodes, the view cone has a diameter of 9.4 cm.

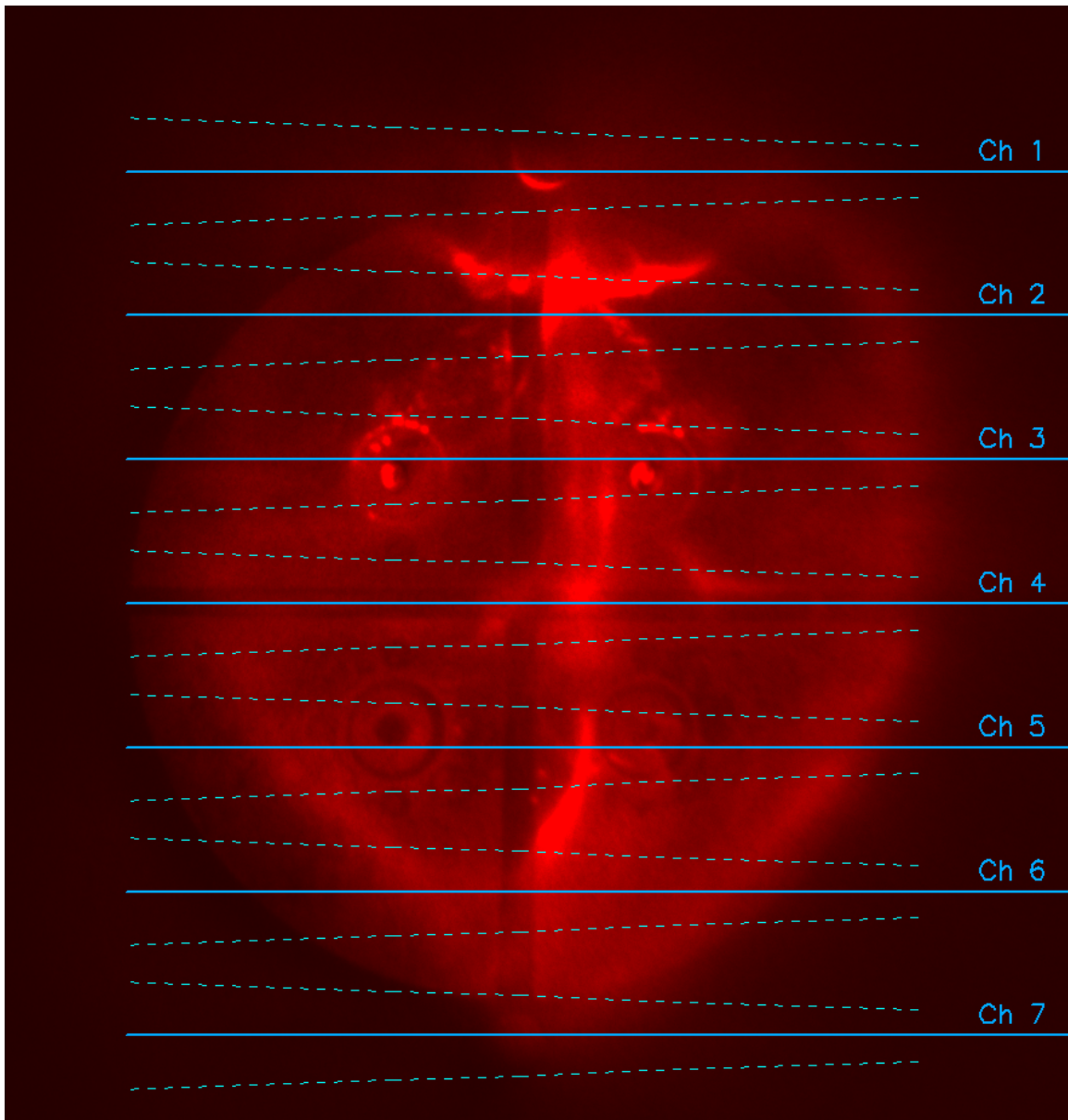


Figure 3.22: This is a head-on photograph of the electrodes in the middle of a shot. The lines superimposed over the image represent the fields of view of the vacuum photodiodes. The thick horizontal line is the central axis of each detector. The dashed lines denote the radius of the effective area of each detector, as computed in Sec. 3.5.3. This radius does not account for the additional shadowing by the magnets.

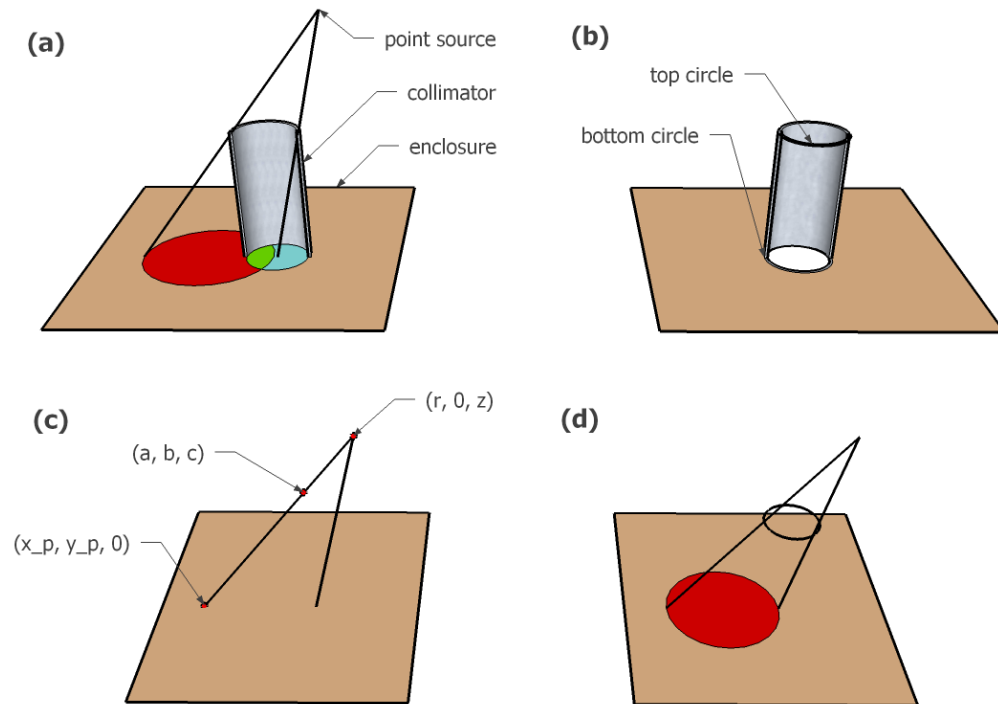


Figure 3.23: (a) The collimator, shown here in a cutaway view, casts a shadow over the entrance to the detector. The illuminated area is drawn in green, whereas the shadow is drawn in blue and red. (b) The top and bottom circles are defined here for clarity. (c) Projection of a point  $(a, b, c)$  onto the  $z = 0$  plane given a point source at  $(r, 0, z)$ . The projection point is labeled  $(x_p, y_p, 0)$ . (d) The projection of a circle is another circle with a shifted center and larger radius.

## Chapter 4

# Radiation Power and Electrode Detachment

This chapter reports the experimental results of the vacuum photodiode array described in Chapter 3. The sheer size of the vacuum photodiode signals implies large levels of radiative power coming from the plasma and has important implications regarding the plasma temperature and ionization balance. These radiation levels are estimated in Sec. 4.1.1 and compared to the rate of Ohmic dissipation in Sec. 4.1.2, where it is proposed that a large majority of the heat deposited by Ohmic dissipation is emitted as extreme ultraviolet (EUV) radiation. Possible mechanisms for the EUV radiation are then discussed in Sec. 4.1.3 and Sec. 4.1.4. Section 4.2 compares the EUV emission levels between co- and counter-helicity plasma. As anticipated from Hansen et al. [20], counter-helicity plasmas emit large bursts of radiation that are not seen in their co-helicity counterparts. A new finding, however, is that the locations of these bursts depends on the amount of neutral gas injected into the chamber. In Sec. 4.3, we shall explore how the charging voltage of the fast gas valve capacitor bank, discussed in Sec. 2.1.2, influences the vacuum photodiode signals as well as other diagnostic data.

### 4.1 Radiative Losses, Ohmic Heating, and Line Emission

The vacuum photodiodes register signals on the order of a tenth of a volt and higher, depending on the plasma parameters. These signals, obtained without amplification, suggest very high radiation levels that appear consistent with the theory that low-temperature plasmas radiate away any heat deposited by Ohmic dissipation, as will be discussed in Sec. 4.1.2. The exact cause of the vacuum photodiode signals has not been identified, but the chief suspect is presently hydrogen line emission as opposed to impurity radiation or thermal bremsstrahlung.

### 4.1.1 Vacuum Photodiode Power Flux

From the magnitude of the vacuum photodiode signals, we can roughly estimate the radiation intensity incident on a vacuum photodiode as well as the total power radiated by a hydrogen plasma. This estimate suggests that the plasma radiates megawatts of power. The vacuum photodiode output current is equivalent to the number of electrons photoemitted per second and equals the vacuum photodiode output voltage divided by  $50 \Omega$ . To estimate the number of incident photons required to emit these electrons, we assume that the vacuum photodiode signals are entirely due to the hydrogen Lyman  $\alpha$  ( $H_{L\alpha}$ )<sup>1</sup> line, which we expect to be the dominant line emission. The error incurred by this assumption will be discussed below.  $H_{L\alpha}$  photons have an energy of 10.2 eV and a wavelength of 121.6 nm; the yield of an aluminum cathode at 121.6 nm is approximately 0.038 electrons per photon ( $e^-/\gamma$ ) as given by Fig. 3.2. It follows that the power incident on a single diode is

$$P_{\text{diode}} = \frac{V_{\text{diode}}}{50 \Omega} \cdot \frac{1}{1.6 \cdot 10^{-19} \text{ C/e}^-} \cdot \frac{1}{0.038 \text{ e}^-/\gamma} \cdot 10.2 \frac{\text{eV}}{\gamma} = (5 \text{ W/V}) \cdot V_{\text{diode}}, \quad (4.1)$$

where  $V_{\text{diode}}$  is the vacuum photodiode output voltage.

$P_{\text{diode}}$  is the power incident on the diode, which is only a fraction of the power radiated in all directions by the plasma. To estimate this latter quantity, we regard the plasma as a sheet of uniformly emitting material as in Sec. 3.5.3 and compute the power radiated per unit area,  $\sigma$ , using Eq. (3.10), which we reproduce here after setting  $\alpha = 0$ :

$$\sigma = \frac{4\pi\rho^2 P_{\text{diode}}}{A_{\text{diode}} A_e^*}. \quad (4.2)$$

Note that each vacuum photodiode monitors a total area  $A_0 = 69 \text{ cm}^2$ , but we use the *effective* area  $A_e^*$  in Eq. (3.10) to account for the shadowing effects of the collimator. As given by Table 3.2,  $A_e^* = 2.6 \text{ cm}^2$  at the midpoint of the electrodes.  $\rho$  is the distance from the back of the collimator to the midpoint of the electrodes, so  $\rho = 37 \text{ cm}$ , while  $A_{\text{diode}}$  is the cross-sectional area of the collimator, so  $A_{\text{diode}} = 0.45 \text{ cm}^2$ . Given  $\sigma$ , we extrapolate the total plasma emission by multiplying  $\sigma$  by the *total* area  $A_0$  monitored by a vacuum photodiode:

$$P = \sigma A_0 = P_{\text{diode}} \frac{4\pi\rho^2}{A_{\text{diode}} A_e^*} A_0 = (1 \cdot 10^6) \cdot P_{\text{diode}}. \quad (4.3)$$

We emphasize that the factor  $A_0/A_e^*$  is due to the collimation of the detectors and is only accurate to the degree to which the plasma uniformly emits over the vacuum photodiode field of view. Equation (4.3) says that, if a vacuum photodiode reads 0.1 V, then the corresponding area of the plasma is radiating about 0.5 MW.

---

<sup>1</sup>We adopt the following notation for hydrogen lines: the Balmer lines will be denoted as  $H_\alpha$  and  $H_\beta$  while the Lyman lines will be denoted  $H_{L\alpha}$  and  $H_{L\beta}$ .

Of course, the accuracy of Eqs. (4.1) and (4.3) depends on several assumptions. We assumed that the radiation was monochromatic at the  $H_{L\alpha}$  line; we will explain the rationale for assuming that hydrogen emission is dominant in Sec. 4.1.3. We now explore how the estimated power changes with assumed wavelength. If we assume a photon energy of 13.6 eV, where the photoyield of an aluminum cathode peaks at  $0.19 e^-/\gamma$ , we obtain a vacuum photodiode power of 1.4 W/V. If we instead assume photons at 30 nm, near the low-wavelength limit of an aluminum cathode where the yield is roughly  $0.05 e^-/\gamma$ , we obtain a vacuum photodiode power of 16 W/V. Thus, our assumption of monochromatic  $H_{L\alpha}$  radiation is at worst incorrect by a factor of three. This should be compared to the uncertainty of  $\pm 30\%$  in the yield of a metallic cathode in typical laboratory conditions [59]. Finally, we also assumed that the plasma emits homogeneously over the detector viewing area, which leads to the factor of  $A_0/A_e^*$  in Eq. (4.3). However, the exact degree to which the collimator shadows the vacuum photodiode from the plasma radiation depends on how the radiation is distributed within the vacuum photodiode field of view. For instance, if all the radiation originates from a point source at the center of the detector's viewing area, then the collimation has no shadowing effect on the signal, and the factor  $A_e^*/A_0$  would be inaccurate. Nonetheless, we expect Eqs. (4.1) and (4.3) to hold to within an order of magnitude, and we see that vacuum photodiode signals on the order of a volt correspond to megawatts of radiation power.

### 4.1.2 Ohmic Heating and Radiative Losses

Simple calculations suggest that Ohmic dissipation of the plasma current should steadily heat the plasma to higher and higher temperatures if no mechanism exists to carry away this energy. Such heating is not observed in the Caltech experiments, for a plasma made of argon or nitrogen that is steadily heated from 1 eV to 10 eV would rapidly progress through its ionization states, and this behavior is not observed. Instead, radiative losses, primarily in the EUV, carry away the Ohmic heat, and we investigate this possibility by comparing the radiation estimates of the previous section to estimates of Ohmic dissipation. Although the figures reported here are only accurate to within an order of magnitude, it seems plausible that the Ohmic heat is indeed lost to EUV radiation.

To quantify the issue of Ohmic heating, we compute the theoretical rate of increase of temperature assuming the energy of Ohmic dissipation ends up as thermal particle energy with no loss of energy as radiation. The thermal energy is  $(3/2)k_B T$  per particle, so for a singly ionized plasma we sum over electrons and ions to get a thermal energy density of  $3k_B T n$ , where we have assumed that electrons and ions share that same temperature. We take  $n \sim 10^{21} \text{ m}^{-3}$  based on Stark broadening measurements of the  $H_\beta$  lines as discussed in Sec. 2.2.4. This thermal energy density is fueled by Ohmic dissipation, whose power density is  $\mathbf{E} \cdot \mathbf{J} = \eta J^2 = \eta I^2 / A_c^2$ , where  $\eta$  is the plasma resistivity,  $I$  is the plasma current, and  $A_c$  is the cross-sectional area of the plasma loop. If all of the energy of

Ohmic dissipation goes into thermal energy, then

$$\dot{T} = \frac{2\eta I^2}{3A_e^2 n k_B}. \quad (4.4)$$

From fast camera images, the radius of the plasma loop is approximately 2 cm. The plasma resistivity will be estimated using Fokker-Planck theory [2, pg. 451]:

$$\eta = \frac{Z e^2 \sqrt{m_e} \ln \Lambda}{3\pi^{3/2} \epsilon_0^2 (2k_B T_e)^{3/2}} \quad (4.5)$$

$$= 1.03 \cdot 10^{-4} \frac{Z \ln \Lambda}{T_e^{3/2}}, \quad (4.6)$$

where  $\ln \Lambda$  is the usual Coulomb logarithm [75, pg. 34]. Using  $Z = 1$ ,  $\ln \Lambda = 7$ , and  $T_e = 3$  eV gives  $\eta = 1.4 \cdot 10^{-4} \Omega\text{m}$ . Therefore, at a modest current of 10 kA, we would have  $\dot{T} \sim 20$  eV/ $\mu\text{s}$ . Clearly, under such conditions the plasma would rapidly heat up to very high temperatures, which is not observed experimentally. This indicates that radiative losses must be transporting energy out of the plasma at a rate comparable to the Ohmic dissipation.

To estimate the total amount of heat generated in the plasma loop, we model the plasma as a uniform cylinder of radius  $r$ , length  $l$ , and resistivity  $\eta$ , from which the plasma resistance is  $R_p = \eta l / (\pi r^2)$ . We take  $r = 2$  cm and  $l = 20$  cm, which gives an estimated resistance of the plasma cylinder of 20 m $\Omega$ . This is only a rough estimate. The length of the loop grows steadily throughout the course of a shot due not only to the overall expansion but also due to the kinking of the flux tube. The loop radius is not always clearly defined from the camera images. Moreover, the current may not flow entirely through the loop in fast camera images. On the Spheromak experiment, magnetic data indicate that the current flows in a radius over three times larger than the radius seen in camera images [37]. If this is also true for the Solar Loop Experiment, the plasma resistance and Ohmic dissipation would be smaller by a factor of nine. Also, on the Solar Experiment, current still flows between the electrodes even at late times when Imacon images suggest that the plasma has detached from the electrodes. It is not clear where the current flows at this point; it may partially flow through arcs observed between and behind the electrodes. Finally, we note that  $Z$ , which should be averaged over all ions, both majority and impurity, may have a bigger value than  $Z = 1$  depending on the impurity concentration. Thus, there are several factors that make our estimate of 20 m $\Omega$  accurate only to within an order of magnitude.

Radiative losses in the EUV appear to balance Ohmic dissipation. Figure 4.1 plots both these quantities for a single-loop hydrogen plasma formed with a 5 kV discharge (shot 8959). The UV radiation power is obtained by summing all twelve vacuum photodiode signals and applying the conversion factors in Eqs. (4.1) and (4.3). The Ohmic heating power is given as  $R_p I(t)^2$  with  $R_p$  estimated above as 20 m $\Omega$ . The two power levels are close in magnitude; moreover, the shapes of

the two traces are especially similar during the first three microseconds. Both the estimates for Ohmic dissipation and UV emission are rough, and at this level of accuracy it appears very possible that the UV radiation indeed balances the Ohmic dissipation. We note that the vacuum photodiode array does not view the entire plasma, and thus the UV power computed here is smaller than the total UV power. Plans are in place to install another set of vacuum photodiodes whose field of view will cover the entire plasma and whose signal will thus reflect the total UV emission. These vacuum photodiodes will also have reduced uncertainties in regards to computing the total power radiated because they will not be significantly collimated, and the factor of  $A_0/A_c^*$  in Eq. (4.3) will very close to unity.

We can compare the power levels of EUV radiation and Ohmic dissipation to other power levels in the experiment. Figure 4.1 plots the total input power  $P_{\text{tot}} = I(t)V(t)$ , where  $V$  is the electrode voltage. The total input power is an order of magnitude larger than both the UV emission and Ohmic heating, and the rapid decline of the input power corresponds to the voltage going to zero and changing sign. We thus see that while radiative losses are significant, they do not dominate the energy budget, and there is ample energy available for the plasma kinetic and magnetic energy. Figure 4.1 also plots an estimate of the optical power as estimated from an optical photodiode, as will be discussed below. While the optical power is over an order of magnitude smaller than the UV emission, its curve has roughly the same shape during the first several microseconds.

By varying the discharge voltage of the main bank, the UV radiation is seen to be determined by the instantaneous value of the plasma current. In Fig. 4.2.a, the vacuum photodiode signal is plotted as a function of time for different discharge voltages. For larger discharge voltages, the vacuum photodiode signal rises more rapidly in the first several microseconds. In Fig. 4.2.b, however, the vacuum photodiode signals are instead plotted as a function of current and are seen to coincide with each other during early times. During this phase, the UV radiation depends only on the instantaneous value of the current. Moreover, this dependence is roughly quadratic, and fitting the UV power levels with the square of the current gives a plasma resistance of  $5.3 \text{ m}\Omega$ . At a certain point in time, however, the UV signal diverges from this quadratic dependence on current; this occurs at earlier times for lower discharge voltages. The reason from this departure from the quadratic behavior is not yet understood and presents an intriguing possibility for future research.

Also shown in Figs. 4.2.c and 4.2.d are estimates of the optical radiation obtained from optical-photodiode data. A PDA36A photodiode by ThorLabs<sup>2</sup> was mounted on a viewport looking across the vacuum vessel at the electrodes. The advantage of this positioning was that the field of view of the optical photodiode covered the entire plasma, unlike the collimated vacuum photodiodes. For hydrogen plasmas, we assume that the photodiode signals comes entirely from the Balmer  $\alpha$  (656

---

<sup>2</sup>The author graciously acknowledges Matthew Kelley for suggesting this diode and lending one to the lab.

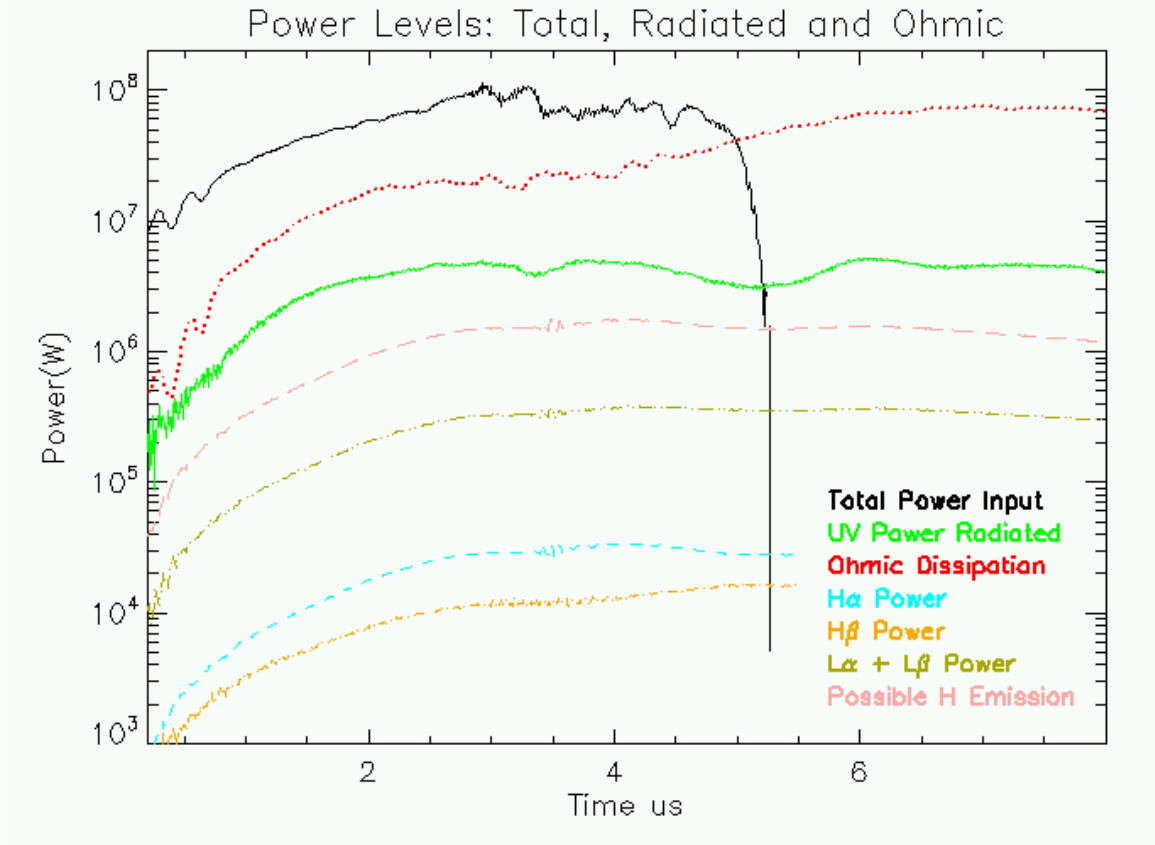


Figure 4.1: A plot of various power levels: the total input power, the estimate for Ohmic dissipation, the total EUV radiative losses, radiative losses from the optical  $H_\alpha$  and  $H_\beta$  lines, the associated power loss from the  $H_{L\beta}$  and  $H_{L\gamma}$  lines, and an estimate for the total hydrogen emission.

nm) line, for which the diode responsivity is 0.408 A/W [76]. Thus,

$$P_{\text{diode}} \approx \frac{V_{\text{diode}}}{50 \, \Omega \cdot 0.408 \, \text{A/W}}. \quad (4.7)$$

The optical photodiode does not have any collimation, so we use Eq. (3.5) to estimate the total optical power radiated,

$$P_{\text{optical}} = P_{\text{diode}} \cdot \frac{4\pi\rho^2}{A_{\text{diode}}} \quad (4.8)$$

$$= (120,000 \, \text{W/V}) \cdot V_{\text{diode}}, \quad (4.9)$$

where the optical photodiode area is  $13 \, \text{mm}^2$  and  $\rho = 1.58 \, \text{m}$  is the separation between the optical photodiode and the electrodes. It is possible that reflections of visible light rays within the chamber can make Eq. (4.9) overestimate the true optical power, but we do not expect reflections to be especially significant based on fast camera images. As shown in Fig. 4.1, the power radiated in the optical domain is much smaller than both the UV power and the Ohmic dissipation. However, as

is seen in Fig. 4.2.c, the optical signals follow the same trend as the vacuum photodiode signals for early times and, when plotted as a function of current, coincide with each other, confirming that radiation at different discharge voltages is indeed a function of the instantaneous current.

The data in Fig. 4.2 were taken holding the charging voltage of the fast gas valve capacitor bank fixed so that the amount of neutral gas available to the plasma is fixed (see Sec. 2.1.2). If the charging voltage is varied, then the traces do not overlap as well even if the discharge voltage is held fixed. We hypothesize that the different charging voltages for the fast gas valve capacitor bank induce different plasma densities that change the emissivity of the plasma, as will be discussed in the next section.

In conclusion, the magnitude of the EUV emission is comparable to and perhaps balances the rate of Ohmic dissipation; this implies that the vacuum photodiode signals, in the absence of other emissive phenomena, are determined by the plasma resistivity and the instantaneous value of the current. Further support for this hypothesis is found by varying the discharge voltage of the main bank while holding the charging voltage of the fast gas valve capacitor bank fixed, for both the UV and optical emission are seen to be functions of the instantaneous value of the current. However, we note that the vacuum photodiode signals typically contain more structure than the optical photodiode signals, as is suggested in Fig. 4.1, and we believe that the vacuum photodiodes are sensitive to a broader range of phenomena than Ohmic dissipation of the main plasma current, as will be discussed further in Sec. 4.2.2.

### 4.1.3 Hydrogen Line Emission

The vacuum photodiode signals are quite large, but the mechanism responsible for producing such copious amounts of UV radiation has not yet been identified. Here, we present evidence that a significant portion of this UV radiation is hydrogen line emission. At first glance, this may seem obvious; since the plasma are composed of hydrogen, hydrogen emission should be significant. However, hydrogen line emission is typically not a significant source of radiation when the plasma is fully ionized, and analytical calculations of an equilibrium hydrogen plasma predict relatively minute radiation levels. However, the Solar Loop Experiment is fast and has magnetic field lines that link the electrodes; these factors keep the plasma out of equilibrium and increase its emission, perhaps explaining the magnitude of the vacuum photodiode signals. Other candidates for the EUV emission, impurity lines and thermal bremsstrahlung, will be presented in Sec. 4.1.4.

Line emission refers to the process whereby a bound electron orbiting an atomic nucleus collides with a free electron or photon, is excited to a higher energy level, and then radiatively decays to a lower energy state. The rate at which bound electrons are excited increases with both the free electron density and temperature, but if the ionization rate is too large then the vast majority of bound electrons will be ionized, resulting in a reduction in line emission. Thus, at fixed electron

density, line emission typically rises to a peak and then falls as a function of temperature: at lower temperatures there are many bound electrons but few exciting collisions and at higher temperatures there are few bound electrons. This rise and then fall in line emission as a plasma heats up is known as a radiation barrier because the energy lost to line emission can balance Ohmic heating and prevent the plasma temperature from rising. If the Ohmic heating is sufficiently strong, though, the temperature will rise high enough such that radiation losses decrease; such a plasma is said to have “burnt through” the radiation barrier. Hydrogen presents a low-temperature radiation barrier of 1 - 2 eV [77, pg. 202] that is usually overcome in experiments, and the significant radiation barriers for a hydrogen plasma typically come from impurities [27, 78]. Indeed, the temperature of the Caltech plasmas is estimated at 2 – 3 eV based on the ionization states of argon and nitrogen plasmas and based on the ionization states of carbon and oxygen impurities; as we shall soon see, such temperatures would suggest a nearly fully ionized plasma and very low hydrogen line emission.

The chief indication that hydrogen line emission is significant in the Solar Loop Experiment is that hydrogen line emission in the optical range is readily observed. By placing an  $H_\alpha$  or  $H_\beta$  optical bandpass filter in front of the fast camera, it is seen that a significant fraction of the optical signal is due to  $H_\alpha$  and  $H_\beta$  line emission. We can quantify the amount of power emitted in  $H_\alpha$  and  $H_\beta$  by placing the same optical filters in front of the photodiode mentioned in Sec. 4.1. By applying conversion factors similar to those used in Eq. (4.9), including the 0.45 peak transmission coefficient of the optical filters, we obtain the  $H_\alpha$  and  $H_\beta$  power traces plotted in Fig. 4.1 for a single loop hydrogen plasma formed with a 5 kV discharge with the fast gas valve capacitor bank charged to 500 V (shots 8987 and 8992). We shall show below that the power levels in these two optical lines alone exceeds the *total* power radiated as predicted by equilibrium models. Moreover, we note that the optical line intensities are strongly correlated with the vacuum photodiode signals and *increase* with time. This is significant because the current and hence Ohmic dissipation is likewise increasing in time, so the plasma temperature must be increasing until the radiative losses again balance the Ohmic dissipation. If during this process the plasma was close to equilibrium and the hydrogen was nearly fully ionized, then we would expect the hydrogen emission to *decrease*, or at least not increase, as the temperature rises even further beyond the radiation barrier. For example, on the Macrotron tokamak, the  $H_\beta$  signal peaks after 1 ms and then falls to a low value as the vacuum photodiode signals and oxygen line intensities continue to increase [48]. The behavior from Macrotron is indicative of full hydrogen ionization, or hydrogen burnthrough, while the optical-photodiode data from the Caltech Loop Experiment indicate that the hydrogen is still ionizing. Since weak hydrogen emission is due to full ionization of the hydrogen population, incomplete ionization would allow for strong hydrogen emission. The strong correlation between the hydrogen optical intensity and the vacuum photodiode signals is consistent with (but certainly does not prove) the possibility that the vacuum photodiode signal is entirely due to hydrogen emission.

Furthermore, from the optical emission we can estimate a portion of the hydrogen EUV emission and show that it is a substantial fraction of the total EUV emission measured by the vacuum photodiodes. The  $H_\alpha$  line results from electron transitions from the  $n = 3$  to  $n = 2$  state; the rate of this transition is given by the transition probability per unit time  $A_{32} = 4.4 \cdot 10^7 \text{ s}^{-1}$  [79, pgs. 275 and 281] so that  $N_{32} = A_{32}N_3$ , where  $N_{32}$  is the number of  $H_\alpha$  photons produced per second and  $N_3$  is the number of hydrogen atoms in the  $n = 3$  state. Knowing the  $H_\alpha$  power level and that each  $H_\alpha$  photons contains 1.89 eV, we estimate  $N_3$ :

$$N_3 = \frac{P_\alpha}{1.89 \text{ eV} \cdot A_{32}}. \quad (4.10)$$

The Lyman  $\beta$  ( $H_{L\beta}$ ) line results from transitions from the  $n = 3$  state to the  $n = 1$  state, which occur at a rate  $A_{31} = 5.6 \cdot 10^7 \text{ s}^{-1}$ . Since each  $H_{L\beta}$  photon contains 12.1 eV of energy, it follows that the power emitted in  $H_{L\beta}$  relative to the  $H_\alpha$  power is

$$P_{L\beta} = A_{31}N_3 \cdot (12.1 \text{ eV}) = 8.15 \cdot P_\alpha. \quad (4.11)$$

A similar calculation relates the power of the Lyman  $\gamma$  line ( $n = 4$  to  $n = 1$ ) to the power from the Balmer  $\beta$  line:  $P_{L\gamma} = 7.74 \cdot P_\beta$ . Using these calculations, we compute the  $H_{L\beta}$  and  $H_{L\gamma}$  contributions to the EUV emission and plot the result in Fig. 4.1. This calculated emission rises to 300 kW, about 10% of the peak EUV power of 3 MW. However, we have not accounted for the most powerful hydrogen line, the  $H_{L\alpha}$  line. Under the assumption of local thermodynamic equilibrium (LTE), to be discussed below, the power of the  $H_{L\alpha}$  would be about five times that of the  $H_{L\beta}$  line [80], in which case the powers of the  $H_{L\alpha}$ ,  $H_{L\beta}$ , and  $H_{L\gamma}$  lines total to about one third of the total EUV emission. Clearly, the hydrogen emission is significant. Moreover, the LTE assumption, which is not expected to hold rigorously for the Caltech experiments, populates states according to the Saha-Boltzmann distribution, which favor the population of high  $n$  states. In Fig. 3 of Ref. [81], which describes plasma conditions very close to those of the Caltech Solar Loop Experiment, the low  $n$  states may have a higher population than that predicted by LTE, so the total hydrogen contribution to EUV emission might be even larger than one third. The current data is insufficient to determine exactly what percentage of the total power radiated comes hydrogen, and an experiment will be described in the next section to answer this question, but the optical photodiode data suggests that a substantial fraction of the EUV signal is hydrogen emission.

We now show that a pure hydrogen plasma in ionization equilibrium does not emit nearly as intensely as the Caltech Solar Loop Experiment. The intensity of line emission is determined by the populations of the associated ionization and excited states. These populations are in turn determined by a detailed balance of atomic processes, including collisional excitation and de-excitation as well as radiative de-excitation [82, 77]. The population levels are typically calculated numerically and

can vary greatly based on the electron temperature and density. The temperatures and densities of the Caltech plasmas happen to be similar to the divertor region in a tokamak, for which effective average cross-sections for ionization and recombination that include multi-step ionization have been calculated [83] and are reproduced in Fig. 4.3. These cross-sections are *effective* because they include all excited states of neutral hydrogen; their utility, as explained by Stangeby, is that “one can proceed as if all the atoms were in the ground state” [84, pg. 138]. Thus, the effective ionization rate  $\langle\sigma\nu\rangle_{\text{iz}}$  gives the rate of neutral hydrogen atoms, including all excited states, being ionized, and the effective recombination rate  $\langle\sigma\nu\rangle_{\text{re}}$  gives the rate at which an electron and proton recombine to form neutral hydrogen of all excited states. The continuity equation for proton density  $n_i$  is then

$$\frac{\partial n_i}{\partial t} + \nabla \cdot (n_i \mathbf{v}) = \langle\sigma\nu\rangle_{\text{iz}} n_e n_0 - \langle\sigma\nu\rangle_{\text{rc}} n_e n_i, \quad (4.12)$$

where  $n_0$  is the neutral hydrogen density, which includes all excited states. In Eq. (4.12), ionization acts as a source for protons whereas recombination acts as a sink. For this calculation, we assume a steady-state and homogenous plasma and set the lefthand side of Eq. (4.12) to zero. This is a poor assumption as the Caltech experiment is very fast (and thus not steady-state) and also has strong flows from the footpoints (implying strong convection), but by making such assumptions we will demonstrate the need for a non-equilibrium process to explain the strong energy discrepancy. The resulting ionization balance from setting the lefthand side of Eq. (4.12) to zero is

$$\frac{n_0}{n_i} = \frac{\langle\sigma\nu\rangle_{\text{rc}}}{\langle\sigma\nu\rangle_{\text{iz}}}. \quad (4.13)$$

We take the electron density to be  $n_e = 10^{21} \text{ m}^{-3}$ , based on Stark broadening of the  $\text{H}_\beta$  line as discussed in Sec. 2.2.4, and  $T_e \sim 2 - 3 \text{ eV}$ , based on the observed ionization states in nitrogen and argon plasmas and estimates from spectral lines of oxygen and carbon impurities. Using Fig. 4.3 at  $T = 3 \text{ eV}$ ,  $\langle\sigma\nu\rangle_{\text{iz}} = 2 \cdot 10^{-9} \text{ cm}^3/\text{s}$  and  $\langle\sigma\nu\rangle_{\text{re}} = 4 \cdot 10^{-13} \text{ cm}^3/\text{s}$ , which gives  $n_0/n_i = 2 \cdot 10^{-4}$ . At  $T = 2 \text{ eV}$ ,  $\langle\sigma\nu\rangle_{\text{iz}} = 4 \cdot 10^{-10} \text{ cm}^3/\text{s}$  and  $\langle\sigma\nu\rangle_{\text{re}} = 9 \cdot 10^{-13} \text{ cm}^3/\text{s}$ , which gives  $n_0/n_i = 2 \cdot 10^{-3}$ . In either case, the vast majority of hydrogen is ionized, and only the small fraction of remaining neutrals can participate in line emission.

To obtain the power radiated by such a hydrogen plasma, we utilize a second quantity called the emissivity,  $L$ . This quantity is related to the power radiated by  $P_{\text{rad}} = Ln_e n_0 \text{ vol}$ , where  $\text{vol}$  is the volume of the plasma. This quantity is computed numerically in Ref. [83] and is reproduced in Fig. 4.4. For a plasma with  $n_e = 10^{21} \text{ m}^{-3}$  and  $T = 3 \text{ eV}$ ,  $L \approx 1.1 \cdot 10^{-20} \text{ ergs cm}^3 \text{ s}^{-1}$ , and  $P_{\text{rad}} = (0.2 \text{ W/cm}^3) \cdot \text{vol}$ . We estimate the plasma volume using the plasma dimensions given in Sec. 4.1.2, namely, a loop length of 20 cm and a radius of 2 cm, giving a volume of  $\text{vol} = \pi r^2 l \approx 250 \text{ cm}^3$ . The total power is then only 50 W, a far cry from the megawatts estimated in the UV range and even from the optical power estimated from the photodiode. For  $T = 2 \text{ eV}$ , we

have  $L \approx 6.5 \cdot 10^{-21}$  ergs  $\text{cm}^3 \text{s}^{-1}$ , and  $P_{\text{rad}} = 400$  W, which is again too small.

Another theoretical estimate of the plasma radiation can be done assuming local thermodynamic equilibrium (LTE). The LTE model assumes that the population levels are balanced by collisional excitations and de-excitations so that the excited states assume a Saha-Boltzmann distribution [77, pg. 118]. The calculations, performed by Vernon Chaplin, predict radiation levels that are somewhat higher than the ones derived above but that are still too low to account for the experimental observations. Even within the uncertainty used in estimating the plasma parameters, the theoretical emission from an equilibrium plasma appears too low to explain the experimental observations.

The large radiation levels suggest that the Caltech plasmas contain more neutrals than suggested by Eq. (4.13). High neutral densities are often associated with a lower-temperature plasma that is only partially ionized. Indeed, equilibrium hydrogen plasmas are typically most emissive when the electron temperature is such that the concentrations of ions and neutrals are about equal [77, pg. 202]. At 1 eV,  $\langle \sigma \nu \rangle_{\text{iz}} = 1.5 \cdot 10^{-12}$   $\text{cm}^3/\text{s}$  and  $\langle \sigma \nu \rangle_{\text{re}} = 6.0 \cdot 10^{-12}$   $\text{cm}^3/\text{s}$  from Fig. 4.3, which together with  $L = 9 \cdot 10^{-22}$  ergs  $\text{cm}^3 \text{s}^{-1}$  and a plasma volume of 250  $\text{cm}^3$  predict an emission of 90 kW, which is significantly closer to the radiation losses observed experimentally. The temperature of hydrogen plasmas on the Caltech Solar Loop Experiment have not yet been accurately diagnosed, so our hydrogen plasmas may be slightly cooler than expected. However, C III (e.g., carbon ions with two electrons stripped) lines have been observed, which suggests an electron temperature greater than 2 eV [80]<sup>3</sup>. However, we shall now see that non-equilibrium effects can allow a hydrogen plasma to radiate like a lower-temperature and partially ionized plasma even when the electron temperature suggests burnthrough.

The above calculations involve several assumptions that are quite dubious, and questioning these assumptions may help to explain the large vacuum photodiode signals. First, we assumed that the plasma is in equilibrium, but the duration of the Caltech Solar Experiment is not much longer than the ionization equilibration time for hydrogen atoms in the plasma conditions described. This equilibration time is roughly the time needed to ionize neutral hydrogen atoms injected into the plasma and is computed as follows. The analog of Eq. (4.12) for neutral hydrogen is

$$\frac{\partial n_0}{\partial t} + \nabla \cdot (n_0 \mathbf{v}) = - \langle \sigma \nu \rangle_{\text{iz}} n_e n_0 + \langle \sigma \nu \rangle_{\text{rc}} n_e n_i. \quad (4.14)$$

We ignore convection by setting  $\mathbf{v} = 0$ . Let the equilibrium densities be  $n_{i,eq}$  and  $n_{0,eq}$ . If we then add a extra amount of neutral atoms, i.e.  $n_0 = n_{0,eq} + \delta n_0$ , then the continuity equation becomes

$$\frac{\partial(\delta n_0)}{\partial t} = - \langle \sigma \nu \rangle_{\text{iz}} n_e (\delta n_0), \quad (4.15)$$

---

<sup>3</sup>This statement is based on the LTE assumption. While LTE may not be accurate for the Caltech experiments, we believe that it provides a rough estimate. In this case, at temperatures below 2 eV, carbon ions are predicted to be almost exclusively in the C II ionization state.

from which the relaxation time  $\tau$  is  $\tau = 1/(\langle\sigma\nu\rangle_{iz} n_e)$ . At  $T = 3$  eV and  $n_e = 10^{15}$  cm<sup>-3</sup>, we have  $\tau \approx 0.5$   $\mu$ s, and at  $T = 2$  eV we have  $\tau \approx 2.5$   $\mu$ s. This relaxation time is not much shorter than the time scale of the plasma itself, so we cannot expect the plasma to be in equilibrium. This essentially means that the hydrogen does not have enough time to achieve the ionization balance predicted by Eq. (4.13) and that we can expect a larger number of neutrals. This proposed situation is similar to that investigated by Carolan and Piotrowicz, who studied the emission of impurities that have had insufficient time to achieve coronal equilibrium [85]. They found that impurities such as carbon and oxygen radiate more intensely at temperatures above burnthrough when not given enough time to equilibrate. We propose that hydrogen, the majority species, is behaving similarly: even though the temperatures of the Solar Loop Experiment may exceed burnthrough, the plasma may still radiate at very high levels as the neutrals gradually ionize over the course of microseconds. Note also that  $L$ , the emissivity, is two orders of magnitude higher at 3 eV than at 1 eV. Thus, it may be that the Solar Loop Experiment, because of its fast timescale, has a large population of neutrals like a lower-temperature, partially ionized plasma but, at the same time, has a larger value of  $L$  due to its higher electron temperature.

We also ignored convection in Eq. (4.13), but the Caltech Solar Loop Experiment certainly exhibits strong flows from the footpoints [43, 17]. It is generally accepted that plasma interaction with the chamber wall results in a larger density of neutral atoms as ions recombine with electrons from the wall. It is possible that this higher concentration of neutrals is then pumped out of the gas inlet via the MHD mechanism described in Sec. 2.1.5. Away from the wall, the neutrals would ionize on a microsecond timescale, during which time they would radiate far more intensely than an equilibrium plasma. Moreover, as suggested by Post, the presence of molecular hydrogen could increase the recombination rate by up to four orders of magnitude [83]! The molecular hydrogen concentration is expected to be very minute in the plasma itself but could be significant in the gas inlet.

In summary, a substantial fraction of the vacuum photodiode signals is hydrogen line emission, but the magnitude of such emission cannot be explained by emission from an equilibrium plasma. However, *non-equilibrium* effects might cause the plasma to radiate more intensely due to a large number of neutral atoms; the enhanced neutral concentration might be attributed to the short time scale of the experiment as well as the MHD pumping force that drives strong plasma flows from the wall. Given the uncertainties in the calculation, it is even conceivable that the vacuum photodiode signals are entirely caused by hydrogen line emission; this hypothesis is supported by the correlation between the vacuum photodiode signals and the hydrogen optical line intensity. Of course, there are other sources of EUV radiation; in the following section we shall look into both impurity radiation and thermal bremsstrahlung and discuss their potential contributions to the vacuum photodiode signals.

#### 4.1.4 Other Emission Processes

We now discuss two other radiation mechanisms: line emission from plasma impurities and thermal bremsstrahlung. Impurity line emission typically dominates the radiative losses of a hydrogen plasma, and one might suspect that the large vacuum photodiode signals are due to impurity emission. However, the previous section demonstrated that hydrogen emission is a substantial fraction of the total radiation, and we discuss in this section why impurity emission may not be as dominant for the Caltech Solar Loop Experiment as it is for other experiments. We also outline a future experiment to determine the relative contributions of hydrogen and impurity emission. Thermal bremsstrahlung, in contrast, is far too weak to contribute significantly the observed radiation levels.

In previous laboratory hydrogen plasmas, impurity line emission typically dominated the radiative losses. The reason for this, as discussed in the previous section, is that the hydrogen atoms quickly ionize and cease line emission. Impurities, although low in concentration, continue to radiate until fully stripped of all bound electrons, which may not occur until very high temperatures have been achieved. Moreover, the line emission of certain impurity ionization states can be quite intense. Impurities are a major hindrance to tokamak start-up [78] and have thwarted previous spheromak experiments [27]. In light of these previous experiences with impurity radiation, one might suspect that the excessively large vacuum photodiode signals should be due to impurity emission and that the hydrogen emission is negligible, as suggested by the analytical calculations. However, we have seen in the previous section that hydrogen emission is a non-negligible fraction of the total emission, so the role of impurities in the Caltech experiments may be less significant than for other previous experiments. This is probably because these previous experiments are typically hotter (so that the impurities are more emissive), last longer (so that the hydrogen has time to ionize more fully), and involve more interactions with the chamber walls (so that more impurities are introduced into the plasma). Indeed, from Figs. 3(d) and 4(d) from Ref. [85], the burnthrough temperature for carbon is 9 eV, and the burnthrough temperature for oxygen is about 20 eV. Because the Caltech plasmas are colder than both of these burnthrough temperatures, the impurity emission from these species will not be as intense as it is for other experiments at higher temperatures.

If impurity emission dominates the hydrogen emission, then one would expect impurity lines to be readily observed with the spectrometer. On the contrary, while the  $H_\beta$  line is readily measured on the Caltech Solar Loop Experiment, locating impurity lines has been somewhat difficult. Impurity lines were finally observed on one of the final experimental runs before a shutdown for maintenance; these lines were located by assuming that the plasma was slightly cooler (2 eV) than previously expected (3-5 eV) and also by aiming the spectrometer directly at the gas inlets from which the impurities originate. A sample of the spectrometer data with identified impurity lines<sup>4</sup> is shown in

---

<sup>4</sup>This spectral window is particularly rich in impurity lines, and analysis of this window, which is beyond the scope of this thesis, is expected to yield very useful information concerning temperature and relative impurity concentrations.

Fig. 4.5.a, whereas Fig. 4.5.b shows the  $H_\beta$  line, whose magnitude far exceeds that of any impurity line. There are many factors that must be taken into account when comparing the intensities of these spectral lines. The impurity spectra were obtained on shot 9163, a co-helicity hydrogen plasma with the gas valve supply charged to 500 V, while the  $H_\beta$  spectrum was obtained from shot 9024, a counter-helicity hydrogen plasma also formed with the gas valve supply charged to 500 V. For the impurity spectra, the spectrometer was gated for the entire lifetime of the plasma, whereas the  $H_\beta$  spectrum was obtained by gating only over a microsecond. For the impurity spectra, the spectrometer was aimed at the gas inlets, the brightest portion of the plasma, whereas the  $H_\beta$  spectrum was acquired from a line of sight about ten centimeters away from the electrodes. Clearly, the spectra should be compared under identical conditions, but, if the  $H_\beta$  spectra was measured with the spectrometer gated for the entire plasma duration and pointed directly at the gas inlets, we would expect the  $H_\beta$  line to be even more intense than shown in Fig. 4.5.

If the radiative losses are due entirely to impurity emission, then the implied impurity concentrations are suspiciously large. Carbon and oxygen are the “usual suspects” for low-Z impurities; the emissivity of carbon at  $T_e = 3$  eV is roughly  $10^{-32}$   $\text{Wm}^3$ , while that of oxygen at the same temperature is  $2 \cdot 10^{-33}$   $\text{Wm}^3$  [85, 83]. Carbon is thus more emissive at these temperatures, so we ignore oxygen. If we assume that the entire radiative losses, up to 1 MW as predicted by the vacuum photodiodes, are due to carbon emission alone, then

$$P_C = 1 \text{ MW} = L_C n_e n_C \text{vol}, \quad (4.16)$$

and using  $n_e = 10^{21}$   $\text{m}^3$  and  $\text{vol} = 250$   $\text{cm}^{-3}$  we get

$$n_C = \frac{1\text{MW}}{L n_e \text{vol}} = 4 \cdot 10^{20} \text{ m}^{-3}. \quad (4.17)$$

This implies that the carbon concentration is 40 percent of the electron density, or that the carbon concentration is roughly equal to the hydrogen concentration. This does not seem realistic. In the Swarthmore Spheromak Experiment, the carbon concentration is estimated to be 2 percent of the hydrogen concentration, which is nominally  $5 \cdot 10^{20}$   $\text{m}^{-3}$  [47]. The Swarthmore vacuum chamber is baked out to reduce impurity levels, but the Swarthmore plasmas also interact with a much larger surface area, including the coaxial spheromak guns that create the plasma. On the PISCES-B experiment, the baseline carbon ion fraction is 0.2%, and active injection of methane raises this fraction to only 2% [86]. Thus, a 40% carbon fraction seems unreasonably high.<sup>5</sup> Before concluding

<sup>5</sup>A similar analysis for hydrogen, with  $L = 10^{-33}$   $\text{W m}^3$  at  $T_e = 3$  eV, would require  $n_H = 4 \cdot 10^{21}$   $\text{m}^{-3}$  to produce a megawatt of power. This would imply that the plasma is far from ionization equilibrium, which agrees with the rising optical hydrogen line intensities observed during a shot. The density of the neutral gas puff on the Spheromak Experiment is believed to be well below  $10^{21}$   $\text{m}^{-3}$  [46], but this density has not been measured on the Solar Loop Experiment. Since the Solar Loop Experiment uses different power supplies for the gas valves, and since the gas valves are quite sensitive to the power supply [87], the Solar Loop Experiment may have a different density of neutral gas

too much from Eq. (4.17), though, we note that the values of  $n_e$  and  $T_e$  are not precisely known, and  $n_C$  is inversely proportional to  $n_e$  and is a strong function of  $T_e$ . For instance, if  $T_e = 2$  eV then the  $L_C = 2 \cdot 10^{-33}$  W m<sup>3</sup>, and the required carbon concentration is five times higher. The plasma parameters are not currently known to sufficient precision to constrain the impurity concentration, and it is quite possible that impurities are contributing substantially to the radiative losses.

An experiment has been designed to determine the contribution of the H<sub>Lα</sub> line to the vacuum photodiode signal in isolation from other lines. A pair of vacuum photodiodes will be installed in the middle of the vacuum chamber, roughly in the same location as the x-ray diodes shown in Fig. 2.1. By adjusting the collimation, these vacuum photodiodes will view the entire plasma on the Solar Loop Experiment. A lithium fluoride window will be installed over one vacuum photodiode; lithium fluoride has a sharp cutoff in the VUV just above the H<sub>Lα</sub> line and has roughly a 50% transmission the H<sub>Lα</sub> line. Surveying the main lines from low-Z impurities, the LiF window should filter out all impurity lines in the EUV. Thus, if the filtered vacuum photodiode registers a very small signal compared to the unfiltered vacuum photodiode, then the H<sub>Lα</sub> line is not contributing significantly to the EUV emission. If, however, the filtered signal is roughly half of the unfiltered signal, then the Solar Loop Experiment does indeed possess strong hydrogen line emission even though the electron temperature suggests nearly complete ionization of hydrogen.

Bremsstrahlung is a radiation mechanism that is important for high-temperature plasmas but is insignificant for the Caltech experiments. Bremsstrahlung is the radiation emitted by an accelerated charge; in a plasma, an electron is continually being accelerated by Coulomb collisions with each particles, and the plasma emits a continuous spectrum based on the particle distribution function. Bremsstrahlung radiation from a thermal plasma is given in cgs units as [79, pg. 160]

$$\epsilon_\nu^{ff} = \frac{dW}{dt dV d\nu} = \frac{2^5 \pi e^6}{3mc^3} \sqrt{\frac{2\pi}{3mk_B T}} Z^2 n_e n_i e^{-h\nu/k_B T} \bar{g}_{ff}. \quad (4.18)$$

$\bar{g}_{ff}$  is the velocity-averaged Gaunt factor and can be taken to be about one for this calculation. The energy spectrum dies off exponentially for photon energies above the plasma temperature. As the Caltech plasmas have a temperature  $T \approx 3$  eV, most of the bremsstrahlung energy is concentrated above the wavelength  $\lambda_{\text{thermal}} = ch/(k_B T) = 410$  nm; this makes bremsstrahlung an unlikely can-

---

than the Spheromak Experiment. We can roughly estimate the neutral gas density as follows. The neutral gas flows from the fast gas valves through teflon tubes of volume 19 cm<sup>3</sup> into the main vacuum chamber, which has a volume of 1.8 m<sup>3</sup>. When the gas valves are puffed, the chamber pressure rises on the order of 1 mtorr, which corresponds to  $8 \cdot 10^{19}$  gas particles let in by a single puff. Since these particles travel through four teflon tubes (one for each gas inlet), when the gas puff is just exiting the gas inlets and occupies the tube volume, the neutral density is roughly  $1 \cdot 10^{24}$  m<sup>-3</sup>. We assume that, once the neutral gas reaches the gas inlet, it expands in a cone of opening angle 45° and that the linear density scales inversely with the cone radius squared. Under these assumptions, the neutral gas density a distance 4 cm away from the gas inlet would be  $4 \cdot 10^{21}$  m<sup>-3</sup> since the radius of the teflon tube is about 0.26 cm. This suggests that the Solar Loop Experiment may indeed start at a relatively high neutral density as would be required by the vacuum photodiode data assuming the radiation is mostly hydrogen line emission. Of course, neutral gas density measurements should be made on the Solar Loop Experiment to corroborate these “back of the envelope” calculations. The author would like to thank Auna Moser for assistance in comparing these calculations to measurements made on the Spheromak Experiment.

didate for explaining the large EUV emission observed by the vacuum photodiodes. Moreover, the overall power emitted by bremsstrahlung is rather small; integrating Eq. (4.18) over all frequencies gives

$$\frac{dW}{dt dV} = \frac{2^5 \pi e^6}{3mc^3} \sqrt{\frac{2\pi}{3m}} Z^2 n_e n_i \frac{\sqrt{k_B T}}{h}, \quad (4.19)$$

again in cgs units. Using  $Z = 1$ ,  $n_e = n_i \sim 10^{21} \text{ m}^{-3}$ , and  $T \sim 3 \text{ eV}$ , Eq. (4.19) gives  $0.026 \text{ W/cm}^3$ . From a plasma of volume  $250 \text{ cm}^3$  the power of bremsstrahlung radiation is  $P_{\text{brem}} \sim 6.6 \text{ W}$ , which is far too small to account for the power levels estimated by the vacuum photodiodes. Thermal bremsstrahlung is typically more important for hot plasmas because it increases with temperature whereas line radiation decreases assuming the plasma has burned through the radiation barriers. For a colder plasma like the ones produced in the Caltech experiment, though, thermal bremsstrahlung is inconsequential.

## 4.2 Co- Vs. Counter-Helicity Merging

The original purpose of the vacuum photodiode array was to provide spatial resolution to the EUV emission of co- and counter-helicity hydrogen plasmas. In this function, the array has indeed detected enhanced emission from counter-helicity merging that can, in many instances, be correlated with spikes in the x-ray diode signals. In this section, we shall compare co- and counter-helicity hydrogen plasmas formed with a 6 kV discharge voltage and a 500 V charging voltage on the fast gas valve capacitor bank. We shall find that something quite dramatic occurs for the counter-helicity plasma around  $2.7 \mu\text{s}$ . At this time, EUV emission rises sharply, x-ray spikes are observed, the upper legs of the plasma brighten and appear to interact with the chamber wall, and a noise pulse is observed in the electronics. These events are believed to be related to magnetic reconnection and do not occur for a co-helicity plasma formed under the same conditions. As we shall see in Sec. 4.3, these events can be tamed by increasing the charging voltage of the fast gas valve capacitor bank, which admits more neutral gas into the chamber prior to breakdown.

For all counter-helicity shots presented in this section and in Sec. 4.3, the bias magnetic field was created in the RL configuration discussed in Sec. 2.1.3. The second configuration of the bias field that produces counter-helicity loops, LR, produces markedly different plasma behavior, as is discussed in Sec. 4.4. Such a dramatic difference in behavior is not observed between the two co-helicity configurations, and we will not distinguish between these two.

### 4.2.1 Comparing Co- and Counter-Helicity Plasmas

Fig. 4.6 overlays the vacuum photodiode signals for both a co-helicity shot (shot 7774) and a counter-helicity shot (shot 7763). All twelve channels of the array are plotted with the vertical channels

plotted on the left column and the horizontal on the right. The upper left corner of each plot contains a legend to identify the position of the individual detector within the array. The emission from the two plasmas is remarkably similar for the first several microseconds, suggesting that co- and counter-helicity configurations have the same emission during this time and that this part of the vacuum photodiode signals is highly reproducible. Between 1.7 and 2.7  $\mu\text{s}$ , however, the counter-helicity signal rises, sometimes precipitously, above the co-helicity signal. We hypothesize that this time is the beginning of the merging and that the large counter-helicity emission is due to the additional magnetic reconnection of the axial fields, as proposed in Ref. [20]. The mechanisms by which magnetic reconnection can cause enhanced radiation will be discussed in Sec. 4.2.2. The plots in Fig. 4.6 end at 4.7  $\mu\text{s}$ ; beyond this time, the vacuum photodiode signals vary significantly, and the signal levels can be quite high. We will not focus on these later signals as they do not correspond with the main plasma activity: the formation and growth of the plasma loop.

For counter-helicity plasmas, the large UV signals obtained from the topmost channels on the array are corroborated by fast camera images such as Fig. 4.7. Around the time of the UV burst, an intense brightness appears in the upper legs of the plasma, in the vicinity of channels 1 and 2 of the vacuum photodiode array, as the plasma loops merge and detach from the electrodes. This merging is seen more clearly in Fig. 4.9, in which the interframe timing of the Imacon fast camera is reduced to focus on this time period. Interactions with a bolt in the chamber wall several centimeters above the electrodes can occasionally be seen; the bolt is shown most clearly in Fig. 2.2. It is possible that the UV and x-ray signals originate from this interaction with the chamber wall. However, the UV burst typically persists for some time, up to a microsecond, while the arcing to the bolt dies down more quickly. Such intense activity is not seen in images of a co-helicity plasma, as shown in Fig. 4.8.

The rapid rise in the vacuum photodiode for counter-helicity plasmas is sometimes coincident with x-ray bursts on the x-ray diodes. Fig. 4.10 plots two such occurrences. The x-ray bursts that are plotted were obtained through the 200 nm thick Al foil filter whose transmission curve is plotted in Fig. 2.9; since this filter does not transmit hydrogen lines, the x-ray bursts, and perhaps part of the vacuum photodiode signals, must be caused by something other than hydrogen line emission. Different possibilities, such as bremsstrahlung from energetic electrons, are discussed in Sec. 4.2.2. We also note that the x-ray bursts presented here rise more sharply and at a slightly later time than the EUV bursts; this fact may be useful in determining the nature of the x-ray bursts.

The correlation between the x-ray diode data and the vacuum photodiodes data is not perfect; there are times when the x-ray diodes register a peak while no special activity is seen on the vacuum photodiodes, and vice versa. This lack of consistent correlation may be due to the sensitivity of the x-ray diodes to their alignment as discussed in Sec. 2.2.3. In fact, during the set of shots in which Fig. 4.10 was obtained, no significant x-ray activity was seen before 4.7  $\mu\text{s}$  for the first several

shots. Based on the large UV emission observed on the upper channels of the array, the x-ray diodes were re-aligned to point slightly upwards, after which x-ray bursts were seen on two of the next four shots. This anecdote demonstrates how sensitive the x-ray diode signals are to alignment and how the vacuum photodiode data can aid in aligning the x-ray diodes to optimize the chance of registering an x-ray burst. To improve the x-ray diode setup, a mechanical system should be implemented to precisely align the x-ray diodes in a reproducible fashion, or the collimation of the diodes should be redone in order to give the diodes a wide-angle view that covers the entire plasma.

Other differences between co- and counter-helicity plasmas can be seen in the plasma current and electrode voltage. Fig. 4.11 shows the plasma current and electrode voltage for both a co- and counter-helicity shot. The vertical dashed line is at  $2.4 \mu\text{s}$ . At this time, the counter-helicity current begins to oscillate and fails to rise as rapidly as the co-helicity current. The oscillations are due to ringing in the electronics of the Rogowski coil and do not represent true current oscillations; they are similar to the oscillations that are induced by breakdown and that are seen at the beginning of the shot for both co- and counter-helicity plasmas. The deviance of the mean counter-helicity current, obtained by a boxcar average over  $0.8 \mu\text{s}$ , from the co-helicity mean current may indicate that the reconnection process disrupts the current flow and that the plasma has trouble in re-establishing a current path. The primary motion of particles within a magnetized plasma is along magnetic field lines. As the bias field links the anode and cathode, the initial flow of current can be along these field lines. The reconnection process for counter-helicity plasmas, however, rearranges the field lines so that lines initially linking the anode and cathode now link the two quadrants of the anode and the two quadrants of the cathode. Electrons cannot flow along such field lines and contribute to the main current without drifting across such field lines.

The electrode voltages for both co- and counter-helicity shots are initially very similar. At  $2.4 \mu\text{s}$ , both voltages drop, but the counter-helicity electrode voltage drops more sharply and afterwards has several rises and falls while the co-helicity trace progress more steadily to zero. As discussed in Sec. 2.2.2, a larger voltage may be associated with a rapidly expanding plasma, and a sudden drop in the electrode voltage may signify the change of the current to a shorter and lower-inductance path. The voltage drop at  $2.4 \mu\text{s}$  might be similar to the voltage drop that occurs at breakdown. Also, a voltage spike can be interpreted in analogy to the spark that occurs when one unplugs an electrical appliance. In any electrical circuit carrying a current, if the circuit is suddenly opened, a large voltage will appear across the gap. This voltage spike is an attempt by the circuit to maintain the current flow. When unplugging toasters, the large voltage spike can result in a spark that allows current to continue flowing. The spikes that appear on the electrode voltage might be the analogous voltage spike as the loops detach and disrupt the flow of current. Regardless of the exact interpretation of the voltage signals, something drastic is occurring in a counter-helicity plasma after  $2.4 \mu\text{s}$  but not in co-helicity plasmas.

### 4.2.2 Magnetic Reconnection, Current Sheets, and Energetic Electrons

Comparisons of the vacuum photodiode signals between co- and counter-helicity suggest that the signals consists of two components. The first component is a broad and smooth signal with a duration of several microseconds, while the second component consists of faster bursts that rise sharply and last from a microsecond down to tens of nanoseconds. This second component appears mainly in counter-helicity shots. In Sec. 4.1, we hypothesized that the vacuum photodiode signal are proportional to the rate of Ohmic dissipation, but in counter-helicity shots the vacuum photodiode signals spike significantly while the current does not. It seems unlikely that the resistivity of a counter-helicity plasma suddenly becomes much greater than its co-helicity counterpart, and we believe that some other mechanism is creating the large UV bursts seen in counter-helicity shots. We now discuss the possible ways in which magnetic reconnection, seen in Fig. 4.9, could produce the enhanced emission.

Magnetic reconnection involves current sheets that could produce local Ohmic heating in excess of the heating produced by the main plasma current; this excess heat would then lead to larger radiative losses. Current sheets arise during magnetic reconnection because the merging magnetic fields induce an electric field that drives currents via Ohm's law [2, ch. 12]. In this way, the energy contained in the magnetic fields that are being annihilated can be transferred via Ohmic dissipation to the plasma particles, and, under the hypothesis of Sec. 4.1.2, the Ohmic heat generated inside the current sheet will be radiated away. We can estimate the plausibility of this argument by calculating the energy contained in the magnetic field and comparing it to the power radiated by the counter-helicity bursts in excess of the co-helicity signals. We use a typical magnetic field strength of  $B \approx 0.1$  T. The volume of plasma within the view of a single vacuum photodiode is  $\text{vol} = 2\pi r^2 \cdot l$ ; the factor of two comes from the fact that there are two loops, the loop radius  $r$  will be taken to be 0.02 m, and the length  $l$  will be the diameter of the vacuum photodiode's viewcone, calculated in Sec. 3.5.3 to be about 9.4 cm. With these values, the energy contained in the axial field is roughly 1 J; liberating this energy over the course of a microsecond would correspond to power levels of 1 MW. The observed difference between counter- and co-helicity radiation levels, estimated from channel 1 of the vacuum photodiode array data plotted in Fig. 4.6, is approximately 0.25 MW. Thus, it is not unreasonable to suggest that the counter-helicity EUV bursts are energized by the reconnection of the axial field.

Another radiation mechanism is bremsstrahlung from a small population of energetic, non-thermal electrons excited by magnetic reconnection. Such bremsstrahlung would be of a higher frequency and intensity that of the thermal electrons. Electrons may be energized by the induced electric field associated with magnetic reconnection; this has been observed in tokamaks [31, 32], the magnetosphere [88, 89], and in numerical simulations [28, 29]. One interesting feature of plasmas is that faster-moving particles experience fewer collisions, so populations of energized electrons may exist for some time before being thermalized by collisions. Energetic electrons might explain the

bursts seen on the filtered x-ray diode, for the filter blocks all hydrogen lines as shown in Fig. 2.9. Therefore, the filtered x-ray diode signals must come from another mechanism, either energetic electrons or perhaps some impurity line that only begins to radiate during reconnection.

### 4.3 Counter-Helicity Behavior as a Function of Neutral Gas Levels

The above comparison between co- and counter-helicity experiments was conducted with the gas valve power supply charged to 500 V, for which a relatively spectacular event occurs in counter-helicity plasmas sometime between 1.7 and 2.7  $\mu\text{s}$ . These spectacular events, however, can be diminished by increasing the charging voltage of the fast gas valve capacitor bank, which lets more neutral gas into the chamber before the shot. In general, counter-helicity plasmas formed with a higher charging voltage of the fast gas valve capacitor bank produce sharper fast camera images, emit less UV and x-ray radiation, expand and detach slower, and have smaller electrode voltage rises. These observations are consistent across counter-helicity plasmas made from hydrogen, nitrogen, and argon. Interestingly, though, while the overall EUV emission from a hydrogen plasma decreases as the charging voltage of the fast gas valve capacitor bank is changed from 500 V to 550 V, extremely large emission appears on the outer channels of the vacuum photodiode array; these bursts in UV are believed to originate from the central bright spots described in Ref. [20] and in Sec. 1.4.1.

Increasing the charging voltage of the fast gas valve capacitor bank creates a plasma of higher peak density. This is suggested in Table 2.1, which shows that the total amount of hydrogen puffed into the chamber rapidly rises with the charging voltage, but these measurements do not prove that the extra gas ends up as ionized plasma in the loops. However, electron density measurements confirm that the peak density of a counter-helicity hydrogen plasma formed with a 550 V charging voltage on the fast gas valve capacitor bank is indeed larger than that of a similar plasma formed with a 500 V charging voltage. The density is determined by measuring the Stark broadening of the  $\text{H}_\beta$  lines as described in Sec. 2.2.4. For these measurements, the spectrometer's channels were aligned horizontally so that the twelve spectrometer chords extend out along the midplane away from the electrodes, as shown in Fig. 4.12. The gate time of the spectrometer's CCD camera was set to a 1  $\mu\text{s}$  time window, and this time window was systematically shifted to locate the time of peak density for each gas voltage setting. For a 500 V charging voltage of the fast gas valve capacitor bank, the average peak density was  $n_e = (6.5 \pm 1.0) \cdot 10^{20} \text{ m}^{-3}$  obtained by gating from 2 to 3  $\mu\text{s}$ . For a 550 V charging voltage, the average peak density was  $n_e = (12.2 \pm 2.3) \cdot 10^{20} \text{ m}^{-3}$  obtained by gating from 3 to 4  $\mu\text{s}$ . Figure 4.12 plots the density profiles at these times. Note that the plasma does not become less dense after this time but rather drifts past the spectrometer field of view; more work should be done to investigate the densities at later times. The peak density values reported

here are obtained by first averaging over several shots and then averaging the three channels with the largest density values. The error bars in fig. 4.12 represent the shot-to-shot variations. The ratio of peak density is  $1.88 \pm 0.47$ . These measurements are rough and can be improved by refining the experimental techniques, but the preliminary results indicate that the plasma does indeed become denser when the charging voltage of the gas supply is increased.

For the remainder of this section, we shall use the following nomenclature. Plasmas formed with the fast gas valve capacitor bank charged to 500 V will be referred to as low-mass plasmas, plasmas formed with the fast gas valve capacitor bank charged to 550 V will be referred to as mid-mass plasmas, and plasmas formed with the fast gas valve capacitor bank charged to 600 V will be referred to as high-mass plasmas. Obviously, the words “low,” “mid,” and “high” are relative and perhaps subjective, but this naming scheme is more concise than specifying the value of the charging voltage on the fast gas valve capacitor bank for each plasma.

Fast camera images show that increasing the charging voltage of the fast gas valve capacitor bank produces sharper images, slows the expansion of the loops, and delays detachment from the electrodes. Fig. 4.13 shows a sequence of images for a mid-mass plasma (shot 7982); it is sharper than its low-mass counterpart shown in Fig. 4.7. We also note that both the lower and upper legs of the mid-mass plasma become bright, in contrast to the low-mass plasma. Fig. 4.14 superimposes both Fig. 4.7, colored green, and Fig. 4.13, colored blue. This superposition clearly demonstrates that the mid-mass plasma expands slower than its low-mass counterpart. This is not surprising, as the mid-mass plasma was shown by spectroscopic measurements to be denser and is thus accelerated less by the magnetic forces than the low-mass plasma. Since the mid-mass plasma expands more slowly, its footpoints detach from the electrodes at a later time than the low-mass plasma; in Fig. 4.14, the low-mass plasma appears detached at frame 7, or  $2.30 \mu\text{s}$ , but the mid-mass plasma does not detach until frame 10, or  $3.35 \mu\text{s}$ .

The two different charging voltages of the fast gas valve capacitor bank produce different levels of EUV emission as well. Fig. 4.15 overlays the vacuum photodiode signals for a low-mass plasma (shot 7755) with that of a mid-mass plasma (shot 7980). For the low-mass plasma, the strongest emission comes from the very top of the plasma with strong emission propagating down the inner channels, which are plotted in the lefthand column. The signals from the upper channels are not as intense in the mid-mass plasma, but channel 11 registers enormous radiation that seems isolated to the outermost channels.<sup>6</sup> Such large yet localized radiation is not seen on the outer channels for low-mass plasmas, and we hypothesize that this radiation is emanating from the bright central region. When the vacuum photodiode signals are summed over the entire array, the EUV emission from the low-mass plasma is comparable to or even larger than the mid-mass plasma for the first several

---

<sup>6</sup>The data presented in Fig. 4.15 shows an intense radiation burst only on channel 11 in the mid-mass plasma, but other shots with the same parameters show large emission from channel 10 as well.

microseconds. This is surprising, as plasma emission typically scales like the square of density, so denser plasma are expected to have higher radiation losses. The Caltech plasmas may be so dense that they have achieved the high-density limit of radiation losses observed in magnetic confinement devices [78].

Both the plasma current and voltage change appreciably in response to increasing the charging voltage of the fast gas valve capacitor bank. We focus first on the current. Increasing the charging voltage causes the plasma current to peak sooner and at a larger value as seen in Fig. 4.16, which plots the discharge currents for a low-mass, mid-mass, and high-mass plasma together (shots 8203, 8205, and 8208 respectively). The mean current, obtained by a boxcar averaging over  $0.8 \mu\text{s}$  to remove the spurious oscillations, reaches a peak value of 65 kA for the low-mass plasma but reaches 85 kA for the mid-mass plasma and 90 kA for the high-mass plasma. We observed in Sec. 4.2.1 that the low-mass plasma current undergoes a disruption and deviates from the expected sinusoidal behavior; Fig. 4.16 shows that this disruption is less apparent for the mid-mass and high-mass plasmas. The current data also contains spurious oscillations on the Rogowski coil that appear at breakdown and again in the middle of the shot. These spurious oscillations are less severe for the mid-mass plasma and are almost entirely absent for the high-mass plasma.

Imacon images show that low-mass plasmas expand faster and detach sooner from the electrodes, and we hypothesize that this abrupt detachment may be responsible for disrupting the flow of current and inducing the oscillations. A mid-mass plasma expands at a slower pace and perhaps detaches in a smoother fashion, resulting in less disruptions and a steadier current. Imacon images for high-mass plasmas show that the plasma remains attached to the electrodes for a very long time, and indeed, the current trace for a high-mass plasma is the smoothest of all, peaking at more than 90 kA and suffering the least disruption around  $2.7 \mu\text{s}$ .

Because the current traces obtained with a larger gas valve voltage return to zero at earlier times, one might attribute the change in current to the differences in plasma inductance due to the change in expansion rates. A rapidly expanding plasma quickly grows in size and has a larger inductance than a slowly expanding plasma. If we model the plasma and capacitor bank as an *LRC* circuit, then the current would have larger amplitude and shorter period with a smaller inductance. However, a close look at Fig. 4.16 shows that the mean values of the three currents are almost identical over the first microsecond even though the plasmas are expanding at different rates at this time. The difference in current appears to begin at a particular time, which seems more consistent with a change in magnetic topology that begins at the onset of reconnection rather than a difference in expansion rates, which is in action even at the beginning of the shot. Moreover, if the current finds a new path as the plasma detaches, then the size and inductance of the plasma loop will have little influence on the current profile after detachment. Really, to study this matter further, the path of the current should be determined before and after detachment. This may involve detailed

measurements using the magnetic probe or perhaps the development and installation of small and moveable Rogowski coils inside the chamber.

More insight can be obtained from the voltage traces. Three voltage traces for a low-mass, a mid-mass, and a high-mass plasma (shots 8203, 8205, and 8208 respectively) are plotted together in Fig. 4.17. The traces are synchronized such that breakdown for all three shots occurs at  $0.0 \mu\text{s}$ . The large signals prior to  $0.0 \mu\text{s}$  are simply the main bank applying the discharge voltage to the electrodes before current can flow. For the low-mass plasma, the neutral gas takes more than a microsecond to breakdown; for mid-mass and high-mass plasmas the breakdown time is progressively shorter. For non-hydrogen plasmas, the breakdown time can be even longer. After breakdown, all three voltage traces drop to about 2 kV. However, the low-mass plasma voltage starts to rise significantly to 4 kV until, at about  $2.7 \mu\text{s}$ , it plummets again. The voltage rise is presumed to be associated with the rapid expansion while the voltage plummet is associated detachment as the current finds an alternate, lower inductance path. We do not see this steady rise for mid-mass plasmas, but we do see a voltage spike at  $2.7 \mu\text{s}$ . For high-mass plasmas, the voltage is more or less flat with a minimal rise at  $2.7 \mu\text{s}$ . This trend of a flatter voltage trace with increased charging voltage of the fast gas valve capacitor bank is seen in both nitrogen and argon plasmas as well.

In summary, all of the disruptive features exhibited by counter-helicity plasmas that are absent in co-helicity plasmas can be mitigated by increasing the charging voltage of the fast gas valve capacitor bank, which admits more neutral gas into the chamber and produces denser plasmas. We hypothesize that these disruptive features are signatures of a change in magnetic topology and that this change is slowed down by increasing the plasma's density and hence inertia. Of course, this hypothesis needs to be verified by measurements of the magnetic field in the vicinity of the footpoints. Another intriguing possibility is that the plasma becomes "gas starved" for lower charging voltages. That is, the MHD pumping force described in Sec. 2.1.5 may exhaust the local density of plasma in the footpoints for lower charging voltages, leading to disruptive behavior. It may be possible to align the spectrometer in such a way as to measure the density in the gas inlet without simultaneously measuring the density of the plasma loop immediately outside the inlet. Such measurements would shed light on the nature of the plasma detachment.

## 4.4 Bias Field Configuration

In the course of these studies, an interesting observation has been made regarding the polarity of the bias magnetic field. This section documents this finding in the hopes that a future graduate student will someday explain this phenomena. As noted in Sec. 2.1.3, there are two field configurations that produce counter-helicity shots. In principle, these two configurations should produce plasmas that are mirror-images of each other. Experimentally, though, significant differences have been found

between the two field configurations. The RL configuration produces bright spots and enhanced x-ray emission as has been discussed. The LR configuration, however, does not form bright spots and does not emit strongly in x-ray during the first several microseconds of the experiment. In fact, at times when the RL configuration becomes bright at the legs, the LR configuration becomes quite dim. However, at much later times, around  $7.2 \mu\text{s}$  after breakdown, the LR configuration begins to arc brightly across the electrodes while a plume of plasma is seen to brighten, erupt, and detach. Fig. 4.18 shows an LR configuration formed with a 500 V charging voltage on the fast gas valve capacitor bank; this figure should be compared with Fig. 4.19, which has the same parameters and camera timings but a bias field configuration RL. It is not clear why reversing the magnetic field configuration should cause such a drastic change in plasma behavior, and this asymmetry should be investigated further. In particular, the delayed eruption of plasma may have implications for solar physics.

## 4.5 Conclusions and Directions for Future Work

This chapter presents two main conclusions regarding the vacuum photodiode signals. First, the signal amplitudes imply intense radiative losses from the plasma that appear consistent with the hypothesis that the plasma radiates away any heat deposited by Ohmic dissipation. Moreover, if this intensity is due to hydrogen line emission, then the plasma must be well out of equilibrium with an enhanced concentration of neutrals. Second, very intense emission is observed at the upper legs of a counter-helicity hydrogen plasma formed with a 500 V charging voltage on the fast gas valve capacitor bank. This burst coincides with localized brightness in camera images at the upper leg, interactions with a chamber bolt, oscillations on the current data, a peak and sharp drop in voltage, and occasional coincidences with x-ray bursts. This intense radiation burst is not observed for co-helicity plasmas and also seems to disappear as the gas voltage is increased. We believe it is related to the magnetic reconnection associated with counter-helicity merging.

The intense radiation from a non-equilibrium hydrogen plasma could be of use in divertor physics. There, radiation is a means by which the plasma temperature can be controlled so that the hot plasma from the core does not damage the divertor plates [83, 90, 81]. The Caltech Solar Loop Experiment suggests that cold plasma with an abnormally high neutral concentration can be magnetically pumped from the wall region into the divertor volume along arched field lines, inducing intense radiation and potentially quenching the local plasma temperature. The use of cold hydrogen plasma, rather than impurities, to induce radiative loss might be advantageous since the hydrogen will eventually ionize and cease radiation after a certain amount of time, whereas impurities will continue to radiate and might also “leak” into the plasma core. Intense hydrogen emission might also have the practical application of producing large amounts of EUV radiation for lithography.

We conclude with some comments concerning directions for future research.

- The most important avenue for future research is the determination of what, exactly, is generating the large vacuum photodiode signals for a hydrogen plasma. Section 4.1.4 discussed an experiment involving filtered vacuum photodiodes that will potentially answer this question. Because vacuum photodiodes are inexpensive and easy to construct, a filtered array could be constructed to greatly expand upon the spectral resolution of the EUV data. We note that a more direct, albeit involved and expensive, solution would be to install a vacuum ultraviolet spectrometer to directly observe the EUV lines most responsible for the radiative losses. The filtered vacuum photodiodes would certainly provide the preliminary knowledge needed to decide if a vacuum ultraviolet spectrometer is a worthwhile investment.
- If the source of the large vacuum photodiode signals is indeed hydrogen line emission, then our hydrogen plasmas must be well out of equilibrium. The Caltech Spheromak Experiment can produce similar plasmas with extended current pulses. Therefore, performing similar experiments on the Spheromak Experiment could provide useful tests of the hypothesis proposed here.
- The usefulness of the x-ray diodes is currently limited by their sensitivity to alignment. The signals are collimated in part due to powerful neodymium magnets that protect the diodes against charged particles, just like the vacuum photodiodes. The magnetic deflecting system should be redesigned to increase the field of view so that the x-ray diodes can view the entire plasma, eliminating the sensitivity to alignment.
- Another crucial matter is determining where the current is flowing in the plasma. As mentioned, magnetic data on the Spheromak Experiment suggests that current flows in a channel several times larger than the visible plasma seen in Imacon images. If the same holds true for the Solar Loop Experiment, then calculations performed with a plasma radius determined from Imacon images will be misleading. Furthermore, if the plasma has truly detached from the electrodes, then current should not be flowing through the loop but through some other path. Determining how and when this occurs during a shot will greatly help in the interpretation of diagnostic data.
- The noise burst observed in counter-helicity experiments should be investigated further, as it may be indicative of plasma waves being generated during magnetic reconnection. This can be investigated by building a radiometer to detect plasma radiation in the radio-frequency range, the frequency range of the observed noise. One might also use the magnetic probe or a capacitively coupled probe to detect waves within the plasma.

- These studies have clearly identified the neutral gas density profile as a major factor in the plasma evolution. However, this profile has not been studied in detail on the Solar Experiment. A fast ion gauge should be constructed to map out the density of the neutral gas cloud at the time of breakdown and how this density changes as a function of the charging voltage of the fast gas valve capacitor bank.
- The asymmetry in the bias magnetic field should certainly be investigated further. In particular, this might give insight into why counter-helicity plasmas in the RL configuration has intense emission in the upper half but not the lower half.
- The role of arcing and the bright light from the gas inlet should be investigated. As the x-ray diodes point directly at the electrodes, it is possible that particle bombardment of the electrodes is producing x-rays observed by the x-ray diodes.

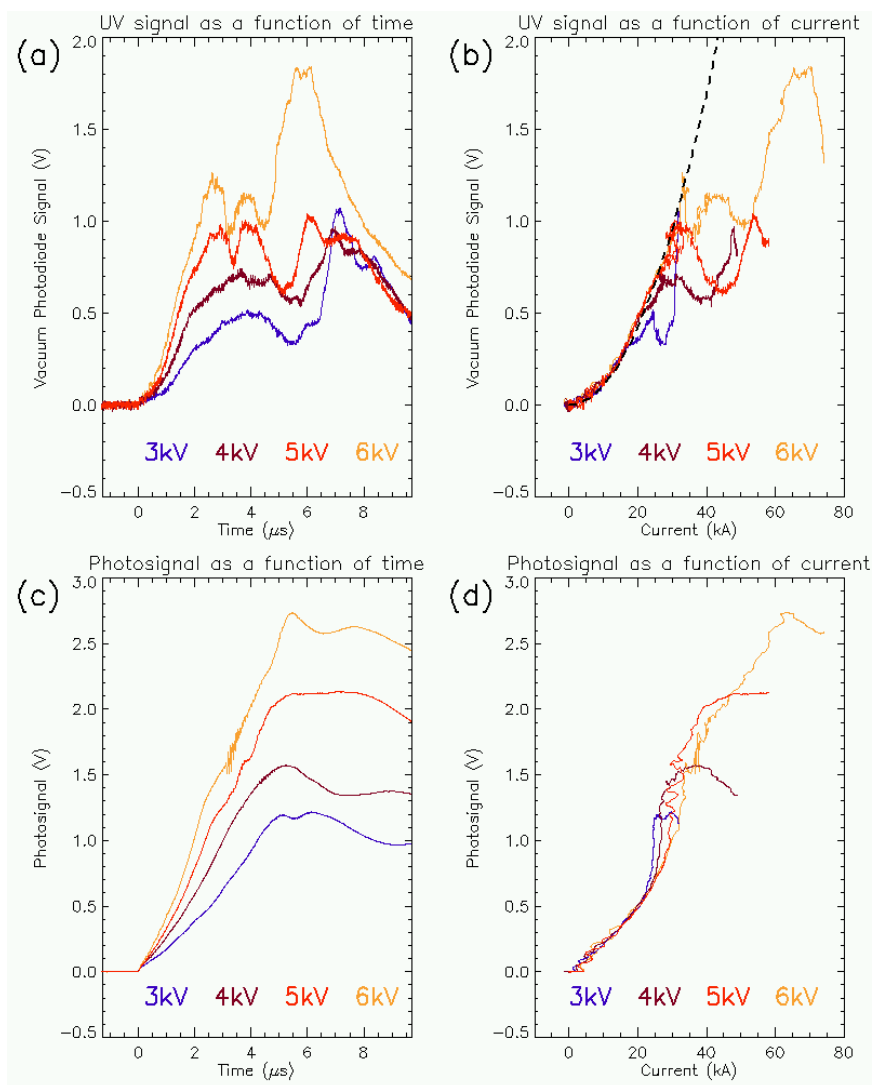


Figure 4.2: (a): Vacuum photodiode signals taken at various discharge voltages and plotted as a function of time. Larger discharge voltages produce faster rising vacuum photodiode signals. (b) The same data are now plotted as a function of current. The UV emission is seen to depend on the instantaneous value of the current. The thick dashed line is a quadratic fit, which yields a plasma resistance of  $5.3 \text{ m}\Omega$ . (c) and (d) are analogous plots made for optical photodiode data; the same trends can be observed. The shots used for these plots were 8957 - 8960, which were single-loop hydrogen shots with the fast gas valve capacitor bank charged to 550 V.

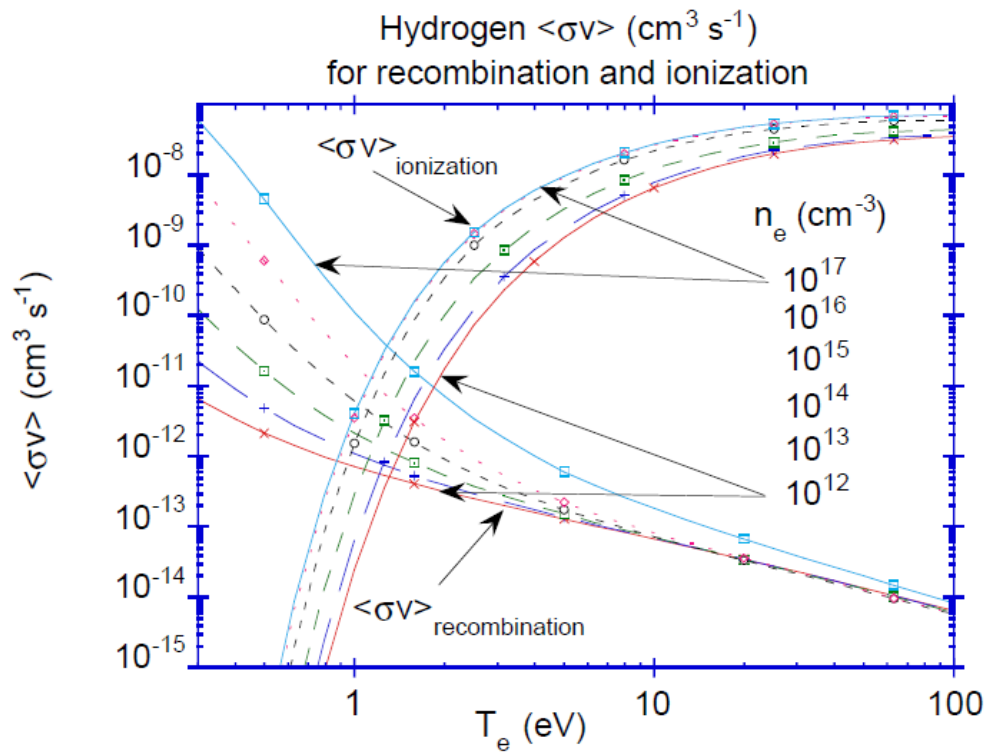


Figure 4.3: The effective ionization and recombination rates for hydrogen at different densities and temperatures, reproduced from Ref. [83]. The ratio of these two rates determines the equilibrium ionization balance and hence neutral hydrogen concentration.

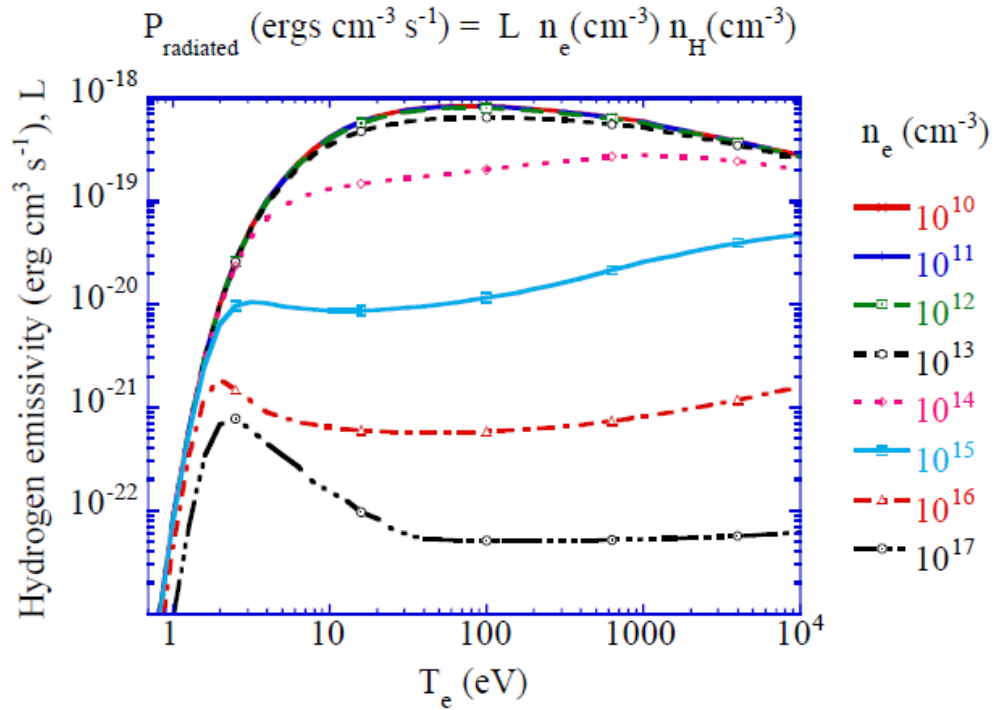


Figure 4.4: The radiation emissivity for hydrogen at different temperatures and densities, reproduced from Ref. [83]. This coefficient, when multiplied by the electron density, neutral density, and plasma volume, gives the radiation power.

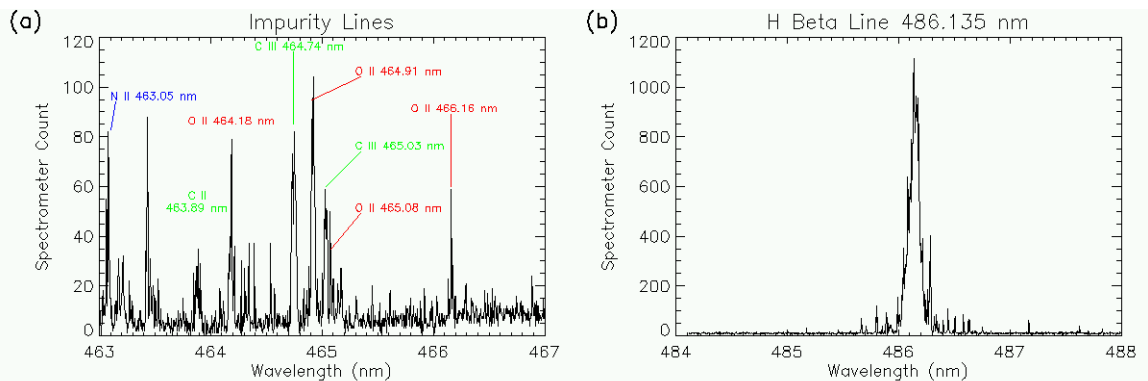


Figure 4.5: (a) A number of impurity lines have been observed in hydrogen plasmas. (b) The  $H_{\beta}$  line is noticeably stronger than the impurity lines.

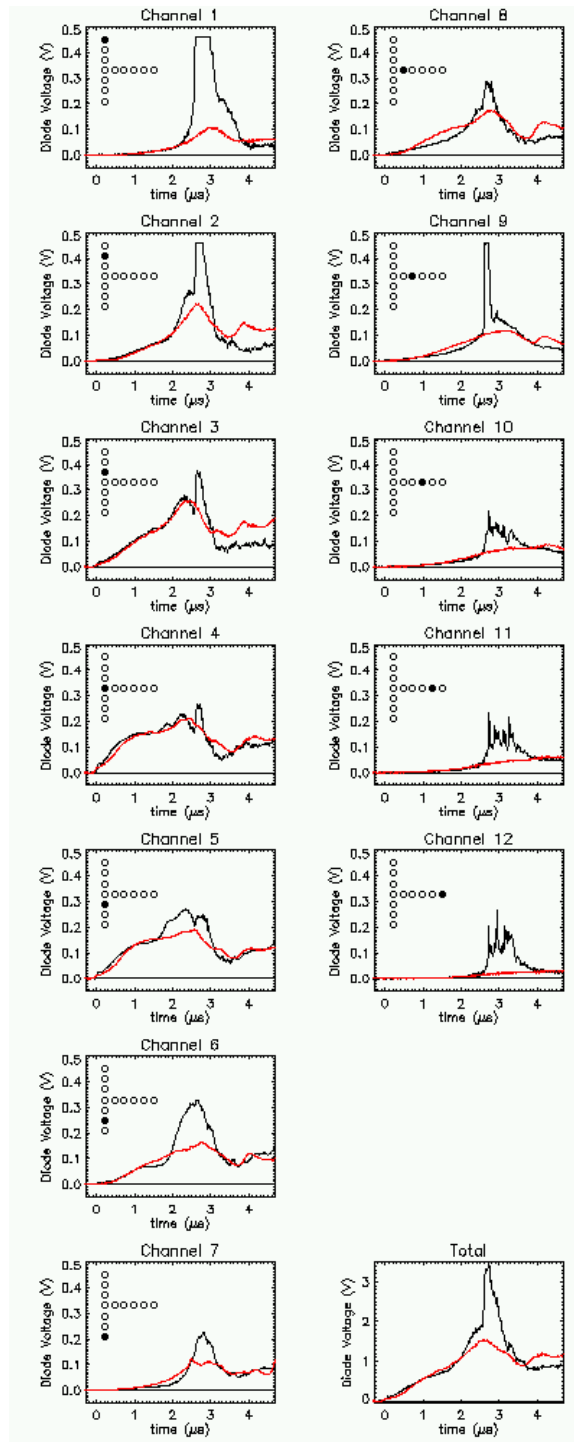


Figure 4.6: An overlay of UV data from both a co-helicity plasma (shot 7778), plotted in red, and a counter-helicity plasma (shot 7755), plotted in black, with the gas valve voltage set at 500 V. The counter-helicity plasma shows strong UV bursts, especially in the upper channels, that are absent in the co-helicity case.

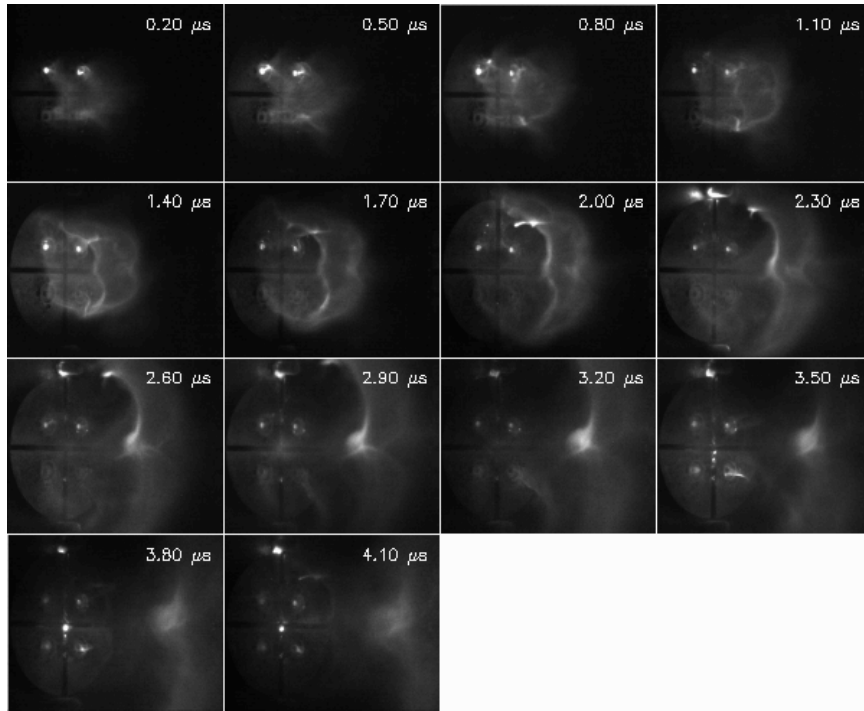


Figure 4.7: Imacon image of a counter-helicity plasma formed with a 500 V charging voltage on the fast gas valve capacitor bank (shot 7754). The plasma becomes very bright in the upper legs around the time the large UV bursts occurs. Arcing to the upper bolt is also apparent.

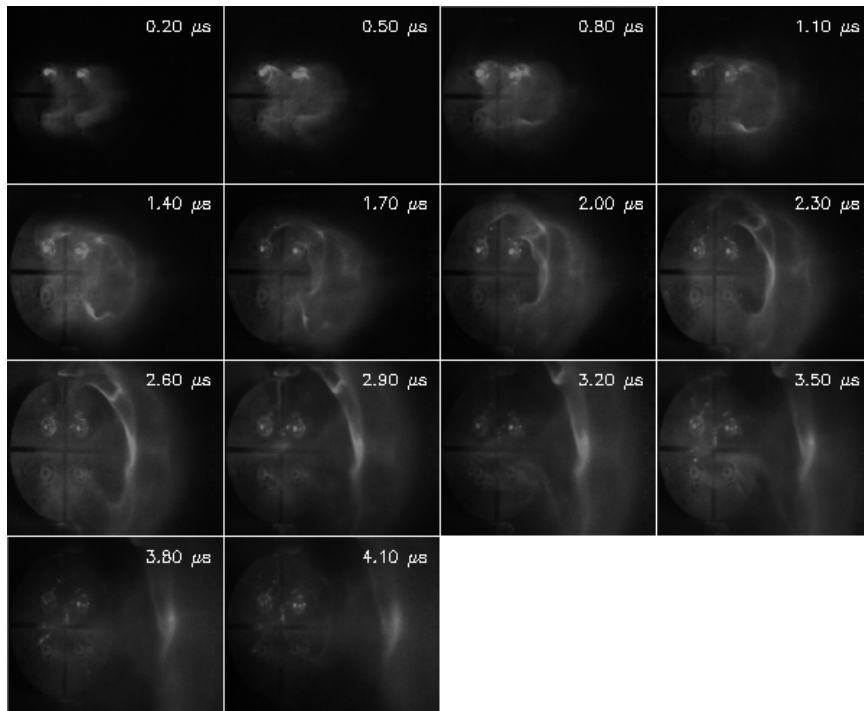


Figure 4.8: Imacon image of a co-helicity plasma with a 500 V charging voltage on the fast gas valve capacitor bank (shot 7774). The upper legs do not become as bright as in the counter-helicity case shown in Fig. 4.7, and arcing to the upper bolt is not observed.

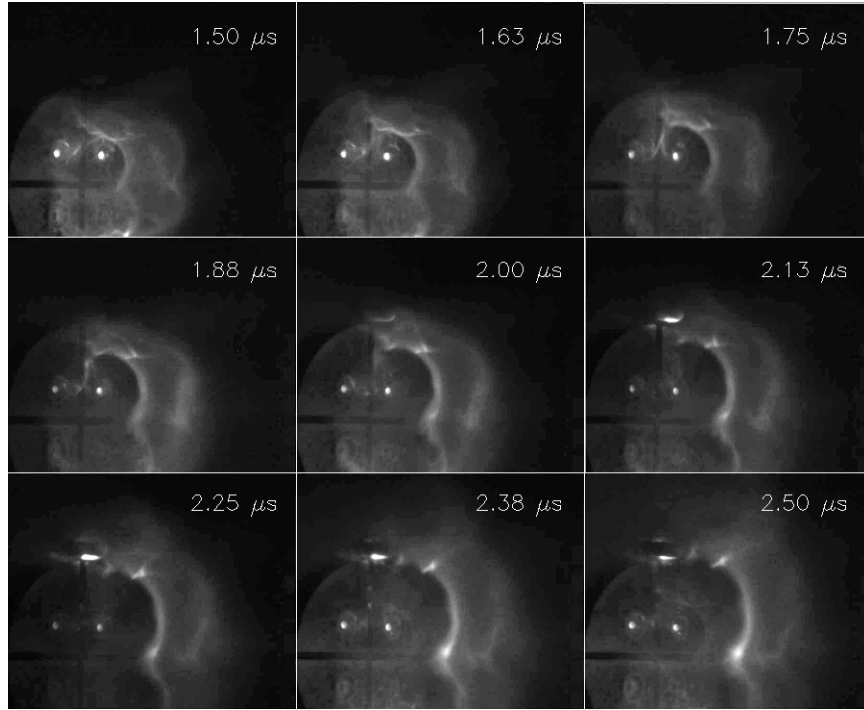


Figure 4.9: Imacon image of a counter-helicity plasma with a 500 V charging voltage on the fast gas valve capacitor bank (shot 7382). The Imacon timings have been adjusted to focus on the merging and detachment.

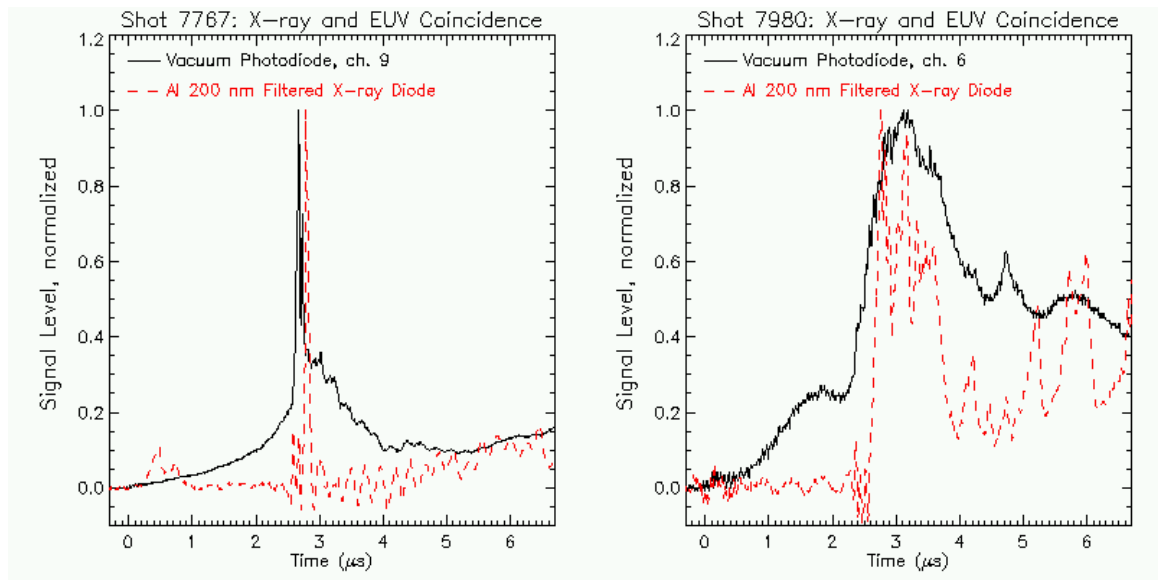


Figure 4.10: At the time of the large UV bursts, an x-ray burst occasionally registers on the x-ray diodes. The UV burst occurs very consistently, but the x-ray burst does not, possibly due to the x-ray diode alignment. Both x-ray bursts shown here were obtained through the 200 nm thick Al foil filter, which does not transmit hydrogen lines, so the x-ray diode signals, and perhaps part of the vacuum photodiode signal, must be produced by another mechanism such as energetic electrons as discussed in Sec. 4.2.2.

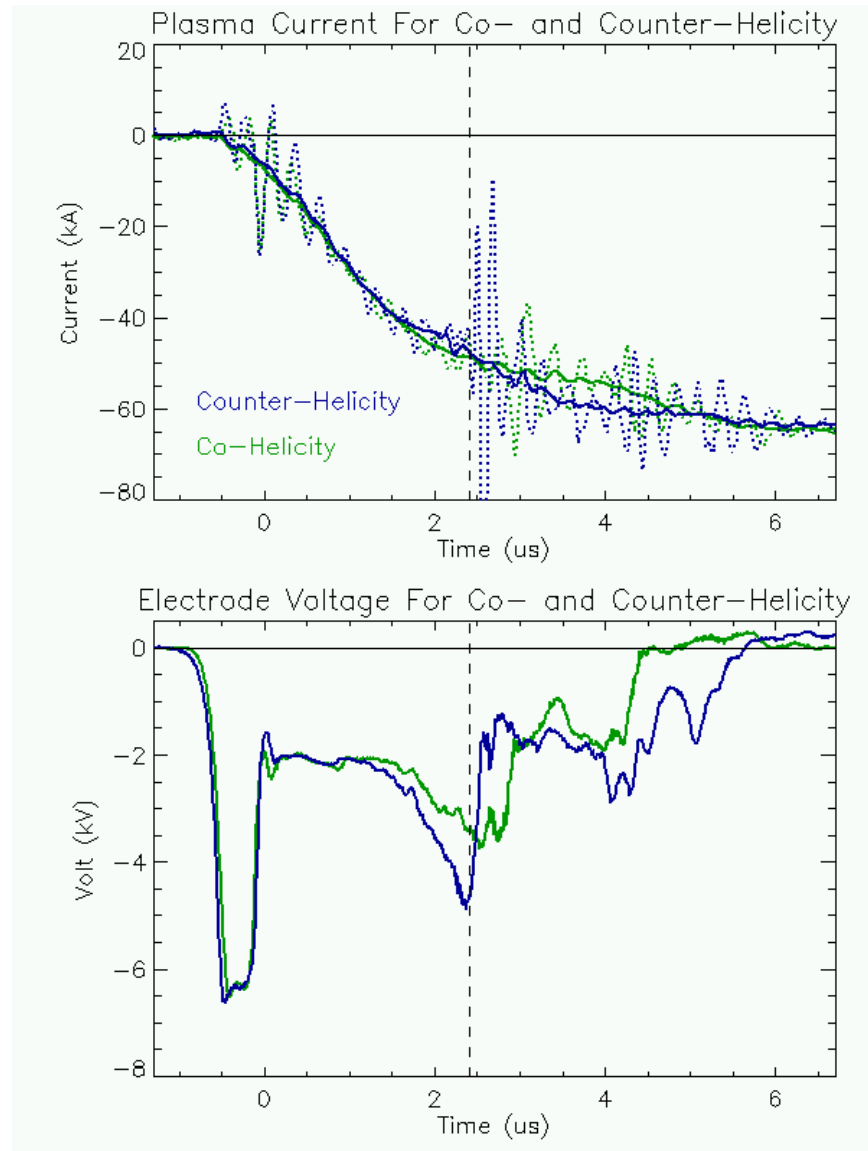


Figure 4.11: An overlay of the (TOP) plasma current and (BOTTOM) electrode voltage for a co-helicity plasma (shot 9163), plotted in green, and a counter-helicity plasma (shot 9024), plotted in blue. The electrode voltage rises in the middle of the shot for both cases, but the counter-helicity voltage drops rapidly at  $2.4 \mu\text{s}$ , depicted with the dashed line, at which time large oscillations appear on the current trace. This time is also coincident with the onset of the UV bursts observed for counter-helicity plasmas.

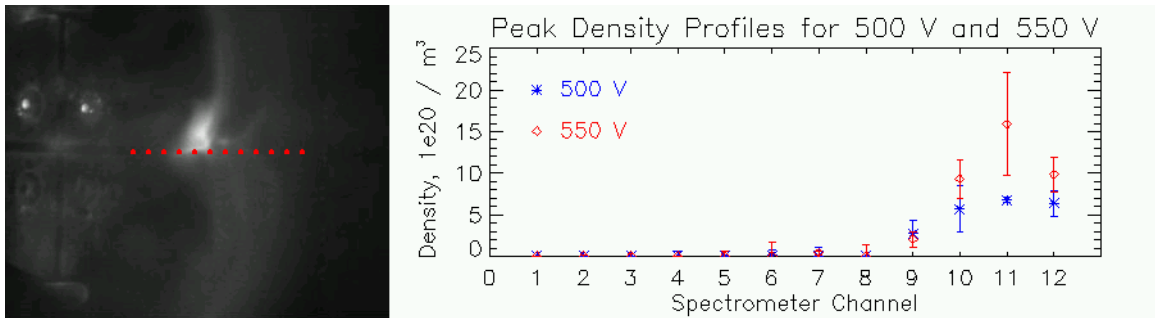


Figure 4.12: (a) The approximate positioning of the spectrometer chords during density measurements. The spacing between chords is about 1.9 cm, but the exact positions were not precisely determined. (b) A plot of the density profiles with error bars shows that a charging voltage of 550 V on the fast gas valve capacitor bank produces a noticeably larger density. The time window for the plasma produced with a 500 V charging voltage case is 2 to 3  $\mu\text{s}$  but is 3 to 4  $\mu\text{s}$  with a 550 V charging voltage.

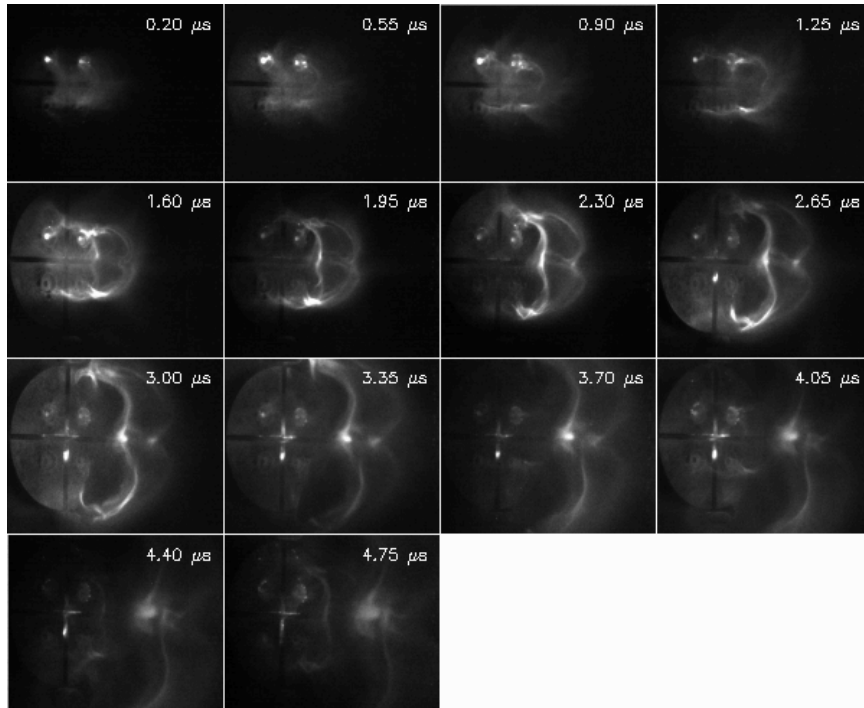


Figure 4.13: Imacon image of a mid-mass plasma; the image is noticeably sharper than its low-mass counterpart shown in Fig. 4.7. The lower legs become just as bright as the upper legs in the mid-mass case. There is significant ghosting in the image, particularly in the last frame.

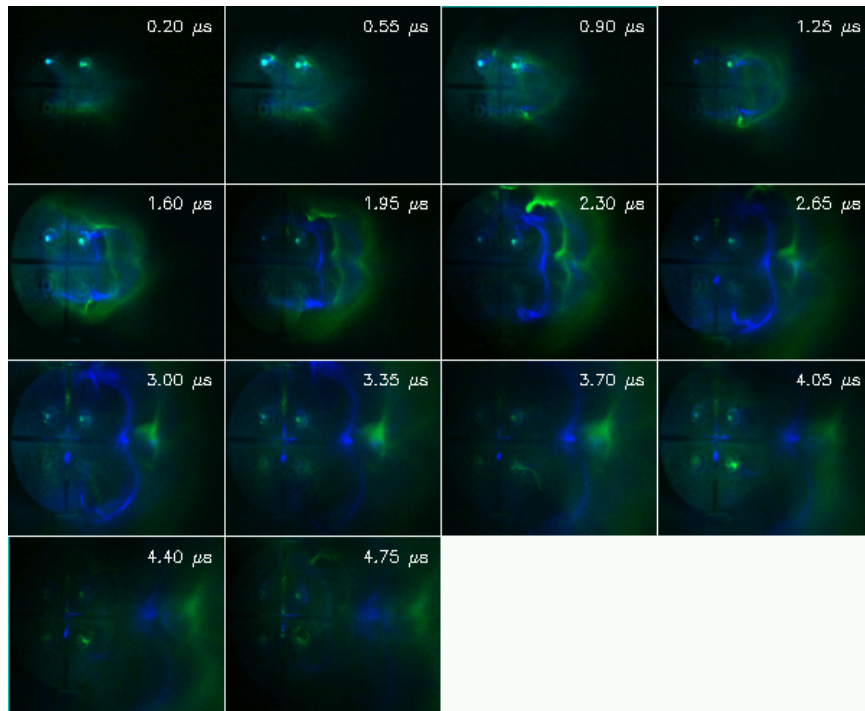


Figure 4.14: This picture is an overlay of Fig. 4.7, a low-mass plasma, and Fig. 4.13, amid-mass plasma, with false coloring to distinguish them. The green color corresponds to the low-mass plasma while blue corresponds to the mid-mass plasma. The Imacon camera had the same timing sequence, and the times of each frame, measured after breakdown, are printed in the upper right corners. Clearly, the low-mass plasma expands faster.

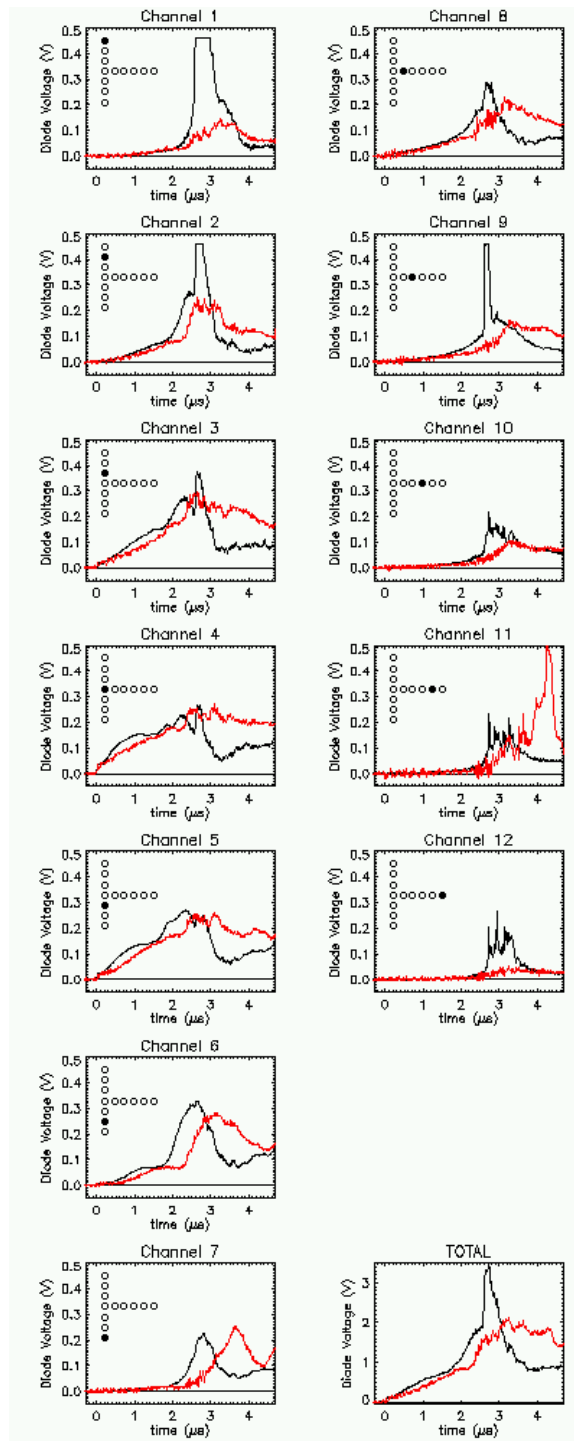


Figure 4.15: Overlays of counter-helicity UV emission for a low-mass plasma (shot 7755, plotted in black) and mid-mass plasma (shot 7980, plotted in red). For the mid-mass plasma, the large burst of UV in the upper channels disappears, but unusually large emission appears on channel 11.

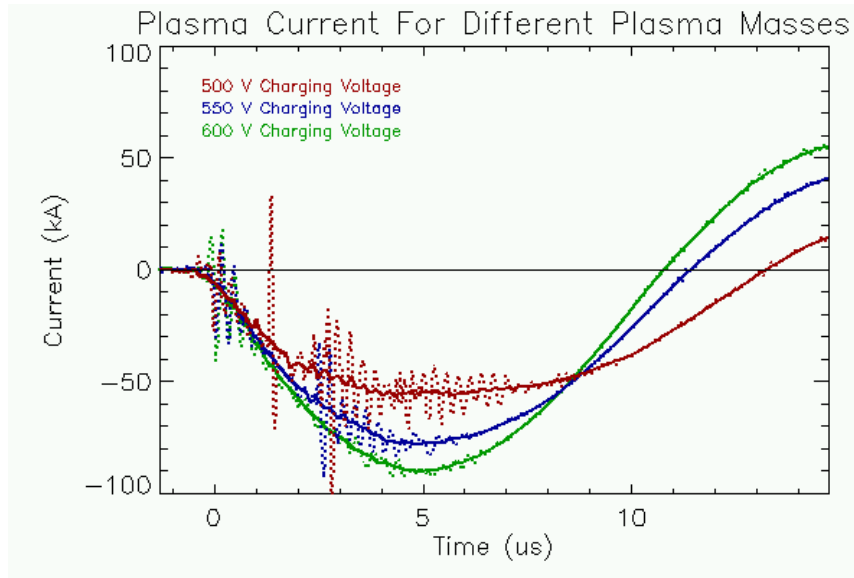


Figure 4.16: As the charging voltage of the fast gas valve capacitor bank is increased, several changes appear in the current trace. The peak current rises while the zero-crossing time decreases. The major disruption around  $2.7 \mu\text{s}$  becomes less severe as well. The shots shown are 8203, 8205, and 8208.

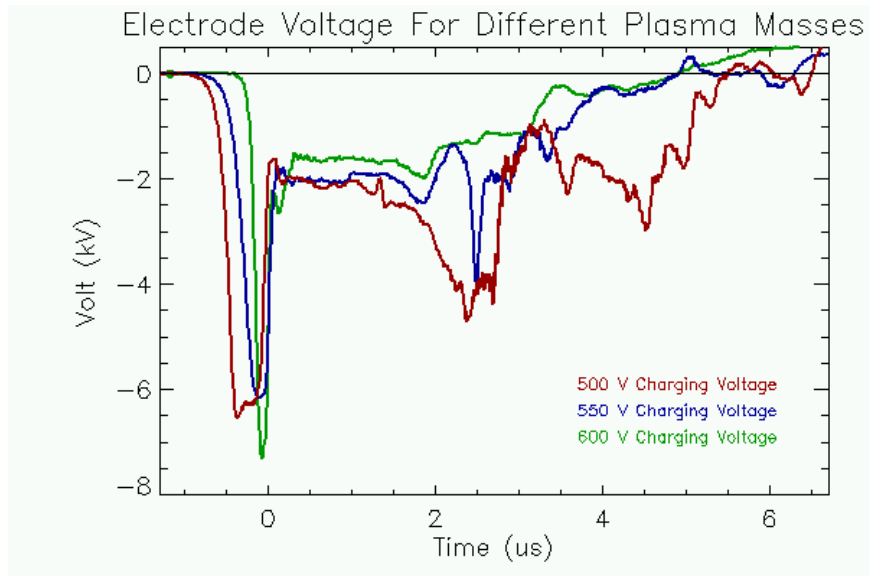


Figure 4.17: The electrode voltage also changes appreciably as the charging voltage of the fast gas valve capacitor bank is increased. The shots shown are 8203, 8205, and 8208 respectively

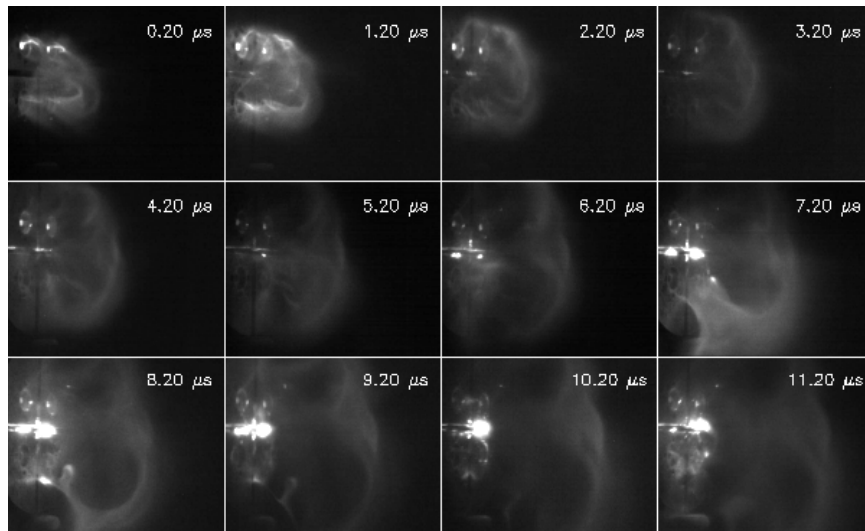


Figure 4.18: A plasma formed with the LR bias field configuration, as shown here, is still a counter-helicity configuration, but its behavior is quite different than its RL counterpart, which has been discussed in detail in this chapter and is shown in Fig. 4.19 for comparison.

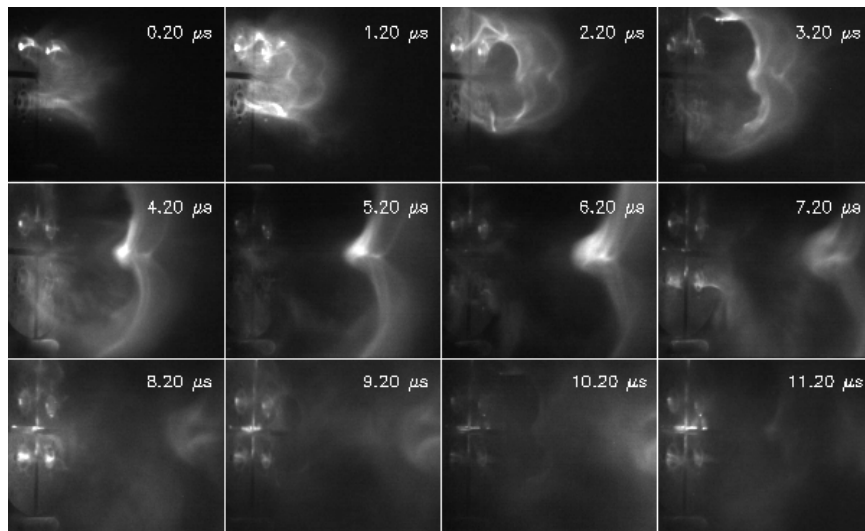


Figure 4.19: An RL plasma, as has been described in this chapter. The camera timing have been chosen to coincide with those of Fig. 4.18, which shows an LR plasma at the same settings. The LR plasma erupts at late times when the RL plasma, pictured here, has detached and is decaying.

## Chapter 5

# Hamiltonian Mechanics and Single Particle Motion

Chapter 4 discusses the process of two parallel plasma loops merging together. Considering this process from the perspective of individual particle orbits, the particles must transition from being localized to one loop to orbiting symmetrically among the two loops. An analogous transition happens on the Spheromak Experiment as the individual spider legs merge into an axisymmetric plasma jet. To study the orbits and transitions, we have employed the Hamiltonian formalism and report here a general theorem of Hamiltonian mechanics that evolved out of studies of charged particle motion. The theorem states that the action integral of the fastest periodic coordinate serves as an effective Hamiltonian for the reduced or orbit-averaged system. Stated alternatively, the action integral encodes the average evolution of the system such that the average evolution of the remaining non-periodic coordinates can all be extracted from this single quantity. Being rooted in Hamiltonian mechanics, the theorem is quite general and, in essence, extends concepts from guiding center theory to a broad class of Hamiltonian systems. Moreover, the theorem provides a unified framework for obtaining the averaged evolution without having to average the individual equations of motion, which can lead to a substantial reduction in the number of computations.

This chapter is organized in the following fashion. Sec. 5.1 will state and prove the theorem formally in two stages. First, we prove the theorem in a restricted setting in which coordinates other than the periodic one are ignorable. Examples such Kepler orbits and the relativistic  $\mathbf{E} \times \mathbf{B}$  drift are provided; in the latter example, we demonstrate the relativistic coupling between orthogonal Cartesian directions and an unexpected non-uniform motion *parallel* to the magnetic field. Sec. 5.1.8 then generalizes the theorem to the adiabatic case, where the action integral is then identified as a Hamiltonian for the reduced system. The exposition of Sec. 5.1 parallels that of Ref. [91] but includes more details and examples. Sec. 5.2 explicitly shows the connection between the general theory and guiding center motion, rederiving the drift equations using the first adiabatic invariant  $\mu$  as an effective Hamiltonian. These drifts include the grad-B drift, the magnetic mirror force, and the

$\mathbf{E} \times \mathbf{B}$  drift; finite Larmor radius effects are also computed for the latter. Sec. 5.2.5 then shows how the magnetic flux enclosed by a gyro-orbit can be computed from the action integral, and Sec. 5.2.6 presents a formula that ties together different calculations presented throughout the chapter. The application of the theorem to the merging of plasma loops is tackled in Chapter 6.

A comprehensive exposition of mechanics can, of course, be found in the classic texts [34, 92]. For charged particle motion through magnetic fields, Northrop provides a detailed exposition [35], but more intuitive texts are available [93, 2]. Finally, more mathematical treatments of Hamiltonian dynamics rooted in differential geometry are available [94, 95].

## 5.1 A Theorem on the Action Integral of Periodic Motion

The theory presented here hinges on the action integral of periodic motion, defined for a periodic coordinate  $Q$  as

$$J = \oint P_Q dQ, \quad (5.1)$$

where  $P_Q$  is the canonical momentum associated with  $Q$ , and the symbol  $\oint$  refers to integration over one full period [92, 94, 34]. Action integrals are adiabatic invariants [34, pg. 154] [94, pg. 297] and play an important role in perturbation theory [94, ch. 10] [92, ch. 12]. A brief review of action integrals in the context of action-angle variables and canonical transformations is given in Appendix C, but canonical transformations will not be needed in this chapter.

The crux of this section is that the action integral of the fastest periodic coordinate in a system acts as an effective Hamiltonian for the reduced or orbit-averaged system. Sec. 5.1.1 explains the meaning of “reduced” or “orbit-averaged” by analogy to a wall clock. In Sec. 5.1.2, a preliminary version of the theorem is stated and proved. Several examples such as Kepler motion and relativistic  $\mathbf{E} \times \mathbf{B}$  drifts make the meaning of the theorem concrete and also demonstrate applications. Sec. 5.1.7 shows how the drifts of guiding center generalize to any Hamiltonian system with a periodic component. Sec. 5.1.8 then generalizes the preliminary theorem to the adiabatic case. This section concludes by applying the theorem to a mechanical system which exhibits the phenomenon of magnetic mirroring without any magnetic field.

### 5.1.1 A Clock Analogy

The context for this theorem will be Hamiltonian systems in which one coordinate undergoes periodic motion while the other coordinates are ignorable, but the essence of the theorem can be described by analogy to a wall clock. As the minute hand makes a full revolution and returns to its original position, say 12:00, the hour hand does not return to its original position but instead increments forward one hour or 30 degrees. One part of the system returns its starting point, but another part

does not. Let us now imagine a peculiar clock whose hour hand does not move at a constant pace; perhaps it moves faster in the beginning of the hour and slower down towards the end or perhaps even moves backwards at times. The only condition we place on the hour hand is that, when the minute hand returns to 12:00, the hour hand has moved its obligatory 30 degrees. Such an hour hand would not be very useful for estimating time in between hours even though it faithfully tells the correct time on the hour and in the long run moves at the correct *average* rate.

Analogously, many Hamiltonian systems have a periodic coordinate that acts like the minute hand and other coordinates that increment with every period. An example is shown in Fig. 5.1 where an electron undergoes planar motion in the magnetic field of a straight wire; the radial coordinate is periodic but the axial position increments with every gyration. Like the peculiar hour hand, the  $z$  position does not change at a steady pace but moves faster, slower, and even backwards depending on the phase of the motion. The crux of Sec. 5.1.2 is to compute the net displacements of the other coordinates by taking partial derivatives of the action integral of the periodic coordinate. Section 5.1.7 then devises an averaged system in which the evolution of these other coordinates is steady, uniform, and free of peculiar non-uniformities.

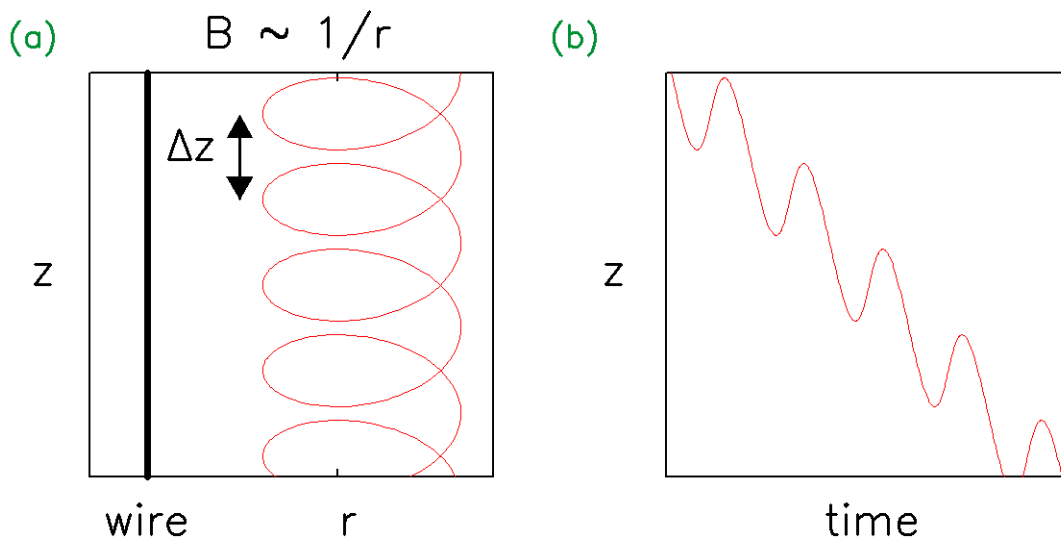


Figure 5.1: (a) An electron orbiting a current-carrying wire has periodic radial motion but displaces itself a net distance  $\Delta z$  with every gyration. (b) Plotting the axial position  $z$  as function of time shows the oscillatory motion superimposed over a net drift.

### 5.1.2 Net Displacements and Differentiating the Action Variable

We now state the theorem formally. Consider a two-dimensional time-independent Hamiltonian system where one coordinate, say  $\eta$ , is ignorable:

$$H = H(\xi, P_\xi, P_\eta). \quad (5.2)$$

Suppose that the  $\xi$  motion is periodic, that is,  $\xi(t + \Delta t) = \xi(t)$  for some time interval  $\Delta t$ . The evolution of  $P_\eta$  is trivial:

$$\dot{P}_\eta = \frac{\partial H}{\partial P_\eta} = 0, \quad (5.3)$$

but the evolution of  $\eta$  is in general non-trivial. For instance, in a central force problem, the canonical angular momentum  $P_\phi$  is constant, but  $\dot{\phi} = P_\phi/mr^2$  varies with  $r$ . Returning to the general setting, over the time interval  $\Delta t$ ,  $\eta$  undergoes a net displacement  $\Delta\eta$ :  $\eta(t + \Delta t) = \eta(t) + \Delta\eta$ . We claim that

$$\Delta\eta = -\frac{\partial J}{\partial P_\eta}, \quad (5.4)$$

where  $J$  is the action integral associated with  $\xi$ ,

$$J(H, P_\eta) = \oint P_\xi(H, \eta, P_\eta) d\xi. \quad (5.5)$$

In Eq. (5.5),  $P_\xi(H, \eta, P_\eta)$  is obtained by solving the Hamiltonian in Eq. (5.2) for  $P_\xi$ . Eq. (5.4) states that if  $J$  is known then the net change of  $\eta$  during one period of  $\xi$  can be calculated without integrating the potentially complicated form of  $\dot{\eta}$ .

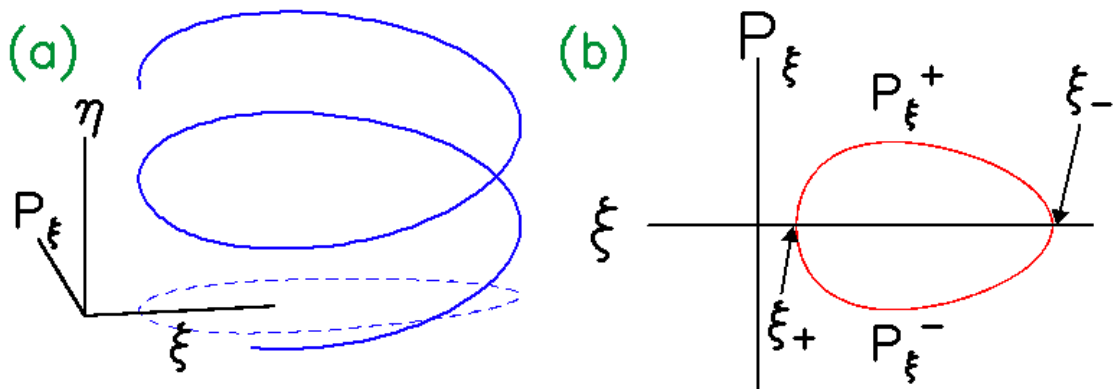


Figure 5.2: (a) The trajectory, in phase space, is helical because of the periodic motion in the  $\xi P_\xi$  plane and the net displacement, or drift, in the  $\eta$  motion. (b) Projecting the trajectory onto the  $\xi P_\xi$  plane produces a closed trajectory. The area of this curve is  $J$ . Also labeled are the turning points  $\xi_\pm$  and the two branches of  $P_\xi$  along a trajectory: the upper and lower branch denoted  $P_\xi^\pm$ .

The proof of Eq. (5.4) is surprisingly neat. First, we note that, in Eq. (5.4), there is no con-

tribution from differentiating the integral bounds because the  $\xi$  motion is periodic. To make this statement concrete, suppose that  $P_\xi$  is a double-valued function of  $\xi$  with value  $P_{\xi+}$  along the upper branch and  $P_{\xi-}$  along the lower branch as suggested in Fig. 5.2. Then

$$\oint P_\xi d\xi = \int_{\xi_1}^{\xi_2} P_{\xi+} d\xi + \int_{\xi_2}^{\xi_1} P_{\xi-} d\xi, \quad (5.6)$$

where  $\xi_1$  and  $\xi_2$  are the turning points of motion. By continuity,  $P_{\xi+}(\xi = \xi_1) = P_{\xi-}(\xi = \xi_1)$  and similarly at  $\xi = \xi_2$ . Differentiating Eq. (5.6), one must differentiate the integral bounds in addition to the integrand:

$$\frac{\partial J}{\partial P_\eta} = \left[ \int_{\xi_1}^{\xi_2} \frac{\partial P_{\xi+}}{\partial P_\eta} d\xi + \int_{\xi_2}^{\xi_1} \frac{\partial P_{\xi-}}{\partial P_\eta} d\xi \right] + \quad (5.7)$$

$$\frac{\partial \xi_1}{\partial P_\eta} [P_{\xi-}(\xi_1) - P_{\xi+}(\xi_1)] + \frac{\partial \xi_2}{\partial P_\eta} [P_{\xi+}(\xi_2) - P_{\xi-}(\xi_2)]. \quad (5.8)$$

However, the boundary terms then cancel by continuity of  $P_\xi$  at the turning points<sup>1</sup>. Hence,

$$\frac{\partial J}{\partial P_\eta} = \oint \frac{\partial P_\xi(H, \xi, P_\xi)}{\partial P_\eta} d\xi. \quad (5.9)$$

Second, the  $P_\xi$  that appears in Eq. (5.9) is obtained by solving the Hamiltonian  $H = H(\xi, P_\xi, P_\eta)$  for  $P_\xi$  along this particular trajectory. Furthermore, we can relate the  $\partial P_\xi / \partial P_\eta$  to partial derivatives of  $H$  as follows. The differential of  $H = H(\xi, P_\xi, P_\eta)$  is

$$dH = \frac{\partial H}{\partial \xi} d\xi + \frac{\partial H}{\partial P_\xi} dP_\xi + \frac{\partial H}{\partial P_\eta} dP_\eta. \quad (5.10)$$

In Eq. (5.9), we hold  $\xi$  and  $H$  fixed, so we set  $d\xi = dH = 0$  in Eq. (5.10) and obtain

$$\frac{\partial P_\xi}{\partial P_\eta} = - \frac{\partial H / \partial P_\eta}{\partial H / \partial P_\xi}. \quad (5.11)$$

Using Eq. (5.11) and Hamilton's equations in Eq. (5.9) gives

$$\frac{\partial J}{\partial P_\eta} = - \oint \frac{\partial H / \partial P_\eta}{\partial H / \partial P_\xi} d\xi = - \oint \frac{d\eta / dt}{d\xi / dt} d\xi = -\Delta\eta. \quad (5.12)$$

This result is exact and no assumption of slowness is needed. It applies whether  $\Delta\eta$  is small and the trajectory is nearly closed or whether  $\Delta\eta$  is large and the trajectory is decidedly not closed. If there are extra ignorable coordinates in the system, Eq. (5.4), suitably adjusted, applies to each of them.

Eq. (5.4) generalizes the theorem [92, pg. 461] [34, pg. 156] that the period of motion is given

<sup>1</sup>Differential geometry provides a more general framework for such proofs; see Ref. [94, pg. 197], for instance.

by a partial derivative of  $J$  with respect to  $H$ ,

$$\Delta t = \frac{\partial J}{\partial H}. \quad (5.13)$$

The resemblance between Eq. (5.4) and Eq. (5.13) is due to the fact that  $(t, -H)$  can be considered a pair of canonical coordinates in extended phase space [96, pg. 15], so Eq. (5.13) can be considered a special case of the theorem presented.

### 5.1.3 Example: The Trivial Case

Our first example will be the trivial case in Cartesian coordinates in which the two dimensions are completely uncoupled:

$$H = \frac{P_x^2}{2m} + \frac{P_y^2}{2m} + V(x). \quad (5.14)$$

There are no forces in the  $y$  direction, so  $y$  evolves linearly,  $\dot{y} = P_y/m$ , and we anticipate  $\Delta y = \dot{y}\Delta t = (P_y/m)\Delta t$ . This is indeed obtained, for

$$J(H, P_y) = \oint \sqrt{2mH - P_y^2 - V(x)} \, dx, \quad (5.15)$$

so

$$-\frac{\partial J}{\partial P_y} = \oint \frac{P_y}{\sqrt{2mH - P_y^2 - V(x)}} \, dx. \quad (5.16)$$

However,  $\Delta t = \partial J/\partial H$ , and

$$\frac{\partial J}{\partial H} = \oint \frac{m}{\sqrt{2mH - P_y^2 - V(x)}} \, dx. \quad (5.17)$$

Therefore,  $-\partial J/\partial P_y = (P_y/m)\Delta t$  as expected. This result is rather boring but illustrates that, for non-trivial examples to exist, there must be some coupling between the periodic and ignorable coordinate. In the following examples, we will see that this coupling can occur either through the expression for kinetic energy or through the introduction of a magnetic field.

### 5.1.4 Example: Kepler Motion

It is well-known that the bounded trajectories of Kepler orbits are ellipses. We therefore know, a priori, that  $\Delta\phi = \pm 2\pi$ , where  $\phi$  is the polar angle in the plane of motion and the radial coordinate  $r$  is taken as the periodic coordinate. Kepler motion thus provides a non-trivial check of Eq. (5.4) and provides an example where the periodic and ignorable coordinates are coupled via the expression for kinetic energy.

The Hamiltonian for Kepler motion is

$$H = \frac{P_r^2}{2m} + \frac{P_\phi^2}{2mr^2} - \frac{mMG}{r}, \quad (5.18)$$

where  $m$  is the mass of the object in orbit,  $M$  is the central mass, and  $G$  is the gravitational constant.  $P_\phi$  is the canonical angular momentum,  $P_\phi = m\dot{\phi}r^2$ , which is conserved along trajectories. The  $\phi$  coordinate is ignorable, but the evolution of  $\phi$  is coupled to the radial coordinate, since  $\dot{\phi} = P_\phi/mr^2$ . The action variable,

$$J = \oint \sqrt{2mH - P_\phi^2/r^2 + 2m\frac{mMG}{r}} dr, \quad (5.19)$$

can be efficiently evaluated by contour integration [92, pg. 468] [97, Appendix II] in the complex  $r$ -plane:

$$J = -2\pi |P_\phi| + 2\pi \frac{m^2MG}{\sqrt{2m|H|}}. \quad (5.20)$$

$\Delta\phi$  and  $\Delta t$  can now be found by applying Eq. (5.4) to Eq. (5.20),

$$\Delta\phi = -\frac{\partial J}{\partial P_\phi} = \pm 2\pi, \quad (5.21)$$

$$\Delta t = \frac{\partial J}{\partial H} = \pi \frac{m^2MG}{\sqrt{2m|H|^3}}. \quad (5.22)$$

The first equation tells us that  $\phi$  always changes by  $2\pi$  over a radial cycle no matter the energy or angular momentum; the  $\pm$  sign is determined by the sign of  $P_\phi$ , i.e., the direction of rotation. This neatly proves that all Kepler orbits are closed and degenerate.<sup>2</sup> The second equation is the well-known formula for the period of a Kepler orbit.

Kepler orbits demonstrate how the periodic and ignorable coordinates can couple through the expression for kinetic energy. In Cartesian coordinates, kinetic energy takes a simple form:

$$T = \frac{m}{2} (\dot{x}^2 + \dot{y}^2 + \dot{z}^2), \quad (5.23)$$

for which there is no coupling. In a more general coordinate system, however, the kinetic energy must be expressed in terms of a position-dependent metric:

$$T = \frac{1}{2} mg_{ij}(q) \dot{q}^i \dot{q}^j. \quad (5.24)$$

---

<sup>2</sup>Degeneracy, in the setting of classical mechanics, is when the frequencies of two coordinates are not independent of each other [92, pg. 465].

For instance, in the polar coordinate system used for Kepler orbits,

$$T = \frac{1}{2}m \begin{pmatrix} \dot{r} & \dot{\phi} \end{pmatrix} \begin{pmatrix} 1 & 0 \\ 0 & r^2 \end{pmatrix} \begin{pmatrix} \dot{r} \\ \dot{\phi} \end{pmatrix}. \quad (5.25)$$

If the Lagrangian is of the form  $L = T - U = (1/2)g_{ij}(q)\dot{q}^i\dot{q}^j - U(q)$ , then the canonical momenta are  $P_i = mg_{ij}(q)\dot{q}^j$ , and one can solve for the velocities  $\dot{q}^i$  as

$$\dot{q}^i = \frac{1}{m}g^{ij}(q)P_j, \quad (5.26)$$

where  $g^{ij}$  is the inverse matrix of the metric. It is the  $q$  dependence of  $g^{ij}$  that couples the periodic variable to the ignorable coordinate's velocity. In Kepler motion,  $\dot{\phi} = P_\phi/mr^2$ , so that the evolution of  $\phi$  is coupled to the motion in the radial direction.

### 5.1.5 Example: Vector Potentials and Charged Particles

The coordinates may couple through the vector potential term of the Lagrangian for a charged particle in a magnetic field:

$$L = \frac{m}{2}v^2 + q\mathbf{v} \cdot \mathbf{A}. \quad (5.27)$$

In Cartesian coordinates, the expression for the canonical momenta is  $P_i = mv_i + qA_i$ , so

$$v_i = \frac{P_i - qA_i(\mathbf{r})}{m}. \quad (5.28)$$

The vector potential depends on the periodic variable and can thus couple the periodic motion to the ignorable coordinate's velocity. Particle motion in magnetic fields is not the only instance of such terms in the Lagrangian that are proportional to velocity. For instance, the transformation to a non-inertial frame introduces similar terms [34, sec. 39], and the Coriolis force  $2m\mathbf{v} \times \boldsymbol{\Omega}$ , where  $\boldsymbol{\Omega}$  is the angular velocity of the non-inertial frame, has a form suggestive of the magnetic Lorentz force  $q\mathbf{v} \times \mathbf{B}$ .

### 5.1.6 Example: Relativistic Mechanics and Relativistic $\mathbf{E} \times \mathbf{B}$ Drift

As a final example, coupling can occur in relativistic expression for kinetic energy. For a velocity-independent potential, the relativistic Lagrangian [92, Ch. 7.9] is

$$L = -mc^2\sqrt{1 - \beta^2} - V(\mathbf{x}) = -\frac{mc^2}{\gamma} - V(\mathbf{x}), \quad (5.29)$$

where  $\beta = v/c$  and  $\gamma = (1 - \beta^2)^{-1/2}$ . The canonical momenta, in Cartesian coordinates, are

$$P_i = \frac{\partial L}{\partial v_i} = -mc^2 \frac{1}{2} \frac{-2v_i}{\sqrt{1 - v^2/c^2}} = \gamma mc^2 v_i. \quad (5.30)$$

Since  $\gamma$  depends on the magnitude of velocity, the relationship between  $v_i$  and  $P_i$  for any Cartesian direction also involves the velocities in the other directions. Suppose that  $z$  is ignorable, so  $P_z$  is conserved. The  $z$  velocity,

$$\dot{z} = \frac{P_z}{\gamma mc^2}, \quad (5.31)$$

is *not* necessarily constant because changes in  $v_x$  and  $v_y$  will change  $\gamma$  and hence  $v_z$ . Thus, the motion in different Cartesian directions can be coupled.

As an example of this coupling, we study the relativistic motion of a charged particle in crossed electric and magnetic fields. We find that the motion along the magnetic field is not constant but rather is modulated at the cyclotron frequency. Let  $\mathbf{E} = E\hat{x}$  and  $\mathbf{B} = B\hat{z}$  with  $E/B < c$ ; Fig. 5.3 shows the configuration of the fields and a sample trajectory. Recall that in the non-relativistic case [2, Sec. 3.5.1] [93, Sec. 2.2.2], the particle drifts in the  $-\hat{y}$  direction with a velocity  $v_{E \times B}$  independent of its charge or mass,

$$\mathbf{v}_{E \times B} = \frac{\mathbf{E} \times \mathbf{B}}{B^2} = -\frac{E}{B} \hat{y}. \quad (5.32)$$

Furthermore, the velocity in the  $z$  direction is uniform and independent of the motion in the  $xy$  plane. Relativistic effects, however, couple the motion in the  $z$  direction to the motion in the  $xy$  plane so that  $v_z$  modulates at the cyclotron frequency, as shown in Fig. 5.4. This modulation contains a net drift that is computable with the Hamiltonian formalism. The full Lagrangian is

$$L = -mc^2 \sqrt{1 - v^2/c^2} - q\phi + q\mathbf{v} \cdot \mathbf{A} \quad (5.33)$$

$$= -mc^2 \sqrt{1 - v^2/c^2} + qEx + qv_y Bx, \quad (5.34)$$

where  $\phi = -Ex$  and  $\mathbf{A} = Bx\hat{y}$  are the appropriate potentials for the fields. The relativistic canonical momenta are the same as Eq. (5.30) with the addition of the vector potential term:  $P_i = m\gamma v_i + qA_i$ .

The relativistic Hamiltonian can be found by performing the Legendre transform:

$$H = c\sqrt{(\mathbf{P} - q\mathbf{A})^2 + m^2c^2} + qV = c\sqrt{P_x^2 + P_z^2 + (P_y - qBx)^2 + m^2c^2} - qEx. \quad (5.35)$$

The  $x$  action,

$$J = \oint P_x dx = \oint \sqrt{\frac{(H + qEx)^2}{c^2} - (P_y - qBx)^2 - P_z^2 - m^2c^2} dx, \quad (5.36)$$

can be evaluated in closed form by expanding the quadratics and completing the square in  $x$ :

$$J = \oint \sqrt{\left(\frac{H^2}{c^2} - P_y^2 - P_z^2 - m^2 c^2\right) + 2q\left(\frac{EH}{c^2} + BP_y\right)x - q^2\left(B^2 - \frac{E^2}{c^2}\right)x^2} dx \quad (5.37)$$

$$= \oint \sqrt{c^2 - a^2(x-b)^2} dx, \quad (5.38)$$

where

$$a = q\sqrt{B^2 - E^2/c^2}, \quad (5.39)$$

$$b = \frac{1}{q} \frac{EH/c^2 + BP_y}{B^2 - E^2/c^2}, \quad (5.40)$$

$$c^2 = \frac{H^2}{c^2} - P_y^2 - P_z^2 - m^2 c^2 + \frac{(EH/c^2 + BP_y)^2}{B^2 - E^2/c^2}. \quad (5.41)$$

This integral represents the area of an ellipse of half-height  $c$  and half-width  $c/a$ . The area of the ellipse is  $\pi c^2/a$ , so the action is

$$J = \pi \left[ \frac{H^2/c^2 - P_y^2 - P_z^2 - m^2 c^2}{q\sqrt{B^2 - E^2/c^2}} + \frac{(EH/c^2 + BP_y)^2}{q(B^2 - E^2/c^2)^{3/2}} \right]. \quad (5.42)$$

From this somewhat gruesome expression, the quantities  $\Delta t$  and  $\Delta z$  follow by partial differentiation:

$$\Delta t = \frac{\partial J}{\partial H} \quad (5.43)$$

$$= \pi \frac{(B^2 - E^2/c^2)(2H/c^2) + 2(EH/c^2 + P_y B)E/c^2}{q(B^2 - E^2/c^2)^{3/2}} \quad (5.44)$$

$$= 2\pi \frac{P_y B E/c^2 + B^2 H/c^2}{q(B^2 - E^2/c^2)^{3/2}} \quad (5.45)$$

$$\Delta z = -\frac{\partial J}{\partial P_z} = \frac{2\pi}{q\sqrt{B^2 - E^2/c^2}} P_z. \quad (5.46)$$

Together, these two quantities give the parallel drift:

$$\frac{\Delta z}{\Delta t} = \frac{B^2 - E^2/c^2}{P_y B E/c^2 + B^2 H/c^2} P_z. \quad (5.47)$$

Eq. (5.47) simplifies by writing  $P_y$ ,  $P_z$ , and  $H$  in terms of initial conditions:

$$P_y = m\gamma_0 v_{y0} + qBx_0, \quad (5.48)$$

$$P_z = m\gamma_0 v_{z0}, \quad (5.49)$$

$$H = \gamma_0 m c^2 - qE x_0. \quad (5.50)$$

Substitution into Eq. (5.47) gives

$$\frac{\Delta z}{\Delta t} = \frac{B^2 - E^2/c^2}{(m\gamma_0 v_{y0} + qBx_0)BE/c^2 + B^2(\gamma_0 mc^2 - qEx_0)/c^2} P_z \quad (5.51)$$

$$= \frac{B^2 - E^2/c^2}{(m\gamma_0 v_{y0})BE/c^2 + B^2(\gamma_0 mc^2)/c^2} P_z \quad (5.52)$$

$$= \frac{B^2 - E^2/c^2}{v_{y0}BE/c^2 + B^2} v_{z0}, \quad (5.53)$$

a simplified form of Eq. (5.47). The  $x_0$  dependence has canceled out as expected. Also, taking the non-relativistic limit by letting  $c \rightarrow \infty$ , we recover the non-relativistic result  $\Delta z/\Delta t = v_{z0}$ .

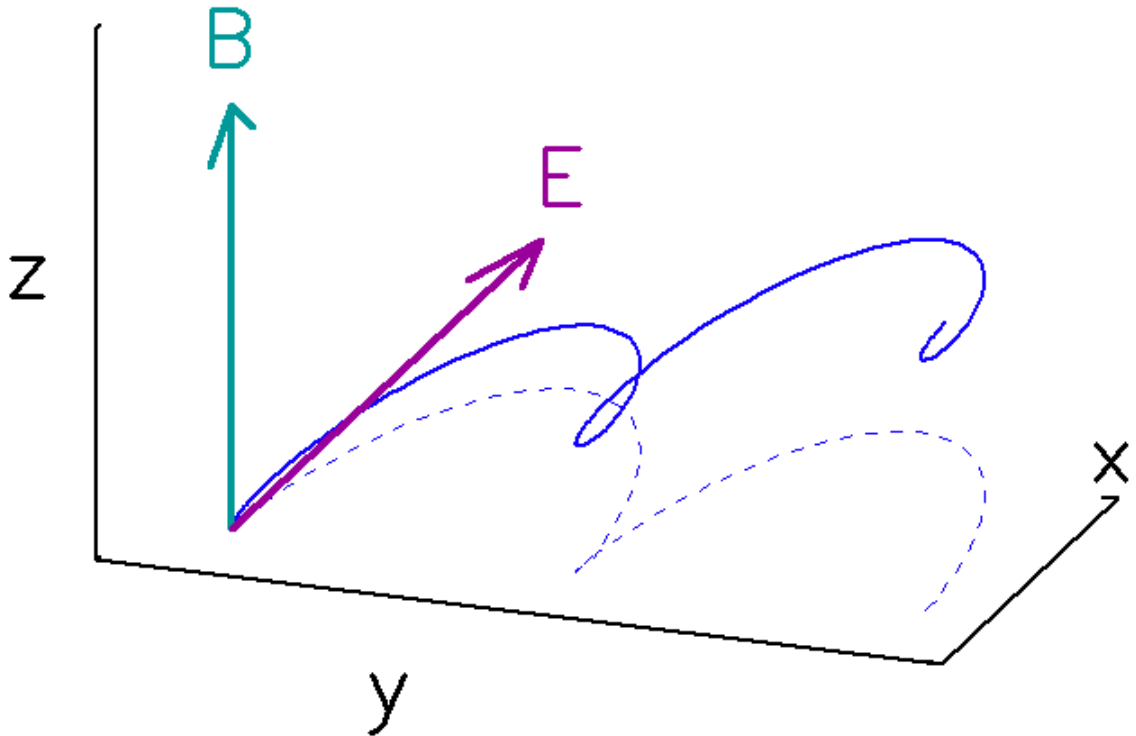


Figure 5.3: In a uniform electric and magnetic field, a charged particle will execute cycloid motion in the plane normal to  $\mathbf{B}$  and also move parallel to  $\mathbf{B}$ . Here, the solid blue line is the actual trajectory, and the dashed line is the projection of this trajectory, showing the cycloid motion. What is *not* apparent in this plot, though, is the fact that the velocity along  $\mathbf{B}$  is not uniform.

This unexpected modulation of the parallel velocity can be understood from Lorentz transformations. In the non-relativistic case, the  $\mathbf{E} \times \mathbf{B}$  drift velocity is the velocity of a frame in which the electric field is transformed to zero, leaving only a magnetic field. In this frame, kinetic energy is

thus conserved, and the charged particle undergoes simple Larmor motion. The cycloid trajectory observed in the lab frame is a superposition of the uniform  $\mathbf{E} \times \mathbf{B}$  drift and the circular Larmor motion. In the relativistic case, kinetic energy is likewise conserved in the  $\mathbf{E} \times \mathbf{B}$  drift frame with no modulation of  $\gamma$  and hence no modulation of  $v_z$ . However, the transformation back to the lab frame involves a non-linear transformation of time, resulting in the modulation of the parallel velocity.

To see this effect, we first note that a Lorentz boost with velocity  $v_d$  along the  $y$  direction transforms the electric and magnetic fields as [98, Eq. (12.108)]

$$E'_x = \gamma_d(E_x + v_d B_z), \quad (5.54)$$

$$B'_z = \gamma_d\left(B_z + \frac{v_d}{c^2} E_x\right), \quad (5.55)$$

where  $\gamma_d = (1 - (v_d/c)^2)^{-1/2}$ . Since  $E/B < c$ , we can choose  $v_d = -E/B$  so that the electric field vanishes in the boosted frame:  $E'_x = 0$ . The magnetic field becomes

$$B'_z = \gamma_d \left( B - \frac{E^2}{Bc^2} \right) = \frac{B - E^2/(Bc^2)}{\sqrt{1 - E^2/B^2c^2}} = \sqrt{B^2 - E^2/c^2}. \quad (5.56)$$

Without an electric field, the particle undergoes simple cyclotron motion, and the trajectory will look something like

$$\begin{pmatrix} ct' \\ x'(t') \\ y'(t') \\ z'(t') \end{pmatrix} = \begin{pmatrix} ct' \\ r_0 \cos \Omega t' \\ r_0 \sin \Omega t' \\ v'_{z0} t' \end{pmatrix}, \quad (5.57)$$

with  $\Omega = qB'_z/m\gamma_d$  the cyclotron frequency in the drift frame [92, Eq. (7.154)]. We transform this solution back to the lab frame with the inverse Lorentz boost:

$$\begin{pmatrix} ct \\ x \\ y \\ z \end{pmatrix} = \begin{pmatrix} \gamma_d & 0 & \gamma_d \beta_d & 0 \\ 0 & 1 & 0 & 0 \\ \gamma_d \beta_d & 0 & \gamma_d & 0 \\ 0 & 0 & 0 & 1 \end{pmatrix} \begin{pmatrix} ct' \\ r_0 \cos \Omega t' \\ r_0 \sin \Omega t' \\ v'_{z0} t' \end{pmatrix} \quad (5.58)$$

$$= \begin{pmatrix} \gamma_d(ct' + \beta_d r_0 \sin \Omega t') \\ r_0 \cos \Omega t' \\ \gamma_d(\beta_d t' + r_0 \sin \Omega t') \\ v'_{z0} t' \end{pmatrix} \quad (5.59)$$

The  $z$  velocity is not uniform because we have to express  $z$  as a function of  $t$  rather than  $t'$ , which

is achieved by inverting the zeroth component of the above transformation:

$$ct = \gamma_d (ct' + \beta_d r_0 \sin \Omega t'). \quad (5.60)$$

It is interesting to note that  $z$  evolves linearly with  $t'$  but not with  $t$ . We shall return to this curious fact in Sec. 5.1.7.

### 5.1.7 Drifts and Averaged Coordinates

The quantity  $\Delta\eta$  is the net change in  $\eta$  over the course of a  $\xi$  cycle. In general,  $\eta$  may have oscillated greatly over this cycle, but, whatever the particulars of its motion, it ends up changing by  $\Delta\eta$ . This allows us to define an averaged  $\eta$  velocity, or drift, as

$$\frac{\Delta\eta}{\Delta t} = -\frac{\partial J/\partial P_\eta}{\partial J/\partial H}. \quad (5.61)$$

This velocity is constant and equal to  $\lim_{t \rightarrow \infty} \eta(t)/t$ . It captures the net rate of change of  $\eta$  without the details of the  $\eta$  evolution. Equation (5.61) generalizes the particle drifts associated with guiding center theory.

The velocity in Eq. (5.61) can be derived from Hamilton's equations by writing  $H$  as a function of  $J$ . That is, the functional form  $J = J(H, P_\eta)$  can be inverted for  $H$  as a function of  $P_\eta$  and  $J$ :  $H = H(J, P_\eta)$ . Then, the differential of  $J = J(H, P_\eta)$ ,

$$dJ = \frac{\partial J}{\partial H} dH + \frac{\partial J}{\partial P_\eta} dP_\eta, \quad (5.62)$$

implies that, by setting  $dJ = 0$ ,

$$\frac{\partial H(J, P_\eta)}{\partial P_\eta} = -\frac{\partial J/\partial P_\eta}{\partial J/\partial H} = \frac{\Delta\eta}{\Delta t}. \quad (5.63)$$

Equation (5.63) has a form suggestive of Hamilton's equation: an  $\eta$  velocity was obtained by differentiation of the Hamiltonian with respect to  $P_\eta$ . However, the velocity obtained is the *average* one, where as Hamilton's equations applied to the original system  $H = H(\xi, P_\xi, P_\eta)$  gives the *instantaneous*  $\eta$  velocity:

$$\frac{\partial H(\xi, P_\xi, P_\eta)}{\partial P_\eta} = \dot{\eta} \neq \frac{\Delta\eta}{\Delta t} = \frac{\partial H(J, P_\eta)}{\partial P_\eta}. \quad (5.64)$$

Thus, when  $H$  is written as a function of  $J$  in place of  $\xi$  and  $P_\xi$ , the velocity furnished by Hamilton's equations is the average or drift velocity. This result is discussed in Appendix C where it is seen that a canonical transformation from  $(\xi, P_\xi)$  to action-angle coordinates simultaneously transforms  $\eta$  to its average version.

Let us recall the peculiar hour hand of Sec. 5.1.1 that has a non-uniform speed even though it moves the requisite 30 degrees every hour. This hour hand is analogous to the ignorable coordinate  $\eta$ , whose evolution is likewise not necessarily uniform. We have seen that writing  $H = H(J, P_\eta)$  instead of  $H = H(\xi, P_\xi, P_\eta)$  transforms the ignorable coordinate into its averaged form; continuing the analogy, this is like transforming the peculiar hour hand into a well-behaved version that moves at a uniform rate and is much more reliable for reading time, as suggested by Fig. 5.5. Similarly, the relativistic example in Sec. 5.1.6 shows that boosting to the drift frame causes the  $z$  coordinate to evolve linearly in drift frame time whereas its evolution in lab frame time is non-uniform. In general, replacing the periodic coordinates  $\xi$  and  $P_\xi$  with the constant of motion  $J$  eliminates the oscillatory components of  $\eta$ .

### 5.1.8 Adiabatic Evolution and Reduced Systems

Eq. (5.4) is proved under the assumption that  $\eta$  is ignorable. Here, we relax the requirement that  $\eta$  is ignorable and instead allow the oscillations to evolve adiabatically. By adiabatic, we mean that the orbits with  $\eta$  dependence resemble the orbits of the ignorable case but that the orbit parameters slowly change over the course of many periods. This relaxation of assumptions not only allows a broader class of systems to be studied but also yields a new result: the action integral  $J$  serves as an effective Hamiltonian for a reduced system in which all the remaining non-periodic coordinates are replaced by their averaged versions.

We proceed by adding  $\eta$  dependence to the Hamiltonian,  $H = H(\xi, P_\xi, \eta, P_\eta)$ , but regard  $(\eta, P_\eta)$  as slowly varying parameters of the  $\xi$  oscillation. This assumption allows the action integral  $J$  to be defined<sup>3</sup>, in which case it will be an adiabatic invariant [34, pg. 154] [94, pg. 297]. To make these statements precise, we separate  $H$  into two parts:

$$H(\xi, P_\xi, \eta, P_\eta) = H_{\text{loc}}(\xi, P_\xi, \eta, P_\eta) + H_{\text{ext}}(\eta, P_\eta). \quad (5.65)$$

$H_{\text{loc}}$  is a *local* Hamiltonian that describes the  $\xi$  oscillations; because  $H_{\text{loc}}$  contains all the  $\xi$  and  $P_\xi$  dependence, the  $\xi$  and  $P_\xi$  evolution depend only on  $H_{\text{loc}}$

$$\frac{d\xi}{dt} = \frac{\partial H_{\text{loc}}}{\partial P_\xi} \quad \frac{dP_\xi}{dt} = -\frac{\partial H_{\text{loc}}}{\partial \xi}. \quad (5.66)$$

We presume that  $\eta$  and  $P_\eta$  play the role of slowly varying parameters in  $H_{\text{loc}}$ ; that is, over the course of a single  $\xi$  period,  $\eta$  and  $P_\eta$  can be held fixed to good approximation. The evolution of

<sup>3</sup>Arbitrary  $\eta$  dependence could result in large variations over a single  $\xi$  period to the point where  $\xi$  is no longer periodic. In such cases, the action integral, or any first integral of motion, will not exist, and such systems are termed non-integrable. The transition from an integrable system to a non-integrable system through introduction of a perturbation, such as the  $\eta$  dependence described here, is the topic of KAM theory [94, Appendix 8] [96, Sec. 1.4].

these “parametric coordinates” is determined by both the local and the *external* Hamiltonian  $H_{\text{ext}}$ :

$$\frac{d\eta}{dt} = \frac{\partial H}{\partial P_\eta} \quad \frac{dP_\eta}{dt} = -\frac{\partial H}{\partial \eta} \quad (5.67)$$

In essence, then,  $H_{\text{ext}}$  describes the way in which the  $\xi$  oscillations interact with the outside world by influencing the evolution of the oscillation parameters. This scheme, by construction, ensures the existence and adiabatic invariance of  $J$ , defined as in Eq. (6.20) but now with  $\eta$  dependence, as follows. Traditionally, the adiabatic invariance of the action integral is demonstrated by adding a time-dependent parameter, say  $\lambda(t)$ , to a Hamiltonian system,  $H = H(\xi, P_\xi; \lambda(t))$  [34, pg. 154]. Here, we treat  $\eta$  and  $P_\eta$  as the slowly varying parameters of the  $\xi$  oscillation and thereby effectively reduce the present system  $H = H(\xi, P_\xi, \eta, P_\eta)$  to the traditional case  $H = H(\xi, P_\xi; \lambda(t))$ . As in Ref. [34, pg. 154], we assume it is a good approximation to hold the parametric coordinates  $\eta$  and  $P_\eta$  fixed while evaluating the  $\xi$  action integral. However, an important distinction of our treatment is that Eq. (5.65) is time-independent and thus conservative, whereas the Hamiltonian  $H = H(\xi, P_\xi; \lambda(t))$  is time-dependent and hence not conservative. Of course, the local and external systems exchange energy but the total energy,  $E = E_{\text{loc}}(t) + E_{\text{ext}}(t)$ , is conserved.

The added  $\eta$  dependence in  $J$  allows the derivation of  $\Delta P_\eta$ , the net change in the previously conserved canonical momentum, in addition to  $\Delta\eta$ . Indeed,

$$\frac{\partial J}{\partial \eta} = \oint \frac{\partial P_\xi}{\partial \eta} d\xi = - \oint \frac{\partial H / \partial \eta}{\partial H / \partial J} d\xi = - \oint -\frac{\dot{P}_\eta}{\dot{\xi}} d\xi = \Delta P_\eta \quad (5.68)$$

Equation (5.68) together with Eq. (5.4) yields the following system of equations:

$$\frac{\partial J}{\partial \eta} = \Delta P_\eta, \quad \frac{\partial J}{\partial P_\eta} = -\Delta\eta. \quad (5.69)$$

Equations (5.69) have the makings of a Hamiltonian system with  $-J$  serving as the Hamiltonian. They are *precisely* Hamiltonian as follows. We define discretized derivatives  $d\eta/dt = \Delta\eta/\Delta t$  and  $dP_\eta/dt = \Delta P_\eta/\Delta t$  that capture the net rates of change of  $\eta$  and  $P_\eta$ . Upon invocation of a rescaled time  $\tau$  normalized by the  $\xi$  period:

$$d\tau = \frac{dt}{\Delta t}, \quad (5.70)$$

Eqs. (5.69) become

$$\frac{d\eta}{d\tau} = \frac{\partial}{\partial P_\eta} (-J), \quad (5.71)$$

$$\frac{dP_\eta}{d\tau} = -\frac{\partial}{\partial \eta} (-J). \quad (5.72)$$

This system of equations is Hamiltonian with  $-J$  playing the role of the Hamiltonian and  $\tau$  playing

the role of time. We note that  $\tau$  is the angle variable conjugate to  $J$ ; it evolves linearly in time and increments by one for every cycle.

We show that  $\Delta\eta$  and  $\Delta P_\eta$  can both be split into two terms, local and external. This observation is not needed for the proof that  $J$  is a Hamiltonian for the reduced system but does offer some insight. We evaluate  $J = \oint P_\xi d\xi$  by first solving for  $P_\xi$  in the Eq. (5.65); this means inverting the equation  $H_{\text{loc}}(\xi, P_\xi, \eta, P_\eta) = H - H_{\text{ext}}(\eta, P_\eta)$ . In this equation,  $H$  and  $H_{\text{ext}}$  appear in the combination  $H - H_{\text{ext}}$ , so  $P_\xi$  and  $J$  depend only on  $H - H_{\text{ext}}$ , which is just  $H_{\text{loc}}$ . In a more intuitive sense,  $J$  depends only on  $H_{\text{loc}}$  because  $H_{\text{loc}}$  is sufficient to prescribe the  $\xi$  dynamics. Up to now, we have written  $J$  as  $J = J(H, \eta, P_\eta)$ , but the above discussion suggests that  $J$  is rather a function of  $H_{\text{loc}}$ :

$$J = J(H, \eta, P_\eta) = \tilde{J}(H_{\text{loc}}(\eta, P_\eta), \eta, P_\eta) = \tilde{J}(H - H_{\text{ext}}(\eta, P_\eta), \eta, P_\eta). \quad (5.73)$$

The symbol  $\tilde{J}(H_{\text{loc}}, \eta, P_\eta)$  is used simply to denote the difference in functional dependence from  $J(H, \eta, P_\eta)$ . This distinction may appear to be a matter of semantics, but we note that  $\tilde{J}(H_{\text{loc}}, \eta, P_\eta)$  depends on  $\eta$  and  $P_\eta$  both implicitly through  $H_{\text{ext}}$  and also explicitly. Accordingly,  $\Delta\eta$  and  $\Delta P_\eta$  have two terms: one term comes from the explicit dependence and one from the implicit dependence. The former is the drift of the system, e.g., the displacements suffered by  $\eta$  and  $P_\eta$  as a result of the  $\xi$  motion completing a full cycle, while the latter is the slow change of  $\eta$  and  $P_\eta$  due to  $H_{\text{ext}}$ . In the example provided in Sec. 5.1.9, these two terms will be computed explicitly.

We obtain a Hamiltonian for the averaged system in regular time in which partial differentiation of  $H$ , written as a function of  $J$ , gives the discretized derivatives defined above. To see this, we use the differential of  $J = J(H, \eta, P_\eta)$ ,

$$dJ = \frac{\partial J}{\partial H} dH + \frac{\partial J}{\partial \eta} d\eta + \frac{\partial J}{\partial P_\eta} dP_\eta, \quad (5.74)$$

to evaluate partial derivatives of  $H(J, \eta, P_\eta)$ :

$$\frac{\partial H}{\partial P_\eta} = -\frac{\partial J / \partial P_\eta}{\partial J / \partial H} = \frac{\Delta\eta}{\Delta t} = \frac{d\eta}{dt} \quad (5.75)$$

$$-\frac{\partial H}{\partial \eta} = -\frac{\partial J / \partial \eta}{\partial J / \partial H} = \frac{\Delta P_\eta}{\Delta t} = \frac{dP_\eta}{dt}, \quad (5.76)$$

giving the discretized derivatives. As in Sec. 5.1.7, writing  $H$  as a function of  $J$  rather than  $(\xi, P_\xi)$  turns the velocities given by Hamilton's equations into the drift velocities. We can further refine  $H = H(J, \eta, P_\eta)$  into local and external parts by solving Eq. (5.73) for  $H_{\text{loc}}$ , i.e.,  $H_{\text{loc}} = H_{\text{loc}}(J, \eta, P_\eta)$ . Since  $H_{\text{loc}} = H - H_{\text{ext}}$ ,

$$H = H_{\text{loc}}(J, \eta, P_\eta) + H_{\text{ext}}(\eta, P_\eta). \quad (5.77)$$

The term  $H_{\text{loc}}(J, \eta, P_\eta)$  is an adiabatic potential [99] and is, in essence, the residue of averaging the

periodic  $\xi$  motion. In fact, for systems approximating a harmonic oscillator,  $J = 2\pi H_{\text{loc}}/\omega(\eta, P_\eta)$ , so the adiabatic potential is  $H_{\text{loc}} = J\omega/(2\pi)$ , showing that  $J$  acts like an electrostatic charge and  $\omega(\eta, P_\eta)$  acts like an electrostatic potential. The magnitude of this effective “ $J$  charge” depends on the amplitude of the  $\xi$  oscillation. The use of  $-J$  as a Hamiltonian with normalized time  $\tau$  and the use of  $H$ , written as a function of  $J$ , with regular time are entirely equivalent<sup>4</sup>. Practically, though, there are techniques to evaluate  $J$  directly [97, Appendix II], so using  $-J$  as the Hamiltonian spares one from inverting  $J$  for  $H$ , which might not be analytically feasible, as will be in the case in Sec. 6.1.

### 5.1.9 Example: Particle in a Groove

The following system was proposed by Prof. Bellan as a mechanical analog of magnetic mirroring [2, Sec. 3.5.6] [93, pg. 29], a phenomenon where charged particles are reflected from regions of strong magnetic field strength. It is well-known that  $\mu$ -invariance is responsible for this mirroring phenomenon: as the field strength increases, the energy of the particle’s Larmor motion also increases as per Eq. (1.10) to the point when the Larmor energy equals the particle’s total kinetic energy. The particle then has no kinetic energy left to move along the field line and is thus reflected. We shall show that this principle is not restricted to charged particles in magnetic fields.

Consider a marble in a long groove where the steepness of the groove varies with position, as shown in Fig. 5.6. The height  $h$  of the groove can be expressed as a function of  $x$  and  $y$ , where  $y$  is the distance along the groove and  $x$  is the distance across the groove,

$$h(x, y) = \frac{1}{2}\kappa x^2 (1 + \alpha y^2) + \frac{1}{2}\lambda y^2. \quad (5.78)$$

The concavity and steepness of the groove is determined by the curvature  $\lambda$  in the  $y$  direction and  $\kappa$  in the  $x$  direction.  $\alpha$  couples the steepness of the  $x$  direction to the  $y$  coordinate. The exact Lagrangian and Hamiltonian for a marble in such a groove is not trivial<sup>5</sup>, but, in the same approximation in which a pendulum can be considered a harmonic oscillator, the Hamiltonian for this system is

$$H = \frac{P_x^2}{2m} + \frac{P_y^2}{2m} + \frac{1}{2}mg\kappa x^2 (1 + \alpha y^2) + \frac{1}{2}mg\lambda y^2. \quad (5.80)$$

Presuming that the particle’s  $y$  position changes slowly relative to the oscillations across the groove

<sup>4</sup>In fact, in Hamiltonian mechanics, one can use any momentum as a Hamiltonian for the system so long as the associated coordinate is used as the “time,” or orbit parameter [96, pg. 15][100].

<sup>5</sup>The exact Lagrangian equals the Lagrangian for a particle in gravitational field with the constraint that the particle remain on the groove. Using the Lagrange multiplier  $\Lambda$  to enforce the constraint:

$$L = \frac{m}{2} (\dot{x}^2 + \dot{y}^2 + \dot{z}^2) - mgz + \Lambda (z - h(x, y)), \quad (5.79)$$

for which the  $z$  equation of motion is  $m\ddot{z} = -mg + \Lambda$ . The approximation used here, like approximating a pendulum as a simple harmonic oscillator, ignores the acceleration in the  $z$  direction, so  $\Lambda = mg$ . Using this value of  $\Lambda$  in the exact Lagrangian gives the approximate Hamiltonian in Eq. (5.80).

(i.e.,  $|\alpha|$  and  $|\lambda|$  are small compared to  $\kappa$ ), the  $y$ -dependent frequency of  $x$  oscillation is

$$\omega(y) = \sqrt{g\kappa}\sqrt{1 + \alpha y^2}. \quad (5.81)$$

We identify  $H_{\text{loc}} = P_x^2/2m + m\omega^2 x^2/2$ , the energy of  $x$  oscillations. The  $x$  action is then that of a harmonic oscillator,  $J = 2\pi H_{\text{loc}}/\omega(y)$ , and Eq. (5.77) becomes

$$H(J, y, P_y) = \frac{P_y^2}{2m} + \frac{1}{2}mg\lambda y^2 + 2\pi\omega(y)J. \quad (5.82)$$

Equation (5.76) gives

$$\dot{P}_y = -\frac{\partial H(J, y, P_y)}{\partial y} = -mg\lambda y + 2\pi\frac{d\omega(y)}{dy}J. \quad (5.83)$$

The first term in Eq. (5.83) is the average force of the external Hamiltonian, in this case the pull of gravity along the groove. The second term, though, comes from differentiating the local Hamiltonian and is due to the adiabatic invariance of  $J$ . This average force in the  $y$  direction is due to the change in  $x$ -oscillation energy as the particle finds itself in a narrower or wider groove.

The adiabatic term in Eq. (5.83) can oppose the pull of gravity, leading to surprising behavior. Suppose that  $\lambda$  is negative so that the groove is concave down along in the  $y$  direction. Intuition dictates that a marble placed in such a groove will rattle its way down the groove with increasing velocity, as shown in Fig. 5.7. However, with the right choice of initial conditions, the adiabatic force can have a negative value, meaning it acts as a restoring force in the  $y$  direction and, if sufficiently strong, can overwhelm the contribution from  $\lambda$  and give oscillatory  $y$  motion! This is the mechanical analog of a magnetic mirror and has been verified by direct numerical integration as shown in Fig. 5.8.

For oscillatory  $y$  motion, Eq. (5.82) admits an action integral in the  $y$  direction. Denote this second action by  $K$ , which can be considered a new Hamiltonian for the  $x$  averaged system. This is an example of a two-tier hierarchy of action variables, or a wheel within a wheel [91]. For the reduced system,  $J$  plays the role of a conserved quantity, so we develop an analog of Eq. (5.4):

$$\frac{\partial K}{\partial J} = \oint \frac{\partial P_y(H, J, y)}{\partial J} dy = \oint \frac{1}{\partial J/\partial P_y} dy \quad (5.84)$$

$$= \oint \frac{-1}{dy/d\tau} dy = -\Delta\tau, \quad (5.85)$$

where Eq. (5.74) has been used to evaluate  $\partial P_y/\partial J$  and Eq. (5.72) has been used to evaluate  $\partial J/\partial P_y$ . Since  $\tau$  counts  $x$  cycles,  $-\partial K/\partial J$  gives the number of  $x$  cycles per  $y$  cycle. If this quantity is rational, then the trajectory is closed, which is of interest when quantizing the system, as there is sometimes a one-to-one correspondence between periodic classical trajectories and quantum energy levels [101].

## 5.2 Charged Particle Motion in a Magnetic Field

Having discussed at length the general theory, we now focus on charged particle motion in magnetic fields. Sec. 5.2.1 shows that, in the guiding center approximation, the action integral  $J$  reduces to the first adiabatic invariant  $\mu$ . Since  $J$  acts as a Hamiltonian for the reduced system, it follows that  $\mu$  is a Hamiltonian for the guiding center drifts, and we shall explicitly recover several of the guiding center drifts from the general theory. Sec. 5.2.5 show an unexpected application of the theory: computing the magnetic flux enclosed by a particle's orbit by differentiating the action variable with respect to the particle's charge. We finally conclude the chapter with a theorem that relates these various partial derivatives of  $J$ .

### 5.2.1 The Connection Between $J$ and $\mu$

The action integral  $J$  is clearly important but often difficult to evaluate in closed form. In the same limit as the guiding center approximation, however, the integral for  $J$  can be approximated and is proportional to  $\mu$ , the first adiabatic invariant [33, p. 16]. This approximation also shows that the guiding center limit is really a harmonic-oscillator approximation to the full problem.

Consider a magnetic field in the  $z$  direction and with  $x$  dependence:  $\mathbf{B} = B_z(x)\hat{z}$ . A charged particle will drift in the  $y$  direction due to the gradient in the magnetic field strength [2, Sec. 3.5.2] [93, Sec. 2.3] and will move freely in the  $z$  direction. The action  $J$  can be written in integral form using the vector potential

$$\mathbf{A} = A_y(x)\hat{y} = \left( \int_{x_0}^x B_z(x')dx' \right) \hat{y}, \quad (5.86)$$

and Hamiltonian

$$H = \frac{P_x^2}{2m} + \frac{(P_y - qA_y(x))^2}{2m} + \frac{P_z^2}{2m}, \quad (5.87)$$

from which

$$J(H, P_y, P_z) = \oint P_x dx = \oint \sqrt{2mH - P_z^2 - (P_y - qA_y(x))^2} dx. \quad (5.88)$$

To help with notation, let us define  $H_\perp$  as the kinetic energy in the Larmor motion (e.g. *not* in the  $z$  direction):

$$H_\perp = H - \frac{P_z^2}{2m}. \quad (5.89)$$

We evaluate  $J$  by first defining the guiding center position  $x_{gc}$  and then performing a Taylor expansion about this point. Let  $x_{gc}$  be the  $x$  location where the  $y$  velocity vanishes:

$$0 = m\dot{y}(x_{gc}) = P_y - qA_y(x_{gc}). \quad (5.90)$$

If the orbit were perfectly circular, as is assumed in guiding center theory, then  $x_{\text{gc}}$  would coincide with the center of the circle.  $x_{\text{gc}}$  is a function of  $P_y$ , and, for future reference, a partial differentiation of Eq. (5.90) with respect to  $P_y$  gives

$$\frac{\partial x_{\text{gc}}}{\partial P_y} = \frac{1}{qB_z(x_{\text{gc}})}. \quad (5.91)$$

We now perform a Taylor expansion of  $A_y$  around  $x_{\text{gc}}$ :

$$A_y(x) \approx A_y(x_{\text{gc}}) + \left. \frac{dA_y}{dx} \right|_{x_{\text{gc}}} (x - x_{\text{gc}}) \quad (5.92)$$

$$= A_y(x_{\text{gc}}) + B_z(x_{\text{gc}})(x - x_{\text{gc}}). \quad (5.93)$$

This expansion allows us to approximate  $J$ . Letting  $x' = x - x_{\text{gc}}$ ,

$$J \approx \oint \sqrt{2mH_{\perp} - (qB_z(x_{\text{gc}})x')^2} dx' \quad (5.94)$$

$$= |qB_z(x_{\text{gc}})| \oint \sqrt{\frac{2mH_{\perp}}{q^2 B_z(x_{\text{gc}})^2} - (x')^2} dx' \quad (5.95)$$

The integral now represents the area enclosed by a circle of radius  $\sqrt{2mH_{\perp}}/|qB|$ , so

$$J \approx \pi \frac{2mH_{\perp}}{|qB_z(x_{\text{gc}})|} = 2\pi \frac{m}{|q|} \left( \frac{mv_L^2}{2|B_z(x_{\text{gc}})|} \right) = 2\pi \frac{m}{|q|} \mu, \quad (5.96)$$

where  $\mu$  is defined as in Eq. (1.10). Thus,  $J$  is proportional to, but not equal to,  $\mu$  in the guiding center limit. The importance of this derivation is the functional dependence of  $B$  on  $x_{\text{gc}}$  and hence on  $P_y$ ; this dependence is key in deriving the grad-B drift below. Note that the absolute value of  $q$  guarantees that the action  $J$  is positive<sup>6</sup> for both positively and negatively charged particles.

In reducing  $J$  to  $\mu$ , we have used the same approximations that reduce any potential well to a harmonic oscillator. To see this, note that the Hamiltonian in Eq. (5.87) can be viewed as a one-dimensional system with an effective potential energy  $U_{\text{eff}} = (P_y - qA_y(x))^2/2m = (m/2)v_y(x)^2$  [2, pg. 119]. That is, the effective potential is equal to the kinetic energy in the  $y$  direction, and  $x_{\text{gc}}$  is clearly the location of the minimum of this potential well. As any potential well can be approximated as a harmonic oscillator by performing a second-order Taylor expansion of the potential around the minimum, Eq. (5.94) is equivalent to the action integral for a harmonic oscillator. The action for a harmonic oscillator is  $J = 2\pi\omega H$ , and, indeed, the Eq. (1.10) is proportional<sup>7</sup> to  $2\pi\omega H$  with  $\omega$  equal to the gyrofrequency. The guiding center limit is thus a harmonic-oscillator approximation.

<sup>6</sup>  $J$  must be positive for such systems because  $J = \oint P_x dx$  and  $P_x = m\dot{x}$ . Therefore, the contour of integration for  $J$  is clockwise in the  $rP_r$  plane, corresponding to a positive value of  $J$ , regardless of the particle charge.

<sup>7</sup> The constant of proportionality between  $J$  and  $\mu$  is  $m/|q|$ , which is suggestive of the gyromagnetic ratio which related the angular momentum of a charged rotating rigid body to its magnetic moment [98, pg. 252].

Section 5.1.8 shows that the action  $J$  can be used as a Hamiltonian for the reduced system. Having shown that  $J$  reduces to  $\mu$  in the guiding center limit, we expect that  $\mu$  will serve as a Hamiltonian for the guiding center motion. Section 5.2.2 shows that Eq. (5.94) for  $\mu$  does indeed contain the grad-B drift of guiding center theory thanks to the definition of  $x_{gc}$  in Eq. (5.90). Sec. 5.2.3 extends the analysis to include parallel dynamics and the magnetic mirror force, and Sec. 5.2.4 adds an electrostatic field to study the  $\mathbf{E} \times \mathbf{B}$  drift.

## 5.2.2 The Grad-B Drift

For the magnetic fields used in the previous section, a charged particle will drift in the  $y$  direction due to the gradient in field strength. We show that this grad-B drift, which is well-established in guiding center theory, can be computed using the Hamiltonian formalism.  $\Delta t$  is given by Eq. (5.13) and (5.96),

$$\frac{\partial J}{\partial H} = 2\pi \frac{m}{|q| B_z(x_{gc})} = \Delta t, \quad (5.97)$$

and is the usual gyroperiod.  $\Delta y$  is given by a partial derivative with respect to  $P_y$ :

$$\Delta y = -\frac{\partial J}{\partial P_y} = 2\pi m \frac{H_{\perp}}{|q| B_z(x_{gc})^2} \frac{\partial B_z}{\partial x} \frac{dx_{gc}}{dP_y} \quad (5.98)$$

$$= 2\pi m \frac{H_{\perp}}{|q| B_z(x_{gc})^2} \frac{\partial B_z}{\partial x} \left( \frac{1}{q B_z(x_{gc})} \right), \quad (5.99)$$

where Eq. (5.91) was used to evaluate  $dx_{gc}/dP_y$ . The drift velocity in the  $y$  direction, computed through the Hamiltonian formalism, is

$$\frac{\Delta y}{\Delta t} = \frac{H_{\perp}}{q B_z(x_{gc})^2} \frac{\partial B_z}{\partial x}. \quad (5.100)$$

Let us compare Eq. (5.100) to the grad-B drift [2, eq. 3.89] from the guiding center approximation:

$$\mathbf{v}_{\nabla B} = -\frac{H_{\perp}}{q B^3} \nabla B \times \mathbf{B} \quad (5.101)$$

$$= -\frac{H_{\perp}}{q B^3} \left( \frac{\partial B_z}{\partial x} \hat{x} \right) \times (B_z \hat{z}) \quad (5.102)$$

$$= \frac{H_{\perp}}{q B_z^2} \frac{\partial B_z}{\partial x} \hat{y}, \quad (5.103)$$

which is in perfect agreement with Eq. (5.100).

## 5.2.3 Parallel Dynamics: The Magnetic Mirror Force

We now consider a magnetic field whose strength slowly changes in the  $z$  direction as well as in the  $x$  direction. The parallel dynamics become non-trivial: the gyrofrequency changes with the field

strength, the parallel motion can slow down, and magnetic mirroring can occur. We show that  $\mu$  serves as a Hamiltonian for both the parallel dynamics in addition to the grad-B drift discussed above.

We first make some assumptions on the magnetic field. Because  $\partial_z B_z \neq 0$ , there must be a second component of  $B$  to ensure  $\nabla \cdot \mathbf{B} = 0$ . We therefore allow  $B_x$  to be non-zero. Since the  $z$  dependence of  $B_z$  is mild,  $B_x$  must be small. All of this can be encapsulated by the vector potential

$$\mathbf{A} = A_y(x, z)\hat{y} = \tilde{A}(x, \epsilon z)\hat{y}; \quad (5.104)$$

that is, the vector potential is some function of  $x$  and  $\epsilon z$ . The  $\epsilon$  in the  $z$  dependence allows us to keep track of the relative magnitudes of terms. For instance, the magnetic field components are

$$B_z = \frac{\partial A_y}{\partial x}, \quad B_x = -\frac{\partial A_y}{\partial z}, \quad (5.105)$$

so that  $B_z$  is zeroth order but  $B_x$  is small to first order. Likewise,  $\partial_z B_z$  is first order, and  $\partial_z B_x$  is second order. We shall only work to first order. In this limit, the magnitude of the magnetic field is

$$B = \sqrt{B_z^2 + B_x^2} \approx B_z, \quad (5.106)$$

and the unit vector of  $\mathbf{B}$  is

$$\hat{B} = \frac{B_z \hat{z} + B_x \hat{x}}{B} \approx \hat{z} + \frac{B_x}{B_z} \hat{x}. \quad (5.107)$$

To proceed with the Hamiltonian formalism, we modify our definition of  $x_{\text{gc}}$  to be a function of both  $P_y$  and  $z$  defined by

$$0 = \dot{y}(x_{\text{gc}}(P_y, z)) = P_y - qA_y(x_{\text{gc}}(P_y, z), z). \quad (5.108)$$

Implicit differentiation gives a modified version of Eq. (5.91):

$$\frac{\partial x_{\text{gc}}}{\partial P_y} = \frac{1}{qB_z}, \quad (5.109)$$

$$\frac{\partial x_{\text{gc}}}{\partial z} = -\frac{\partial A_y / \partial z}{\partial A_y / \partial x} = \frac{B_x}{B_z}. \quad (5.110)$$

The form of  $J$  remains the same,

$$J = 2\pi \frac{m}{|q|} \frac{H_{\perp}}{B_z(x_{\text{gc}}(P_y, z), z)}, \quad (5.111)$$

but there is now  $z$  dependence both in the magnetic field and also in the guiding center position. Neither  $\partial J / \partial H$  nor  $\partial J / \partial P_y$  change in form except for the  $z$  dependence added to  $B_z$ , so the grad-

B drift is the same as Eq. (5.100). The calculation of  $\Delta P_z$ , however, becomes interesting, as the evaluation of  $\partial J/\partial z$  must include differentiation of the  $z$  dependence of both  $B_z$  and also  $x_{\text{gc}}$ . Using Eqs. (5.109) and (5.110), we get

$$\frac{\partial J}{\partial z} = -2\pi \frac{m}{|q|} \frac{H_{\perp}}{B_z^2} \frac{dB_z(x_{\text{gc}}, z)}{dz} \quad (5.112)$$

$$= -2\pi \frac{m}{|q|} \frac{H_{\perp}}{B_z^2} \left[ \frac{\partial B_z}{\partial x} \frac{\partial x_{\text{gc}}}{\partial z} + \frac{\partial B_z}{\partial z} \right] \quad (5.113)$$

$$= -2\pi \frac{m}{|q|} \frac{H_{\perp}}{B_z^2} \left[ \frac{\partial B_z}{\partial x} \frac{B_x}{B_z} + \frac{\partial B_z}{\partial z} \right] \quad (5.114)$$

$$= -2\pi \frac{m}{|q|} \frac{H_{\perp}}{B_z^2} \left[ \frac{B_x}{B_z} \frac{\partial}{\partial x} + \frac{\partial}{\partial z} \right] B_z \quad (5.115)$$

$$= -2\pi \frac{m}{|q|} \frac{\mu}{B_z} \hat{B} \cdot \nabla B_z. \quad (5.116)$$

Then

$$\frac{\Delta P_z}{\Delta t} = \frac{\partial J/\partial z}{\partial J/\partial H} = -\mu \hat{B} \cdot \nabla B_z. \quad (5.117)$$

We can work out the dynamics as predicted by the guiding center approximation and compare them with the conclusions of the previous paragraph. We start with the  $\nabla B$  drift and show that it is unaltered by the added  $z$  dependence. While the gradient of the magnetic field strength is modified to first order  $\epsilon$ :

$$\nabla B \approx \nabla B_z = \frac{\partial B_z}{\partial x} \hat{x} + \frac{\partial B_z}{\partial z} \hat{z}, \quad (5.118)$$

the grad-B drift remains the same as Eq. (5.103) to first order:

$$\mathbf{v}_{\nabla B} = -\frac{H_{\perp}}{qB^3} \nabla B \times \mathbf{B} \quad (5.119)$$

$$= -\frac{H_{\perp}}{qB^3} \left( \frac{\partial B_z}{\partial x} \hat{x} + \frac{\partial B_z}{\partial z} \hat{z} \right) \times (B_x \hat{x} + B_z \hat{z}) \quad (5.120)$$

$$= \frac{H_{\perp}}{qB^2} \frac{\partial B_z}{\partial x} \hat{y}. \quad (5.121)$$

The term  $B_x \cdot \partial_z B_z$  is second order  $\epsilon$  and thus is dropped. Guiding center theory predicts a second drift, the curvature drift [2, Sec. 3.5.2] [93, Sec. 2.3.2], but this is zero to first order:

$$\mathbf{v}_c = -\frac{mv_{\parallel}^2}{qB^2} \hat{B} \cdot \nabla \hat{B} \times \mathbf{B} \quad (5.122)$$

$$= -\frac{mv_{\parallel}^2}{qB_z^2} \left[ \left( \frac{\partial}{\partial z} + \frac{B_x}{B_z} \frac{\partial}{\partial x} \right) \left( \hat{z} + \frac{B_x}{B_z} \hat{x} \right) \right] \times (B_z \hat{z} + B_x \hat{x}), \quad (5.123)$$

because the term in square brackets is second order  $\epsilon$ . The parallel dynamics comes from  $\mu$  conser-

vation:

$$\mu B = H - P_z^2/2m. \quad (5.124)$$

Taking a total time derivative of both sides,

$$\mu \mathbf{v}_d \cdot \nabla B = -P_z \dot{P}_z/m, \quad (5.125)$$

where  $\mathbf{v}_d$  is the drift velocity. Since  $B$  does not vary in the  $y$ -direction,  $\mathbf{v}_d \cdot \nabla B = \dot{z} \partial_z B$ , and dividing by Eq. (5.125) by  $\dot{z} = P_z/m$  gives

$$\mu \hat{B} \cdot \nabla B = -\dot{P}_z, \quad (5.126)$$

which agrees with Eq. (5.117).

### 5.2.4 $\mathbf{E} \times \mathbf{B}$ Drifts

This section incorporates an electrostatic field  $\mathbf{E}(x, y) = -\nabla V(x, y)$  in addition to a magnetic field of the form  $\mathbf{B} = B_z(x) \hat{z}$ . The Hamiltonian becomes

$$H = \frac{P_x^2}{2m} + \frac{(P_y - qA_y(x))^2}{2m} + qV(x, y), \quad (5.127)$$

and the action integral is

$$J(H, y, P_y) = \oint \sqrt{2m(H - qV(x, y)) - (P_y - qA_y(x))^2} dx. \quad (5.128)$$

We would like to approximate this integral and express the result in a form similar to the action  $J_0$  for the purely magnetic case:

$$J_0(H, P_y) = \oint \sqrt{2mH - (P_y - qA_y(x))^2} dx \approx \pi \frac{2mH}{|q| B_z(x_{gc})}. \quad (5.129)$$

The coarsest approximation to Eq. (5.128) is sufficient to recover the  $\mathbf{E} \times \mathbf{B}$  drift [2, ch. 3.5.1] [93, Sec. 2.2.2] in addition to the grad-B drift. More accurate approximations of Eq. (5.128) produce higher-order corrections to the  $\mathbf{E} \times \mathbf{B}$  velocity. We relate one such higher-order correction to a finite Larmor radius effect. In Appendix D, we relate a second such higher-order correction with a pondermotive-like force induced by the cyclotron motion.

The coarsest approximation to Eq. (5.128) is to assume that, over the course of a gyro-orbit,  $V(x, y)$  can be approximated by its value at the guiding center,  $V(x, y) \approx V(x_{gc}, y)$ . With this approximation,

$$J(H, y, P_y) \approx J_0(H - qV(x_{gc}, y), P_y), \quad (5.130)$$

The period  $\Delta t$  is the same as with no potential, but  $\Delta y$  has a new term that comes from the  $P_y$  dependence of  $x_{gc}$  in  $V$ :

$$\Delta y = -\frac{\partial J}{\partial P_y} = -\frac{\partial J_0}{\partial H} \frac{\partial}{\partial P_y} (H - qV) - \frac{\partial J_0}{\partial P_y} = \frac{\partial J_0}{\partial H} \frac{\partial_x V}{B_z} - \frac{\partial J_0}{\partial P_y}, \quad (5.131)$$

where Eq. (5.91) has been used. The drift in the  $y$  direction is thus

$$\frac{\Delta y}{\Delta t} = \frac{\partial_x V}{B_z} - \frac{\partial J_0 / \partial P_y}{\partial J_0 / \partial H}. \quad (5.132)$$

The second term is the grad-B drift discussed in Sec. 5.2.2, and we denote this quantity as  $v_{\nabla B}$ . The first term,  $\partial_x V / B$ , is readily identified as the  $y$  component of the  $\mathbf{E} \times \mathbf{B}$  drift:

$$\left( \frac{\mathbf{E} \times \mathbf{B}}{B^2} \right)_y = \frac{(E_x \hat{x}) \times (B_z \hat{z})}{B_z^2} = \frac{\partial_x V}{B_z}. \quad (5.133)$$

The  $x$  component of the  $\mathbf{E} \times \mathbf{B}$  drift is also contained in the Hamiltonian formalism and can be computed by taking  $\Delta x_{gc}$  and using the definition of  $x_{gc}$  from Eq. (5.90) to obtain  $\Delta P_y = qB_z(x_{gc})\Delta x_{gc}$ . Then, since

$$\Delta P_y = \frac{\partial J}{\partial y} = \frac{\partial J_0}{\partial H} \left( -q \frac{\partial V}{\partial y} \right), \quad (5.134)$$

the drift in the  $x$  direction is

$$\frac{\Delta x_{gc}}{\Delta t} = -\frac{\partial_y V}{B_z}. \quad (5.135)$$

We can retain the two next higher-order terms of the expansion of  $V$  to yield more accurate forms of the action integral. We proceed by using the expansion  $V(x, y) \approx V(x_{gc}, y) + \partial_x V \delta x$  in the integrand of Eq. (5.128) and then completing the square in  $\delta x$ :

$$J \approx \oint \sqrt{2m(H - qV - \partial_x V \delta x) - (qB_z \delta x)^2} dx \quad (5.136)$$

$$= \oint \sqrt{2m \left( H - qV + \frac{m}{2} \left( \frac{\partial_x V}{B_z} \right)^2 \right) - q^2 B_z^2 \left( \delta x + \frac{m \partial_x V}{q B_z^2} \right)^2} dx. \quad (5.137)$$

This integral for  $J$  resembles Eq. (5.128) but with two modifications. First, the oscillation center is shifted by the amount  $m \partial_x V / q B_z^2$ . As discussed in Appendix D, this shift occurs because our definition of guiding center no longer minimizes the effective potential once a potential has been added. However, in evaluating Eq. (5.137), this shift will have no bearing on the value of the action integral<sup>8</sup>. The second modification is the addition of a new potential term  $(m/2)(\partial_x V / B_z)^2$ , which is the kinetic energy of the  $\mathbf{E} \times \mathbf{B}$  drift. In Appendix D, this new potential is proposed to be a

<sup>8</sup>Put succinctly,  $J$  is the phase space area enclosed by the trajectory in the  $xP_x$  plane and thus is clearly not changed by an offset.

pondermotive-like potential induced by the cyclotron motion. Eq. (5.137) allows us to express  $J$  in terms of  $J_0$ :

$$J(H, P_y) = J_0 \left( H - qV(x_{\text{gc}}, y, t) + \frac{m}{2} \left( \frac{\partial_x V}{B_z} \right)^2, P_y \right), \quad (5.138)$$

which serves as a Hamiltonian for the guiding center motion. The effect of the new potential term on the drift will be discussed shortly.

If the potential  $V(x, y)$  is expanded one term further,  $V(x, y) \approx V(x_{\text{gc}}, y) + \partial_x V \delta x + (1/2) \partial_{xx} V (\delta x)^2$ , then the second-order term effectively modifies the magnetic field strength:

$$J \approx \oint \sqrt{2m \left( H - qV - \partial_x V \delta x - \frac{1}{2} q \partial_{xx} V \delta x^2 \right) - (qB_z \delta x)^2} dx \quad (5.139)$$

$$= \sqrt{2m (H - qV - \partial_x V \delta x) - (q^2 B_z^2 + m q \partial_{xx} V) (\delta x)^2} dx \quad (5.140)$$

$$= \sqrt{2m (H - qV - \partial_x V \delta x) - (qB_z^* \delta x)^2} dx, \quad (5.141)$$

where  $B_z^*$  is

$$B_z^* = \sqrt{B_z^2 + \frac{m}{q} \partial_{xx} V}. \quad (5.142)$$

One can then proceed as before and obtain Eq. (5.138) with  $B_z$  replaced with  $B_z^*$ .

$$J(H, P_y) = J_0 \left( H - qV(x_{\text{gc}}, y, t) + \frac{m}{2} \left( \frac{\partial_x V}{B_z^*} \right)^2, P_y \right), \quad (5.143)$$

This is the most accurate approximation of the action integral and has many instances of implicit  $P_y$  dependence through  $x_{\text{gc}}$  in  $V$  and  $B_z^*$ .

The added potential term in Eq. (5.138) contributes a new term to  $\Delta y$ , leading to a higher-order drift. The new term in  $\Delta y$  is obtained by differentiating the  $(m/2)(\partial_x V/B_z)^2$  in Eq. (5.138) with respect to  $P_y$ . To organize the growing number of terms, we write  $\Delta y = (\Delta y)_0 + (\Delta y)_1$ , where  $(\Delta y)_0$  consists of the terms from Eq. (5.131) and  $(\Delta y)_1$  is the new higher-order term. Then

$$(\Delta y)_1 = -\frac{\partial J_0}{\partial H} \frac{\partial}{\partial P_y} \left( \frac{m}{2} \left( \frac{\partial_x V}{B_z} \right)^2 \right) \quad (5.144)$$

$$= -\frac{\partial J_0}{\partial H} \left( \frac{\partial_x V}{B_z} \right) \frac{\partial}{\partial P_y} \left( m \frac{\partial_x V}{B_z} \right) \quad (5.145)$$

$$= -\frac{\partial J_0}{\partial H} \left( \frac{\partial_x V}{B_z} \right) \frac{dx_{\text{gc}}}{dP_y} \frac{\partial}{\partial x} \left( m \frac{\partial_x V}{B_z} \right). \quad (5.146)$$

We then rewrite  $\partial_x V/B_z$  as  $v_{\text{E} \times \text{B}}$  and also use Eq. (5.91) to write  $dx_{\text{gc}}/dP_y = 1/qB_z$ . Then

$$(\Delta y)_1 = -\frac{\partial J_0}{\partial H} v_{\text{E} \times \text{B}} \frac{m}{qB_z} \frac{\partial}{\partial x} (v_{\text{E} \times \text{B}}). \quad (5.147)$$

This new term in  $\Delta y$  leads to new terms in the drift velocity  $\Delta y/\Delta t$ . Combining Eq. (5.131) with Eq. (5.147) gives

$$v_d = v_{\nabla B} + v_{\mathbf{E} \times \mathbf{B}} - v_{\mathbf{E} \times \mathbf{B}} \frac{m}{qB_z} \frac{\partial}{\partial x} (v_{\mathbf{E} \times \mathbf{B}}). \quad (5.148)$$

Since the higher-order drift involves a gradient of  $v_{\mathbf{E} \times \mathbf{B}}$ , one might regard it as a ‘‘grad-E’’ drift. However, in Appendix D.1 we show that the existence of this higher-order drift really depends on how one defines the guiding center.

Finally, we show that Eq. (5.143) can be used to derive a finite Larmor radius effect discussed by Chen in [93, sec. 2.4]. A finite Larmor radius effect is a higher-order correction to guiding center theory due to the fact that the particle’s orbit has non-zero size. Following Chen, we assume that the magnetic field is uniform and work in the guiding center limit so that  $J_0$  is given by Eq. (5.96) with the modified field strength  $B^*$ . Then

$$J(H, P_y) = 2\pi m \frac{H - qV(x_{\text{gc}}) + (m/2)(\partial_x V/B_z)^2}{|q| B_z^*}. \quad (5.149)$$

We have already computed the contribution to  $\Delta y$  from differentiation of both  $qV$  and  $(m/2)(\partial_x V/B_z)^2$ . Here, we will focus on the contribution from differentiating  $B_z^*$ :

$$(\Delta y)_2 = -\frac{\partial J}{\partial P_y} = 2\pi m \frac{H - qV(x_{\text{gc}})}{|q| B_z^{*2}} \frac{\partial B_z^*}{\partial P_y}. \quad (5.150)$$

Using the definition of  $B_z^*$  from Eq. (5.142) and bearing in mind that  $B_z$  is constant, we have

$$\frac{\partial B_z^*}{\partial P_y} = \frac{1}{2B_z^{*2}} \frac{m}{q} \frac{\partial(\partial_{xx} V)}{\partial P_y} \quad (5.151)$$

$$= \frac{m}{2qB_z^*} \frac{\partial^3 V}{\partial x^3} \frac{\partial x_{\text{gc}}}{\partial P_y} \quad (5.152)$$

$$= \frac{m}{2q^2 B_z^* B_z} \frac{\partial^3 V}{\partial x^3}, \quad (5.153)$$

where Eq. (5.91) has been used to evaluate  $\partial x_{\text{gc}}/\partial P_y$ . At this point, we take  $B_z^* \approx B_z$  and evaluate the resulting drift:

$$\frac{(\Delta y)_2}{\Delta t} = \frac{H - qV(x_{\text{gc}})}{|q| B^{*2}} \frac{m}{2qB_z} \frac{\partial^3 V}{\partial x^3}. \quad (5.154)$$

Since  $B_z$  is constant and  $H - qV = (m/2)v_{\perp}^2$ , we can write

$$\frac{\Delta y}{\Delta t} = \frac{m^2 v_{\perp}^2}{|q| B^{*2}} \frac{1}{4qB^*} \frac{\partial^2}{\partial x^2} \left( \frac{E_x}{B_z} \right) \quad (5.155)$$

$$= \frac{1}{4} r_L^2 \frac{\partial^2}{\partial x^2} \left( \frac{E_x}{B_z} \right), \quad (5.156)$$

which is equal to the finite Larmor radius correction to the  $\mathbf{E} \times \mathbf{B}$  drift given in Ref. [93, sec. 2.4].

### 5.2.5 Magnetic Flux Enclosed by a Gyro-Orbit

Here, we show that the action integral  $J$  can be used to compute the magnetic flux enclosed by a gyro-orbit. As magnetic flux is only defined through a closed surface and charged particle trajectories are typically not closed, we evaluate the flux using the orbit in the drift frame. We give an alternate derivation of the same formula in Appendix C.

For any orbit in an electromagnetic field for which one coordinate, say  $\xi$ , is periodic, we have

$$\frac{\partial J}{\partial q} = \oint \frac{\partial P_\xi}{\partial q} d\xi = \oint \frac{\partial H(\mathbf{r}, \mathbf{P}; q)/\partial q}{\partial H(\mathbf{r}, \mathbf{P}; q)/\partial P_\xi} d\xi \quad (5.157)$$

$$= - \oint \left[ -\frac{\mathbf{p} - q\mathbf{A}}{m} \cdot \mathbf{A} + V \right] \frac{d\xi}{\xi} \quad (5.158)$$

$$= - \int_{t_0}^{t_0+\Delta t} [-\mathbf{v} \cdot \mathbf{A} + V] dt \quad (5.159)$$

$$= \int \mathbf{A} \cdot d\mathbf{l} - \int_{t_0}^{t_0+\Delta t} V dt. \quad (5.160)$$

The line integral of  $\mathbf{A}$  is over one period of motion; since the motion is in general not periodic, we cannot identify this integral as the magnetic flux enclosed by the orbit. However, in the drift frame, the orbit is closed by definition, and the integral of  $\mathbf{A}$  over the orbit in the drift would indeed yield a well-defined flux. We extract this integral from Eq. (5.159) by writing the lab frame velocity as  $\mathbf{v} = \mathbf{v}' + \mathbf{v}_d$ , where  $\mathbf{v}_d$  is the drift velocity and  $\mathbf{v}'$  is the particle velocity as seen in the drift frame. We then have

$$\frac{\partial J}{\partial q} = - \int_{t_0}^{t_0+\Delta t} [-(\mathbf{v}' + \mathbf{v}_d) \cdot \mathbf{A} + V] dt \quad (5.161)$$

$$= \oint \mathbf{A} \cdot d\mathbf{l}' + \int_{t_0}^{t_0+\Delta t} \mathbf{v}_d \cdot \mathbf{A} dt - \int_{t_0}^{t_0+\Delta t} V dt. \quad (5.162)$$

The first term is the flux, which we denote by  $\Phi$ . The second term<sup>9</sup> can be rewritten using  $q\mathbf{A} = \mathbf{P} - m\mathbf{v}$ . As the drift is in a direction of symmetry, the component of  $\mathbf{P}$  along the drift is conserved. We then obtain

$$\frac{\partial J}{\partial q} = \Phi + \frac{1}{q} (\mathbf{P} - m\mathbf{v}_d) \cdot \Delta\mathbf{r} - \int_{t_0}^{t_0+\Delta t} V dt, \quad (5.163)$$

showing the relationship between  $\partial J/\partial q$  and  $\Phi$ . If there is a non-zero potential  $V$ , then its average over one period must be computed.

We mention in passing that  $\oint \mathbf{A} \cdot d\mathbf{l}$  is related to the phase shift due to the Aharonov-Bohm effect [102], so the quantity  $\partial J/\partial q$ , when no potential is present, could be of particular value in

<sup>9</sup>We note that, if one had formally boosted to the drift frame in the non-relativistic limit, then the potential  $V$  would be transformed precisely by the amount  $-\mathbf{v}_d \cdot \mathbf{A}$  while the vector potential would not be transformed. This can be seen by boosting the four-vector  $(-V, c\mathbf{A})$  in the non-relativistic limit.

quantum systems.

### 5.2.6 Drift, Action, and Euler's Formula

We conclude this chapter with a formula that relates the various partial derivatives of  $J$ . The derivation here utilizes Euler's formula for homogenous functions. An alternate derivation that integrates the action over special phase space contours is included in Appendix D.5; the derivation there uses a technique developed by Montgomery in the case of rigid body dynamics [103].

Suppose that, for a charged particle in a magnetic field, the  $x$  coordinate is periodic and the  $y$  and  $z$  coordinates are ignorable. We write  $H$ , which is kinetic energy, as  $(m/2)v^2$ . Then  $J$  is a homogenous function of degree one in the variables  $v$ ,  $P_y$ ,  $P_z$ , and  $q$ :

$$J = \oint \sqrt{m^2 v^2 - (P_y - qA_y)^2 - (P_z - qA_z)^2} dx. \quad (5.164)$$

Applying Euler's theorem of homogenous functions to  $J$ , we obtain

$$J(v, P_y, P_z; q) = v \frac{\partial J}{\partial v} + q \frac{\partial J}{\partial q} + P_y \frac{\partial J}{\partial P_y} + P_z \frac{\partial J}{\partial P_z}, \quad (5.165)$$

or

$$J(H, P_y, q) = 2H\Delta t + q \frac{\partial J}{\partial q} + P_y \frac{\partial J}{\partial P_y} + P_z \frac{\partial J}{\partial P_z}. \quad (5.166)$$

The flux enclosed by a gyro-orbit is given by Eq. (D.26), which can be rewritten as

$$q\Phi = q \frac{\partial J}{\partial q} + P_y \frac{\partial J}{\partial P_y} + P_z \frac{\partial J}{\partial P_z} + mv_d^2 \frac{\partial J}{\partial H}. \quad (5.167)$$

Using Eq. (5.167) in Eq. (5.165),

$$J = q\Phi + 2 \left( H - \frac{1}{2}mv_d^2 \right) \Delta t. \quad (5.168)$$

This formula ties together the action integral, the flux, and the period, and the drift velocity. As discussed in Sec. 5.2.1,  $J$  becomes proportional to  $\mu$  in the guiding center limit. In the same limit, the drift-velocity energy is negligible compared to the total energy  $H$ , so

$$2\pi \frac{m}{|q|} \mu = q\Phi + 2H\Delta t. \quad (5.169)$$

## 5.3 Conclusions

We have shown that, in any Hamiltonian system where one coordinate undergoes periodic evolution, the action integral for that coordinate encodes the evolution of the system once the periodic motion

has been averaged over. In fact, this action integral acts as a Hamiltonian for the reduced system and provides the averaged equations of motion provided that time is measured in periods of motion. This formalism can be used to rederive the drifts of the guiding center approximation using  $\mu$  as a Hamiltonian and can even be used to derive the flux enclosed by a gyro-orbit, but the scope of the results goes far beyond charged particle motion in magnetic field.

In regards to future work, the curvature drift from guiding center theory has not yet been derived from the Hamiltonian formalism, and this could be a very interesting problem. As the curvature drift involves motion along curved field lines, one approach would be to rotate the coordinate system to align with the magnetic field after each period of motion. It is conceivable that the Hamiltonian formalism could be used to compute the required rotation matrix; this framework is reminiscent of an  $SO(3)$  fiber bundle [104, ch. 1] over the  $\xi P_\xi$  plane. Another application would be to situations where the guiding center approximation breaks down. Guiding center theory is essentially a harmonic-oscillator approximation, but the Hamiltonian theory depends on periodic motion that is not necessarily harmonic. Therefore, the latter is more robust and may supplant guiding center theory in cases of large orbit sizes or vanishing magnetic fields. Indeed, the beginnings of such work are seen in the next chapter.

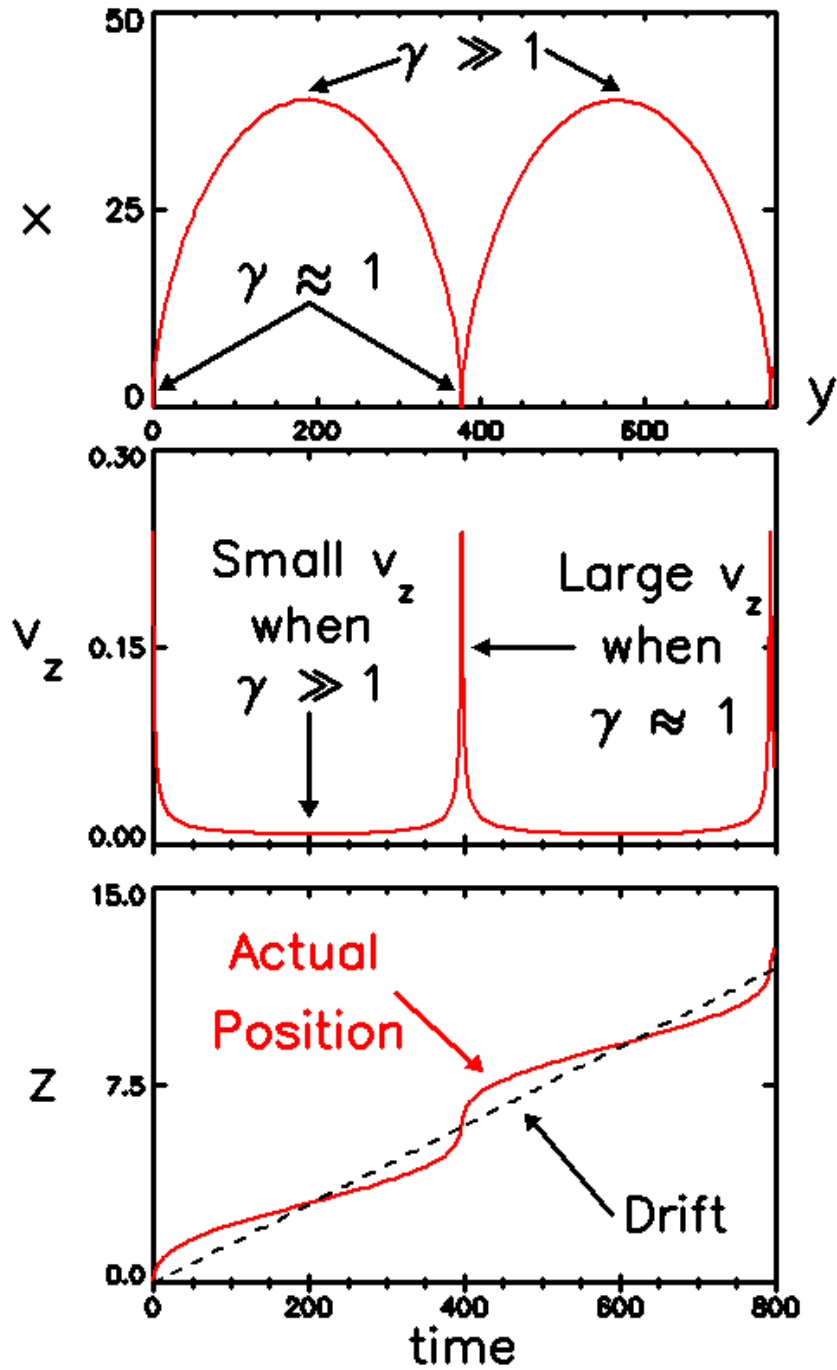


Figure 5.4: The top plot shows the cycloid motion in the  $xy$  plane.  $\gamma$  is large at the top of the cycloid, where the electric field has accelerated the particle to relativistic velocities.  $\gamma$  is approximately one at the bottom of the cycloid where the particle is nearly at rest. The middle plot shows the  $z$  velocity as a function of time. When  $\gamma$  is large,  $v_z$  is small in accordance with Eq. (5.28), but when  $\gamma \approx 1$   $v_z$  is large. The bottom plot shows the effects of this modulated velocity on  $z$  position, drawn with a solid red line. The dashed line is the theoretical drift value predicted by Eq. (5.47); the agreement is perfect.

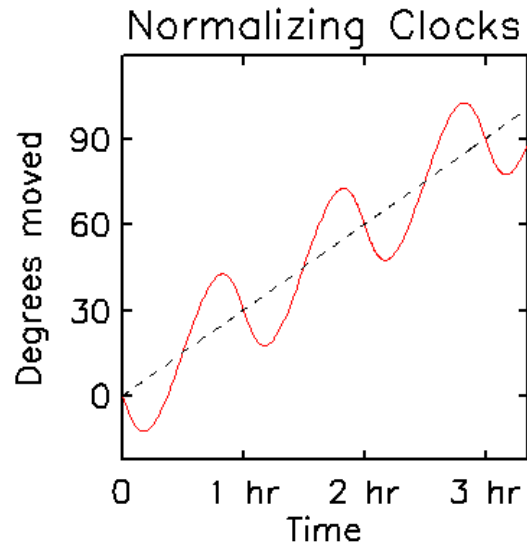


Figure 5.5: A peculiar hour hand with a non-uniform rate is plotted in red; it is analogous to the  $\eta$  motion. Although the hour hand moves at the correct average rate, the dashed black line, representative of the drift  $\Delta\eta/\Delta t$ , is much more convenient for reading time.

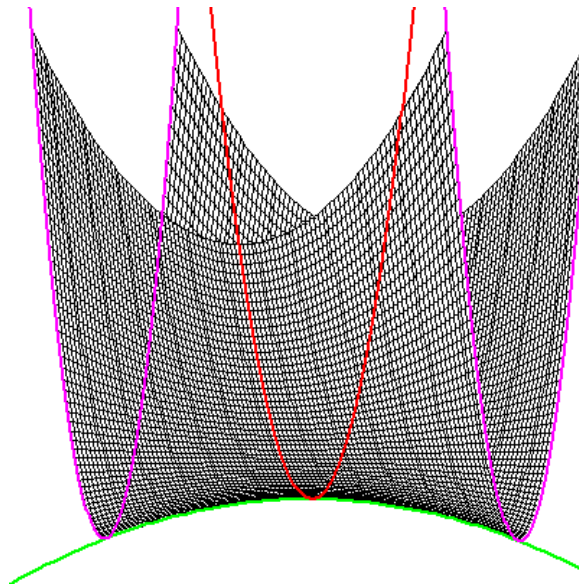


Figure 5.6: A side view of the groove. The green line runs along the spine of the groove which is in the  $y$  direction; you can clearly see that the groove is concave down in this direction. The red parabola is a cross-section of the groove at its apex where the groove is widest. The pink parabolas are cross-sections further down the groove and are steeper and more narrow than the red one.

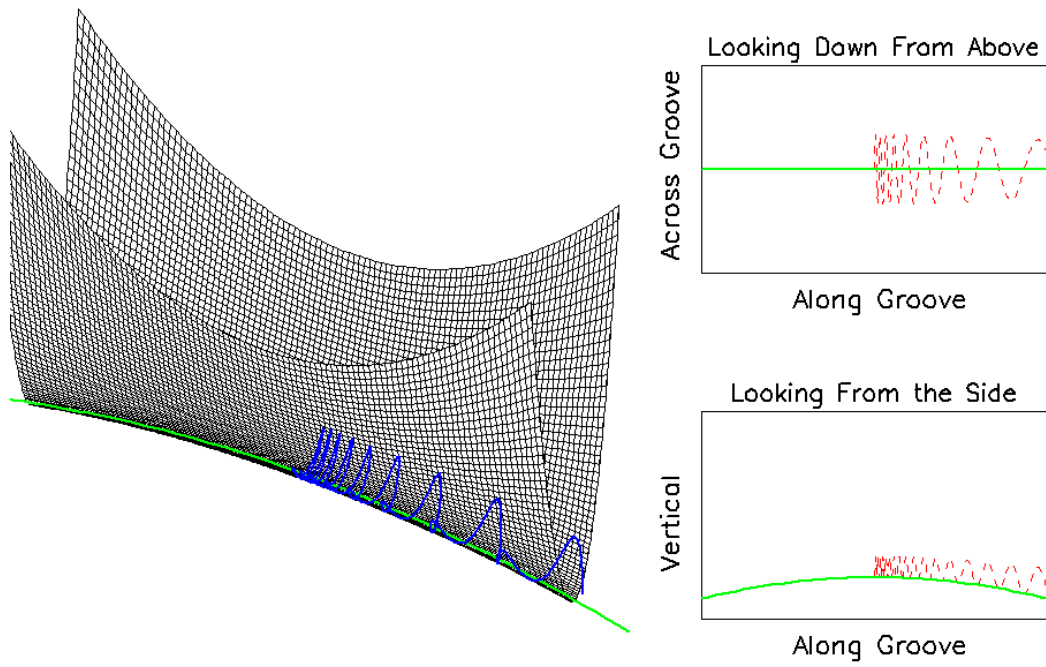


Figure 5.7: Intuition dictates that a particle placed in a saddle-like groove will eventually roll down the groove with increasing velocity. Indeed, this is observed in this numerical simulation.  $y$  the direction along the groove, and  $z$  the vertical direction. The Hamiltonian is given by Eq. (5.80) with  $m = 1$ ,  $\kappa = 1$ ,  $\alpha = 1$  and  $\lambda = -0.01$ , and particle starts at  $x = y = 0$  with  $v_x(0) = 0.1$  and  $v_y(0) = -0.004$ .

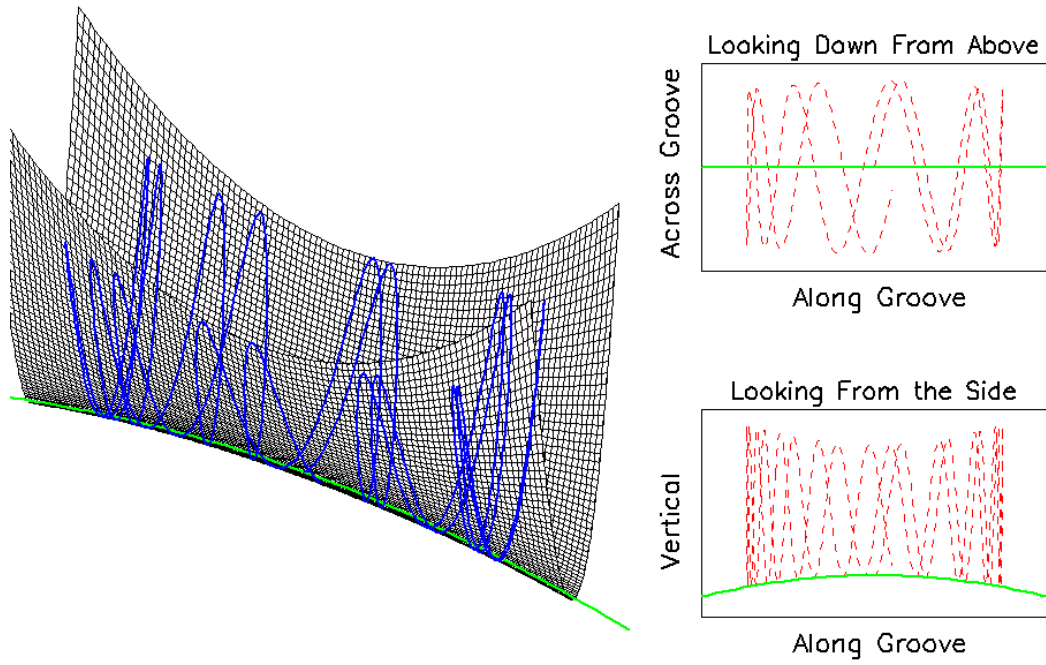


Figure 5.8: With the right initial conditions, a particle in a thin saddle-like groove can undergo oscillatory motion due to the narrowing of the groove.  $x$  is the direction across the groove,  $y$  the direction along the groove, and  $z$  the vertical direction. The Hamiltonian is given by Eq. (5.80) with  $m = 1$ ,  $\kappa = 1$ ,  $\alpha = 1$  and  $\lambda = -0.01$ , and particle starts at  $x = y = 0$  with  $v_x(0) = 0.25$  and  $v_y(0) = -0.1$ .

## Chapter 6

# Plasma Loop Merging and the Two-Wire Problem

Chapter 5 presents a general theorem of Hamiltonian mechanics concerning the role of action integrals in systems with periodic motion. Keeping this formalism in mind, we now attempt to explain the coalescence of the spider legs in the Caltech Spheromak Experiment into a single axisymmetric structure. Recall from Sec. 1.4.2 that Taylor's theory of magnetic relaxation predicts this evolution towards the axisymmetry of the magnetic field boundary conditions. This explanation is macroscopic and based on helicity-conservation arguments; our approach will be microscopic to identify the mechanism behind the transition. We will study the trajectories of particles at the edge of or just outside of a spider leg; the behavior of such particles will be taken as indicative of the evolution of the spider leg boundary. We find that, when multiple plasma loops are present, the trajectories can be divided into two classes: those that are essentially confined to the vicinity of one loop and those that are shared more symmetrically between loops. When time dependence is added to the system, trajectories can transition from one class to the other. Obviously, transitions from confined to symmetric orbits would indicate the onset of loop merging, but such transitions occur only when the induced electric field takes a particular form. The ultimate success of the model in explaining the merging thus depends critically on the actual induced electric field in the experiments, which, in all likelihood, must be determined experimentally. Note that this same analysis also applies to dual-loop merging experiments on the Caltech Solar Loop Experiment.

The electromagnetic fields of the Caltech experiments are quite complex, and we will employ several approximations to make the problem tractable. Both the Spheromak and Solar experiments produce plasma loops arching from anode to cathode. These loops carry time-dependent currents and helical magnetic field lines. On the Spheromak Experiment, the spider legs are more tightly spaced on the inner disk than the outer annulus, while on the Solar Loop Experiment the two loops attract each other. Even establishing the electric and magnetic fields in either experiment is quite a challenge; determining the particle orbits in such fields is even more difficult. We seek model

magnetic and electric fields that capture the essential physics while remaining tractable. To this end, we begin with a modest model: straight plasma loops with no bias (axial) magnetic field. This approximation essentially treats the plasma loops as straight current-carrying wires and ignores the curved geometry and helical nature of the magnetic field lines.

In Sec. 6.1, we begin by analyzing a single wire, for which the particle trajectories all have the same qualitative behavior. We compute the action integral for planar motion and develop approximations for non-planar motion. We broach the difficulties of determining the induced electric field when the wire current changes in time, and we show how the Hamiltonian formalism of Chapter 5 applies to particles trajectories in such time dependent fields. In Sec. 6.2, we add a second wire, parallel to the first, and find a richer set of trajectories that fall into several classes: some are confined to one wire, and some are shared between both wires. When time-dependence is added to the two-wire scenario in Sec. 6.3, the induced electric field can cause transitions of confined orbits to shared orbits, but only if the induced electric field is anti-parallel to the wire current. We discuss the plausibility of such a field and show exactly how it would induce transitions.

## 6.1 Single Wire and $\mathbf{B} \sim \hat{\phi}/r$ Fields

Before attempting to study particle orbits in a system of plasma loops, it is best to first understand orbits about a solitary wire. Such orbits are of the type described in Chapter 5: the particle executes periodic radial motion but increments in the axial and angular coordinates. Fig. 6.1.a depicts planar electron motion about a wire for which there is no angular motion while Fig. 6.1.b depicts electron motion with non-zero angular momentum. We shall first discuss various occurrences of the magnetic field  $\mathbf{B} \sim \hat{\phi}/r$ . The action integral for planar orbits will then be evaluated in closed form, leading to an exact expression for the drift velocity. Approximate results are derived for non-planar orbits. The case of a time-dependent current is then explored, and issues concerning the induced electric field are discussed.

The magnetic field of a straight, infinitely thin wire carrying a current  $I$  is given by Ampere's law:

$$\mathbf{B} = \frac{\mu_0 I}{2\pi r} \hat{\phi}. \quad (6.1)$$

However, this magnetic field is not limited to infinitely thin wires. In general, the magnetic field for any axisymmetric, poloidal current density is  $\mathbf{B}(r) = \mu_0 I(r)/(2\pi r) \hat{\phi}$ , where  $I(r) = \int_0^r 2\pi r' J_z(r') dr'$ , which scales as  $1/r$  wherever  $J_z(r) = 0$ . This includes the vacuum region outside any axisymmetric current channel as well as the interior of a toroidal solenoid. More generally,  $\mathbf{B}$  decays like a  $1/r$  field when  $J_z(r) \ll I(r)/(2\pi r^2)$ , for then

$$\frac{dB_\phi}{dr} = -\frac{\mu_0 I(r)}{2\pi r^2} + \mu_0 J_z(r) \approx -\frac{\mu_0 I(r)}{2\pi r^2}. \quad (6.2)$$

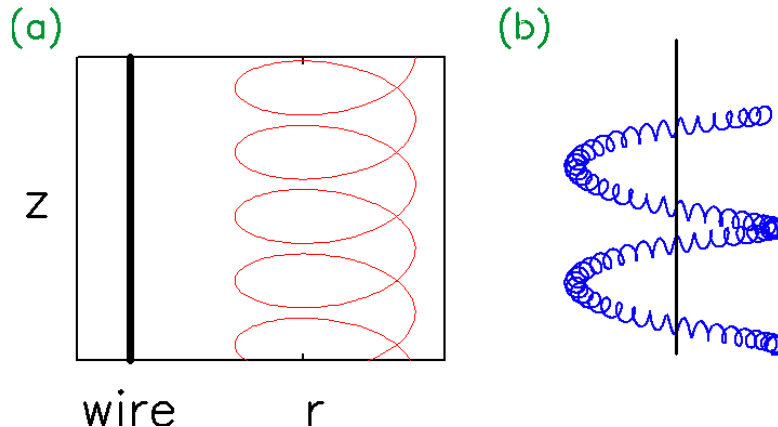


Figure 6.1: (a) An electron executes planar motion in the magnetic field of a current-carrying wire (b) A three-dimensional plot of an electron orbit with non-zero angular momentum.

The term  $\mu_0 I(r)/2\pi r$  of Eq. (6.2) is  $\mu_0/2$  times the average current density up to a radius  $r$ , so the condition  $J_z(r) \ll I(r)/(2\pi r^2)$  requires that the local current density be much smaller than the average current density up to that radius. This condition will most likely be satisfied at the edge of current channels such as those described in Ref. [105]. Thus,  $\mathbf{B} \sim \hat{\phi}/r$  both in the vacuum region outside of a current channel and also at the channel's edge. We also expect the field outside a filamentary but curved current channel to scale as  $\mathbf{B} \sim \hat{\phi}/r$  wherever the distance to the channel is much smaller than the channel's radius of curvature. Clearly, many physical scenarios can have magnetic fields that behave approximately like  $1/r$  fields, and the results presented here may have broad applications.

### 6.1.1 The Action and Drift Velocity for Planar Orbits

We now calculate the action variable  $J$ , the drift velocity, and magnetic flux of planar trajectories around a wire. For any toroidal magnetic field, there exists a class of planar orbits that is confined to a plane containing the wire [106]. This follows from conservation of angular momentum  $P_\phi = mr^2\dot{\phi}$  because planar orbits have  $P_\phi = 0$ , which immediately implies  $\dot{\phi} = 0$ . For such trajectories, we relate results obtained in Chapter 5 for fields  $\mathbf{B} = B_z(x)\hat{z}$  to orbits in toroidal fields  $\mathbf{B} = B_\phi(r)\hat{\phi}$  by making the identifications  $x \leftrightarrow r$ ,  $y \leftrightarrow -z$ , and  $\hat{z} \leftrightarrow \hat{\phi}$ .

We first establish the Hamiltonian and basic orbit properties. We use the vector potential

$$\mathbf{A} = A_z(r)\hat{z} = -\left(\int_R^r B(r')dr'\right)\hat{z} = -\frac{\mu_0 I}{2\pi} \ln \frac{r}{R}\hat{z}, \quad (6.3)$$

where  $R$  is an arbitrary radius that affects  $\mathbf{A}$  only by the addition of a constant. To simplify constants, we introduce the characteristic velocity  $\beta := \mu_0 Ie/2\pi m$  [106]. The canonical momenta

are

$$P_r = m\dot{r}, \quad (6.4)$$

$$P_\phi = mr^2\dot{\phi}, \quad (6.5)$$

$$P_z = m\dot{z} + (-e)A_z(r) = m\dot{z} + m\beta \ln \frac{r}{R}, \quad (6.6)$$

and the Hamiltonian is

$$H = \frac{P_r^2}{2m} + \frac{P_\phi^2}{2mr^2} + \frac{(P_z - m\beta \ln(r/R))^2}{2m}. \quad (6.7)$$

$P_z$ ,  $P_\phi$ , and  $H$  are conserved along trajectories. For planar orbits, we set  $P_\phi = 0$  and use the Hamiltonian

$$H = \frac{P_r^2}{2m} + \frac{(P_z - m\beta \ln(r/R))^2}{2m}. \quad (6.8)$$

Every orbit has two radial turning points where  $v_r = 0$  and a single radius at which  $v_z = 0$ . Denoting the inner turning point by  $r_-$  and the outer one by  $r_+$ , we set  $P_r = 0$  in Eq. (6.8) and solve for  $r$  to obtain

$$r_\pm = R \exp \left[ \frac{P_z \pm \sqrt{2mH}}{m\beta} \right]. \quad (6.9)$$

These turning points allow us to determine whether the guiding center approximation holds true for a particular trajectory. The guiding center approximation requires that the fractional change in the magnetic field be small over the course of a gyration:  $\delta B/B \ll 1$ . The fractional change from the outer turning point to the inner one is

$$\frac{\delta B}{B} = \frac{B(r_-) - B(r_+)}{B(r_+)} = e^{2v/\beta} - 1, \quad (6.10)$$

which gives the simple condition  $v \ll \beta$ . Note that, due to the lack of an inherent length scale associated with the magnetic field, this condition is completely independent of the electron's position. We define the guiding center radius  $r_{\text{gc}}$  in analogy to Eq. (5.90) as the radius at which the axial velocity  $v_z$  vanishes:

$$r_{\text{gc}} = R \exp \left( \frac{P_z}{m\beta} \right). \quad (6.11)$$

For orbits with  $v \ll \beta$ , this radius coincides with the gyrocenter radius [106]. This definition relates  $R$  and  $P_z$ , neither of which is a physical quantity, to a physical location along an orbit.

For planar orbits, the action integral,

$$J(H, P_z) = \oint \sqrt{2mH - \left( P_z - m\beta \ln \frac{r}{R} \right)^2} dr, \quad (6.12)$$

can be evaluated exactly using the substitution

$$\cos \theta = \frac{P_z - m\beta \ln r/R}{\sqrt{2mH}}. \quad (6.13)$$

$\theta$  is simply the angle the velocity vector makes with the  $z$  axis; note that  $\theta = 0$  at  $r_-$ ,  $\theta = \pi/2$  at  $r_{\text{gc}}$ , and  $\theta = \pi$  at  $r_+$ . We can solve Eq. (6.13) for  $r$  as a function of  $\theta$ :

$$r = r_{\text{gc}} \exp \left[ -\frac{v}{\beta} \cos \theta \right]. \quad (6.14)$$

The action variable can be evaluated by observing that  $P_r = mv_r = mv \sin \theta$  and then integrating by parts:

$$J = \oint P_r dr = \oint mv \sin \theta \frac{dr}{d\theta} d\theta = - \oint mv \cos \theta r d\theta. \quad (6.15)$$

Then, using Eq. (6.14) and the integral representation of the modified Bessel function:  $\int_0^\pi e^{x \cos \theta} \cos(n\theta) d\theta = \pi I_n(x)$  [107, Eq 9.6.19], we find that

$$J = 2\pi r_{\text{gc}} m v I_1 \left( \frac{v}{\beta} \right). \quad (6.16)$$

$\Delta t$  and  $\Delta z$  can both be computed by partial differentiation as per Eq. (5.4):

$$\Delta z = -\frac{\partial J}{\partial P_z} = -2\pi \frac{v}{\beta} r_{\text{gc}} I_1 \left( \frac{v}{\beta} \right), \quad (6.17)$$

$$\Delta t = \frac{\partial J}{\partial H} = 2\pi \frac{r_{\text{gc}}}{\beta} I_0 \left( \frac{v}{\beta} \right). \quad (6.18)$$

Note that Eqs. (6.17), (6.18), and (6.16) have a simple dependence on  $r_{\text{gc}}$  that could have been predicted beforehand using only dimensional analysis. This is so because the vacuum magnetic field lacks an inherent length scale. The substitution of Eq. (6.13) was apparently known to Wouters, who derived similar formulae for the betatron half-wavelength in his charge/mass separator [108].

The exact drift velocity, computed without appealing to the guiding center approximation, is

$$\mathbf{v}_d = \frac{\Delta z}{\Delta t} \hat{z} = -v \frac{I_1(v/\beta)}{I_0(v/\beta)} \hat{z}. \quad (6.19)$$

This formula is exact and holds for orbits where the guiding center approximation breaks down. The  $v \ll \beta$  limit of Eq. (6.19) is  $\mathbf{v}_d = -v^2/(2\beta)$ , obtained by the small argument limit of the modified Bessel functions:  $I_n(x) \approx (x/2)^n$  [107, Eq. 9.1.7]. Of course, this agrees with the grad-B drift of the guiding center approximation as discussed in Sec. 5.2.2. The  $v \gg \beta$  limit of Eq. (6.19) is  $\mathbf{v}_d \approx -v\hat{z}$ , obtained by the large argument limit of the modified Bessel functions:  $I_\alpha(x) \approx e^x/\sqrt{2\pi x}$  when  $x \gg |\alpha^2 - 1/4|$  [107, Eq. 9.7.1]. Such electrons drift downward with a drift speed approaching

their full trajectory speed. We draw two conclusions from this. First, all electrons drift downward regardless of their velocity or the wire current, and, similarly, all ions drift upwards. The current driven by the drift flows in the same direction as the original wire current, so the wire current “bootstraps” itself. Secondly, larger currents have larger values of  $\beta$  and hence smaller drift velocities, so the bootstrap effect is actually greatest for small wire currents. Similar observations were made by Alfven on the limit of current channels [109].

### 6.1.2 Non-Planar Orbits

For non-planar orbits, the action integral,

$$J(H, P_z, P_\phi) = \oint \sqrt{2mH - P_\phi^2/r^2 - (P_z - m\beta \ln(r/R))^2} dr, \quad (6.20)$$

cannot be evaluated exactly as in the planar case, but we can perform a Taylor expansion about  $P_\phi = 0$ . This treats the kinetic energy of the angular motion as a perturbation of the planar problem. The first-order expansion is

$$J(J, P_z, P_\phi) \approx J_0(H, P_z) + \frac{1}{2} \oint \frac{(-P_\phi^2/r^2) dr}{\sqrt{2mH - (P_z - m\beta \ln(r/R))^2}}, \quad (6.21)$$

where  $J_0(H, P_z)$  is the planar action integral given by Eq. (6.16). Using the substitution  $u/R = R/r$ , we get

$$J(J, P_z, P_\phi) \approx J_0(H, P_z) + \frac{1}{2} \oint \frac{(P_\phi^2/R^2) du}{\sqrt{2mH - (P_z + m\beta \ln(u/R))^2}}, \quad (6.22)$$

which can then be evaluated with the substitution  $\sqrt{2mH} \cos \theta = P_z + m\beta \ln(u/R)$ ,

$$J(H, P_z, P_\phi) \approx J_0(H, P_z) - \frac{\pi P_\phi^2}{m\beta r_{\text{gc}}} I_0 \left( \frac{\sqrt{2mH}}{m\beta} \right) \quad (6.23)$$

$$= J_0(H, P_z) - \frac{P_\phi^2}{2mr_{\text{gc}}^2} \Delta t_0. \quad (6.24)$$

$\Delta t_0$  is the period for planar motion given by Eq. (6.18). Note that the correction term in Eq. (6.24) contains the kinetic energy of angular motion,  $P_\phi^2/(2mr^2)$ , evaluated at  $r = r_{\text{gc}}$ . Indeed, Eq. (6.24) could have been derived from Eq. (6.21) by approximating  $P_\phi^2/r^2$  as  $P_\phi^2/r_{\text{gc}}^2$  and then evaluating the resulting integral:

$$\frac{1}{2} \oint \frac{(-P_\phi^2/r_{\text{gc}}^2) dr}{\sqrt{2mH - (P_z - m\beta \ln(r/R))^2}} = -\frac{P_\phi^2}{2mr_{\text{gc}}^2} \oint \frac{dr}{\dot{r}_0} = -\frac{P_\phi^2}{2mr_{\text{gc}}^2} \Delta t_0, \quad (6.25)$$

where  $\dot{r}_0$  is the unperturbed radial velocity. We can think of Eq. (6.21) as an averaging of the perturbation over an unperturbed orbit, in which case Eq. (D.22) could be used to obtain an even

more accurate estimate of  $J$ .

The  $P_\phi$  term in Eq. (6.24) provides the first-order correction to all quantities derived from  $J$  due to angular motion. For instance, in the  $v \ll \beta$  limit, the drift velocity agrees with the guiding center approximation once the curvature drift is added to the dominant grad-B drift.

### 6.1.3 Time-Varying Currents

In preparation for the time-dependent two-wire problem, we consider particle motion in a time-varying  $1/r$  magnetic field. The primary difficulty in this case is actually not the particle orbits themselves but rather determining the appropriate electric field to use. It is well-known that a time-varying magnetic field induces an electric field, but Faraday's law,  $\nabla \times \mathbf{E} = -\partial_t \mathbf{B}$ , only specifies the curl of  $\mathbf{E}$ , leaving  $\mathbf{E}$  undetermined up to the addition of the gradient of a scalar. In the single-wire case, we can write  $\mathbf{E}$  in terms of the potentials

$$\mathbf{E} = -\frac{\partial \mathbf{A}}{\partial t} - \nabla V = \frac{\mu_0 \dot{I}}{2\pi} \ln \frac{r}{R} \hat{z} - \nabla V, \quad (6.26)$$

using the vector potential of Eq. (6.3). We cannot proceed, however, because we have no prescription for determining  $V$ : there are no boundary conditions for  $\mathbf{E}$  due to the infinite extent of the wire, its infinite thinness, and its lack of return current. In order to determine the electric field, these details, which could be ignored in the static case, must be specified [110, 111]; a solitary infinite wire carrying a time-dependent current is an ill-posed problem. In this section, we present two return currents for the wire and their possible relevance to the Caltech experiments.

Consider the configuration shown in Fig. 6.2.a, where the wire current is fed by two large planar disks; this configuration is similar to a toroidal solenoid. We also assume that the wire has a non-zero radius  $r = a$ . If all surfaces are perfectly conducting, then the tangential component of the electric field must vanish on the surface. The appropriate electric field is obtained from Eq. (6.26) by setting  $V = 0$  and  $R = a$ :

$$\mathbf{E} = \frac{\mu_0 \dot{I}}{2\pi} \ln \frac{r}{a} \hat{z}. \quad (6.27)$$

$\mathbf{E}$  then satisfies the boundary conditions at the plates because it is axial, and it satisfies the boundary condition on the wire surface because it vanishes at  $r = a$ . This electric field is aligned with the wire current, and the associated Poynting flux is radially inward, suggesting that the source of energy for the circuit is located at  $r = \infty$ .

Now consider the configuration shown in Fig. 6.2.b where the current returns coaxially at radius  $r = b$ . For perfectly conducting surfaces, the axial electric field must vanish at both  $r = a$  and  $r = b$ .

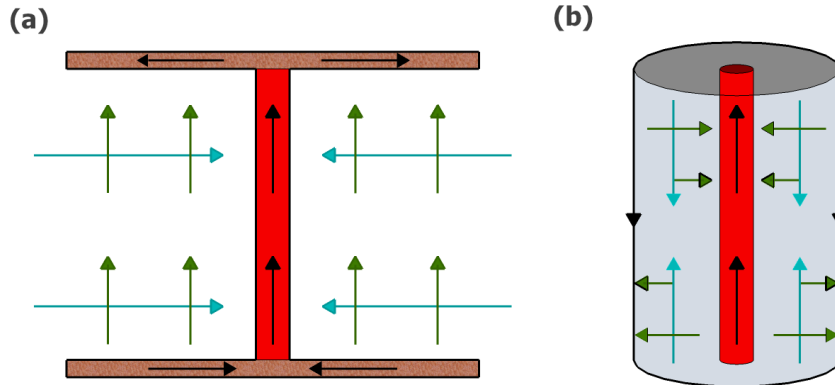


Figure 6.2: Two different possible returns for a wire: (a) two planar plates radially feed the wire and (b) a coaxial return. The direction of current flow is drawn in black, the electric field is drawn in green, and the Poynting vector is drawn in blue.

Evaluating Eq. (6.26) on these surfaces implies

$$E_z(r = a) = 0 \quad \rightarrow \quad \left. \frac{\partial V}{\partial z} \right|_{r=a} = \frac{\mu_0 \dot{I}}{2\pi} \ln \frac{a}{R}, \quad (6.28)$$

$$E_z(r = b) = 0 \quad \rightarrow \quad \left. \frac{\partial V}{\partial z} \right|_{r=b} = \frac{\mu_0 \dot{I}}{2\pi} \ln \frac{b}{R}, \quad (6.29)$$

$V$  must also satisfy Laplace's equation because  $\mathbf{E}$  satisfies Poisson's equation:  $\nabla \cdot \mathbf{E} = 0$ . For azimuthal symmetry,  $\nabla^2 V = 0$  has solutions of the form  $V \sim z \ln r$ . Matching the boundary condition, we have

$$V = \frac{\mu_0 \dot{I}(t)}{2\pi} z \ln \frac{r}{R}. \quad (6.30)$$

The axial component of the electric field vanishes, leaving a radial electric field,

$$\mathbf{E} = -\frac{\mu_0 \dot{I}(t)}{2\pi} \frac{z}{r} \hat{r}, \quad (6.31)$$

which is independent of  $R$  and the radii of the cable. Note that  $V$  breaks the axial symmetry of the configuration, and in particular there is a  $z$  position at which  $\mathbf{E}$  vanishes. This location might be physically set by placing an electrical short between the inner and outer conductors. A zero in the radial (normal) electric field is also seen in the electrostatic field of a circuit, and the location of the zero depends on the circuit geometry [112]. Also note that the Poynting vector directs energy axially towards the zero of the electric field.

Neither the fields in Eq. (6.27) nor Eq. (6.31) are entirely accurate. Both fields are unbounded and rise to arbitrarily high values. Also, neither field truly satisfies Ampere's law because the displacement current  $\epsilon_0 \partial_t \mathbf{E}$  does not vanish. However, if we work in the limit of adiabatic slowness, then the displacement current, which is proportional to  $\dot{I}$  in both cases, can be ignored. For com-

pleteness, we note that the fields that fully satisfy Ampere’s and Faraday’s law are TEM modes; the electric field in Eqs. (6.27) and (6.31) are approximately equal to the sum of an ingoing wave and a reflected wave, the waves traveling radially and axially, respectively, and being reflected at  $r = a$  and  $z = 0$ , respectively.

Which of these two field configurations most closely resembles the actual fields in the Caltech experiments is an open question. On the one hand, the plates that radially feed the wire in Fig. 6.2.a resemble the plasma electrodes on which each flux tube starts and ends. The boundary conditions imposed by these plates cannot be satisfied by the radial electric field in Eq. (6.31), and, from this argument, the field is likely to resemble the axial field of Eq. (6.27) bent into a curved geometry as depicted in Fig. 6.3. On the other hand, plasmas are liable to form thin sheaths at all the boundaries, and the electric field in the sheath is likely to be normal to the surface. In this case, the plasma might have a field structure shown in Fig. 6.4. Given the possible existence of sheaths, it is unlikely that the correct electric field can be easily derived from first principles, and in all likelihood an experimental measurement will be needed to determine the actual field.

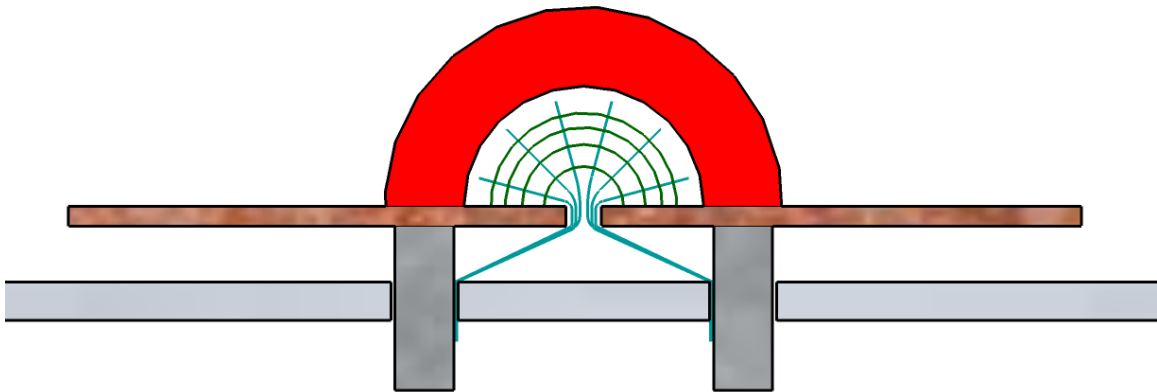


Figure 6.3: The Solar Loop Experiment might have an induced electric field that is “axial,” as shown here by the green lines. The electric field begins and ends on the electrodes. The associated Poynting flux, shown by the blue lines, transports energy radially through the gap in the electrodes.

The induced electric field thus depends on the particulars of the setup, but we can still establish a reduced Hamiltonian for particle orbits and derive general properties without going into the full details. We leaving  $V$  arbitrary except for two requirements: that  $V$  is proportional to  $\dot{I}$  and hence vanishes when the current is static, and that the current changes very slowly so that terms involving  $\ddot{I}$  and  $\dot{I}^2$  can be ignored. The exact Hamiltonian for particle motion is

$$H = \frac{P_r^2}{2m} + \frac{(P_z - m\beta(t)\ln(r/R))^2}{2m} - eV(r, z, t), \quad (6.32)$$

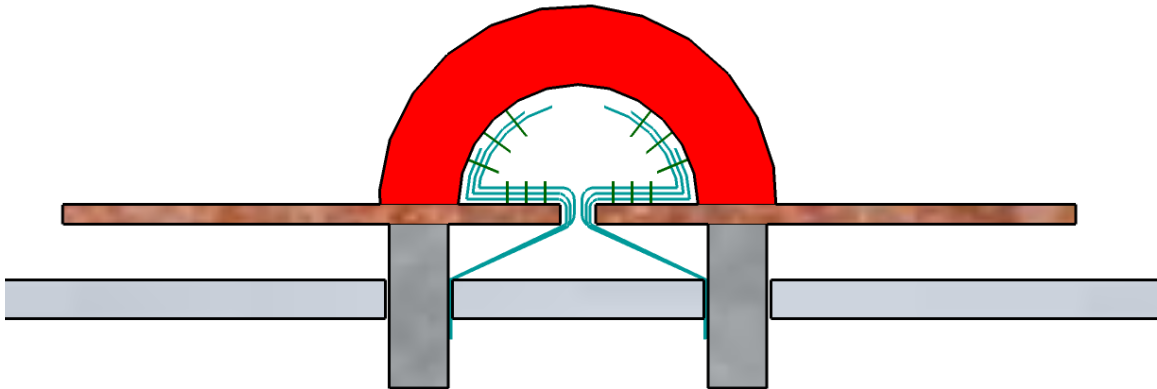


Figure 6.4: Alternatively, the Solar Loop Experiment might have an induced electric field that is “radial,” as shown here by the green lines. The electric field lines are normal to the plasma surface. The associated Poynting flux transports energy axially along the flux tube.

The Hamiltonian now contains explicit time and  $z$  dependence, so  $H$  and  $P_z$  are no longer conserved quantities but instead evolve as

$$\dot{H} = \frac{\partial H}{\partial t} = \frac{P_z - m\beta \ln(r/R)}{m} \left( -m\dot{\beta} \ln \frac{r}{R} \right) - e \frac{\partial V}{\partial t} \quad (6.33)$$

$$\approx -m\dot{\beta} \dot{z} \ln \frac{r}{R} \quad (6.34)$$

$$\dot{P}_z = -\frac{\partial H}{\partial z} = -e \frac{\partial V}{\partial z}. \quad (6.35)$$

The term  $\partial_t V$  in Eq. (6.33) is dropped because it is proportional to  $\ddot{I}$ . These equations give the instantaneous evolution of  $H$  and  $P_z$  and fluctuate over the course of a gyro-orbit. In Chapter 5, we developed a formalism to obtain the orbit-averaged equations of motion. Using Eq. (5.137) with  $J_0$  being the action given by Eq. (6.16) for the static magnetic field:

$$J(H, P_z) \approx J_0 \left( H - qV(r_{gc}, z, t) + \frac{m}{2} \left( \frac{\partial_r V}{B_z} \right)^2, P_z + m \frac{\partial_r V}{B_z}; \beta(t) \right) \quad (6.36)$$

$$\approx J_0 \left( H + eV(r_{gc}, z, t), P_z + e \frac{r}{\beta} \partial_r V; \beta(t) \right). \quad (6.37)$$

The term  $(m/2) (\partial_r V/B_z)^2$  is dropped because it was proportional to  $\dot{I}^2$ . Also, we have explicitly written the  $\beta$  dependence of  $J_0$  because it will be needed below. We use Eq. (6.37) to compute the average evolution  $\Delta H/\Delta t$  and  $\Delta P_z/\Delta t$ . We can compute  $\Delta P_z$  and hence  $\Delta P_z/\Delta t$  from Eq. (5.4):

$$\Delta P_z = \frac{\partial J}{\partial z} = \frac{\partial J_0}{\partial H} \left( e \frac{\partial V}{\partial z} \right) + \frac{\partial J_0}{\partial P_z} \left( e \frac{r}{\beta} \frac{\partial^2 V}{\partial r \partial z} \right) = \Delta t \left( e \frac{\partial V}{\partial z} \right) - \Delta z_0 \left( e \frac{r}{\beta} \frac{\partial^2 V}{\partial r \partial z} \right), \quad (6.38)$$

$$\frac{\Delta P_z}{\Delta t} = \left(1 + \frac{r}{\beta} \frac{\Delta z_0}{\Delta t} \frac{\partial}{\partial r}\right) \left(e \frac{\partial}{\partial z}\right) V. \quad (6.39)$$

This is the average evolution of  $P_z$ , which is related to the instantaneous evolution in Eq. (6.35) by the averaging formula Eq. (D.22).

We can also work out the change in energy  $\Delta H$  over one period of motion. We briefly return to the general Hamiltonian theory of Chapter 5 and assume that the Hamiltonian contains explicit time dependence,  $H = H(\xi, P_\xi, \eta, P_\eta; t)$ , but that adiabatic invariance of  $J$  is maintained. Then the action integral  $J$  contains explicit time-dependence, and

$$\frac{\partial J}{\partial t} = \oint \frac{\partial P_\xi}{\partial t} d\xi = \oint -\frac{\partial H/\partial t}{\partial H/\partial P_\xi} d\xi = -\oint \frac{\dot{H}}{\xi} d\xi \quad (6.40)$$

$$= -\oint \dot{H} dt = -\Delta H. \quad (6.41)$$

We have made use of the fact that the total time derivative of  $H$  along a trajectory is equal to its partial time derivative. Applying this theorem to Eq. (6.37),

$$\Delta H = -\frac{\partial J}{\partial t} = -\frac{\partial J_0}{\partial H} \left(e \frac{\partial V}{\partial t}\right) - \frac{\partial J_0}{\partial P_z} \left(e \frac{r}{\beta} \frac{\partial^2 V}{\partial r \partial t}\right) - \frac{\partial J_0}{\partial t} \approx -\frac{\partial J_0}{\partial t} = -\dot{\beta} \frac{\partial J_0}{\partial \beta}, \quad (6.42)$$

since all other terms are proportional to  $\dot{\beta}$ . The relationship between  $\Delta H$  and  $\dot{H}$  may not be apparent, but integrating Eq. (6.34) with respect to time over one period of unperturbed motion gives

$$\Delta H = \oint -m\dot{\beta} \dot{z} \ln \frac{r}{R} dt = -m\dot{\beta} \oint \ln \frac{r}{R} dz = -\frac{2\pi m\dot{\beta}}{\mu_0 I} \oint \mathbf{A} \cdot d\mathbf{r}. \quad (6.43)$$

As discussed in Sec. 5.1.8, we can pull  $\dot{\beta}$  and  $I(t)$  out of the integral sign because we can effectively hold these quantities constant over the course of a single period. Applying Eq. (5.160) with  $V = 0$ <sup>1</sup> to Eq. (6.43) and obtain

$$\Delta H = -q \frac{\dot{\beta}}{\beta} \frac{\partial J_0}{\partial q} = -\dot{\beta} \frac{\partial J_0}{\partial \beta}, \quad (6.44)$$

where the last step follows because  $q$  only appears the expression for  $J_0$  in Eq. (6.16) through  $\beta$ .

We could further pursue the nature of particle orbits in these time-dependent fields, but this is not a fruitful task. The lessons that should be taken from this section are that time-dependent currents induce electric fields that can be difficult to compute and that require the global circuit geometry to be specified. Furthermore, the electric field might break some of the symmetries present in the static problem, causing previously conserved momenta to gradually evolve in time.

<sup>1</sup>We set  $V = 0$  here because we are integrating Eq. (6.34) over an unperturbed trajectory.

## 6.2 The Two-Wire Problem

The previous section described particle orbits around a single solitary wire. We now turn our attention to trajectories in the magnetic field generated by two parallel wires carrying equal currents. Planar orbits still exist in the plane containing both wires, but now these planar orbits fall into several distinct classes. Some of these orbits are localized to one wire and resemble the orbits observed in the previous section for a single wire. Other orbits, however, are shared symmetrically between the two wires. This distinction between confined and symmetric orbits is exactly what is needed to describe the merging of two parallel plasma loops.

We will work in Cartesian coordinates with the  $z$  axis aligned with the wires and  $x$  being the direction separating the wires. Let the wires be located at  $x = \pm a/2$  so that the wire separation distance is  $a$ . The magnetic field in the plane containing the wires is

$$\mathbf{B} = \frac{\mu_0 I}{2\pi} \left[ \frac{1}{a/2 + x} - \frac{1}{a/2 - x} \right] \hat{y} = \frac{\mu_0 I}{2\pi} \frac{-2x}{a^2/4 - x^2} \hat{y}. \quad (6.45)$$

We note that there is a magnetic null at  $x = 0$  where the field vanishes; this null will play an important role in the classification of orbits. The vector potential can be chosen such that

$$\mathbf{A} = -\frac{\mu_0 I}{2\pi} \left[ \ln \frac{a/2 + x}{R} + \ln \frac{a/2 - x}{R} \right] \hat{z} = -\frac{\mu_0 I}{2\pi} \ln \frac{a^2/4 - x^2}{R^2} \hat{z}, \quad (6.46)$$

where  $R$  is again arbitrary. The canonical  $z$  momentum for an electron of charge  $q = -e$  is

$$P_z = mv_z + m\beta \ln \frac{a^2/4 - x^2}{R^2}, \quad (6.47)$$

and is conserved, yielding  $v_z$  as a function of  $x$ :

$$v_z(x) = \frac{1}{m} \left[ P_z - m\beta \ln \frac{a^2/4 - x^2}{R^2} \right]. \quad (6.48)$$

We will work with scaled variables, scaling distance by  $a/2$ , velocity by  $\beta$ , and momentum by  $m\beta$ . Since  $R$  is arbitrary, we set it equal to  $a/2$  so that it is scaled to unity. Then, in scaled variables, Eq. (6.47) becomes

$$P_z = v_z + \ln(1 - x^2). \quad (6.49)$$

From Eq. (6.49), we can derive the existence and location of turning points where the  $x$  motion reverses. These turning points exist because the magnitude of the  $z$  velocity  $v_z$  can never exceed the magnitude  $v$  of the total velocity, so the locations where Eq. (6.49) predicts  $|v_z| = v$  denote turning points. We can find these turning points by setting  $v_z$  in Eq. (6.49) equal to either  $\pm v$  and solving

for  $x$ :

$$x = \pm\sqrt{1 - e^{P_z \pm v}}. \quad (6.50)$$

The choice of  $+$  and  $-$  is independent between the two  $\pm$  signs, so up to four turning points exist for any given orbit. These turning points come in mirrored pairs about the magnetic null  $x = 0$ . We shall show that one of these pairs exists for all orbits, while the second pair only exists if certain conditions are met.

When  $P_z + v < 1$ , all four turning points exist, and the orbit resembles those of a single wire. One set of turning points, which we denote by  $x_+$ , is given by choosing the  $+$  sign in the exponential of Eq. (6.50):

$$x_+ = \pm\sqrt{1 - e^{P_z + v}}. \quad (6.51)$$

Since  $P_z + v < 0$  by assumption, we have  $\exp(P_z + v) < 1$ , and the argument of the radical in Eq. (6.51) is positive. The second set of turning points, which we denote by  $x_-$ , is given by choosing the  $-$  sign in the exponential in Eq. (6.50),

$$x_- = \pm\sqrt{1 - e^{P_z - v}}. \quad (6.52)$$

The argument of the radical in Eq. (6.52) is also positive, because  $P_z - v < P_z + v$ , so

$$1 - \exp(P_z - v) > 1 - \exp(P_z + v) > 0. \quad (6.53)$$

This argument also establishes that  $|x_-| > |x_+|$ , so the turning points  $\pm x_+$  lie between the turning points  $\pm x_-$ . In such orbits, the particles rattle back and forth between an inner and outer turning point and never crosses the magnetic null at  $x = 0$ . Such a particle is thus “trapped” in one half of the plane and is “confined” to one of the two wires. These orbits resemble the orbits seen in Sec. 6.1, and an example of such an orbit is plotted in Figs. 6.5.a and 6.5.b.

When  $P_z + v > 0$ , the inner turning points  $\pm x_+$  given by Eq. (6.51) fail to exist, and the particle is instead confined by the two outer turning points  $\pm x_-$  given by Eq. (6.52). This constitutes a new class of trajectories not seen in the single wire case. The non-existence of the inner turning points  $x_+$  follows simply by noting that the argument of the radical in Eq. (6.51) is negative because  $P_z + v > 0$ . The two outer turning points are still defined; to see this, we prove that  $P_z - v < 0$  for any orbit using Eq. (6.49),

$$P_z - v > P_z - v_z(x) = \ln(1 - x^2) < 0. \quad (6.54)$$

In physical terms, the outer turning points always exist because the magnetic field becomes infinitely

strong at the wires<sup>2</sup>, so all orbits are deflected from the wires. The inner turning points, however, are not always defined because some particles reach the magnetic null at  $x = 0$ . As the particle crosses the null, the sign of field reverses, reversing the radius of curvature of the trajectory as well. The particle then moves back and forth between the two outer turning points; such an orbit is symmetric between the two wires and is not confined to a single flux tube; compare Figs. 6.5.b and 6.5.c.

We can further classify symmetric orbits based on the direction of their drifts. Figures. 6.5.c through 6.5.f show several examples of symmetric orbits; some orbits, such as that shown in Fig. 6.5.c, have the same drift direction as in the single wire case, but other orbits, such as that shown in Figs. 6.5.e and 6.5.f, have the opposite drift. To derive this distinction, we first solve for the  $x$  positions where  $v_z(x) = 0$ :

$$x = \pm \sqrt{1 - e^{P_z}}. \quad (6.55)$$

These  $x$  positions are not defined when  $P_z > 0$ . For such cases,  $v_z$  is never zero but rather always positive. The particle never turns around in the  $z$  direction; it bounces back and forth between the two turning points while snaking its way up the  $z$  axis as shown in Fig. 6.5.f. This drift is in the opposite direction as the drift of a particle around a single wire. If, however,  $P_z < 1$ , then the particle has  $v_z < 0$  for part of its orbit. Such particles can drift in either the positive or negative  $z$  direction, as demonstrated by Fig. 6.5.c and 6.5.e. There is a special class of orbits that have no net movement in the  $z$  direction but rather make figure-eight motion; an example is shown in Fig. 6.5.d.

The distinction between confined and symmetric orbits can be explained using effective potentials [2, sec. 119]. The Hamiltonian for a planar orbits between two wires is, for an electron of charge  $q = -e$

$$H = \frac{P_x^2}{2m} + \frac{(P_z^2 + eA_z(x))^2}{2m}. \quad (6.56)$$

This is a two-dimensional Hamiltonian system, but, because  $z$  is ignorable, we can instead view it as a one-dimensional system in  $x$  with a parameter  $P_z$ . In this one-dimensional system, the particle is confined in an effective potential

$$U_{\text{eff}} = \frac{1}{2m} \left( P_z - m\beta \ln \frac{a^2/4 - x^2}{R^2} \right)^2, \quad (6.57)$$

where Eq. (6.46) has been used. We can express this effective potential in terms of scaled coordinates, with scaled energy as  $\bar{U} = U/(m\beta^2)$ ,

$$\bar{U}_{\text{eff}} = (P_z - \ln(1 - x^2))^2 \quad (6.58)$$

The shape of this potential is determined by the value of  $P_z$ . Fig. 6.6.a plots  $U_{\text{eff}}$  when  $P_z > 0$ ; in this case the potential well is always concave up, and the magnetic null at  $x = 0$  is a minimum of the

<sup>2</sup>If the wires were not infinitely thin, this would not be the case, and orbits could also pass into the wire.

potential. Fig. 6.6.b, however, plots  $U_{\text{eff}}$  when  $P_z < 0$ . The potential well develops a central bump, and the null is now a local maximum. It is also clear that particles of low energy will be confined to one of the smaller side wells, whereas particles of sufficient energy will travel over the null and will not be confined to either side well.

In summary, we have five types of motion:

- Snaking motion, shown in Fig. 6.5.f, where the orbit always moves in the positive  $z$  direction and bounces back and forth symmetrically between the two wires
- Jigsaw motion, shown in Fig. 6.5.e, in which the orbit still bounces symmetrically between the wires and has a positive drift but also travels in the negative  $z$  direction for certain periods of time
- Closed figure-eight orbits, shown in Fig. 6.5.d where the electron has no net  $z$  motion
- Loopy motion, shown in Fig. 6.5.c, in which the orbit is symmetrical but has a negative  $z$  drift
- Confined motion, shown in Fig. 6.5.a and 6.5.b, where the orbit never crosses the magnetic null at  $x = 0$  and drifts downward as in the single-wire case

These results are also summarized in a parameter space plot in Fig. 6.7. To make the plot more intuitive, we express  $P_z$  in terms of  $x_-$  via Eq. (6.52). For instance, the condition  $P_z + v < 0$  can be recast as  $v < -(1/2) \ln(1 - x_-^2) < 0$ , and the condition  $P_z > 0$  can be recast as  $v < -\ln(1 - x_-^2)$ . Also plotted in Fig. 6.7 are several isolated points where the conditions for a closed orbit have been calculated numerically.

## 6.3 Time Dependence and Orbit Transitions

The previous section established distinct classes of orbits in the plane between two parallel current-carrying wires. However, in this static system, orbits cannot transition between the different classes. We therefore seek a mechanism that causes orbits confined to one-half of the plane to drift inward towards the magnetic null where they can transition to symmetric orbits. An axial electric field induced by two plasma loops attracting one another provides exactly such a mechanism.

### 6.3.1 Axial Electric Fields

Trajectories will be drawn to the magnetic null line if an axial electric field points in the negative  $z$  direction anti-parallel to the current because the  $\mathbf{E} \times \mathbf{B}$  drift will be inward towards  $x = 0$ . This scenario is similar to Speiser's current sheet [113] where an electric field anti-parallel to the current causes particle to drift towards the null sheet where they are then accelerated by the electric field

along the null sheet. In order to achieve such a transition, we must have an electric field that is (i) axial and (ii) pointing in the negative  $z$  direction anti-parallel to the wire current.

In Sec. 6.1.3, we discussed possible electric fields associated with a single wire carrying a time-dependent current. In particular, we considered two configurations, shown in Fig. 6.2, for which the induced electric fields are entirely different, as shown by comparing Eqs. (6.27) and (6.31). An argument was made for the axial field, Eq. (6.27), based on the fact that the radial component must vanish at the electrodes, which cannot be satisfied by the radial electric field in Eq. (6.31). Also, as we shall see below, there must be an axial component to the electric field when the wires attract and move towards each other, so a purely radial electric field is not possible. However, the actual experiment has curved, finite geometry, as suggested by Figs. 6.3 and 6.4, and also probably involves sheaths, which makes determining the actual field configuration very difficult. We will proceed using an axial electric field but acknowledge that the actual field may be different.

Even if  $\mathbf{E}$  is assumed to be axial, relative motion between the wires is necessary for  $\mathbf{E}$  to be anti-parallel. To see this, assume that  $\mathbf{E}$  is axial and that the current  $I(t)$  is increasing but that the wires are stationary; we shall show that the induced electric field is *parallel* to the current and draws particles *away* from the magnetic null. For a current profile  $I(t)$ , we have, from the vector potential Eq. (6.46),

$$\mathbf{E} = -\frac{\partial \mathbf{A}}{\partial t} = \frac{\mu_0 \dot{I}}{2\pi} \ln \frac{a^2/4 - x^2}{R^2} \hat{z}. \quad (6.59)$$

$\rho$  must be selected so that  $\mathbf{E}$  satisfies the boundary condition at the plasma surface. If the plasma has radius  $\rho$ , then the boundaries of the loops are  $x = \pm(-a/2 + \rho)$ ; see Fig. 6.8. If  $\mathbf{E}$  is to vanish at these locations, then we must set  $R = a^2/4 - (a/2 - \rho)^2$ . Then

$$\mathbf{E} = \frac{\mu_0 \dot{I}}{2\pi} \ln \frac{a^2/4 - x^2}{a^2/4 - (a/2 - \rho)^2} \hat{z}, \quad (6.60)$$

and  $\mathbf{E}$  points in the positive  $z$  direction everywhere. An increasing plasma current cannot explain the merging of the two loops; if anything, the increase in current would cause the orbits to constrict radially.

One can have an anti-parallel electric field if the inner boundaries of the plasma loops move towards each other; that is, if  $\rho$  increases or  $a$  decreases in Fig. 6.8. This is certainly the case in the Solar Loop Experiment, where the plasma loops attract. This is also true on the Spheromak side for plasma moving towards the cathode because the loops are more tightly spaced there. We assume that the plasma loops are perfectly conducting so that the electric field *in the co-moving frame of the loop edge* must vanish. Since this surface is moving due to the loops' attraction, the electric field in the lab frame is not zero but is related to the field in the co-moving frame by  $\mathbf{E}' = \mathbf{E} + \mathbf{v} \times \mathbf{B} = 0$ , where  $\mathbf{E}'$  denotes the electric field in the moving boundary's frame. Since  $\mathbf{E}' = 0$  by assumption, the lab frame electric field at the boundary is  $\mathbf{E} = -\mathbf{v} \times \mathbf{B}$ . The boundary located at  $x = -a/2 + \rho$

has a velocity of  $\mathbf{v} = (-\dot{a}/2 + \dot{\rho})\hat{x}$ ; using this  $\mathbf{v}$  and the magnetic field of Eq. (6.45) gives  $\mathbf{E}$  at the boundary

$$\mathbf{E} = -\mathbf{v} \times \mathbf{B} = -[(-\dot{a}/2 + \dot{\rho})\hat{x}] \times \left[ \frac{\mu_0 I}{2\pi} \frac{-2(-a/2 + \rho)}{a^2/4 - (-a/2 + \rho)^2} \hat{y} \right] \quad (6.61)$$

$$= -(-\dot{a}/2 + \dot{\rho}) \frac{\mu_0 I}{2\pi} \frac{2(a/2 - \rho)}{\rho(a - \rho)} \hat{z}. \quad (6.62)$$

This electric field is anti-parallel to the current and induces drifts towards the magnetic null.

### 6.3.2 Computing the Field

To continue, we assume that the electric field is entirely axial and has the boundary condition given by Eq. (6.62). We then use Faraday's law to compute  $\mathbf{E}$  everywhere in the plane. Using the magnetic field in Eq. (6.45) and an axial electric field, we have

$$\nabla \times \mathbf{E} = -\frac{\partial E_z}{\partial x} \hat{y} = -\frac{\partial \mathbf{B}}{\partial t} = \left[ \frac{\mu_0 \dot{I}}{2\pi} \ln \frac{2x}{a^2/4 - x^2} - \frac{\mu_0 I}{2\pi} \frac{2x}{(a^2/4 - x^2)^2} \frac{a\dot{a}}{2} \right] \hat{y}. \quad (6.63)$$

Performing the  $x$  integral,

$$E_z = \frac{\mu_0 \dot{I}}{2\pi} \ln(a^2/4 - x^2) + \dot{a} \frac{\mu_0 I}{2\pi} \frac{a/2}{a^2/4 - x^2} + C, \quad (6.64)$$

where  $C$  is a constant of integration that must be determined by the boundary conditions. Indeed, the value of  $C$  will determine the ultimate polarity of  $E_z$  and hence the direction of the  $\mathbf{E} \times \mathbf{B}$  drift! Evaluating Eq. (6.64) at  $x = -a/2 + \rho$  and setting it equal to Eq. (6.62) determines  $C$ :

$$\frac{\mu_0 \dot{I}}{2\pi} \ln(\rho(a - \rho)) + \dot{a} \frac{\mu_0 I}{2\pi} \frac{a/2}{\rho(a - \rho)} + C = -(-\dot{a}/2 + \dot{\rho}) \frac{\mu_0 I}{2\pi} \frac{2(a/2 - \rho)}{\rho(a - \rho)}. \quad (6.65)$$

Solving for  $C$  and substituting into Eq. (6.64) gives

$$E_z = \frac{\mu_0 \dot{I}}{2\pi} \ln \frac{a^2/4 - x^2}{\rho(a - \rho)} + \dot{a} \frac{\mu_0 I}{2\pi} \left( \frac{a/2}{a^2/4 - x^2} - \frac{1}{a - \rho} \right) - \dot{\rho} \frac{\mu_0 I}{2\pi} \frac{2(a/2 - \rho)}{\rho(a - \rho)}, \quad (6.66)$$

the induced electric field between two wires when the current, wire separation, and wire radius change in time.

The ultimate polarity of the electric field cannot be determined until the three quantities  $\dot{I}$ ,  $\dot{a}$ , and  $\dot{\rho}$  are specified. We can see that the  $\dot{I}$  term of Eq. (6.66) is positive when  $\dot{I}$  is positive, but the  $\dot{a}$  and  $\dot{\rho}$  terms can make the induced electric field negative. Unfortunately,  $a$  and  $r$  are not easily determined to great accuracy. For the purposes of this analytic study, however, we shall assume

that each of these three quantities changes self-similarly on the same time scale. That is,

$$\dot{I} = \frac{I}{\tau} \quad \dot{a} = -\frac{a}{\tau} \quad \dot{\rho} = \frac{\rho}{\tau}. \quad (6.67)$$

This allows us to rewrite Eq. (6.66) as

$$E_z = \frac{\mu_0 I}{2\pi\tau} \left[ \ln \frac{a^2/4 - x^2}{\rho(a - \rho)} - \left( \frac{a^2/2}{a^2/4 - x^2} - \frac{a}{a - \rho} \right) - \frac{2(a/2 - \rho)}{(a - \rho)} \right]. \quad (6.68)$$

We now introduce normalized lengths  $\bar{x} = x/(a/2)$  and  $\bar{\rho} = \rho/(a/2)$  and a normalized field strength  $\bar{E} = 2\pi\tau E/\mu_0 I$  and rewrite Eq. (6.68) as

$$\bar{E}_z = \ln \frac{1 - \bar{x}^2}{\bar{\rho}(2 - \bar{\rho})} - \left( \frac{2}{1 - \bar{x}^2} - \frac{2}{2 - \bar{\rho}} \right) - \frac{2(1 - \bar{\rho})}{(2 - \bar{\rho})}. \quad (6.69)$$

The electric field profile then depends on the dimensionless quantity  $\bar{\rho}$ . We plot this profile for several values of  $\bar{\rho}$  less than one in Fig. 6.9. For a wide range of  $\bar{\rho}$ , the electric field is everywhere negative in the plane between the two wires. Indeed, we can prove that for any  $\bar{\rho} > 0.076$ , the electric field is nowhere positive. We determine this critical value by first observing that the electric field achieves its maximum value at  $\bar{x} = 0$ . Setting  $\bar{x} = 0$  in Eq. (6.69) gives this maximum value of  $\bar{E}_z$  as

$$\ln \frac{1}{\bar{\rho}(2 - \bar{\rho})} - 2 + \frac{2}{2 - \bar{\rho}} - \frac{2(1 - \bar{\rho})}{(2 - \bar{\rho})}. \quad (6.70)$$

Setting Eq. (6.70) equal to zero and numerically solving gives  $\bar{\rho} = 0.076$ . Even when  $\bar{\rho} < 0.076$ , only the electric field in the central region becomes positive; the electric field close to the wires remains negative.

Eq. (6.69) was derived by making assumptions concerning the values of  $\dot{I}$ ,  $\dot{a}$ , and  $\dot{\rho}$  and should not be expected to hold rigorously. However, the conclusion that the effects of an expanding wire radius and decreasing wire separation cause a negative electric field for a large set of parameters is probably robust and can be expected to hold in general. Indeed, on the Solar Loop Experiment, the initial loop separation is about 8 cm and the initial loop radius is about 1.5 cm, giving  $\bar{\rho} = 0.375$ . On the Spheromak Experiment, the spider legs are flared and have different radii and separation distances at the cathode than at the anode. At the cathode, the spider legs have a radius of 0.2 cm and a separation of 4 cm, giving  $\bar{\rho} \approx 0.1$ . At the anode, the spider leg radius is 0.6 cm, and their separation is about 14 cm, so  $\bar{\rho} \approx .09$ . From these values, it seems likely that the dimensions of the Caltech plasma loops are such that the induced electric field, if axial, will be anti-parallel to the current and draw orbits inwards towards the magnetic null.

### 6.3.3 Drift Velocity

The purpose of this study was to determine how two adjacent plasma loops can merge into a single structure. It might seem somewhat circuitous, then, to assume that the plasma loops are expanding and to then show that the  $\mathbf{E} \times \mathbf{B}$  drift is inward. We therefore compare the  $\mathbf{E} \times \mathbf{B}$  drift with the velocity of the loops' boundaries. For larger values of  $\bar{\rho}$ , the  $\mathbf{E} \times \mathbf{B}$  drift is larger than the boundary velocity, and we conclude that the merging process is accelerated the closer the loops get to each other because the  $\mathbf{E} \times \mathbf{B}$  becomes larger.

The  $\mathbf{E} \times \mathbf{B}$  drift is given by combining Eqs. (6.69) and (6.45),

$$\mathbf{v}_{\mathbf{E} \times \mathbf{B}} = \frac{\mathbf{E} \times \mathbf{B}}{B^2} = \frac{a/2}{\tau} \frac{1 - \bar{x}^2}{2\bar{x}} \left[ \ln \frac{1 - \bar{x}^2}{\bar{\rho}(2 - \bar{\rho})} - \left( \frac{2}{1 - \bar{x}^2} - \frac{2}{2 - \bar{\rho}} \right) - \frac{2(1 - \bar{\rho})}{(2 - \bar{\rho})} \right] \hat{x}. \quad (6.71)$$

We will compare Eq. (6.71) with the velocity of the plasma boundaries given by  $-\dot{a}/2 + \dot{\rho} = (a/2\tau)(1 + \bar{\rho})$ . To start, we note that the two velocities are equal at the plasma surface. This is hardly coincidental; the electric field at the boundary is  $\mathbf{E} = \mathbf{v} \times \mathbf{B}$ , so the  $\mathbf{E} \times \mathbf{B}$  drift at the boundary is

$$\frac{\mathbf{E} \times \mathbf{B}}{B^2} = -\frac{(\mathbf{v} \times \mathbf{B}) \times \mathbf{B}}{B^2} = \mathbf{v}. \quad (6.72)$$

However, away from the boundary, the  $\mathbf{E} \times \mathbf{B}$  velocity may be greater or less than  $\mathbf{v}$  depending on the value of  $\bar{\rho}$ . We plot Eq. (6.71) for several values of  $\bar{\rho}$  in Fig. 6.10. When  $\bar{\rho} = 0.5$ , the  $\mathbf{E} \times \mathbf{B}$  drift velocity is indeed greater than the speed of the plasma wall. However, at  $\bar{\rho} = 0.15$ , the two velocities have nearly the same value except at the vicinity of the null. For even lower values of  $\bar{\rho}$ , there are regions where the  $\mathbf{E} \times \mathbf{B}$  drift is slower than the expansion rate of the tube. Of course, when  $\bar{\rho} < 0.076$ , the electric field becomes positive in the region around the null, and particle orbits are drawn away from the null rather than towards it.

This analysis suggests that the merging of two tubes may be a self-enhancing process. As the loops approach each other, the value of  $\bar{\rho}$  increases, giving a faster and faster  $\mathbf{E} \times \mathbf{B}$  drift towards the null. The particles on the outside of the flux tube are thus drawn to the null at a faster and faster rate.

## 6.4 Conclusions and Directions for Future Work

To explain the coalescence of the spider legs in the Caltech Spheromak Experiment into a single axisymmetric structure, we have studied the particle trajectories in a simplified model that treats the arched helical plasma loops as straight current-carrying wires. For a single wire, the particle trajectories all have the same qualitative behavior, but the addition of a second wire opens up new classes of trajectories: those that are confined to one wire, and those that are shared between both

wires. The time dependence of the Solar Loop and Spheromak experiments can cause transitions of confined orbits to shared orbits if the induced electric field is anti-parallel to the wire current. Unfortunately, we cannot presently determine the exact nature of the induced electric field from first principles, but we have argued that the induced electric field must be anti-parallel in the vicinity of the plasma loops when the loops move towards one another.

To further this work, the nature of the induced electric field in the actual experiments should be studied experimentally, as it seems unlikely that it can be determined by first principles alone due to the likely presence of plasma sheaths. If an experiment can determine the direction of the field, then the analysis of this chapter can proceed with confidence. The second set of information needed in the model is the experimental determination of the rate at which the plasma loops expand and attract. Once these parameters are determined, the analysis can proceed to determine exactly how fast orbits from the edge of the plasma loops are sucked into the magnetic null.

Finally, the current model does not investigate non-planar orbits. Analysis of such orbits is clearly more difficult than the study of planar orbits given the extra dimension of motion, and such studies of such orbits would probably proceed numerically. Note, though, that if an axial magnetic field were added to the model, then the field lines would be helical, and the planar orbits of the model presented in this chapter would not exist at all. Therefore, studies of non-planar orbits will be essential to more sophisticated models.

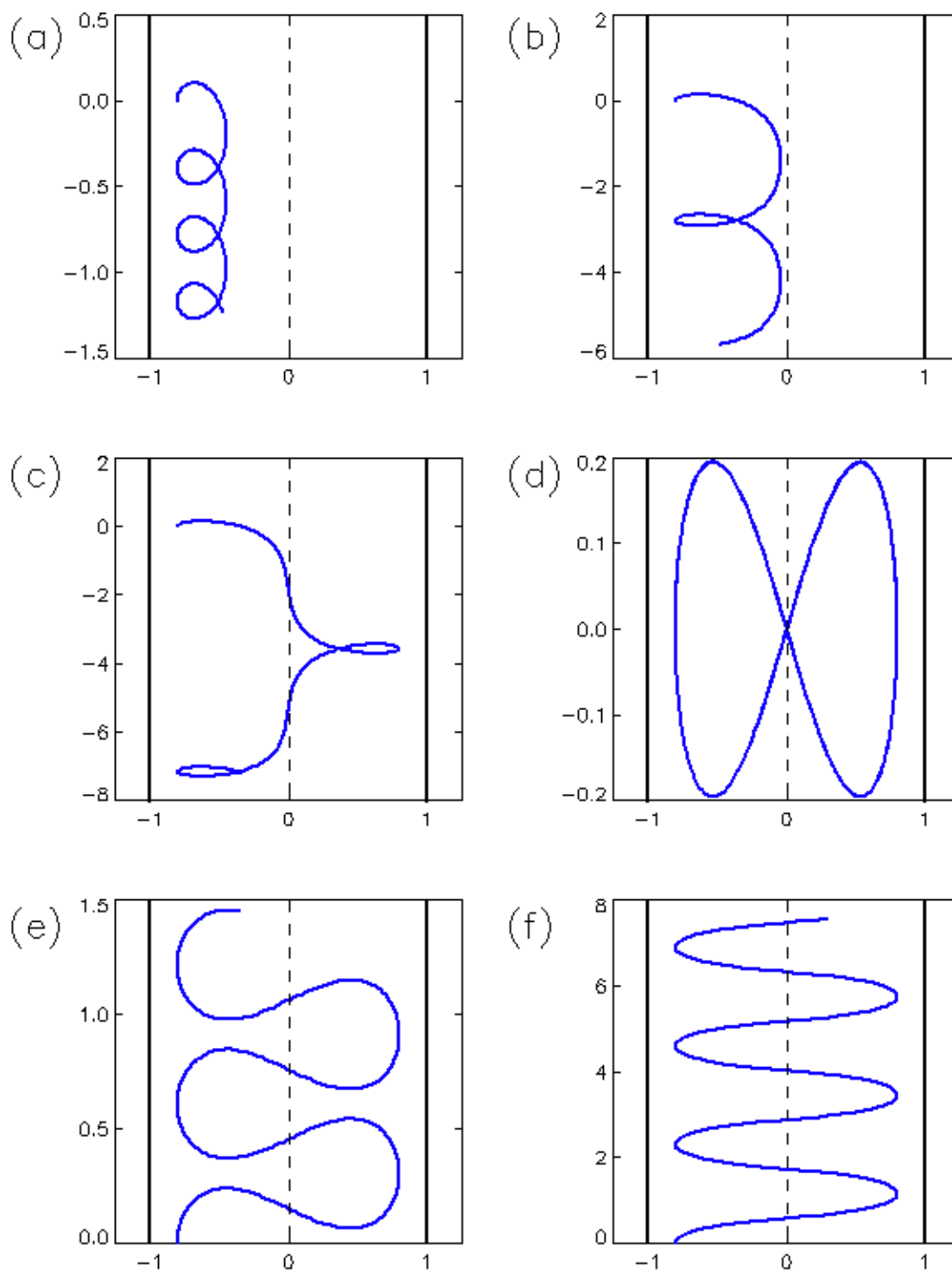


Figure 6.5: Several sample trajectories in the plane of two parallel wires. All orbits begin at  $x = -0.8$  but with different velocities. (a)  $v = 0.4$ , well below the threshold to cross the magnetic null. The orbit is confined to the left wire. (b)  $v = 0.51$ , just below the threshold to cross the magnetic null. (c)  $v = 0.511$ , just above the threshold to cross the null. The orbit is symmetric between the two wires. (d)  $v = 0.687994$ , for which the orbit is closed. (e)  $v = 0.8$ , for which the  $z$  drift becomes positive. (f)  $v = 1.4$ , for which the particle never travels in the negative  $z$  direction.

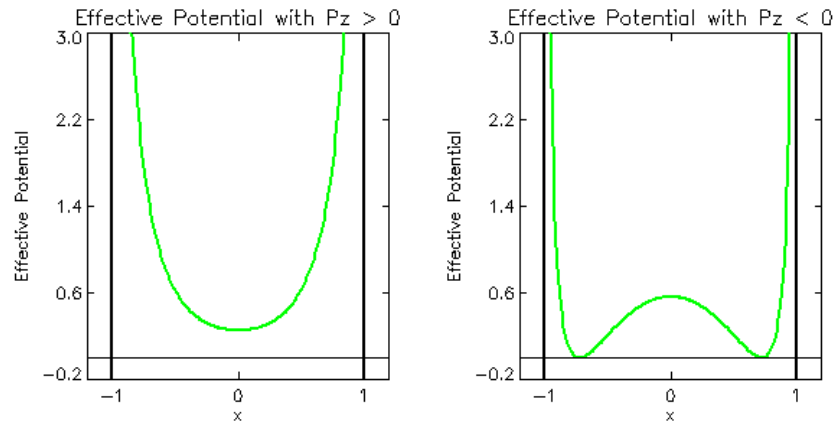


Figure 6.6: The effective potential for (a)  $P_z < 0$  (b)  $P_z > 0$ . In (a), the potential forms a well with infinite walls, and the magnetic null  $x = 0$  is a minimum.  $P_z = 0.5$  for this particular plot. In (b), the potential well develops a central bump, and the magnetic null is a local maximum. Orbits with small energy can be trapped in one of the small wells, while orbits with sufficient energy can pass over the maxima at the null. This particular plot has  $P_z = -0.75$ .

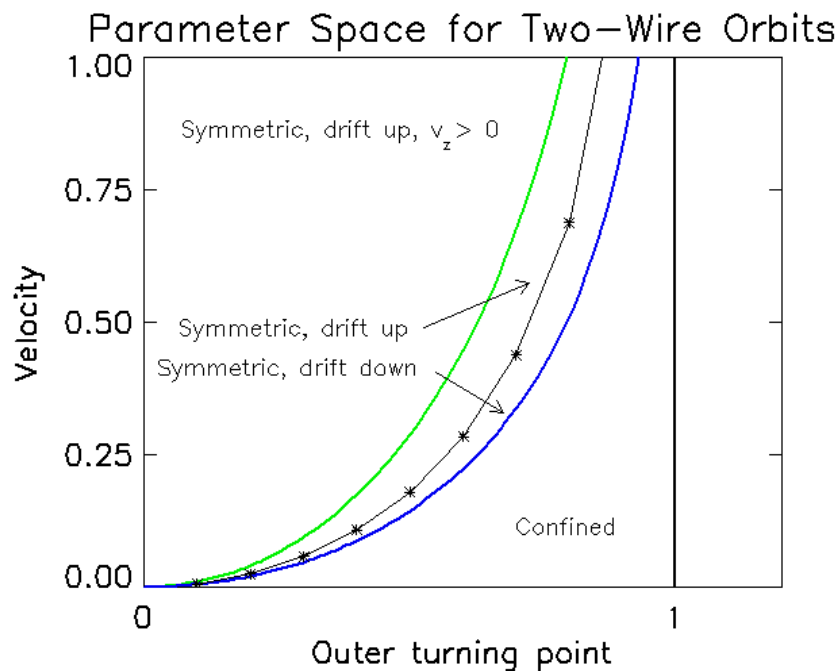


Figure 6.7: A parameter space plot of the different types of orbits. The bounding curves are determined by the values of the total velocity  $v$  and the canonical  $z$  momentum  $P_z$ . The points for which the orbits are closed are determined numerically at isolated points.

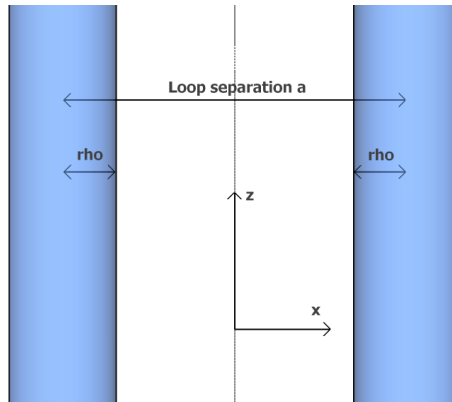


Figure 6.8: We align the  $z$  axis parallel to the current and denote the separation distance between the loops as  $a$ . We also give the loops a non-zero radius  $\rho$ , so the locations of the loops' edges, in the  $y = 0$  plane, are  $x = \pm(-a/2 + \rho)$ .

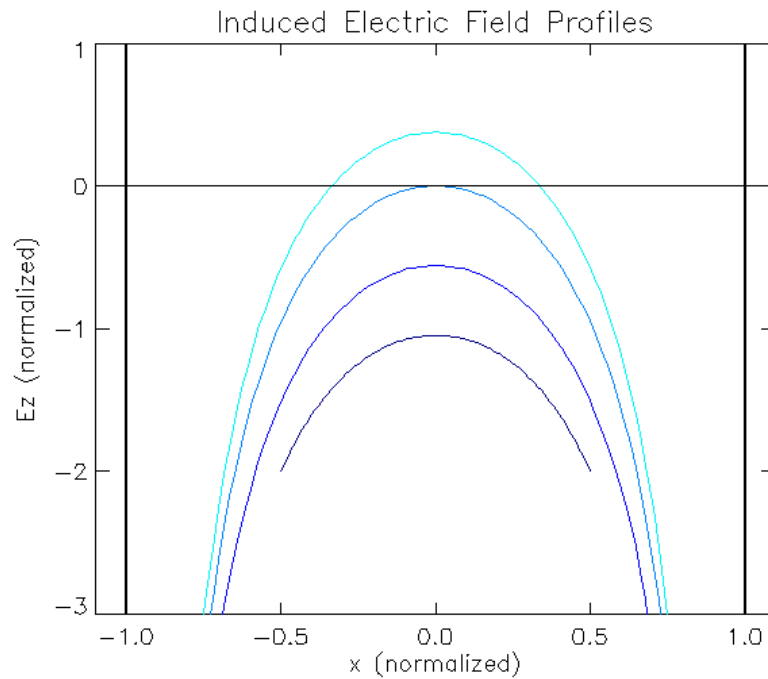


Figure 6.9: The electric field profile for different values of  $\bar{\rho}$ . Starting from the bottom curve, the  $\bar{\rho}$  values are 0.5, 0.15, 0.076, and 0.05.  $\bar{\rho} = 0.076$  is the critical value at which the electric field becomes positive for part of the domain.

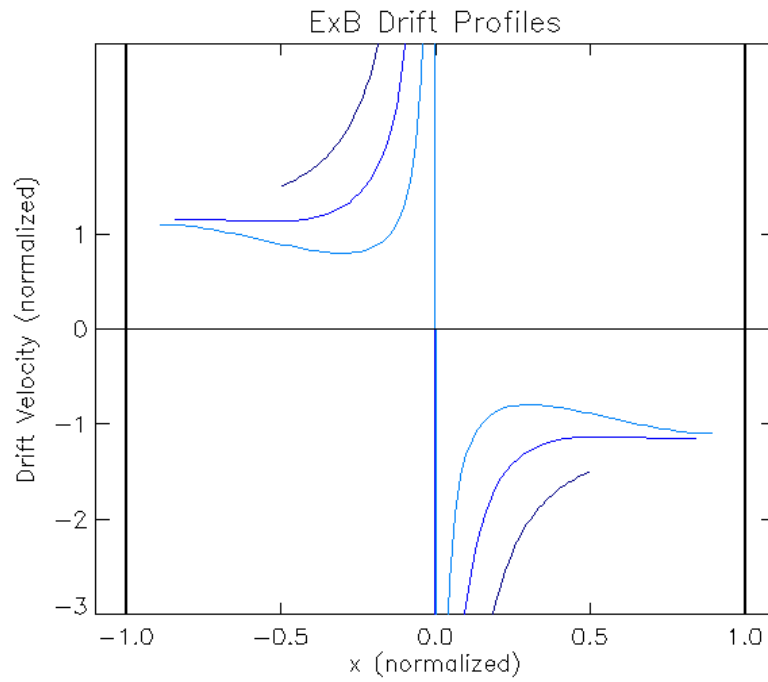


Figure 6.10: The  $\mathbf{E} \times \mathbf{B}$  drift is plotted for three different values of  $\bar{\rho}$ . The horizontal dashed lines denote the value of the plasma surface velocity. The top dark plot is for  $\bar{\rho} = 0.5$ ; the  $\mathbf{E} \times \mathbf{B}$  drift is quite large. The middle blue plot is for  $\bar{\rho} = .015$ ; the drift velocity is nearly equal to the surface velocity over much of the domain. The bottom light-blue plot is for  $\bar{\rho} = 0.1$ ; the  $\mathbf{E} \times \mathbf{B}$  drift is slower than the surface velocity except near the null and the plasma surface.

## Chapter 7

# Conclusion

In this thesis, we have presented two very different projects: experimental work developing vacuum photodiodes for measurements of extreme ultraviolet radiation during the dual-loop experiments on the Caltech Solar Loop Experiment, and theoretical work on Hamiltonian mechanics and particle orbits to explore the coalescence of the spider legs in the Caltech Spheromak Experiment. Common to both projects is the merging of two or more plasma loops into a single structure, a process that is highly influenced by the amount of helicity injected into the plasma. On the Caltech Solar Loop Experiment, the initial helicity content, either co- or counter-helicity, leads to very different phenomena during the merging. On the Caltech Spheromak experiment, the eight-fold symmetry of the spider legs quickly gives way to the axisymmetry demanded by the Taylor state as the current ramps up and the helicity content increases. In essence, this thesis is not particularly concerned with the final state of the plasma after merging but what happens as the plasma evolves towards that state.

The vacuum photodiode array responds primarily to extreme ultraviolet radiation, an important radiation band for low-temperature plasmas that lose much of their thermal energy to extreme ultraviolet line emission. Each individual vacuum photodiode has a fast time response that allows for the observation of the rapid radiation bursts. The array has twelve detectors arranged to observe both variations both along the loop and also at the loop apex as it expands outward. In addition to the cathode and anode, the array includes an enclosure to shield the detectors, collimators to narrow the field of view of each detector, powerful permanent magnets to protect the array from plasma particles, and a bias voltage to help overcome space charge limitations. Electromagnetic interference can completely distort and obscure the desired signals, and several techniques are employed for noise reduction. These include reduction of capacitive coupling and use of semi-rigid cables. Perhaps most importantly, a major source of noise, radio-frequency ground currents that magnetically couple to the signal, has been identified, and a technique for diverting these currents has been developed to drastically eliminate the associated noise. Many of the solutions devised here can be applied to other diagnostics. The vacuum photodiode signals are extremely clean and free of spurious signals.

Now that the issues that once prevented the use of vacuum photodiodes have been resolved, and because the material costs of a vacuum photodiode are quite low, there is very little to stop one from implementing many such detectors on the Solar Loop Experiment, the Spheromak Experiment, and any future plasma experiments housed at Caltech.

With the spurious signals removed from the vacuum photodiode signals, the array has unveiled several interesting findings. The total power radiated from the plasma can now be estimated and can be up to a megawatt and higher. We believe that the plasma is shedding any heat deposited by Ohmic dissipation in the form of extreme ultraviolet radiation, and plotting the vacuum photodiode signal against the plasma current for a number of shots shows that, even at different discharge voltages, the vacuum photodiode signal is a function of current. The source of these large radiation levels might be hydrogen emission, for filtered photodiode data suggests that hydrogen optical emission is quite strong. This contradicts the usual notion that the hydrogen in such a plasma is completely ionized and has very low line emission. We invoke non-equilibrium effects, including the fast time scale of the experiment and the strong flow of plasma from the gas inlet, to explain the large fraction of neutral hydrogen that must accompany strong hydrogen emission. Impurity emission might be a significant contributor to the radiation losses but is not expected to be quite as important for the Solar Loop Experiment due to its lower temperatures and reduced interaction with the walls. If the large radiative losses are indeed due to hydrogen emission, then this has significant implications for the heating and temperature of fast hydrogen plasma experiments, namely, such experiments will not burn through the hydrogen as quickly as predicted by the electron temperature and will radiate more intensely as a consequence; such a plasma might not heat up to the carbon or oxygen radiation barrier. This could actually be useful in tokamak divertors, where radiative losses can be beneficial in cooling the hot plasma to temperatures safe for the divertor plates. The Solar Loop Experiment even suggests that it might be possible to pump cool and neutral-rich plasma from the wall region along magnetic field lines into the divertor volume to provide temporary cooling as the injected plasma ionizes. Another application might be the generation of abundant hydrogen Lyman  $\alpha$  lines for lithography purposes.

Co- and counter-helicity dual loop plasma experiments produce nearly identical vacuum photodiode signals up until a certain time, at which point counter-helicity merging produces large extreme ultraviolet bursts. The onset of the bursts are believed to be the onset of the merging and magnetic reconnection. The bursts may be shedding of heat deposited by strong current sheets in counter-helicity merging that convert magnetic energy from the annihilated fields into particle thermal energy, which is then radiated away as line emission. Energetic electrons might also be produced, and interactions with the chamber wall might also generate ultraviolet radiation and soft x-rays. The radiation bursts observed in counter-helicity experiments are accompanied by other phenomena: brightening of the upper legs, plasma detachment from the electrodes, a rise and sudden

drop in the electrode voltage, and a noise pulse in the electronics. However, these effects diminish as the gas valve is pulsed harder to admit more gas into the experiment. Strangely, though, as the gas valve is pulsed harder, a new radiation burst is observed at the loop apex; this burst is believed to originate from the bright spot. Thus, these studies, with the aid of the vacuum photodiode array, have determined that dual-loop merging experiments depend just as strongly on the amount of gas admitted by the fast gas valve as they do on the helicity content of the loops.

The second project discussed in this thesis, theoretical work into particle orbits, has led to a new theorem of Hamiltonian dynamics. Chapter 5 shows that, in any Hamiltonian system where one coordinate undergoes periodic evolution, the action integral for that coordinate encodes the evolution of the system once the periodic motion has been averaged. In fact, this action integral acts as a Hamiltonian for the reduced system and provides the averaged equations of motion provided that time is measured in periods of motion. With this formalism, one can rederive the guiding center drift equations using  $\mu$  as a Hamiltonian, and one can even derive the flux enclosed by a gyro-orbit, but the scope of the results goes far beyond charged particle motion in magnetic field.

Chapter 6 presented a model to explain how two current-carrying plasma loops might start to merge together. In the model, two classes of particle trajectories in the region between the two loops are found: those that are localized to one loop and those shared symmetrically between the two loops. If the loops are attracted to each other due to their parallel currents, then the induced electric field will point in such a direction as to make the  $\mathbf{E} \times \mathbf{B}$  drift inwards towards the magnetic null where an orbit can transition from being localized to being shared. To pursue this model, the induced electric field should be studied experimentally, as it seems unlikely that it can be determined by first principles alone. From there, non-planar orbits should be studied numerically to see if they exhibit the same general behavior as the planar orbits, namely, that they transition from being localized to a single loop to being shared among two or more loops. More sophisticated models would include the axial magnetic field as well.

## Appendix A

# Improvements to the Plasma Current and Electrode Voltage Diagnostics

The plasma current and electrode voltage are extremely important measurements, and this section outlines steps taken to improve both sets of data. The main result is the connection of the grounding clip of the HV probe to the lower electrode and proper attenuation of the voltage signal. These improvements are vital in studying the detachment of the plasma from the electrode in Chapter 4. We also discuss the optoelectric converters that transmit the current and voltage (IV) data, spurious signals due to ground loops, and noise-reduction techniques.

### A.1 Optoelectric Modules

The HV probe and Rogowski coil transmit their signals to the DAQ via optoelectric modules [Analog Modules, Inc., Model 732T-2.5-33K-10M]. Each module consists of two devices: a transmitter, which converts an electrical signal into an optical one, and a receiver, which receives the optical signal and converts it back into an electrical one. The transmitter and receiver communicate via a fiber optic cable. The two transmitters, one each for the Rogowski coil and the HV probe, are located by the vacuum chamber and connect their respective probe, while the two receivers are located by the DAQ. The modules transmit frequencies from 10 MHz down to DC. They have a 33 k $\Omega$  input resistance and can transmit signals in the range of  $\pm 2.5$  V; beyond this voltage range, the modules clip the signal.

The optoelectric modules offer several advantages. First, both the HV probe and the Rogowski coil are designed to be read by a high-impedance device such as an oscilloscope. The DAQ, however, has a built-in 50  $\Omega$  termination that would distort the probes' signals. For instance, if the Rogowski coil circuit of Fig. 2.6 were terminated in 50  $\Omega$ , the integrating capacitor would see its resistor  $R$  in parallel with the 50  $\Omega$  termination, so the circuit time constant would be  $(R \parallel 50 \Omega)C$ . This new

time constant is much shorter than the intended time  $RC$ , and the signal would suffer distortion. A similar argument applies to the HV probe. The optoelectric modules therefore act as a buffer circuit; the transmitter input impedance is  $33\text{ k}\Omega$ , providing both probes with a relatively high impedance, and the receivers, powered by active electronics, can drive the  $50\ \Omega$  termination of the DAQ that would load the probes. Second, signal transmission via fiber optic cables is less susceptible to noise than transmission via braided coaxial cable. While the modules do introduce some noise, this noise is smaller than that associated with transmitting the signal via braided coaxial cable. Finally, the modules offer electrical isolation as the fiber optic cables do not electrically connect the transmitter and receiver. This prevents the formation of ground loops and allows the use of the HV probe grounding clip, as is discussed next.

## A.2 The HV Probe Grounding Clip

The HV probe has a grounding clip relative to which it measures large potential differences. As the HV probe measures the electrode voltage and the probe itself is connected to the upper electrode, the grounding clip should be connected to the lower electrode. However, it had been long-standing practice to leave the grounding clip of the HV probe detached from the lower electrode and not connected to anything. In this configuration, the probe measures the voltage of the upper electrode relative to some unknown floating potential. Ostensibly, the omission of the grounding clip was done to prevent the formation of a ground loop as follows. The lower electrodes are electrically connected to the chamber through the grounding cables of the main capacitor bank; connecting the grounding clip to the lower electrodes would form a second electrical connection to the chamber through the DAQ as discussed in Sec. 3.3.2; this second connection would form a large ground loop spanning the laboratory. However, the grounding clip *can* be safely attached to the lower electrodes because the optoelectric module provide electrical isolation, preventing the second ground loop from forming. Indeed, attaching the grounding clip changed the nature of the voltage signal; Fig. A.1 compares the voltage data with and without the clip in use. The clipping at  $1.5\text{ kV}$  is due to the optoelectric module and is avoided by adding a frequency-compensated voltage divider as will be described in Sec. A.4. However, even with the clipping, the difference in the HV probe output with and without the grounding clip is apparent, and the signal with the grounding clip in use is believed to be more accurate.

## A.3 Ground Loops and Isolation Transformers

Large spurious signals started appearing in both the IV data, seemingly spontaneously. Ultimately, the source of these signals was traced to a small ground loop formed by the I and V cables at the

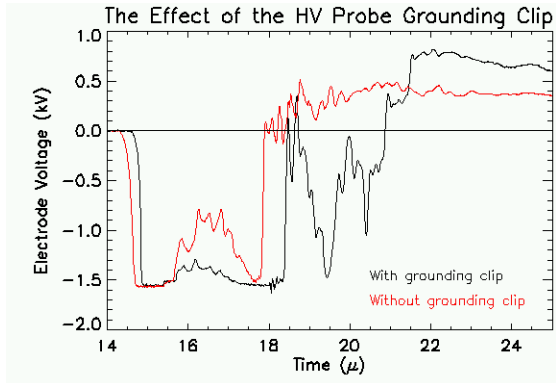


Figure A.1: Use of the HV probe grounding clip on the lower electrode causes significant changes in the signal. Here, the electrode voltage is compared with and without the grounding clip so that the effects of leaving the grounding clip floating can be seen. The clipping is due to the optoelectric modules and will be resolved in Sec. A.4.

DAQ. The cables share a common ground at the DAQ but also at the receiver modules because both modules are powered off the same power supply. To break up the ground loop, a 1:1 isolation transformer was added to the voltage line. However, the low-frequency response of the transformer was quite poor, and to understand this problem we need to look at the equations for a transformer.

Ideally, a 1-1 transformer transmits the signal without distortion or attenuation. From the circuit diagram in Fig. A.2, the voltage loop equations in the left and right circuits are

$$V = i\omega LI_1 - i\omega MI_2 + R_1 I_1, \quad (\text{A.1})$$

$$0 = i\omega LI_2 - i\omega MI_1 + R_2 I_2, \quad (\text{A.2})$$

where  $M$  is the mutual inductance of the transformer and is assumed to be nearly equal to  $L$ . Ideal operation occurs when we assume  $M = L$  and  $\omega L \gg R_1 R_2 / (R_1 + R_2)$ . Defining the difference  $\delta I = I_1 - I_2$ , Eq. (A.2) becomes  $i\omega L \delta I = R_2 I_2$ , and Eq. (A.1) becomes

$$V = i\omega L \delta I + R_1 (I_2 + \delta I) \quad (\text{A.3})$$

$$= R_2 I_2 + R_1 I_2 + \frac{R_1 R_2}{i\omega L} I_2 \quad (\text{A.4})$$

$$\approx R_2 I_2 + R_1 I_2. \quad (\text{A.5})$$

It follows that the output voltage, which is the voltage across  $R_2$ , is

$$V_{\text{out}} = \frac{R_2}{R_1 + R_2} V, \quad (\text{A.6})$$

which is the equation for a simple voltage divider. In this ideal case, the transformer couples the two circuits so well that the circuit behaves as if the transformer were not present. Moreover,

the internal resistance of the optoelectric module is probably quite small, meaning that  $R_1 \approx 0$ . hence, the condition for ideal operation,  $\omega L \gg R_1 R_2 / (R_1 + R_2)$ , will almost always be met because  $R_1 R_2 / (R_1 + R_2) \approx 0$ .

However, when  $R_2 \geq \omega L \gg R_1 R_2 / (R_1 + R_2)$ , the optoelectric module becomes severely loaded and cannot provide the current necessary to maintain ideal operation. Let us compute the theoretical output requirement of the module in this regime. We showed that  $i\omega L \delta I = R_2 I_2$ , so

$$I_1 = \delta I + I_2 = \left(1 + \frac{R_2}{i\omega L}\right) I_2 \approx \left(1 + \frac{R_2}{i\omega L}\right) \frac{V}{R_1 + R_2}, \quad (\text{A.7})$$

where Eq. (A.5) has been used in the last line.  $I_1$  therefore increases as  $\omega$  decreases below  $R_2/L$ . We suspect that the receiver module becomes extremely loaded at low frequencies and cannot provide this theoretical current. To remedy the problem, a 100  $\Omega$  resistor was placed in series in the voltage line in between the receiver module and the transformer, effectively changing  $R_1$  from 0 to 100  $\Omega$ . This changes the denominator in Eq. (A.7) from 50  $\Omega$  to 150  $\Omega$ , cutting the current requirement by a factor of three. This is sufficient to relieve loading of the module in the frequency range of interest, and the transformer faithfully transmits the voltage signals. The added 100  $\Omega$  resistance forms an effective voltage divider with the 50  $\Omega$  of the DAQ, and this voltage attenuation factor of  $50/150 = 1/3$  must be incorporated into the voltage signal.

The reason why the ground loop started misbehaving was not identified. The cause may have been a change in the cabling in other diagnostics, particularly the magnetic probes, which had been recently swapped around the time the spurious signals appeared. The magnetic probes contain many cables that could bear large ground currents (see discussion in Sec. 3.3.5) that could couple to the ground loop.

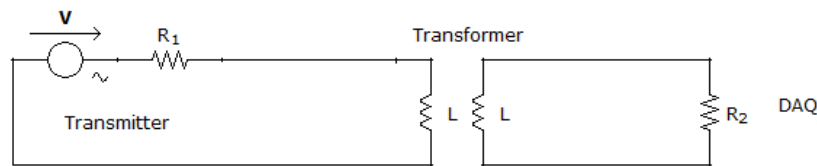


Figure A.2: A circuit diagram for the transmitter module coupled to the DAQ via a 1-1 transformer. The low frequency response of the circuit is poor unless extra resistance is added to  $R_1$ .

## A.4 HV Probe Termination, Compensation, and Attenuation

The optoelectric modules can only transmit signals up to  $\pm 2.5$  V, beyond which they clip the signal. The HV probe attenuates the signal by a factor of roughly 923<sup>1</sup>, so that a 6 kV electrode voltage is attenuated to about 6 V and would be clipped by the transmitter. To avoid clipping, a simple voltage divider was implemented by placing a 50 k $\Omega$  resistor in series with the 33 k $\Omega$  input resistance of the transmitter, as shown in Fig. A.3. This provides a theoretical attenuation of  $33/(50 + 33) \approx 0.4$ . However, adding this resistance caused the HV probe to integrate the input signal. To understand why, we need to look into the probe's design.

The HV probe has a compensation circuit whose purpose is cancel the effects of stray capacitance across the probe's 10 M $\Omega$  and also the oscilloscope's 1 M $\Omega$  resistor. By adjusting the components in the compensation circuit, the distortion from the stray capacitance can be minimized such that, for example, a square-wave signal is attenuated without distortion such as rounding the corners (poor high frequency transmission) or drooping (poor low frequency transmission). The compensation circuit is optimized for use with an oscilloscope of 1M $\Omega$  impedance and thus is not compatible with different termination impedances such as the 33 k $\Omega$  of the transmitter module. To check this experimentally, the probe was terminated in 33 k $\Omega$  and given a 100 KHz square-wave input; the square wave was clearly seen to droop as is shown in Fig. A.4.a, indicating less than ideal transmission of low frequencies. This poor low-frequency transmission had always been present in the voltage data even before any of the modifications described here were enacted. However, when the 50 k $\Omega$  resistor described above was added, the output changed from less-than-ideal to completely distorted. This is probably because the 50 k $\Omega$  resistor combined with both the input capacitance of the optoelectric module and a capacitor in the compensation circuit to form an RC-circuit that integrated the input signal.

To remove this unwanted integration, a small capacitor was added in parallel to the 50 k $\Omega$  resistor, as shown in Fig. A.3. This trick is exploited in oscilloscope probes. Consider the circuit in Fig. A.5; and let the complex impedances  $Z_1$  and  $Z_2$  be the parallel combination of  $R_1$  and  $C_1$  and the parallel combination of  $R_2$  and  $C_2$  respectively:

$$Z_1 = \frac{R_1}{1 + i\omega R_1 C_1}, \quad (\text{A.8})$$

$$Z_2 = \frac{R_2}{1 + i\omega R_2 C_2}. \quad (\text{A.9})$$

If  $R_1 C_1 = R_2 C_2$ , then it is seen that  $Z_1$  and  $Z_2$  are proportional to each other with the proportion-

---

<sup>1</sup>This calibration was done independently by Deepak Kumar and Mark Kendall

ality constant  $Z_1/Z_2 = R_1/R_2$ . The output voltage, measured across  $R_2$ , is then

$$V_{\text{out}} = \frac{Z_2}{Z_1 + Z_2} V_{\text{in}} = \frac{R_2}{R_1 + R_2} V_{\text{in}}, \quad (\text{A.10})$$

which is the equation for a simple voltage divider. When  $R_1 C_1 = R_2 C_2$ , the effects of the capacitors cancel each other in the output. Indeed, when a 7 pF capacitor was added across the 50 k $\Omega$  resistor, the HV probe attenuated square-wave inputs more accurately than had previously been achieved with the probe going straight into the module as shown in Fig A.4.b. The value of 7 pF was determined by trial and error and can, perhaps, be improved.

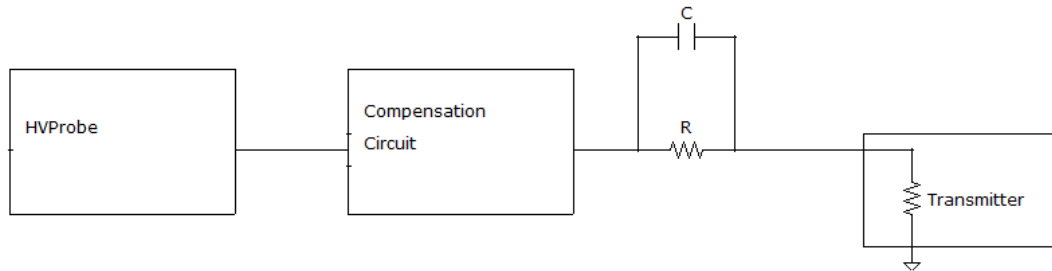


Figure A.3: A resistor  $R$  is inserted between the HV probe and the transmitter module creates a voltage divider to avoid signal clipping. The capacitor  $C$  is needed for frequency compensation.

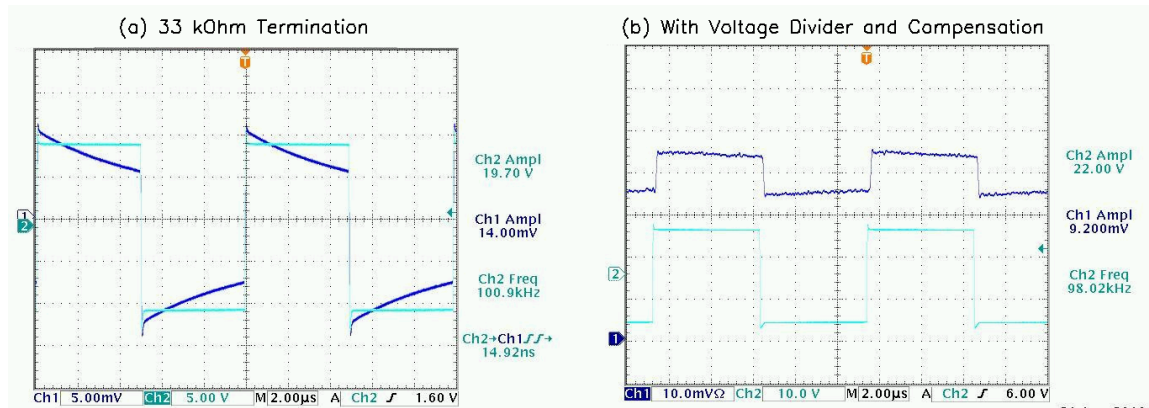


Figure A.4: (a) The HV probe output given a 100 kHz square-wave input when the probe is terminated in 33 k $\Omega$ . The output is seen to droop, indicated poor low-frequency response. This distortion had always been present in the signal before any of the modifications outlined here were enacted; however, adding the 50 k $\Omega$  resistor shown in Fig. A.3 without the compensating capacitor produced far worse distortion. (b) The probe's output once the 50 k $\Omega$  resistor *and* its compensating capacitor have been added. The signal is attenuated by the appropriate amount, and the frequency response is actually a little better than in (a).

Finally, both the 50 k $\Omega$  resistor and 7 pF capacitor are soldered directly into the HV probe's compensation circuit box rather than being placed in a separate electrical box in between the com-

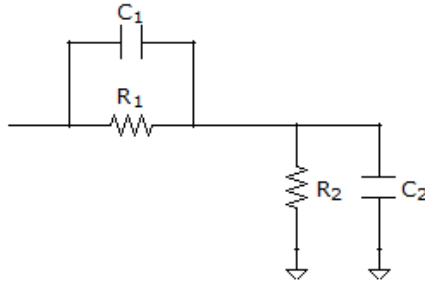


Figure A.5: Given  $R_2$ ,  $C_2$ , and  $R_1$ ,  $C_1$  can be chosen so that the capacitive effects vanish in the output voltage. The output, as measured across  $R_2$ , is then frequency-independent.

pensation circuit and the transmitter. This was done because using a separate box caused arcing at the transmitter due to the large potential difference between the HV probe cable, which is connected to the lower electrode, and the chamber frame on which the transmitter rests. This is not a problem when the HV probe connected directly to the module because the probe is equipped with a high voltage connector. Thus, this arcing is avoided by placing the extra resistor and capacitor inside the compensation circuit.

## A.5 Reducing Noise

Some of the modification described so far introduced extra noise into the signals. The isolation transformer added to the voltage signal line introduced high-frequency noise. The attachment of the grounding clip to the lower electrode exacerbated oscillations in the current data that occur at the beginning and middle of the shot. This section describes several attempts to reduce these unwanted side-effects.

Noise reduction in both the IV signals was achieved by moving the receiver modules closer to the DAQ and using shorter lengths of cable to transmit the signals. In general, braided coaxial cable are susceptible to high-frequency noise via transfer impedance as discussed in Sec. 3.3.3, and using less cable sometimes results in less noise. Another possible reason for the noise reduction is that the IV cables were moved further away from the large bundle of cables for the spheromak magnetic probe array, which is suspected to carry large ground currents. Whatever the reason, this relocation mollified the high frequency noise on the voltage traces. The current data improved as well, although this improvement may be due to the added ferrite cores, discussed below.

Large oscillations of about 1 - 2 MHz in the current data are mitigated by the use of ferrite cores. For instance, a ferrite core placed on the HV probe cable offers significant oscillation reduction. Connecting the grounding clip to the lower electrodes connects the local ground of the transmitter

modules; the Rogowski coil ground is also connected to the lower electrodes. We believe that the increased oscillation amplitude on the Rogowski coil is related to sudden changes in the lower electrode voltage which suddenly change the coil ground. The added ferrite around the HV cable makes the connection between the Rogowski coil ground and the lower electrodes high impedance and hence reduces the degree of coupling between lower electrode voltage and transmitter ground voltage. We note that powering the transmitters module with different power supplies could completely isolate the two diagnostics and reduce the oscillations; however, oscillations are still present even when the HV probe is completely detached. Also, adding a ferrite core around the current signal line between the receiver and the DAQ results in modest noise reduction, although the reason for this is not clear.

The remaining oscillations on the current data are probably caused by electrostatic coupling of the Rogowski coil to the main capacitor. The coil sits on top of a copper plate bolted to the capacitor; when the capacitor fires, the voltage of the plate changes drastically, which could induce charge flow on the Rogowski coil [114]. These oscillations are seen at the beginning of the experiment when the voltage is switched on and in the middle of the experiment when the plasma detaches. Indeed, changing the length of braided cable between the coil and the integrating circuit changed the nature of these oscillations. Using a shorter length of cable to connect the coil to the integrating circuit increased the oscillation frequency, presumably because of the reduced stray capacitance of the cable. However, additional spurious signals simultaneously appeared, probably because the integrating circuit was significantly closer to the main capacitor. For the time being, the best place for the integrating circuit appears to be at the transmitter module. To eliminate the oscillation, a shield might be added to the Rogowski coil as per Ref. [114].

## Appendix B

# Magnetic Scattering of Charged Particles

The vacuum photodiodes described in Chapter 3 utilize permanent magnets to deflect charged particles from the array's interior. In this section, we determine how effectively such magnets shield the array and what particle energies would be required to penetrate through the magnetic field to the detectors. We consider two regimes: the first applies when the particle remains far enough away from the magnet so that the field can be approximated as a pure dipole field. One can then calculate a forbidden region into which particles cannot enter, and the dimensions of this forbidden region measure the deflecting capabilities of the magnet. From these calculations, we determine that electrons are deflected by the magnets but that ions penetrate close to the magnet where the dipole approximation fails. This latter case constitutes the second regime, and we derive a simple formula relating direct measurements of the field close to the magnet to the deflective power of the magnetic geometry.

### B.1 The Stormer Region

At large distances from a magnet, the field approximates that of a pure dipole. Particle motion in a dipole field is an old problem first considered by Stormer [115], who established the existence of forbidden regions into which particles of particular energies cannot enter. This region, commonly called the Stormer region, offers an easy criteria for deciding whether or not a particle can enter the detector. The analysis can be extended to other axisymmetric multipole fields [116] and has even been considered for shielding spacecraft [117].

Stormer regions arise through conservation of both kinetic energy and canonical angular momentum. The expression for canonical angular momentum comes from the Lagrangian for a particle in

a magnetic field:

$$L = \frac{m}{2} \mathbf{v}^2 + q \mathbf{v} \cdot \mathbf{A} \quad (\text{B.1})$$

$$= \frac{m}{2} (\dot{\rho}^2 + \rho^2 \dot{\phi}^2 + \dot{z}^2) + q (\dot{\rho} A_\rho + \rho \dot{\phi} A_\phi + \dot{z} A_z), \quad (\text{B.2})$$

$$P_\phi = \frac{\partial L}{\partial \dot{\phi}} = m \rho^2 \dot{\phi} + q \rho A_\phi, \quad (\text{B.3})$$

where  $(\rho, \phi, z)$  form a cylindrical coordinate system. An ideal magnetic dipole  $\mathbf{m} = m_d \hat{z}$  has a vector potential

$$\mathbf{A} = \frac{\mu_0}{4\pi} \frac{\mathbf{m} \times \hat{r}}{r^3} = \frac{\mu_0 m_d}{4\pi} \frac{\rho}{(\rho^2 + z^2)^{3/2}} \hat{\phi}, \quad (\text{B.4})$$

where  $r$  is the spherical radius,  $r^2 = \rho^2 + z^2$ . By azimuthal symmetry,  $P_\phi$  is conserved. Eqs. (B.3) and (B.4) allow us to express the kinetic energy of  $\phi$  motion as a function of position:

$$\frac{m}{2} v_\phi^2 = \frac{m}{2} \rho^2 \dot{\phi}^2 = \frac{1}{2m} \left( \frac{P_\phi}{\rho} - q \frac{\mu_0 m_d}{4\pi} \frac{\rho}{(\rho^2 + z^2)^{3/2}} \right)^2. \quad (\text{B.5})$$

For a particle moving in a time-independent magnetic field, kinetic energy is also conserved. Of course, the particle's  $\phi$  kinetic energy can never exceed the total kinetic energy, so those spatial locations where Eq. (B.5) predicts an energy greater than  $(m/2)v^2$  are forbidden to the particle. It thus follows that the boundary of the forbidden region is where Eq. (B.5) equals  $(m/2)v^2$ , or

$$\frac{m}{2} v^2 = \frac{1}{2m} \left( \frac{P_\phi}{\rho} - q \frac{\mu_0 m_d}{4\pi} \frac{\rho}{(\rho^2 + z^2)^{3/2}} \right)^2. \quad (\text{B.6})$$

Dividing Eq. (B.6) by  $(m/2)v^2$  gives

$$1 = \left( \frac{P_\phi}{m v \rho} - \frac{q \mu_0 m_d}{4\pi m v} \frac{\rho}{(\rho^2 + z^2)^{3/2}} \right)^2. \quad (\text{B.7})$$

The coefficient of the second terms has the units of length squared and defines the Stomer length  $C$  as

$$C := \sqrt{\frac{q \mu_0 m_d}{4\pi m v}}. \quad (\text{B.8})$$

We normalize length by  $C$  so that

$$1 = \left( \frac{P_\phi / m v C}{\rho} - \frac{\rho}{(\rho^2 + z^2)^{3/2}} \right)^2. \quad (\text{B.9})$$

The size of the forbidden region thus depends on the dimensionless parameter  $P_\phi / m v C$ , which we

shall call  $k$ . We can solve Eq. (B.9) for  $z$  as a function of  $\rho$ ,

$$\pm 1 = \frac{k}{\rho} - \frac{\rho}{(\rho^2 + z^2)^{3/2}}, \quad (\text{B.10})$$

$$\frac{\rho}{(\rho^2 + z^2)^{3/2}} = \frac{k}{\rho} \mp 1, \quad (\text{B.11})$$

$$(\rho^2 + z^2)^{3/2} = \frac{\rho^2}{k \mp \rho}, \quad (\text{B.12})$$

$$z^2 = \left( \frac{\rho^2}{k \mp \rho} \right)^{2/3} - \rho^2. \quad (\text{B.13})$$

There are two curves: an upper curve and a lower curve given by the minus sign and the plus sign in Eq. (B.13) respectively. We plot these curves for several value of the parameter  $k$  in Fig. B.1, which shows that the lower curve defines a toroidal forbidden region for all  $k$  whereas the upper curve undergoes a morphological change at  $k = 2$ . We will discuss each region in turn.

We first analyze the lower curve, which defines a toroidal forbidden region. The  $k \rightarrow 0$  case corresponds to particle trajectories with vanishingly small value of canonical angular momentum; these trajectories can be considered “head-on” such that the particle is aimed directly at the collimator with  $\dot{\phi}(t = 0) \approx 0^1$ . For such trajectories, the upper curve, to be discussed below, is vanishingly small, and the only forbidden region is that defined by the lower curve, as shown in Fig. B.1.a. The size of this region is set by  $C$  alone, as can be seen by setting  $P_\phi = 0$  in Eq. (B.6). The height of this toroidal region is  $0.17C$  and the radial extent is  $C$ . Therefore, if  $0.17C$  is greater than or equal to the diameter of the collimator, the toroidal regions will deflect head-on trajectories aimed at the collimator.

However, as  $k$  increases, the toroidal region shrinks, as can be seen graphically in Fig. B.1. Analytically, the lower curve has precisely one root, which defines the radial extend of the forbidden region:

$$\rho_{\max} = \frac{\sqrt{k^2 + 4} - k}{2}. \quad (\text{B.14})$$

$\rho_{\max}$  approaches  $\rho = 0$  as  $k$  increases, confirming that the toroidal region diminishes with increasing angular momentum. Fig. B.2 plots the height and radial extent of the toroidal region as a function of  $k$ . From this analysis, one might conclude that particles of non-zero angular momentum could pass the magnet even when  $0.17C$  is greater than or equal to the diameter of the collimator. However, we shall now show that the second forbidden region, defined by the upper curve, will deflect such particles for larger  $k$ .

The second forbidden region vanishes for small  $k$  but grows in extent for larger  $k$ , eventually enveloping the toroidal region considered above and defining a very large forbidden region. For

---

<sup>1</sup>By Eq. (B.3), the condition  $\dot{\phi}(t = 0) = 0$  does not mean that  $P_\phi$  vanishes but rather  $P_\phi = q\mu_0 m_d / 4\pi\rho_0$ . However, we assume that such “head-on” particle begins at sufficiently large  $\rho_0$  that  $P_\phi$  can be taken to be zero.

$k < 2$ , the upper curve has no roots but instead has a singularity at  $\rho = k$ , so the upper forbidden region is topologically conical as suggested by Fig. B.1.b. This singularity also defines the radial extend of the upper region, which then clearly grows as  $k$  increases. As  $k \rightarrow 2$ , the upper curve begins to dip down and eventually meets the  $z = 0$  plane as shown in Fig. B.1.c. For  $k > 2$ , the forbidden region is cylindrical and shaped like an hourglass; additionally, there is a hollow torus inside, as shown in Fig. B.1.d. This hollow space between the upper and lower regions can confine particles in the dipole field, and such trajectories are of particular interest to geophysicists, but this region is accessible to the trajectories considered here which begin far away from the magnets. We note that the upper curve has two roots when  $k > 2$ :

$$\rho = \frac{k \pm \sqrt{k^2 - 4}}{2}. \quad (\text{B.15})$$

The  $-$  sign is the radial extend of the hollow region while the  $+$  sign is the minimum radius of the cylindrical forbidden region (e.g. the narrowest radius of the hourglass). When this latter quantity is equal to or larger than the radius of the collimator, the cylindrical region protects the detector from the charged particle. Since  $(k + \sqrt{k^2 - 4})/2 \geq 1$ , this minimum radius of the cylindrical region is greater than or equal to the Stormer length  $C$ .

We thus conclude that particles with a Stormer length  $0.17C$  greater than or equal to the collimator radius will most likely be deflected regardless of the particle's canonical angular momentum. For small values of  $k$ , the particle is deflected by the toroidal region, and for large  $k$  the particle is instead deflected by the cylindrical forbidden region. Fig. B.2 plots the size of both the toroidal and cylindrical region as a function of  $k$  and clearly shows this transition for  $k > 2$ . We acknowledge that, even if  $0.17C$  is nearly equal to the collimator radius, a small population of particles may have initial conditions such that the forbidden region is slightly smaller than the collimator radius, and these particles could in principle slip past the magnets. However, we also note that such particles may still acquire some degree of angular deflection and may subsequently crash into the collimator wall after passing the magnetic. Thus, we will still use the Stormer length as the appropriate scale in determining whether a particle is deflected or not.

## B.2 Estimates of the Dipole Moment

To compute the Stormer length, we need an estimate of the dipole moment of the deflector magnets. This is estimated both analytically and experimentally; the two results agree well enough to proceed with order-of-magnitude calculations.

The data sheets for the magnets do not give the dipole moment but instead provide the remanence field  $B_r$ , which is the field left in the magnet after the external magnetizing field is removed. Ideally,

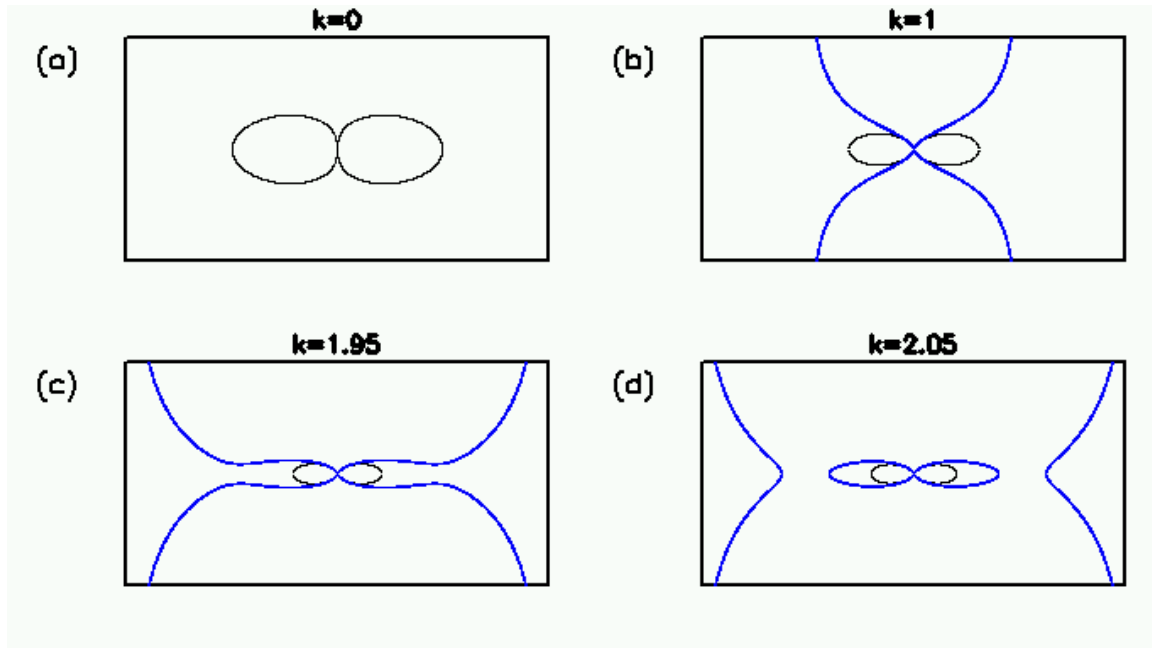


Figure B.1: The forbidden regions plotted for different values of  $k$ . (a) At  $k = 0$ , the upper curve is essentially non-existent, leaving only a toroidal forbidden region. (b) For  $0 < k < 2$ , the upper curve becomes apparent and defines a cylindrical forbidden region while the toroidal regions diminish in size. (c) As  $k \rightarrow 2$ , the upper curve begins to bend down towards the  $z = 0$  plane. (d) For  $k > 2$ , the upper curve forms a large cylindrical forbidden region that encloses the smaller toroidal region.

this remanence field is uniform, axial, and of constant strength  $B_r$  inside the magnet. Such a field is equivalent to that of an infinite solenoid, and we therefore estimate the dipole moment by treating the magnet like a solenoid. To produce an interior field of strength  $B_r$ , the linear current density would have to be  $\lambda = B_r/\mu_0$ . The magnetic dipole moment density per unit length is then  $\lambda$  times the magnet's area  $\pi R^2$ , and the total dipole moment is

$$m_d = \lambda(\pi R^2)h = \frac{B_r}{\mu_0} \text{Vol}, \quad (\text{B.16})$$

where Vol is the volume of the magnet. This formula implies a magnetization  $\mathbf{M} = \mathbf{B}_r/\mu_0$ . Indeed, for a uniformly magnetized sphere, the dipole moment is proportional to the product of the interior magnetic field times the sphere's volume [98, pg. 264], although in the case of a sphere there is an additional multiplicative factor due to the different geometry. The magnets originally used on the vacuum photodiodes were neodymium disks of radius  $R = 0.75$  cm and height  $h = 0.30$  cm and remanence field  $B_r = 0.68$  T. This gives an estimated dipole moment of

$$m_d = 0.287 \text{ Am}^2. \quad (\text{B.17})$$

To validate Eq. (B.17), the on-axis field of several disk magnets was measured using a 5100

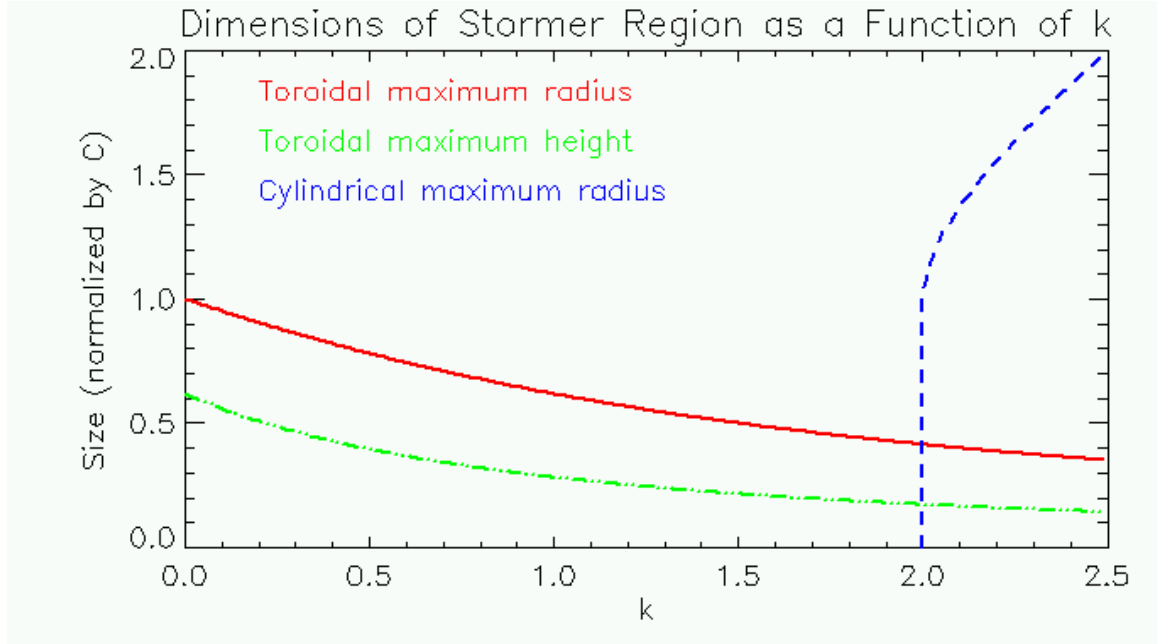


Figure B.2: The spatial extend of the forbidden regions as a function of  $k$ . We see that even though the toroidal region diminishes both in radial extent and in height, the larger cylindrical region forms at  $k = 2$  and continues to deflect particles as the toroidal region continues to shrink for large  $k$ .

Series Gauss meter from F.W. Bell for various heights above the magnet. The height measurements are accurate to within  $\pm 2$  mm. At every height, the magnet was placed both face up and face down. Subtracting the two values and dividing by two then removes any offsets due to Earth or lab fields. The measurements were done on two of the disk magnets described above. Additionally, a third magnet was measured to check the scaling of magnetic moment with volume; this magnet had  $R = 0.75$  cm and height of  $h = 0.50$  cm.

We fit the measured magnetic field with the analytical formula for a dipole field. The magnetic field of a pure dipole is

$$\mathbf{B} = \frac{\mu_0 m_d}{4\pi} \frac{2 \cos \theta \hat{r} - \sin \theta \hat{\theta}}{r^3}, \quad (\text{B.18})$$

which means that its on-axis value is

$$\mathbf{B}(\rho = 0) = \frac{\mu_0 m_d}{2\pi} \frac{1}{z^3} \hat{z}. \quad (\text{B.19})$$

In principle,  $z^3 \cdot B(z)$  should be constant and proportional to the dipole moment. This is not observed in the actual data, indicating that  $\mathbf{B}$  is not a pure dipole field but weakens as one approaches the magnet. An octupole multipole moment is therefore added to the fit<sup>2</sup>. We write the octupole field

<sup>2</sup> A quadrupole moment does not obey the symmetry of a disk magnet.

as

$$\mathbf{B}_{\text{oct}} = -\nabla \left( m_o \frac{\mu_0 P_3(\cos \theta)}{4\pi r^4} \right) \quad (\text{B.20})$$

$$= -m_o \frac{\mu_0}{4\pi} \left( -4 \frac{P_3(\cos \theta)}{r^5} \hat{r} - \sin \theta \frac{P_3'(\cos \theta)}{r^4} \hat{\theta} \right). \quad (\text{B.21})$$

For on-axis measurements,  $\theta = 0$ . The  $\hat{\theta}$  component vanishes, and for all Legendre polynomials,  $P_n(1) = 1$ , so

$$B_{\text{oct}}(\rho) = \frac{\mu_0 m_o}{\pi} \frac{1}{z^5} \hat{z}. \quad (\text{B.22})$$

When this octupole field is added to the dipole field, our analytic formula is

$$B(z) = \frac{\mu_0 m_d}{2\pi} \frac{1}{z^3} + \frac{\mu_0 m_o}{\pi} \frac{1}{z^5}. \quad (\text{B.23})$$

The resulting fit gives a dipole moment of  $m_d = 0.2275 \pm 0.0031 \text{ Am}^2$  and an octupole moment of  $m_o = (-1.371 \pm 0.15) \cdot 10^{-5} \text{ Am}^4$  for the first of the 5902K61 magnets and  $m_d = 0.2292 \pm 0.0031 \text{ Am}^2$  and  $m_o = (-1.4034 \pm 0.15) \cdot 10^{-5} \text{ Am}^4$  for the second. The  $\chi^2$  values for these fits are 1.15 and 1.19, indicating a good fit. The analytical estimate of the dipole moment given by Eq. (B.17) is thus fair but too large; the discrepancy might be due imperfect magnetization or the approximate nature of the analytical estimate. The octupole moments determined by the fits tells us how the field deviates from a pure dipole field; the distance at which the octupole field strength equals the dipole field is 1.1 cm. If a particle's Stormer length is much larger than 1.1 cm, then we can safely ignore the octupole field as the particle never enters regions where the octupole field becomes significant. However, for Stormer lengths close to or less than 1.1 cm, the actual field is not as strong as predicted by the dipole approximation, and the predictions based on Stormer analysis cannot be used.

Finally, the dipole moment of the larger 5902K62 magnet is determined by the fit to be  $0.4049 \pm 0.0037 \text{ Am}^2$ . The ratio of the dipole moments of the two magnets is 1.8, while the ratio of their volumes is 1.7, confirming that the dipole moment scales linearly with volume.

### B.3 Estimates of Stormer Lengths

Having determined a formula for the Stormer length and the dipole moment of the deflector magnets, we can now estimate the Stormer lengths of plasma particles in the Solar Experiment. We find that, with the original magnets used on the array, electrons were assuredly deflected but that energetic ions might penetrate through the magnetic field into the array. Motivated by these results, we installed a new set of magnets into increase the Stormer length to safer values.

The typical plasma temperature on the Solar Experiment is 1 – 4 eV [19]. We shall take the kinetic energy of the average plasma particle to be 5 eV but keep in mind that a population of

high-energy particles may be present. 5 eV corresponds to velocities of  $9.4 \cdot 10^5$  m/s for electrons and  $2.2 \cdot 10^4$  m/s for protons, and the associated Stormer lengths for these velocities are

$$C_e = 7.3 \text{ cm}, \quad (\text{B.24})$$

$$C_p = 1.1 \text{ cm}. \quad (\text{B.25})$$

The collimator has a diameter of roughly 1.0 cm, so the Stormer length for a 5 eV electron is nearly an order of magnitude greater than the collimator diameter, and we conclude that 5 eV electrons are successfully deflected by the magnets. However, the Stormer length of a 5 eV ion is on the order of the collimator diameter. Since the field close to the magnet is weaker than a pure dipole field, we expect the Stormer length to overestimate the deflective power of the magnet near the magnet and hypothesize that the spurious signals discussed in Sec. 3.4 could be created by energetic ions streaming past the deflector magnets. Substantial populations of energetic ions might be expected in counter-helicity experiments, as anomalously high ion energies have been observed in merging spheromak experiments [23], as have fast ionic jets [118].

To eliminate the possibility of ions entering the detector, the following upgrades were made on the magnetic deflecting system. Powerful neodymium magnets were ordered; they have a remanence field of  $B_r = 1.24$  T, a radius of  $R = 0.79$  cm, and a height of 0.64 cm, and an estimated dipole moment of  $m_d = 1.2$  A m<sup>2</sup> from Eq. B.16. Furthermore, two magnets were used per collimator, doubling the dipole moment. The Stormer lengths for 5 eV particles become  $C_e = 22$  cm and  $C_p = 3.3$  cm, both of which are larger than the collimating diameter. However, another major change was the geometry of the magnets in the collimator. The original magnets sat on the outer diameter of the collimator. In this setup, the height of the toroidal Stormer region would have to equal the diameter of the collimator in order to completely cover the collimator region. In the new setup, shown in Fig. (3.17), the Stormer region is now centered in the collimator, so the height of the toroidal region only has to exceed the collimator radius to entirely cover the collimator interior.

Note that the Stormer length scales with particle velocity as  $v^{-1/2}$  and thus with kinetic energy as  $\text{KE}^{-1/4}$ . Thus, the Stormer length does not vary much with particle energy. Also,  $C$  scales with  $m^{-1/4}$  once  $v$  has been written in terms of energy, so more massive ions penetrate further into the magnetic field. A singly charged nitrogen ion has a Stormer length that is 1.9 times smaller than a hydrogen ion of the same energy, and the Stormer length for a singly charged argon ion is 2.5 times smaller than that of a hydrogen ion of the same energy.

## B.4 Deflection Near Magnets

In the region close to the magnets, the magnetic field is not as strong as that predicted by the dipole approximation, and Stormer analysis cannot be expected to hold. To determine the deflection of an energetic ion that penetrates into this region, consider an extremely energetic ion that is only slightly deflected by the magnets. Let the ion travel primarily in the  $x$  direction along the axis of the collimator, and let the magnetic field point in the  $z$  direction. The Lorentz force will deflect the ion in the  $y$  direction, and

$$m \frac{d\mathbf{v}}{dt} = qvB\hat{y}, \quad (\text{B.26})$$

from which  $d\mathbf{v} = (q/m)Bdx$ , and

$$\Delta\mathbf{v} = \frac{q}{m} \int Bdx\hat{x}, \quad (\text{B.27})$$

where the integration follows the ion trajectory through the field. In the case of slight deflection, though, we can take the trajectory to be a straight line through the collimator. The figure of merit for particle deflection is  $\int Bdx$  along the path through the collimator. If  $\Delta v \ll v$ , then deflection angle is approximately  $\Delta v/v$ . We thus consider the ion deflected when

$$v \sim \Delta v = \frac{q}{m} \int Bdx\hat{x}. \quad (\text{B.28})$$

That is, when  $\Delta v$  becomes of the same order as  $v$ , the ion is significantly deflected. Of course, the actual trajectory of such particles is significantly different from a straight line through the collimator, so the exact deflection cannot be easily determined, but Eq. (B.28) estimates the onset of significant deflection. To calculate this deflection parameter, the magnetic field of the upgraded deflection system was measured with a Hall probe as a function of distance into the collimator; the measurements were made as close to the collimator axis as possible with the probe aligned as nearly as possible with the axis of the magnets. These measurements are shown in the lefthand columns of Table B.1. The righthand columns tabulate  $\Delta v$  for each singly charged ion species up to the specified distance into the collimator and express these velocities in units of electron volts. An ion of the given species must have at least that much energy to penetrate that far into the collimator. It is thus predicted that ions would need energies of keV to penetrate through the magnetic field and reach the collimator. We note that since the deflection parameter depends on  $\int Bdx$  rather than just the maximum value of  $B$ , the deflection can be improved by increasing the length of the magnetic field without necessarily increasing the maximum field strength. Longer strips of magnets could be laid along the collimator, potentially increasing  $\int Bdx$  even if the maximum value of  $B$  is not as strong.

We note that, if both ions and electrons approach the collimator together, collective effects may enable the charged particles to pass the magnets even if single-particle analysis forbids each particle

Distance (mm)	Field Strength (T)	$\Delta v_{\text{H}^+}$ (keV)	$\Delta v_{\text{N}^+}$ (keV)	$\Delta v_{\text{Ar}^+}$ (keV)
6.4	0.463	0.41	0.029	0.010
9.5	0.583	3.4	0.25	0.086
12.7	0.599	12	0.89	0.31
17.1	0.587	33	2.3	0.82
19.1	0.456	58	4.2	1.5

Table B.1: Measurements of the magnetic field as a function of distance through the collimator provide an estimate of the energies of particles needed to penetrate through the field. The right three columns give the energies of ions for which the deflection parameter  $(q/m) \int B dx$  is equal to the ion velocity at that distance into the collimator.

from passing individually. As the upgraded magnetic deflection system has successfully eliminated the spurious signals, we do not believe collective effects are in action.

## Appendix C

# Review of Action-Angle Variables

Action-angle variables are a useful set of phase space coordinates in Hamiltonian mechanics. The action variable is synonymous with the action integral, whose utility is discussed at length in Chapter 5. However, classical mechanics texts usually introduce action-angle variables only after a long discussion of Hamilton-Jacobi theory [92][34]. The purpose here is to introduce action-angle variables through a more direct presentation. We shall briefly review canonical transformations and generating function so that the full significance of the action-angle pair can be understood. At the end of the section, we formally demonstrate the claim made in Sec. 5.1.7 that the canonical transformation that introduces action-angle variables for the  $\xi P_\xi$  variables simultaneously transforms the  $\eta P_\eta$  pair into their averaged versions.

### C.1 Canonical Transformations

We first discuss canonical transformations, a set of changes in phase space coordinates that preserve Hamilton's equations. Suppose we have a one-dimensional time-independent system  $H = H(q, p)$ . The equations of motion for  $q$  and  $p$  follow from Hamilton's equations:

$$\dot{q} = \frac{\partial H}{\partial p}, \quad (\text{C.1})$$

$$\dot{p} = -\frac{\partial H}{\partial q}. \quad (\text{C.2})$$

Suppose that we want to use a different set of coordinates  $QP$  that are some function of the old coordinates, i.e.,  $Q = Q(q, p)$  and  $P = P(q, p)$ . We then wish to determine the evolution of  $Q$  and  $P$ . One approach would be to take time derivatives of  $Q = Q(q, p)$  and  $P = P(q, p)$ ,

$$\dot{Q} = \frac{\partial Q}{\partial q} \dot{q} + \frac{\partial Q}{\partial p} \dot{p}, \quad (\text{C.3})$$

$$\dot{P} = \frac{\partial P}{\partial q} \dot{q} + \frac{\partial P}{\partial p} \dot{p}, \quad (\text{C.4})$$

and then substitute Eqs. (C.1) and (C.2) for  $\dot{q}$  and  $\dot{p}$ , taking care to express  $q$  and  $p$  in terms of  $Q$  and  $P$ . This approach is guaranteed to produce the correct equations of motion for  $Q$  and  $P$ . A second tack would be to first express  $H$  in terms of  $Q$  and  $P$ :  $H = H(q(Q, P), p(Q, P))$  and then invoke Hamilton's equations. This approach does *not* work, in general; that is, the equations of motion  $\dot{Q} = \partial H / \partial P$  are not correct. However, there is a special subclass of transformations for which this second procedure does work, and such transformations are called canonical.

The reason why Hamilton's equations will not apply in general to the QP coordinates can be seen in the derivation of Hamilton's equation from the principle of least action, which states that small variations of system trajectories do not change the action, e.g.,  $\delta S = \delta \int L dt = 0$ . For the canonical coordinates  $q$  and  $p$ , the Lagrangian can be written as a function of  $q$  and  $p$  through the Legendre transform:  $L = p\dot{q} - H$ . To derive Hamilton's equations, we set the variation of the action to zero:

$$0 = \delta \int_{t_1}^{t_2} [p\dot{q} - H(q, p)] dt \quad (\text{C.5})$$

$$= \int_{t_1}^{t_2} \left[ \dot{q}\delta p + p\delta\dot{q} - \frac{\partial H}{\partial q}\delta q - \frac{\partial H}{\partial p}\delta p \right] dt \quad (\text{C.6})$$

$$= \int_{t_1}^{t_2} \left[ \dot{q}\delta p - p\delta\dot{q} - \frac{\partial H}{\partial q}\delta q - \frac{\partial H}{\partial p}\delta p \right] dt, \quad (\text{C.7})$$

where the third line is derived from the second through integration by parts and from the usual assumption of no variations of the end points. Requiring that the  $\delta q$  and  $\delta p$  terms vanish independently yields Hamilton's equation. Thus, we see that Hamilton's equations are equivalent to the Lagrangian having the form  $L = p\dot{q} - H$ . However, when we rewrite the Lagrangian in terms of the new coordinates  $(Q, P)$ , we will not, in general, obtain  $P\dot{Q} - H$ :

$$L = p\dot{q} - H \neq P\dot{Q} - H, \quad (\text{C.8})$$

as can be seen by expanding the time derivative of  $P\dot{Q}$ :

$$P\dot{Q} = P \frac{\partial Q}{\partial q} \dot{q} + P \frac{\partial Q}{\partial p} \dot{p} \neq p\dot{q}. \quad (\text{C.9})$$

However, the new phase space coordinates QP are canonical if one can find a so-called generating function for the transformation. We show this by exploiting a peculiar facet of the principle of least action: namely, the variation of the action  $S = \int_{t_1}^{t_2} L dt$  is unchanged if we add to  $L$  the total time derivative of some other function, say  $F$ , because the contribution of  $F$  to the action,

$$\int_{t_1}^{t_2} \frac{dF}{dt} dt = [F(t_2) - F(t_1)], \quad (\text{C.10})$$

depends only on  $F$  evaluated at the end points, and variations of the action keep the end points fixed. This function  $F$  will become the generating function used to enact canonical transforms. As discussed above, the Lagrangian  $L$ , when written in terms of  $QP$ , is different than  $P\dot{Q} - H$ . However, if these two quantities differ only by a total derivative, then variations of  $P\dot{Q} - H$  are equivalent to variations of  $L = p\dot{q} - H$ , and Hamilton's equations will hold for the QP coordinates. We therefore require

$$P\dot{Q} - H(P, Q) + \frac{dF}{dt} = p\dot{q} - H(p, q). \quad (\text{C.11})$$

If we let  $F$  have the following form,

$$F = F_1(q, P) - PQ, \quad (\text{C.12})$$

then

$$\frac{dF}{dt} = \frac{\partial F_1}{\partial q} \dot{q} + \frac{\partial F_1}{\partial P} \dot{P} - \dot{P}Q - P\dot{Q}, \quad (\text{C.13})$$

and using this expression in Eq. (C.11),

$$-\dot{P}Q + \frac{\partial F_1}{\partial q} \dot{q} + \frac{\partial F_1}{\partial P} \dot{P} = p\dot{q}. \quad (\text{C.14})$$

If  $F_1$  is chosen such that

$$Q = \frac{\partial F_1}{\partial P}, \quad (\text{C.15})$$

$$p = \frac{\partial F_1}{\partial q}, \quad (\text{C.16})$$

then the lefthand side of Eq. (C.14) will indeed be equal to the righthand side, and the Lagrangians will be equivalent. Equations (C.15) and (C.16) then define the transform  $(q, p) \rightarrow (Q, P)$ . Whenever a generating function is specified, the resulting coordinates will be canonical, and Hamilton's equations will apply.

## C.2 Action-Angle Variables

We introduced the action integral  $J = \oint pdq$  for periodic motion in Chapter 5, but  $J$  is only one half of a canonical set of variables called action-angle variables. The second coordinate is the angle variable  $\phi$ , which shall be explained in this section. We will also explicitly show the generating function to obtain action-angle coordinates.

We begin by discussing the action variable. For a one-dimensional system,  $H = H(q, p)$ , the

action variable is

$$J(H) = \oint p(H, q) dq, \quad (\text{C.17})$$

That is, given a trajectory of energy  $H = H(q, p)$ , we solve for  $p$  as a function of  $H$  and  $q$  and integrate  $p(H, q)$  over  $q$  along the orbit.  $J$  is a function of  $H$ , which is a constant of motion, so  $J$  is likewise a constant of motion. Moreover, we have, in analogy to the proof given in Sec. 5.1.2,

$$\frac{dJ}{dH} = \oint \frac{\partial p}{\partial H} dq = \oint \frac{1}{\partial H / \partial p} dq = \oint \frac{dq}{\dot{q}} = \Delta t. \quad (\text{C.18})$$

For this one-dimensional system, the Hamiltonian  $H$  uniquely labels each trajectory by its energy. As  $J$  is a function of  $H$ , it also labels each trajectory, but this label is the phase space area enclosed by the orbit as is seen from Eq. (C.17).

If we assume that  $(J, \phi)$  are canonical, then Hamilton's equations show that the angle coordinate  $\phi$  essentially counts period of motion. We write the Hamiltonian  $H$  as a function of the action-angle coordinates  $J$  and  $\phi$  by inverting the expression  $J(H)$  for  $H = H(J)$ . Thus,  $H$  written in action-angle coordinates only depends on  $J$  and not  $\phi$ . By Hamilton's equation, then,  $\dot{J} = \partial H / \partial \phi = 0$ , which confirms that  $J$  is a constant of motion. Hamilton's equation also yields  $\dot{\phi}$ :

$$\dot{\phi} = \frac{\partial H}{\partial J} = \frac{1}{\Delta t}. \quad (\text{C.19})$$

$\Delta t$  is itself a constant of motion, so  $\dot{\phi}$  is likewise constant along a trajectory, and

$$\phi(t) = \frac{t}{\Delta t} + \phi(0). \quad (\text{C.20})$$

At the moment when the particle has completed its  $n$ th orbit,  $t = n\Delta t$  and  $\phi = n + \phi(0)$ , so  $\phi$  essentially counts cycles of the trajectory. As noted by Littlejohn [119], the different orbits in phase space may have different periods, and thus particles traverse the orbits at different rates, but if the motion is parametrized by the angle variable  $\phi$  then all particles complete a single period as  $\phi$  approaches one.

Indeed, using  $(J, \phi)$  as phase space coordinates has a simple analogy. Suppose we have a set of perfectly circular trajectories in the  $xy$  plane:  $x = r \cos(\omega t)$  and  $y = r \sin(\omega t)$ . We know that these trajectories are greatly simplified by switching to polar coordinates  $(r, \theta)$ , for, along a circular trajectory, the radial coordinate  $r$  is constant while  $\theta = \omega t$ . Put another way, the  $r$  coordinate labels the particular circle, while the  $\theta$  coordinate measures position along the circle. Action-angle variables are simply a generalization of this situation to non-circular curves.  $J$  is analogous to  $r$  and labels every trajectory by a geometric quantity, namely the phase space area enclosed by the curve. Similarly,  $\phi$ , like  $\theta$ , measures the location along the trajectory in terms of the fraction of time taken

to reach that point compared to the period of that orbit.

We now demonstrate a canonical transformation from  $(q, p)$  to action-angle coordinates. The appropriate generating function is

$$F_1(q, J) = \int_{q_0(J)}^q p(H(J), q') dq'. \quad (\text{C.21})$$

Several points must be explained. First, since our generating function depends on  $J$ , we must write  $H$  as a function of  $J$ . Second,  $q_0$  denotes a reference point on each trajectory from which we begin integration; the choice of  $q_0$  is quite arbitrary and will be seen to affect the motion only in a minor fashion. This generating function is the so-called abbreviated action<sup>1</sup> for motion starting at  $q_0$  up to the point  $q$ . For a complete cycle of motion, the value of the generating function is  $J$ .

We now evaluate the transformation through Eqs. (C.15) and (C.16) with  $J$  playing the role of the new momentum  $P$  and  $\phi$  playing the role of the new coordinate  $Q$ . From Eq. (C.16),

$$p = \frac{\partial F_1}{\partial q} = p(H(J), q), \quad (\text{C.22})$$

which simply re-expresses  $p$  as a function of  $q$  and  $J$ . Using Eq. (C.21) in Eq. (C.15) and remembering to differentiate the integral bounds, we obtain:

$$\phi = \frac{\partial F_1}{\partial J} = \int_{q_0}^q \frac{\partial p}{\partial H} \frac{\partial H}{\partial J} dq' + \frac{\partial q_0}{\partial J} \cdot p(H(J), q_0) \quad (\text{C.23})$$

$$= \frac{1}{\Delta t} \int_{q_0}^q \frac{1}{\dot{q}} dq' + \phi_0(J), \quad (\text{C.24})$$

where  $\phi_0$  is defined as

$$\phi_0 = \frac{\partial q_0}{\partial J} \cdot p(H(J), q_0). \quad (\text{C.25})$$

Eq. (C.24) defines the angle variable  $\phi$ . The integral in Eq. (C.24) is really just an expression for the time it takes the particle to travel from  $q_0$  to  $q$ . Thus,  $\phi$  evolves linearly with time and increments by unity for every period of motion, as anticipated above.

### C.3 Action-Angle Transformations for Multi-Dimensional Systems

Here, we verify the claim made in Sec. 5.1.7 that, in multi-dimensional systems, the transformation of a periodic coordinate to action-angle variables simultaneously removes the periodic oscillations from the other coordinates. As in Chapter 5, we let  $\xi$  be a periodic coordinate and  $\eta$  be an ignorable coordinate. In this notation, the claim is that writing  $H$  as  $H = H(J, P_\eta)$  rather than  $H =$

<sup>1</sup>The action is  $\int L dt = \int (p_i \dot{q}^i - H) dt$ , whereas the abbreviated action is just  $\int p_i \dot{q}^i dt$ .

$H(\xi, P_\xi, P_\eta)$  transforms the  $\eta$  coordinate to an averaged version of  $\eta$  that evolves linearly in time at the drift velocity, and we will make this statement more rigorous by treating the substitution of  $J$  for  $(\xi, P_\xi)$  as a canonical transformation. Because  $J$  is also a function of  $P_\eta$ , the transformation  $(\xi, P_\xi) \rightarrow (J, \phi)$  simultaneously transforms the  $(\eta, P_\eta)$  pair into a new set of coordinates, say,  $(\bar{\eta}, \bar{P}_\eta)$ . That is, the action-angle transformation for one pair of coordinates cannot be carried out independently of the second pair of coordinates. The situation is similar to a gauge transformation. Given the vector potential  $\mathbf{A} = y\hat{x} + x^2\hat{y}$ , we can enact a transformation to eliminate the  $x$  component; for instance, we can add the gradient of  $\chi = -xy$  to  $\mathbf{A}$ . However, this simultaneously transforms the  $y$  component of the vector potential. By analogy, one cannot transform the pair  $(\xi, P_\xi) \rightarrow (\phi, J)$  without also transforming  $(\eta, P_\eta) \rightarrow (\bar{\eta}, \bar{P}_\eta)$ . The remarkable fact about this ‘‘incidental’’ transformation is that  $\bar{\eta}$  is the averaged version of  $\eta$  that evolves linearly in time at the drift velocity. One can think of  $\bar{\eta}$  as an angle variable conjugate to  $\bar{P}_\eta$  since its evolution is linear in time.

We develop a generating function that enacts  $(\xi, P_\xi) \rightarrow (\phi, J)$ . The generating function will be

$$F = S(\xi, J, \bar{\eta}, \bar{P}_\eta) - \phi J + \eta P_\eta, \quad (\text{C.26})$$

with  $S$  to be specified shortly. Equating Lagrangians in analogy to Eq. (C.11),

$$J\dot{\phi} + \bar{P}_\eta\dot{\bar{\eta}} - H + \frac{dF}{dt} = P_\xi\dot{\xi} + P_\eta\dot{\eta} - H, \quad (\text{C.27})$$

and expanding  $dF/dt$  gives the following transformation equations:

$$\phi = \frac{\partial S}{\partial J}, \quad P_\xi = \frac{\partial S}{\partial \xi}, \quad (\text{C.28})$$

$$\eta = -\frac{\partial S}{\partial P_\eta}, \quad \bar{P}_\eta = -\frac{\partial S}{\partial \bar{\eta}}. \quad (\text{C.29})$$

We chose  $S$  to be the abbreviated action integrated along the trajectory,  $\int P_\eta d\eta + P_\xi d\xi$ , in analogy to the case above. We must take care to express  $S$  as a function of  $(\xi, J, \bar{\eta}, \bar{P}_\eta)$ :

$$S(\xi, J, \bar{\eta}, \bar{P}_\eta) = \int_{\xi_0(J, P_\eta)}^{\xi} P_\xi(H(J, P_\eta), P_\eta, \xi') d\xi' - \bar{\eta}\bar{P}_\eta. \quad (\text{C.30})$$

$\xi_0$  is again some arbitrary function which instructs us where to begin integration along a trajectory.

We now evaluate the transformation. We have

$$\bar{P}_\eta = -\frac{\partial S}{\partial \bar{\eta}} = P_\eta, \quad (\text{C.31})$$

so the transformation leaves the  $\eta$  momentum the same. We also have

$$P_\xi = \frac{\partial S}{\partial \xi} = P_\xi(H(J, P_\eta), P_\eta, \xi), \quad (\text{C.32})$$

which is simply expressing  $P_\xi$  along a trajectory as a function of  $J$ ,  $P_\eta$ , and  $\xi$ . The angle variable is

$$\phi = \frac{\partial S}{\partial J} = \int_{\xi_0}^{\xi} \frac{\partial P_\xi}{\partial H} \frac{\partial H}{\partial J} d\xi' - \frac{\partial \xi_0}{\partial J} P_\xi(H(J, P_\eta), P_\eta, \xi_0) \quad (\text{C.33})$$

$$= \frac{1}{\Delta t} \int_{\xi_0}^{\xi} \frac{1}{\dot{\xi}} d\xi' - \phi_0(J, P_\eta) \quad (\text{C.34})$$

$$= \frac{t}{\Delta t} - \phi_0(J, P_\eta), \quad (\text{C.35})$$

where

$$\phi_0(J, P_\eta) = \frac{\partial \xi_0}{\partial J} P_\xi(H(J, P_\eta), P_\eta, \xi_0). \quad (\text{C.36})$$

Again,  $\phi$  equals the amount of time taken to reach  $\xi$  from  $\xi_0$  divided by the period of motion.

Finally, using Eq. (5.4) to evaluate  $\partial H(J, P_\eta)/\partial P_\eta$ , we have

$$\eta = -\frac{\partial S}{\partial P_\eta} = -\int_{\xi_0}^{\xi} \left[ \frac{\partial P_\xi}{\partial H} \frac{\partial H(J, P_\eta)}{\partial P_\eta} + \frac{\partial P_\xi}{\partial P_\eta} \right] d\xi' - \frac{\partial \xi_0}{\partial P_\eta} P_\xi(H(J, P_\eta), P_\eta, \xi_0) + \bar{\eta} \quad (\text{C.37})$$

$$= -\int_{\xi_0}^{\xi} \left[ \frac{1}{\dot{\xi}} \frac{\Delta \eta}{\Delta t} - \frac{\dot{\eta}}{\dot{\xi}} \right] d\xi' - \eta_0(J, P_\eta) + \bar{\eta} \quad (\text{C.38})$$

$$= \int_{\xi_0}^{\xi} \frac{\dot{\eta}}{\dot{\xi}} d\xi' - \frac{\Delta \eta}{\Delta t} t - \eta_0(J, P_\eta) + \bar{\eta}, \quad (\text{C.39})$$

where

$$\eta_0(J, P_\eta) = \frac{\partial \xi_0}{\partial P_\eta} P_\xi(H(J, P_\eta), P_\eta, \xi_0). \quad (\text{C.40})$$

The integral evaluates to  $\eta$ , and canceling  $\eta$  from both sides of Eq. (C.39) gives

$$\bar{\eta} = \frac{\Delta \eta}{\Delta t} t + \eta_0(J, P_\eta). \quad (\text{C.41})$$

This shows that  $\bar{\eta}$  evolves linearly in time at the drift velocity  $\Delta \eta/\Delta t$ . This fact was derived as consequence of effecting a transformation to action-angle coordinates for the  $(\xi, P_\xi)$  pair.

## Appendix D

# Additional Calculations

The following sections contain several calculations that can be omitted from Chapter 5 on a first read but that may be of interest to those desiring more detail.

### D.1 First-Order Correction and Guiding Center Definitions

In Sec. 5.2.4, we retained the first-order term in the expansion of the potential  $V$  and obtained

$$J(H, P_y) = J_0 \left( H - qV(x_{\text{gc}}, y, t) + \frac{m}{2} \left( \frac{\partial_x V}{B_z} \right)^2, P_y \right), \quad (\text{D.1})$$

where  $J_0$  is the action integral when  $V = 0$ . We observed that the effects of retaining the  $\delta x$  term of  $V$  is to add to the energy the term  $(m/2)(\partial_x V/B)^2$ , which leads to a higher-order correction to the drift velocity shown in Eq. (5.147). However, we shall now see that this terms can be viewed as a consequence of the the definition of guiding center. We highlight this fact because any comparison of higher-order drifts derived in Ch. 5 with other work on guiding center drifts needs to take into account the possibility of a discrepancy guiding center definitions.

We defined the guiding center as the  $x$  location where the  $y$  velocity vanished. In Sec. 5.2.1, this definition was consistent with the fact that the guiding center approximation is a harmonic-oscillator approximation because  $x_{\text{gc}}$  is the minimum of the effective potential

$$U_{\text{eff}} = \frac{(P_y - qA_y)^2}{2m}. \quad (\text{D.2})$$

In Sec. 5.2.4, we continued to use this definition of guiding center even after introducing the potential  $V$ . However, the effective potential is now different:

$$U_{\text{eff}} = \frac{(P_y - qA_y)^2}{2m} + qV, \quad (\text{D.3})$$

so that  $x_{\text{gc}}$ , as previously defined, is no longer the minimum of  $U_{\text{eff}}$ .

If we assume that the electric field is a perturbation to the problem of a charged particle in a magnetic field, then we expect that the true location of the minimum, which we will denote  $x_m$ , is not very different from  $x_{\text{gc}}$ , that is,  $x_m = x_{\text{gc}} + \delta x_{\text{gc}}$ , where  $\delta x_{\text{gc}}$  is assumed small. We determine  $\delta x_{\text{gc}}$  by requiring that  $x_m$  minimizes  $U_{\text{eff}}$ :

$$0 = \left. \frac{dU_{\text{eff}}}{dx} \right|_{x=x_m} = \left[ -qB_z \frac{P_y - qA_y}{m} + q \frac{dV}{dx} \right]_{x=x_m}. \quad (\text{D.4})$$

We do a Taylor expansion about  $x_{\text{gc}}$

$$0 = -q \left( B_z(x_{\text{gc}}) + \frac{dB_z}{dx}(x_{\text{gc}})\delta x_{\text{gc}} \right) \frac{P_y - qA_y(x_{\text{gc}}) - qB_z(x_{\text{gc}})\delta x_{\text{gc}}}{m} + q \frac{dV}{dx} + q \frac{d^2V}{dx^2} \delta x_{\text{gc}}, \quad (\text{D.5})$$

where all derivatives are evaluated at  $x_{\text{gc}}$ . We now recall that, by definition,  $P_y = qA_y(x_{\text{gc}})$  (see Eq. (5.90)), so, keeping terms up to first order in  $\delta x_{\text{gc}}$ ,

$$0 = \frac{q^2}{m} B_z^2 \delta x_{\text{gc}} + q \frac{dV}{dx} + q \frac{d^2V}{dx^2} \delta x_{\text{gc}}. \quad (\text{D.6})$$

Solving for  $\delta x_{\text{gc}}$ ,

$$\delta x_{\text{gc}} = - \frac{\partial_x V}{qB_z^2/m + \partial_{xx} V}. \quad (\text{D.7})$$

In the case where the second derivative of  $V$  is small enough to be dropped, we would have  $\delta x_{\text{gc}} = -m\partial_x V/qB_z^2$ .

We now show that the corrected drift velocity in Eq. (5.148) is actually the value of the  $\mathbf{E} \times \mathbf{B}$  velocity evaluated at  $x_m$  rather than  $x_{\text{gc}}$ . Indeed,

$$\frac{\mathbf{E}(x_m) \times \mathbf{B}(x_m)}{B^2(x_m)} = \frac{\partial_x V(x_m)}{B_z(x_m)} \quad (\text{D.8})$$

$$\approx \frac{\partial_x V(x_{\text{gc}})}{B_z(x_{\text{gc}})} + \delta x_{\text{gc}} \frac{d}{dx} \left[ \frac{\partial_x V}{B_z} \right]_{x=x_{\text{gc}}} \quad (\text{D.9})$$

$$= \frac{\partial_x V(x_{\text{gc}})}{B_z(x_{\text{gc}})} - \frac{m\partial_x V}{qB_z^2} \frac{d}{dx} \left[ \frac{\partial_x V}{B_z} \right]_{x=x_{\text{gc}}} \quad (\text{D.10})$$

$$= \frac{\partial_x V(x_{\text{gc}})}{B_z(x_{\text{gc}})} - v_{\mathbf{E} \times \mathbf{B}} \frac{m}{qB_z} \frac{d}{dx} \left[ \frac{\partial_x V}{B_z} \right]_{x=x_{\text{gc}}}. \quad (\text{D.11})$$

Hence, the higher-order term in Eq. (5.148) can be viewed as a correction to the  $\mathbf{E} \times \mathbf{B}$  that corrects for the fact that the  $\mathbf{E} \times \mathbf{B}$  was evaluated at  $x_{\text{gc}}$  rather than  $x_m$ .

## D.2 Cyclotron-Driven Pondermotive-Potential

In Eq. (5.138), the energy is modified by the addition of the term  $(m/2)(\partial_x V/B)^2$ . Here, we show that this added term is a pondermotive-like potential that arises due to the cyclotron motion.

Pondermotive potentials arise when a charged particle is placed in an oscillating electric field when the field amplitude varies with position. By averaging the equation of motion for the charged particle, it is seen that there is an effective force that drives the particle away from the large field regions and that this force can be described by an effective pondermotive potential [120]:

$$U_{\text{pon}} = \frac{q^2 E(x)^2}{4m(\omega - \mathbf{k} \cdot \mathbf{v})}. \quad (\text{D.12})$$

$\omega$  is the wave frequency,  $\mathbf{k}$  is the wave vector of the wave generating the electric field, and  $\mathbf{v}$  is the averaged velocity of the charged particle. For a particle in a crossed electric and magnetic field, there are no waves, but the particle *experiences* an oscillating electric field due to the cyclotron motion. We take Eq. (D.12) and set  $\mathbf{k} = 0$ , since we are not dealing with a wave, and set  $\omega = qB_z/m$ , the cyclotron frequency. Since the oscillations are in the  $x$  direction, we use  $E = E_x = -\partial_x V$ . Then Eq. (D.12) becomes

$$U_{\text{pon}} = \frac{q^2 (\partial_x V)^2}{4m(qB_z/m)} = \frac{m}{4} \left( \frac{\partial_x V}{B_z} \right)^2, \quad (\text{D.13})$$

which equals the added term in Eq. (5.138) up to a factor of two. This factor of two can be explained as follows. In the wave case, the particle experiences a sinusoidal electric field, but in the cyclotron-driven case the particle experiences a square-wave-like  $\mathbf{E}$ . The  $E$  that appears in Eq. (D.12) is the field amplitude of a sinusoidal field; if we rewrite Eq. (D.12) in terms of the root mean square of the field, we would have

$$U_{\text{pon}} = \frac{q^2 (2E_{\text{RMS}}(x))^2}{4m(\omega - \mathbf{k} \cdot \mathbf{v})}, \quad (\text{D.14})$$

in which case Eq. (D.13) is

$$U_{\text{pon}} = \frac{m}{2} \left( \frac{E_{\text{RMS}}}{B_z} \right)^2. \quad (\text{D.15})$$

Since, in the cyclotron-driven case,  $E_{\text{RMS}} = E = \partial_x V$ , Eq. (D.15) is precisely the extra potential term in Eq. (5.138).

### D.3 A Lemma on Averaging

We develop a lemma concerning the averaging of a scalar function  $f(x)$  over a gyro-orbit again for the case of a magnetic field  $\mathbf{B} = B_z(x)\hat{z}$ . Let the average of  $f(x)$  be defined as

$$\bar{f} = \frac{\int_{t_0}^{t_0+\Delta t} f(x(t)) dt}{\Delta t}, \quad (\text{D.16})$$

and define  $\delta x = x - x_{\text{gc}}$ . Using Eq. (5.91), we can relate  $\delta x$  to  $\dot{y}$ :

$$m\dot{y}(x) = P_y - qA_y(x_{\text{gc}} + \delta x) \quad (\text{D.17})$$

$$\approx P_y - qA_y(x_{\text{gc}}) - q \left. \frac{dA_y}{dx} \right|_{x_{\text{gc}}} \delta x \quad (\text{D.18})$$

$$= qB_z(x_{\text{gc}})\delta x. \quad (\text{D.19})$$

We exploit Eq. (D.19) in a Taylor expansion  $f(x)$  so that the average of  $f$  becomes

$$\bar{f} = \frac{1}{\Delta t} \int_{t_0}^{t_0+\Delta t} \left[ f(x_{\text{gc}}) + \frac{f'(x_{\text{gc}})}{qB_z(x_{\text{gc}})} m\dot{y}(x) \right] dt \quad (\text{D.20})$$

$$= f(x_{\text{gc}}) + \frac{m}{qB_z(x_{\text{gc}})} f'(x_{\text{gc}}) v_d, \quad (\text{D.21})$$

where  $v_d = \Delta y/\Delta t$  is the drift velocity in the  $y$  direction. The second term is a correction term which involves the  $y$  drift. Because  $m/qB_z = \Delta t/2\pi$ , we also have

$$\bar{f} = f(x_{\text{gc}}) + \frac{1}{2\pi} f'(x_{\text{gc}}) \Delta y, \quad (\text{D.22})$$

and it is interesting to note that the correction involve an  $x$  derivative of  $f$  times the net  $y$  displacement.

## D.4 Flux Enclosed by an Orbit: Lab Frame Calculation

In this section, we rederive the magnetic flux enclosed by one gyration of a charged particle in a magnetic field through a different technique than that presented in Sec. 5.2.5. In the lab frame, the flux is not well-defined because the trajectory does not close on itself, so we do not have a definite surface through which to compute flux. We surmount this difficulty by artificially closing the trajectory, computing the flux, and then judiciously averaging the answer over a period of motion. The flux obtained is equal to that given in Eq. (D.26). For clarity, we shall work with magnetic fields  $\mathbf{B} = B_z(x)\hat{z}$  so that the only drift is the grad-B drift, which is in the  $y$  direction.

While the trajectory does not close on itself, we can define a flux value for each point along the trajectory. Given a point  $(x_0, y_0)$  on the trajectory, the regions through which we will measure flux are bounded by two curves defined as follows. The first curve follows the trajectory for one period as the particle moves from  $(x_0, y_0)$  to  $(x_0, y_0 + \Delta y)$ . The second curve is a vertical segment of length  $\Delta y$  that joins the starting point with the endpoint. Fig. D.1 shows several such regions for different starting locations; it is apparent that every region encloses a different amount of flux.

We now evaluate the flux, which we denote by  $\Phi(x_0)$ , through each region defined above for a point  $(x_0, y_0)$ . The surface integral for flux can, by Stokes' theorem, be converted into a line integral of  $\mathbf{A}$ , and this line integral is split into two parts: the segment that follows the trajectory and the

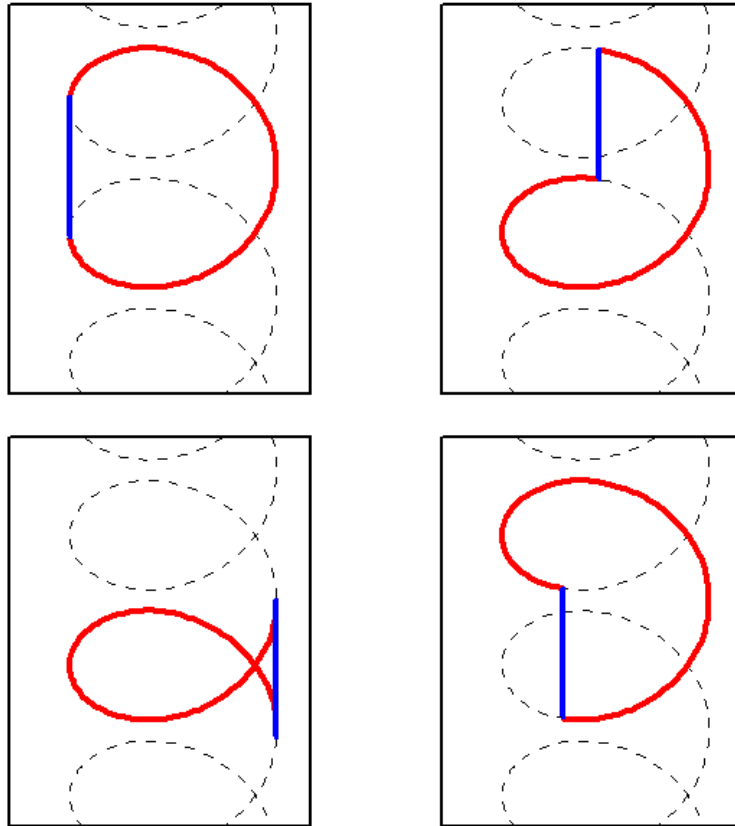


Figure D.1: In the lab frame, the flux of a gyration depends on how one defines the starting point; this figure explicitly shows four possibilities. The dotted lines represent an electron trajectory, and the solid red and blue lines together bound the region through which we measure flux. The solid red lines trace one period of motion, while the solid blue lines are the connecting paths used to close the gyro-orbits. Clearly, the amount of flux enclosed is different for each region.

vertical segment that joins the starting and ending points.

$$\Phi(x_0) = \oint \mathbf{A} \cdot d\mathbf{l} = \int_{\text{trajectory}} \mathbf{A} \cdot d\mathbf{l} + \int_{\text{connecting}} \mathbf{A} \cdot d\mathbf{l}, \quad (\text{D.23})$$

The first integral is equal to  $\partial J / \partial q$  by virtue of Eq. (5.160) with  $V = 0$ . Therefore

$$\Phi(x_0) = \frac{\partial J}{\partial q} - A_y(x_0)\Delta y. \quad (\text{D.24})$$

The first term is the contribution from the trajectory itself and is independent of  $x_0$ . The second term comes from the connecting path and clearly depends upon  $x_0$ . This  $x_0$  dependence is undesirable, for we would like flux to be a property of the entire orbit just as the area of a geometric shape has nothing to do with any particular point along the perimeter.

To obtain a flux that is independent of starting point and representative of the entire orbit, we

take the democratic approach and average  $\Phi(x_0)$  over all points on a trajectory. The averaging will be weighted by the amount of time the particle in orbit spends at position  $x_0$ , just as in Eq. (D.16).  $A_y(x)$  is easily averaged by considering  $P_y = mv_y + qA_y(x)$  and observing that the average of  $v_y$  is the drift velocity  $v_d = \Delta y/\Delta t$ , from which

$$\bar{A}_y = \frac{1}{q} \left( P_y - m \frac{\Delta y}{\Delta t} \right). \quad (\text{D.25})$$

Strangely, this is the same answer as would have been obtained from the approximate averaging formula given by Eq. (D.22), which apparently holds exactly for the function  $A_y(x)$ . Substituting  $\bar{A}_y$  from Eq. (D.25) into Eq. (D.24) gives

$$\Phi = \frac{\int \Phi(x(t)) dt}{\Delta t} = \frac{\partial J}{\partial q} - \frac{1}{q} \left( P_y - m \frac{\Delta y}{\Delta t} \right) \Delta y. \quad (\text{D.26})$$

This result will be verified in the following section, where we will evaluate the flux by a different technique.

## D.5 Phase Space Contours

We rederive Eq. (5.168) by integrating over special phase space contours using techniques from differential geometry as described by Montgomery [103]. The contours lie entirely within the submanifolds of phase space defined such that  $P_y$  is constant. Such submanifolds have three dimensions with coordinates  $(x, P_x, y)$ . The contours consist of two parts: the first part follows the trajectory over one gyration, while the second part travels in the  $y$  direction to rejoin its starting point. Fig. D.2 depicts such a contour. The contours used in Sec. D.4 to compute the flux are the projections of these contours onto the  $xy$  plane.

The proper way of proceeding would be to invoke techniques from differential geometry [94, pg. 174]. Differential geometry generalizes concepts from multivariate calculus to manifolds of arbitrary dimensions, and these generalizations often do not require a metric, or definition of distance, on the manifold. Phase space, for example, is an abstract space in which we cannot talk about notions of distance, but differential geometry allows us to talk about integrals over lines and surfaces. Fortunately, the manifolds we will consider have three dimensions, and this allows us to identify techniques from differential geometry with those from three-dimensional calculus. For instance, a one-form is a mathematical object from differential geometry that is integrated over lines, and a two-form is integrated over two-dimensional surface. On a three-dimensional manifold, however, these are analogous to line and surface integrals of vector fields. Montgomery provides a very readable explanation of differential forms in this context.

With that preamble, we integrate the canonical one-form, also known as Poincaré's form [94, pg.

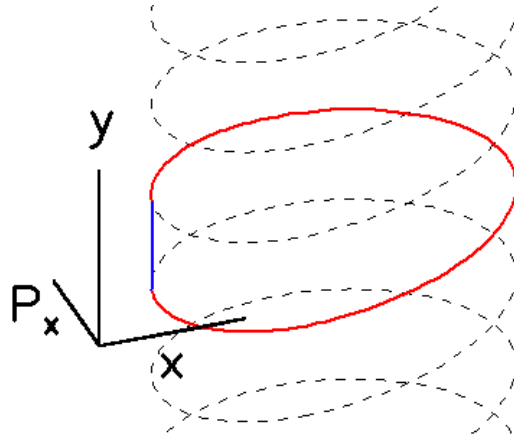


Figure D.2: The phase space contour under consideration follows the trajectory for one period, as shown by the red line, and then rejoins its starting point by traveling straight up the  $y$  axis, as shown by the blue line.

238], over the contours discussed above. The canonical one-form is

$$\theta = P_x dx + P_y dy, \quad (\text{D.27})$$

but we can identify  $\theta$  with a phase space vector field  $\mathbf{V}$ :

$$\mathbf{V} = P_x \hat{x} + P_y \hat{y}. \quad (\text{D.28})$$

We now perform the integration. Over the first part of the contour, kinetic energy is constant, so

$$\int_I \theta = \int_I \mathbf{V} \cdot d\mathbf{l} \quad (\text{D.29})$$

$$= \int_I [mv_x dx + mv_y dy + qA(x)dy] \quad (\text{D.30})$$

$$= \int_I m [v_x^2 + v_y^2] dt + q \int_I A(x) dy \quad (\text{D.31})$$

$$= 2H\Delta t + q \frac{\partial J}{\partial q}. \quad (\text{D.32})$$

Integrating over the second branch,

$$\int_{II} \theta = \int_{II} \mathbf{V} \cdot d\mathbf{l} = \int_{II} P_y dy = -P_y \Delta y. \quad (\text{D.33})$$

The minus sign occurs because we are traveling backwards in the sense opposite to  $\Delta y$ . Since the total contour is closed, we apply Stokes' theorem. In differential geometry, we would take the differential of  $\theta$  and obtain the two-form  $d\theta = dP_x \wedge dx$ , since  $P_y$  is constant on the submanifold. Thinking in terms of vector calculus, taking the differential of  $\theta$  is equivalent to taking the curl of

$\mathbf{V}$ ,  $\nabla \times \mathbf{V} = \hat{y}$ . Either way, we integrate over the surface spanned by the contour:

$$\int_{I+II} \mathbf{V} \cdot d\mathbf{l} = \int \nabla \times \mathbf{V} \cdot d\mathbf{S} = \int \hat{y} \cdot d\mathbf{S} = J(H, P_z), \quad (\text{D.34})$$

because  $\hat{y} \cdot d\mathbf{S}$  is the project of the area element onto the  $xP_x$  plane, and this area is indeed the  $x$  action. Equating the line integral, which is the sum of Eqs. (D.32) and (D.33), with the surface integral given by Eq. (D.34), gives

$$J(H, P_y, q) = 2H\Delta t + q \frac{\partial J}{\partial q} + P_y \frac{\partial J}{\partial P_y}. \quad (\text{D.35})$$

which is equivalent to Eq. (5.168).

# Bibliography

- [1] Paul Murray Bellan. Spheromaks: a practical application of magnetohydrodynamic dynamos and plasma self-organization. Imperial College Press, London River Edge, NJ, 2000.
- [2] Paul Murray Bellan. Fundamentals of plasma physics. Cambridge University Press, Cambridge, UK ; New York, 2006.
- [3] M. A. Berger. Introduction to magnetic helicity. Plasma Physics and Controlled Fusion, 41:B167–B175, 1999.
- [4] H. K. Moffatt. Magnetic field generation in electrically conducting fluids. Cambridge University Press, Cambridge; New York, 1978.
- [5] H. K. Moffatt. The degree of knottedness of tangled vortex lines. Journal of Fluid Mechanics, 35(01):117, 1969.
- [6] J. B. Taylor. Relaxation of toroidal plasma and generation of reverse magnetic fields. Physical Review Letters, 33(19):1139–1141, 1974.
- [7] E. G. Zweibel and M. Yamada. Magnetic reconnection in astrophysical and laboratory plasmas. volume 47 of Annual Review of Astronomy and Astrophysics, pages 291–332. 2009.
- [8] H. Pfister and W. Gekelman. Demonstration of helicity conservation during magnetic reconnection using Christmas ribbons. American Journal of Physics, 59(6):497–502, 1991.
- [9] L. Woltjer. A theorem on force-free magnetic fields. Proceedings of the National Academy of Sciences of the United States of America, 44(6):489–491, 1958.
- [10] T. Jarboe. Review of spheromak research. Plasma Physics and Controlled Fusion, 36(6):945–990, 1994.
- [11] Y. Nakagawa, M. Raadu, E. Billings, and D. McNamara. Topology of filaments and chromospheric fibrils near sunspots. Solar Physics, 19(1):72, 1971.
- [12] J. Heyvaerts and E. Priest. Coronal heating by reconnection in DC current systems - a theory based on Taylor’s hypothesis. Astronomy and Astrophysics, 137(1):63–78, 1984.

- [13] A. Choudhuri and A. Konigl. Magnetic energy dissipation in force-free jets. *Astrophysical Journal Letters*, 310(1):96–103, 1986.
- [14] J. M. Finn, P. N. Guzdar, and D. Usikov. Three-dimensional force-free looplike magnetohydrodynamic equilibria. *Astrophysical Journal*, 427(1):475–482, 1994. Part 1.
- [15] D. M. Rust and A. Kumar. Helical magnetic fields in filaments. *Solar Physics*, 155(1):69–97, 1994.
- [16] T. H. Jensen. Current drive and helicity injection. *The Physics of Fluids*, 27(12):2881, 1984.
- [17] D. Kumar and P. M. Bellan. Nonequilibrium Alfvénic plasma jets associated with spheromak formation. *Physical Review Letters*, 103(10), 2009.
- [18] P. M. Bellan and J. F. Hansen. Laboratory simulations of solar prominence eruptions. *Physics of Plasmas*, 5(5):1991–2000, 1998.
- [19] J. F. Hansen and P. M. Bellan. Experimental demonstration of how strapping fields can inhibit solar prominence eruptions. *Astrophysical Journal*, 563(2):L183–L186, 2001.
- [20] J. F. Hansen, S. K. P. Tripathi, and P. M. Bellan. Co- and counter-helicity interaction between two adjacent laboratory prominences. *Physics of Plasmas*, 11(6):3177–3185, 2004.
- [21] John Freddy Hansen. *Laboratory Simulations of Solar Prominences*. PhD thesis, California Institute of Technology, Pasadena, CA, May 2001.
- [22] S.W. Kahler, R.L. Moore, S.R. Kane, and H. Zirin. Filament eruptions and the impulsive phase of solar flares. *Astrophysical Journal*, 328:824–829, 1988.
- [23] Y. Ono, M. Yamada, T. Akao, T. Tajima, and R. Matsumoto. Ion acceleration and direct ion heating in three-component magnetic reconnection. *Physical Review Letters*, 76(18):3328–3331, 1996.
- [24] M. Yamada, Y. Ono, A. Hayakawa, M. Katsurai, and F. W. Perkins. Magnetic reconnection of plasma toroids with co-helicity and counterhelicity. *Physical Review Letters*, 65(6):721–724, 1990.
- [25] C. D. Cothran. Observation of a helical self-organized state in a compact toroidal plasma. *Physical Review Letters*, 103(21):215002, 2009.
- [26] T. Gray. Three-dimensional reconnection and relaxation of merging spheromak plasmas. *Physics of Plasmas*, 17(10):102106, 2010.
- [27] Claude Côté. *Power balance and characterization of impurities in the Maryland Spheromak*. PhD thesis, University of Maryland, 1993.

- [28] J. F. Drake, M. A. Shay, W. Thongthai, and M. Swisdak. Production of energetic electrons during magnetic reconnection. Physical Review Letters, 94(9):095001, 2005.
- [29] J. F. Drake, M. Swisdak, H. Che, and M. A. Shay. Electron acceleration from contracting magnetic islands during reconnection. Nature, 443(7111):553–556, 2006.
- [30] S. von Goeler, W. Stodiek, and N. Sauthoff. Studies of internal disruptions and  $m = 1$  oscillations in tokamak discharges with soft-x-ray techniques. Physical Review Letters, 33(20):1201–1203, 1974.
- [31] P. V. Savrukhn. Generation of suprathermal electrons during magnetic reconnection at the sawtooth crash and disruption instability in the T-10 tokamak. Physical Review Letters, 86(14):3036, 2001.
- [32] P.V. Savrukhn and S.V. Tsaun. Sawtooth instability and magnetic reconnection in tokamak plasma. In 19th IAEA Fusion Energy Conference. IAEA, 2002.
- [33] Hannes Alfvén and Carl-Gunne Fälthammar. Cosmical electrodynamics; fundamental principles. Clarendon Press, Oxford, 1963.
- [34] L. D. Landau and E. M. Lifshitz. Mechanics. Course of theoretical physics. Pergamon Press, Oxford; New York, 3rd edition, 1976.
- [35] T. G. Northrop and E. Teller. Stability of the adiabatic motion of charged particles in the Earth’s field. Physical Review, 117(1):215–225, 1960.
- [36] Gunsu Soonshin Yun. Dynamics of plasma structures interacting with external and self-generated magnetic fields. PhD thesis, California Institute of Technology, Pasadena, CA, July 2007.
- [37] D. Kumar, A. Moser, and P. Bellan. Energy efficiency analysis of the discharge circuit of Caltech Spheromak Experiment. IEEE Transactions on Plasma Science, 38(1):47–52, 2010.
- [38] M. D. Kruskal. Hydromagnetic instability in a stellarator. The Physics of Fluids, 1(5):421, 1958.
- [39] V.D. Shafranov. On magnetohydrodynamical equilibrium configurations. Soviet Physics JETP, 6:545–54, 1958.
- [40] P. M. Bellan. Why current-carrying magnetic flux tubes gobble up plasma and become thin as a result. Physics of Plasmas, 10(5):1999–2008, 2003. 44th Annual Meeting of the Division of Plasma of the American Physical Society.

- [41] G. Yun and P. Bellan. Plasma tubes becoming collimated as a result of magnetohydrodynamic pumping. Physics of Plasmas, 17(6):062108, 2010.
- [42] S. K. P. Tripathi, P. M. Bellan, and G. S. Yun. Observation of kinetic plasma jets in a coronal-loop simulation experiment. Physical Review Letters, 98(13), 2007.
- [43] E. V. Stenson. Dual-species plasmas illustrate MHD flows. IEEE Transactions on Plasma Science, 36(4):1206, 2008.
- [44] The Center for X-Ray Optics. X-ray interactions with matter. URL [http://henke.lbl.gov/optical\\_constants](http://henke.lbl.gov/optical_constants).
- [45] G. S. Yun, S. You, and P. M. Bellan. Large density amplification measured on jets ejected from a magnetized plasma gun. Nuclear Fusion, 47(3):181–188, 2007.
- [46] S. You, G. S. Yun, and P. M. Bellan. Dynamic and stagnating plasma flow leading to magnetic flux tube collimation. Physical Review Letters, 95(4), 2005.
- [47] V. H. Chaplin, M. R. Brown, D. H. Cohen, T. Gray, and C. D. Cothran. Spectroscopic measurements of temperature and plasma impurity concentration during magnetic reconnection at the Swarthmore Spheromak Experiment. Physics of Plasmas, 16(4), 2009.
- [48] S. J. Zweben, C. R. Menyuk, and R. J. Taylor. Vacuum photodiode detector array for broadband UV detection in a tokamak plasma. Review of Scientific Instruments, 50(8):972–978, 1979.
- [49] P. Lee, J. Gernhardt, C. J. Armentrout, and R. T. Snider. Vacuum ultraviolet and ultrasoft x-ray diode detectors for tokamak plasmas. Review of Scientific Instruments, 59(6):883–888, 1988.
- [50] S. J. Zweben and R. J. Taylor. Filtered and bare vacuum photodiode detectors for VUV monitoring of tokamak plasmas. Plasma Physics and Controlled Fusion, 23(4):337–346, 1981.
- [51] H. N. Kornblum and V. W. Slivinsky. Flat-response, subkiloelectronvolt x-ray detector with a subnanosecond time response. Review of Scientific Instruments, 49(8):1204–1205, 1978.
- [52] F. P. Adams, A. Ng, and Y. Gazit. Simple, high-speed x-ray diode. Review of Scientific Instruments, 58(6):1130–1132, 1987.
- [53] J. R. Kerns and D. J. Johnson. Study of an electron-beam discharge into a vacuum diode with polyethylene anode. Journal of Applied Physics, 45(12):5225–5228, 1974.
- [54] G. Idzorek and H. Oona. Properties of plasma radiation diagnostics. Review of Scientific Instruments, 68(1):1065–1068, 1997.

- [55] F. H. Seguin, R. D. Petrasso, and C. K. Li. Radiation-hardened x-ray imaging for burning-plasma tokamaks. Review of Scientific Instruments, 68(1):753–756, 1997. 11th Topical Conference on High-Temperature Plasma Diagnostics.
- [56] Y. V. Gott and M. M. Stepanenko. Vacuum photodiode detectors for soft x-ray ITER plasma tomography. Review of Scientific Instruments, 76(7), 2005.
- [57] Space environment (natural and artificial) - Process for determining solar irradiances. Technical Report ISO 21348, International Organization for Standardization, 2007.
- [58] J. A. R. Samson and R. B. Cairns. Photoelectric yield of aluminum from 300 to 1300 Å. The Review of Scientific Instruments, 36(1):19–21, January 1965.
- [59] R.B. Cairns and J.A.R. Samson. Metal photocathodes as secondary standards for absolute intensity measurements in the vacuum ultraviolet. Journal of the Optical Society of America, 56(11):1586, 1573 1966.
- [60] PerkinElmer. Short Arc Xenon Flashlamp.
- [61] Janis Research. Window transmission curves. URL <http://www.janis.com/products/accessoriesandancillaryequipment/WindowTransmissionCurves.aspx>.
- [62] C. Kenty. Photoelectric yields in the extreme ultraviolet. Physical Review, 44:891–897, 1933.
- [63] N. Wainfan, W.C. Walker, and G.L. Weissler. Preliminary results on photoelectric yields of Pt and Ta and on photoionization in O<sub>2</sub> and N<sub>2</sub> in the vacuum ultraviolet. Journal of Applied Physics, 24(10):1318–1321, October 1953.
- [64] W.C. Walker, N. Wainfan, and G.L. Weissler. Photoelectric yields in the vacuum ultraviolet. Journal of Applied Physics, 26(11):1366–1371, November 1955.
- [65] H.E. Hinteregger and K. Watanabe. Photoelectric cells for the vacuum ultraviolet. Journal of the Optical Society of America, 43(7):604–608, July 1953.
- [66] H.E. Hinteregger. Photoelectric emission in the extreme ultraviolet. Physical Review, 96(2):538–539, 1954.
- [67] R. Brogle, P. Muggli, P. Davis, G. Hairapetian, and C. Joshi. Studies of linear and nonlinear photoelectric emission for advanced accelerator applications. Proceedings of the 1995 Particle Accelerator Conference, Vols 1-5, pages 1039–1042, 1996.
- [68] Stuart M. Wentworth. Applied electromagnetics: early transmission lines approach. Wiley series in electrical and computer engineering. John Wiley, Hoboken, NJ, 2007.

- [69] I. Langmuir. The effect of space charge and residual gases on thermionic currents in high vacuum. Physical Review, 2(6):450–486, 1913.
- [70] E. Vance. Shielding effectiveness of braided-wire shields. IEEE Transactions on Electromagnetic Compatibility, EM17(2):71–77, 1975.
- [71] Y. H. Lin and D. C. Joy. A new examination of secondary electron yield data. Surface and Interface Analysis, 37(11):895–900, 2005.
- [72] F. M. Propst and E. Luscher. Auger electron ejection from tungsten surfaces by low-energy ions. Physical Review, 132(3):1037, 1963.
- [73] I. A. Abroyan, M. A. Ereemeev, and N. N. Petrov. Excitation of electrons in solids by relatively slow atomic particles. Soviet Physics Uspekhi, 10(3):332–367, 1967.
- [74] V. Baglin, J. Bojko, O. Grobner, B. Henrist, N. Hillret, C. Scheuerlein, and M. Taborelli. The secondary electron yield of technical materials and its variation with surface treatment. Proceedings of EPAC 2000, pages 217 – 221, 2000.
- [75] J. D. Huba. NRL plasma formulary. Naval Research Laboratory, 2009.
- [76] ThorLabs. 150 nm to 4.6  $\mu\text{m}$  amplified photodetectors. URL <http://www.thorlabs.us/thorProduct.cfm?partNumber=PDA36A>.
- [77] Takashi Fujimoto. Plasma Spectroscopy. Clarendon Press ; Oxford University Press, Oxford; New York, 2004.
- [78] S. Costa, R. Deangelis, S. Ortolani, and M. Puiatti. Total radiation measurements in the ETA-BETA II experiment. Nuclear Fusion, 22(10):1301–1311, 1982.
- [79] George B. Rybicki and Alan P. Lightman. Radiative processes in astrophysics. Wiley-VCH, New York, 2004.
- [80] Yu. Ralchenko, A.E. Kramida, J. Reader, and NIST ASD Team. NIST Atomic Spectra Database (ver. 4.0.1). National Institute of Standards and Technology, Gaithersburg, MD, 2010. URL <http://physics.nist.gov/asd>.
- [81] J. L. Terry, B. Lipschultz, A. Yu. Pigarov, S. I. Krasheninnikov, B. LaBombard, D. Lumma, H. Ohkawa, D. Pappas, and M. Umansky. Volume recombination and opacity in Alcator C-Mod divertor plasmas. Physics of Plasmas, 5(5):1759–1766, 1998.
- [82] R. W. P. McWhirter and A. G. Hearn. A calculation of instantaneous population densities of excited levels of hydrogen-like ions in a plasma. Proceedings of the Physical Society of London, 82(529):641–654, 1963.

- [83] D. E. Post. A review of recent developments in atomic processes for divertors and edge plasmas. Journal of Nuclear Materials, 220-222:143–157, 1995.
- [84] Peter C. Stangeby. The plasma boundary of magnetic fusion devices. Institute of Physics Pub., Bristol; Philadelphia, 2000.
- [85] P. G. Carolan and V. A. Piotrowicz. The behavior of impurities out of coronal equilibrium. Plasma Physics and Controlled Fusion, 25(10):1065–1086, 1983.
- [86] D. G. Whyte, R. P. Seraydarian, and R. P. Doerner. Carbon impurity characterization on a linear plasma device using visible emission spectroscopy. Journal of Vacuum Science and Technology A: Vacuum, Surfaces, and Films, 17(5):2713–2718, 1999.
- [87] P. M. Bellan. Thermal instability of electrolytic capacitor bank used for gas puff valve. Review of Scientific Instruments, 73(8):2900–2905, 2002.
- [88] M. Øieroset, R.P. Lin, T.D. Phan, D.E. Larson, and S.D. Bale. Evidence for electron acceleration up to  $\sim 300$  keV in the magnetic reconnection diffusion region of earth’s magnetotail. Physical Review Letters, 89(19):195001, 2002.
- [89] L. J. Chen. Observation of energetic electrons within magnetic islands. Nature Physics, 4(1):19, 2008.
- [90] D. Lumma, J.L. Terry, and B. Lipschultz. Radiative and three-body recombination in the Alcator C-Mod divertor. Physics of Plasmas, 4(7):2555, 1997.
- [91] R. J. Perkins and P. M. Bellan. Wheels within wheels: Hamiltonian dynamics as a hierarchy of action variables. Physical Review Letters, 105(12), 2010.
- [92] Herbert Goldstein, Charles P. Poole, and John L. Safko. Classical mechanics. Addison Wesley, San Francisco, 3rd edition, 2002.
- [93] Francis F. Chen. Introduction to plasma physics. Plenum Press, New York, 1974.
- [94] V. I. Arnol’d. Mathematical methods of classical mechanics. Graduate texts in mathematics 60. Springer, New York, 2nd edition, 1997.
- [95] Jerrold E. Marsden and Tudor S. Ratiu. Introduction to mechanics and symmetry: a basic exposition of classical mechanical systems. Texts in applied mathematics 17. Springer, New York, 2nd edition, 1999.
- [96] Allan J. Lichtenberg and M. A. Leiberman. Regular and chaotic dynamics. Springer-Verlag, New York, 1992.

- [97] Max Born. The mechanics of the atom. F. Ungar Pub. Co., New York,, 1960.
- [98] D. J. Griffiths. Introduction to electrodynamics. Prentice Hall International, London, 1999.
- [99] K. Stefanski and H. S. Taylor. New approach to understanding quasiperiodicity in nonintegrable Hamiltonian systems. Physical Review A, 31(5):2810–2820, 1985.
- [100] D. L. Bruhwiler and J. R. Cary. Particle dynamics in a large-amplitude wave packet. Physical Review Letters, 68(3):255–258, 1992.
- [101] M.C. Gutzwiller. Energy spectrum according to classical mechanics. Journal of Mathematical Physics, 11(6):1791–1806, 1970.
- [102] Y. Aharonov. Significance of electromagnetic potentials in the quantum theory. Physical Review, 115(3):485, 1959.
- [103] R. Montgomery. How much does the rigid body rotate? A Berry’s phase from the 18th century. American Journal of Physics, 59(5):394–398, 1991.
- [104] Dariusz Chruscinski and Andrzej Jamiolkowski. Geometric phases in classical and quantum mechanics. Birkhäuser, Boston, 2004.
- [105] J. D. Lawson. Simple models of solid and hollow relativistic electron beams with arbitrarily high current. Physics of Fluids, 16(8):1298–1299, 1973.
- [106] J. Neuberger and J. Gruenebaum. Trajectories of charged particles near a long straight wire. European Journal of Physics, 3, 1982.
- [107] Milton Abramowitz and Irene A. Stegun. Handbook of mathematical functions with formulas, graphs, and mathematical tables. U.S. Government Printing Office, Washington D.C., 1964.
- [108] M. J. Wouters. Ion optical properties of a co-axial Wien filter. Journal of Physics D-Applied Physics, 28(8):1547–1552, 1995.
- [109] H. Alfvén. On the motion of cosmic rays in interstellar space. Physical Review, 55(5):0425–0429, 1939.
- [110] J. G. Chervenak. The back electric-field from a long wire. American Journal of Physics, 54(10):946–947, 1986.
- [111] M. A. Heald. Induced electric field from a time-dependent current. American Journal of Physics, 54(12):1142–1143, 1986.
- [112] M. A. Heald. Electric fields and charges in elementary circuits. American Journal of Physics, 52(6):522–526, 1984.

- [113] T. W. Speiser. Particle trajectories in model current sheets, 2. Applications to auroras using a geomagnetic tail model. Journal of Geophysical Research, 72(15):3919, 1967.
- [114] C. Hewson. The effect of electrostatic screening of Rogowski coils designed for wide-bandwidth current measurement in power electronic applications. IEEE Power Electronics Specialists Conference (PESC), 2:1143, 2004.
- [115] C. Størmer. The Polar Aurora. Oxford at the Clarendon Press, London, 1955.
- [116] J. V. Shebalin. Størmer regions for axisymmetric magnetic multipole fields. Physics of Plasmas, 11(7):3472–3482, 2004.
- [117] S. G. Shepherd and B. T. Kress. Størmer theory applied to magnetic spacecraft shielding. Space Weather, 5(4), 2007.
- [118] T. W. Kornack, P. K. Sollins, and M. R. Brown. Experimental observation of correlated magnetic reconnection and Alfvénic ion jets. Physical Review E, 58(1):R36–R39, 1998.
- [119] R. G. Littlejohn. The semiclassical evolution of wave packets. Physics Reports, 138(4-5):193, 1986.
- [120] I. Y. Dodin and N. J. Fisch. Nonadiabatic ponderomotive potentials. Physics Letters A, 349(5):356–369, 2006.